CENTRO BRASILEIRO DE PESQUISAS FÍSCAS

DOCTORAL THESIS

CP violation studies in three-body charmless $B^{\pm}$ decays and contributions to the LHCb SciFi Tracker

Author:
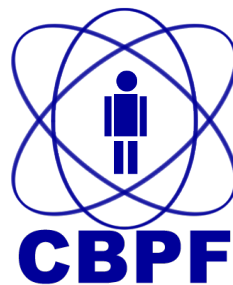Ana Bárbara RODRIGUES
CAVALCANTE

Supervisor:
Dr. Ignácio BEDIAGA
Co-supervisor:
Dr. Christian JORAM

A thesis submitted in fulfillment of the requirements
for the degree of Doctor of Philosophyin Physics
in the Brazilian Center for Research in Physics (CBPF)

Rio de Janeiro
2017

"Notre société, où règne un désir âpre de luxe et richesse, ne comprend pas la valeur de la science. Elle ne réalise pas que celle-ci fait partie de son patrimone suffisamment compte que la science est à la base de tous les progrès qui allègent la vie humaine et en diminuent la souffrance."

Marie Skłodowska Curie

Abstract

In the first part of the thesis we present studies on three body charmless $B^{\pm}$ decays. The analysis is performed using LHCb dataset from proton-proton collisions at the centre-of-mass energy of $7\,\text{TeV}$ and $8\,\text{TeV}$ collected in 2011 and 2012, respectively, corresponding to an integrated luminosity of $3.1\,\text{fb}^{-1}$. We measured the inclusive CP asymmetry of the four channels: $B^{\pm} \rightarrow K^{\pm}\pi^{+}\pi^{-}$, $B^{\pm} \rightarrow K^{\pm}K^{+}K^{-}$, $B^{\pm} \rightarrow \pi^{\pm}\pi^{+}\pi^{-}$ and $B^{\pm} \rightarrow \pi^{\pm}K^{+}K^{-}$. CP asymmetries were also studied along the phase space.

The second part of this thesis is devoted to my contribution to the LHCb SciFi Tracker, a detector made of scintillating fibres. It presents the experimental setups used to characterise the scintillating fibres which needs to meet specific requirements to be able to operate under the running conditions foreseen for the LHCb upgrade. In addition, we discuss the results on the development of fibres made of a new class of scintillating material denominated as Nanostructured Organosilicon Luminophores (NOL). They were found to have a decay time constant at least two times shorter than the fastest scintillating fibres.

Resumo

Na primeira parte desta tese, apresentamos estudos envolvendo decaimentos do méson $B^{\pm}$ em três hádrons. Esta análise foi realizada com amostras de dados do LHCb de colisões próton-próton com energias de $7\,\text{TeV}$ e $8\,\text{TeV}$, no referencial do centro de massa, em 2011 e 2012, respectivamente, correspondendo a uma luminosidade integrada de $3.1\,\text{fb}^{-1}$. Medimos a assimetria de CP inclusiva para os quatro canais de interesse: $B^{\pm} \to K^{\pm}\pi^{+}\pi^{-}$, $B^{\pm} \to K^{\pm}K^{+}K^{-}$, $B^{\pm} \to \pi^{\pm}\pi^{+}\pi^{-}$ and $B^{\pm} \to \pi^{\pm}K^{+}K^{-}$. Além disso, assimetrias ao longo do espaço de fase também foram estudadas.

A segunda parte da tese é dedicada a minha contribuição ao SciFi - o novo detector de trajetórias do LHCb construído com fibras cintilantes. Esse trabalho descreve os aparatos experimentais usados para caracterizar as fibras cintilantes que precisam atender a requerimentos específicos para operarem nas condições previstas para a atualização do LHCb. Também discutimos os resultados de fibras produzidas com uma nova classe de material cintilante denominado como *Nanostructured Organosilicon Luminophores* (NOL). Elas possuem uma constante de decaimento pelo menos duas vezes menor do que as fibras cintilantes mais rápidas.

Palavras-chave: LHCb, Decaimentos do méson $B^{\pm}$ em três corpos, assimetria CP, Fibras cintilantes, *Nanostructured Organosilicon Luminphores*.

To my beloved parents . . .

Acknowledgements

None of the research presented in this thesis have been possible without the help and support of numerous people. I would like to thank my supervisor at Centro Brasileiro de Pesquisas Físicas, Ignácio Bediaga, who taught me that research is about having ideas which need to be discussed and sometimes are very difficult to perform. Also thanks for being patient mainly in this writing period. I would like to thank my supervisor at CERN, Christian Joram, who guided me through the hardware work on SciFi and was essential on the enhacement of my research and presentation skills. You are my example of a great Physicist and an excellent advisor.

I'd like to thank Laura Gavardi for numerous discussions about work and life in our beloved office at bâtiment 21-1-037. More than a colleague who I shared spools with in the laboratory and a bunch of lunches at R1, you became a very good friend who I appreciate your honesty and respectfulness towards everyone. I need to say thanks to the engineers and technicians who made the work on the laboratory possible: Robert Kristic, Thomas Schneider, Miranda Van Stenis and Claude David. I'd like to thank the LHCb secretaries who helped me with all my administrative issues: Nathalie Grub, Cindy Dennis et Carnita Hervet. En plus, grâce à vous tous, j'ai pu amelioré mon Français. Merci beaucoup. Matthew Kenzie, thanks for introducing me to the SciFi simulation code and for giving me a hand on C++ issues. Thanks SciFi German team (Robert, Janine, Max, Roman, David, Matthieu and Blake) for sharing your experience during testbeams. Thanks Maurice Glaser, Federico Ravotti and Giuseppe Pezzullo for all the support during the irradiation tests in the PS IRRAD zone. I wish to offer a special word of thanks my CBPF colleagues: Fernando, Adlene, Álvaro, Irina, Juan, Jussara, Alberto, André, Bruno, Laís and Valdir for sharing your Physics/computing/organization experience and knowledge with me. I also would like to acknowledge the professors from LAPE/Charm group, specially, Érika Polycarpo, Carla Göbel and Sandra Amato for fruitful discussions during my Masters period that paved the way towards the continuity of my research career.

Without the support of my beloved friends, I would not have reached so far. I'd like to thank Oscar Augusto for being there for me as a kind of an older brother while we were at CERN. Thanks Vinícius Franco, another kind of older brother, who seems younger, for being there for me as well. With both of you I can talk about everything: from my computational problems and physics doubts to emotional issues. Thanks Benedetta Nirta, or simply B., my lovely house mate who made the Chemin du Vieux-Bureau

house a more convivial place. Tess Carver, or simply Mess, thanks for sharing eggcinting moments and plans stans and also for making delicious cakes while I was far from home. Joseph Macmahom, or Joe, my friendly house mate, thanks for correcting my English on my first year at CERN and spreading flaute music into the house. I'd like to thank to my house mates in special Antanas Norkus for organising poker nights and offering lifts to home or supermarkets. Thanks Uilia, Irina, Laura, Iva, Lucia, Imy and Lillian for one of the best ladies night I've ever been. JC, thanks for organising and inviting people for awesome hikings on the Jura mountains.

Thanks Matheus Vicente and Carol Pinto, the most cute couple ever, for inviting me for delicious dinners and sharing your happiness. Also, thanks to Matheus I found snowboarding is my favorite winter sport. I'd like to thank my friends from LAPE group (Danielle Martins, Daniel Vieira, Daniela Szilard, Lucas, Luana, Saullo), who shared office with me during my period in UFRJ. A special thanks to Danielle, who read this thesis and spotted some English mistakes. I'd like to say thanks to my friends from UFRJ, in special to Wilton Kort-Kamp, Jéssica blah and Reinaldo de Melo. I'd like to thank an important group of people from CBPF, a.k.a Patota, who I considered as a second family: Maria Elidaiana, Josephine Rua, Anna Paula Bacalhau, Jaime Oliveira, Arthur Scardua, Vanessa Pacheco, Cláudia Buss and Cinthya Blois. I do not have words to describe the role you have in my life.

Por fim, eu gostaria de agradecer aos meus pais, Nelson e Olívia. Vocês são as pessoas que mais me ajudaram e incetivaram os meus estudos e trabalharam todos os dias para que eu pudesse seguir meus passos. Vocês são meu exemplo. Obrigada mãe por sempre estar disposta a fazer tudo o que eu pedir, em especial aquelas comidinhas gostosas para os amigos. Obrigada pai por me trazer serenidade e estar disposto a discutir diversos assuntos (muitas vezes relacionados à Física). Obrigada mein Bruder, Nelson Bernardo ou simplesmente Binho, por ser incrível, uma pessoa que sempre me incentiva. Crescemos e aprendemos tudo juntos; me sinto muito bem de estar ao seu lado. Ich liebe dich.

Por fim, FORA TEMER.

Contents

List of Figures

List of Tables

xxviii

List of Abbreviations

ALICE	**A** Large **I**on **C**ollider at CERN
ATLAS	**A** large **T**oroidal LHC **A**pparatu**S**
CERN	**C**entre Européene pour la **R**echerche **N**ucleaire
CMS	**C**ompact **M**uon **S**oleinoid
CP	**C**harge and **P**arity
DCPV	**D**alitz Plot **C**harge **P**arity **V**iolation
FSI	**F**inal **S**tate **I**teraction
FP	**F**luorinated **P**olymer
HLT	**H**igh **L**evel **T**rigger
IT	**I**nner **T**racker
L0	**L**evel-**0**
LHC	**L**arge **H**adron **C**ollider
LHCb	**L**arge **H**adron **C**ollider **b**eauty
MIP	**M**inimum **I**onizing **P**article
NIM	**N**uclear **I**nstrumentation **M**odule
NOL	**N**anostructured **O**rganosilicon **L**uminophores
OT	**O**uter **T**racker
PMMA	**P**loy**M**ethyl**M**etha**A**crylate
PMT	**P**hoto**M**ultiplier **T**ubes
PS	**P**re **S**hower
RICH	**R**ing **I**maging **CH**erenkov
SiPM	**S**ilicon **P**hoto**M**ultiplier
SM	**S**tandard **M**odel
SPD	**S**cintillator **P**ad **D**etector
ST	**S**ilicon **T**racker
TT	**T**racker **T**uricensis
UV-LED	**U**ltra **V**iolet-**LED**
VELO	**VE**rtex **LO**cator
WLS	**W**ave**L**ength **S**hifter

Introduction

The idea of elementary particles was postulated by the Greek philosopher Democritus 400 BC. He believed that all matter was made of very small and indestructible particles named as atoms. At that time, this could not be proven with experiments and, it was based on reasoning. Only in the seventeenth and eighteenth centuries, the atomism was revived and gained special attention with John Dalton. From then on, not only the concept of atom has changed but also the term 'atom' turned out to be inaccurate, since atoms are made of protons, neutrons and electrons. Also protons and neutrons are constituted of smaller particles known as quarks. Additionally, many other sub-atomic particles have been discovered.

Currently we believe that quarks, together with leptons, the interaction bosons and the Higgs boson are the fundamental particles of the Universe. The Standard Model of particle physics is the best theory we have to describe the behavior of such particles and the interaction among them. However, it is unable to answer many questions. One of them, which is of particular interest of this thesis, is the imbalance between matter and anti-matter. Large asymmetries are foreseen in several B decay channels, thus the study of B meson decays can shed a light onto this discrepancy. In this thesis, we investigate charmless three-body charged B meson decays aiming for the observation of CP violation effects, which may vary significantly across the phase space.

The development of such theories and models leading to the prediction of new particles has only been possible due to the improvement of the detection techniques. For example, in 1930s, the detection of Cherenkov light was made by human naked-eyes adapted to the darkness. Nowadays there exist huge experiments comprising many detection technologies such as the LHCb, located at one of the collision points of the largest particle accelerator in the world, the LHC. The LHCb is dedicated to the measurement of b and c hadrons and performs precise measurements on CP violation and rare decays.

After the Long Shutdown 2 (ends in 2021), the LHC is going to run in upgraded conditions and the event yields are going to increase substantially. The detectors will suffer from increased particle occupancies and radiation damages, imposing drastic modifications in several sub-systems. We are specially interested on the SciFi Tracker designed as a part of the LHCb upgrade. This detector is made of 250 μm-scintillating fibres readout

by silicon photomultipliers in the detector edges. The full detector is going to be made of more than $10000\,\mathrm{km}$ of fibres. This work details my contribution on the characterisation and improvement of scintillating fibres for the LHCb SciFi Tracker.

Division of chapters

This thesis is arranged in two parts totalising 6 chapters. Chapter 1 discusses the design and performance of the LHCb detector and its upgrade. It is the common ingredient for both parts. The first part describes the analysis on the charmless three-body $B^{\pm}$ decays. Chapter 2 presents an overview of the theory foundation. It comprises a summary of the Standard Model of Particle Physics emphasising the CP violation mechanisms and the main features involving charmless three-body decays. The global and local CP asymmetry measurements are discussed in Chapter 3 and 4, respectively. The second part concerns the work developed at CERN related to the LHCb SciFi Tracker. An overview on scintillating fibres is presented on Chapter 5. Chapter 6 details the experimental setups and results, whilst Chapter 7 discusses the development and results on NOL fibres.

Chapter 1

LHC and LHCb detector

The main purpose of a high energy physics experiment is to characterize fundamental particles and understand by which means they interact. To investigate the composition of a macroscopic object, we need to break it and check how the pieces match together and it is not different when we deal with subatomic particles: they need to be accelerated and collide with another particle or a target. In order to observe the particles originated from such a collision, Physicists use detectors which are able to measure their energy, momentum and/or trajectory. In addition, these pieces of information need to be recorded for further analysis.

This chapter briefly describes the world's largest particle accelerator, the Large Hadron Collider (LHC), and its four main experiments: ALICE, AT-LAS, CMS and LHCb. Since the present thesis involves LHCb data analysis and LHCb upgrade, there is a dedicated section for LHCb detector and its upgrade.

1.1 LHC

The Large Hadron Collider (LHC) [1] is the world's largest and most powerful accelerator ever built: it has approximately 27 km of circumference in the underground of the Switzerland-France border. Proton beams are accelerated in opposite directions in two accelerator rings and collide at four specific interaction points where the experiments are placed. The LHC is working since 2010 and the collision energy has been gradually increasing: from 7 TeV (in 2010) to 13 TeV (2015) with the aim to finally reach the expected $\sqrt{s} = 14$ TeV in 2017-2018.

In order to accelerate protons to attain energies at TeV scale in the LHC, the beam first need to pass through a series of pre-accelerating structures (see Figure 1.1). The protons are first injected in the Linear Proton Accelerator (Linac2) which pushes the beam to 50 MeV. The next accelerator is the Proton Synchroton Booster (PSB) which accelerates the protons to an energy of up to 1.4 GeV followed by the Proton Booster (PS), where the proton beams attain an energy of 26 GeV. Then the protons are injected into the Super Proton Synchroton (SPS) and they are accelerated to 450 GeV. The

last accelerator in the injection chain, the LHC, was designed to accelerate proton beams up to 7 TeV.

A natural question would be: why TeV scale? The TeV energy scale is interesting because some theoretical models can be validated or discarded. Take for instance, supersymmetry (SUSY) theory which the lack of evidence has constrained SUSY models [2]. Moreover, since those energies were never attained before, we may find appealing results which are not foreseen by SM and/or any theory.

In general, the most interesting physics results come from very rare events. Hence, a large amount of collisions must be generated in to produce such events that may be detected. The LHC was planned to collide proton beams every 25 ns (rate of 40 MHz) and in 2016 it reached a luminosity of $1.4 \times 10^{34}\,\mathrm{cm}^{-2}\mathrm{s}^{-1}$ (40% above the designed value) [3]. The luminosity is the parameter used to quantify the amount of collected data and is defined as:

$$\mathcal{L} = \frac{N_1 N_2}{St}, \tag{1.1}$$

where N_1 and N_2 are the number of protons per bunch, S is the cross section of the interaction region and t is the time between two collisions.

The ATLAS [4] (a large Toroidal LHC ApparatuS) and the CMS [5] (Compact Muon Solenoid) are the largest and general purpose experiments designed for probing pp and heavy ions collisions. The ALICE (A Large Ion Collider Experiment at CERN LHC) [6] is also a general purpose detector dedicated to heavy-ion collisions with a focus on QCD. The smallest of them is the LHCb [7] (Large Hadron Collider Beauty) detector is dedicated to precision measurements of CP violation and rare decays of beauty and charm hadrons.

1.2 LHCb

The LHCb is an experiment dedicated to heavy flavour physics, i.e. involving b and c-hadrons. One of the most fundamental questions which until today we have no answer concerns the matter-antimatter asymmetry. The predicted level of CP violation in the SM does not account for the amount of matter in the Universe, therefore new sources of CP violation (forbidden by the SM) are expected. In order to investigate them, it is essential the study of rare B and D mesons decays with very high statistics. The LHC is able to produce B hadrons copiously ($\sigma \sim 500\,\mu\mathrm{b}$ at $\sqrt{s} = 14\,\mathrm{TeV}$) and the LHCb was designed to profit from it [7].
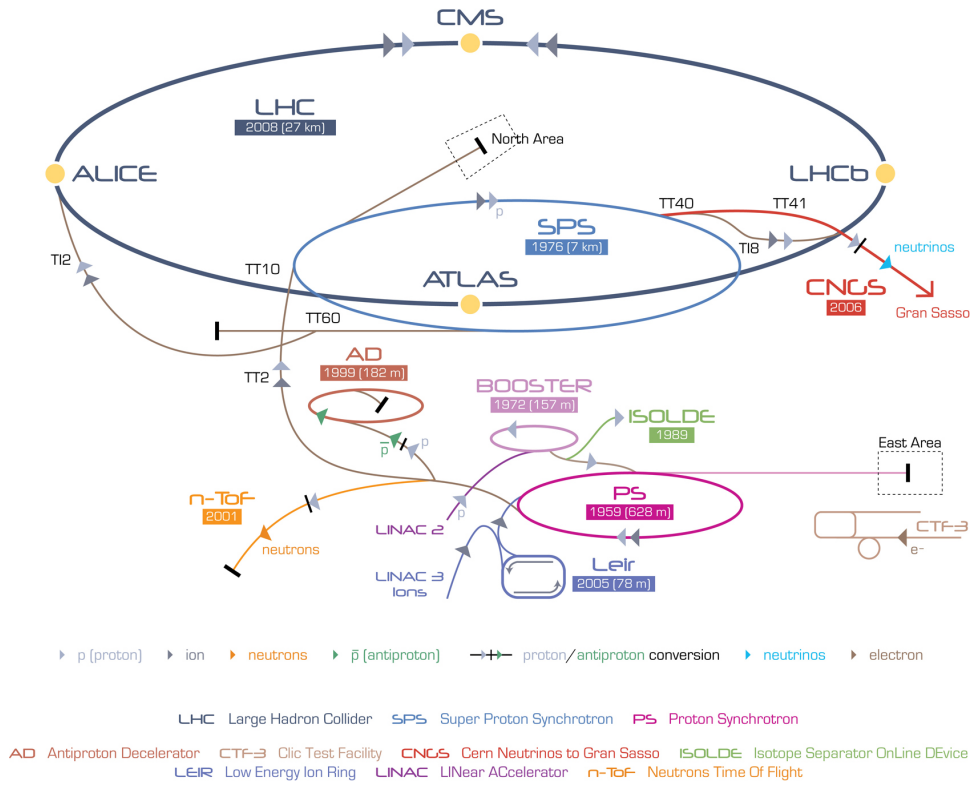
FIGURE 1.1: LHC accelerator complex.

Source: [8] (28-Mar-2017).
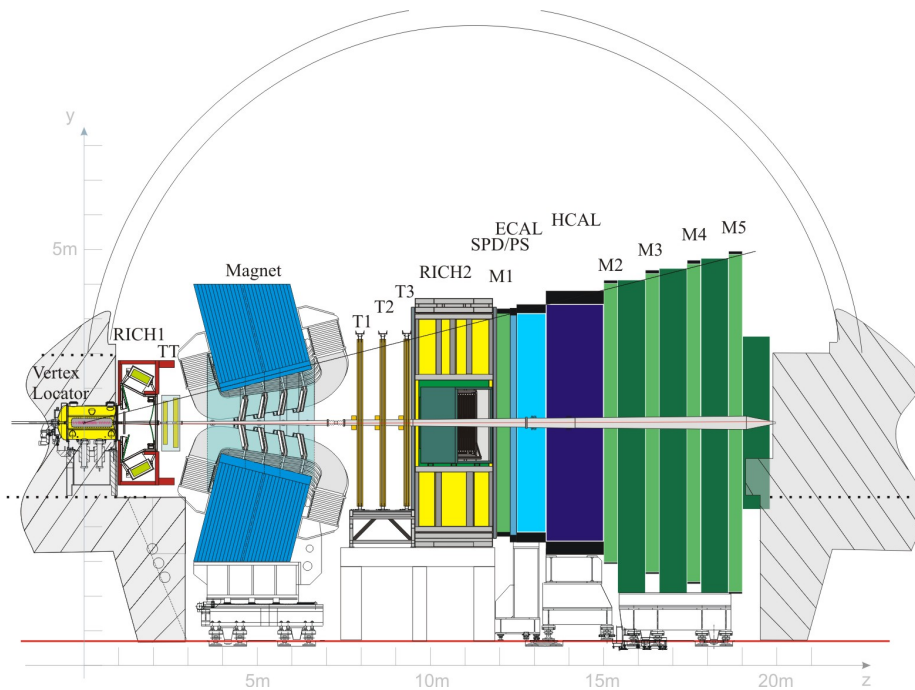
FIGURE 1.2: LHCb detector overview.

Source: [7].

The LHCb detector is a single arm forward spectrometer as shown in

Figure 1.2[1]. It is the smallest of the four main experiments with dimensions of $13\,\text{m} \times 10\,\text{m} \times 21\,\text{m}$ allowing a angular coverage of approximately ± 300 mrad (± 250 mrad) in the vertical (horizontal) plane. This geometry is justified by the fact that for b and $\bar{b}$ hadrons originated from high energy collisions are predominantly produced in the beam axis (backward and forward) directions (see Figure 1.3). The fact that LHCb detector covers only the forward direction is due to financial limitations.

One special feature of LHCb detector concerns its luminosity. The LHC is able to provide a luminosity of the order of $10^{34}\,\text{cm}^{-2}\text{s}^{-1}$ as mentioned above. However, the LHCb detector works with a modest luminosity of $2 \times 10^{32}\,\text{cm}^{-2}\text{s}^{-1}$ (by defocalisation of the beam close to the interaction point) to guarantee that only single pp interactions per bunch crossing. The advantages of that procedure are: 1) the events are simpler to analyse; 2) there is a reduction of the detector occupancy; 3) there is less radiation damage.

At the interaction points collisions happen every $25\,\text{ns}$. To cope with the huge amount of data at $40\,\text{MHz}$, the LHCb detector has a trigger system that selects only the interesting events coming from b or c hadrons. Also, to identify such hadrons and their decay products, LHCb must exhibit outstanding tracking, vertexing and particle identification systems. The following sections are dedicated to describe the LHCb sub-detectors together with the trigger and online systems.
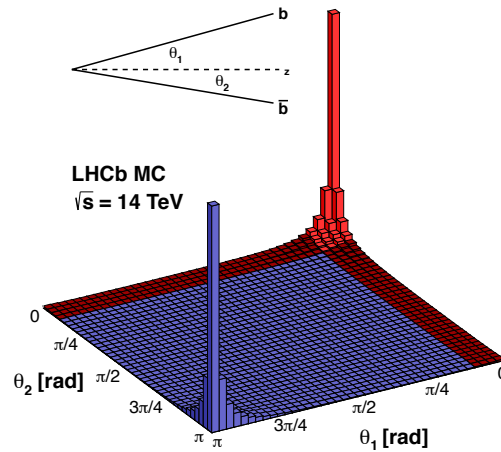
FIGURE 1.3: Simulation of the angular distribution of the $b\bar{b}$
pair production with respect to the beam direction.

Source: [9].

---

[1]The coordinate system is right-handed so that z axis is the direction along the beam and the y axis corresponds to the vertical direction.

1.2.1 Magnet

The main purpose of the LHCb magnet [7, 10] is to bend the trajectory of the charged particles allowing to measure their momentum. The magnet polarity is reversed periodically in order to control the systematic effects of the detector which is essential for CP asymmetry measurements.

As shown in Figure 1.2, the magnet is placed between the Trigger Tracker and the T1 station. It provides an integrated magnetic field of 4 T m for tracks of 10 m length, with a peak intensity of 1.1 T m. The magnet design with saddled shape coils, as shown in Figure 1.4, matches the detector acceptance.
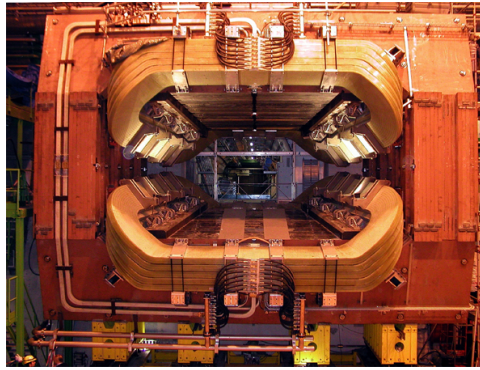
FIGURE 1.4: The LHCb magnet.

Source: [11].

1.2.2 VErtex LOcator (VELO)

The LHCb vertex detector, denominated as VELO [7, 12], is located around the interaction region and provides precise measurements of the tracking coordinates of the b and c hadrons decays, which allowed the determination of the primary and secondary vertexes[2] and impact parameter. These pieces of information is essential for the trigger decision and offline analysis.

VELO detector consists of 21 stations arranged along the beam axis as shown in Figure 1.5. Each station is composed by a R and a ϕ-sensor halves made of silicon strips technology,that provide the radial and azimuthal position of the tracks, respectively. The two VELO stations are placed in a secondary vacuum chamber, which is separated from the primary LHC vacuum by means of a 300 μm thick aluminium foil.

In order to perform such measurements precisely the VELO detector must be placed very close to the beam pipe. Since this radial distance is smaller than the aperture requirement for injection in LHC, the detector halves must be retracted. During injection, the sensors are 30 mm away

---

[2]The primary vertex is the interaction point while the secondary vertex is the decaying vertex.

from the beam pipe and this distance is reduce to $8\,\text{mm}$ while the beam is
ready for collisions.

Concerning its performance, the VELO provides a best hit resolution of
$4\,\mu\text{m}$ and a PV resolution of $\sigma_{xy} = 12\,\mu\text{m}$ [13].
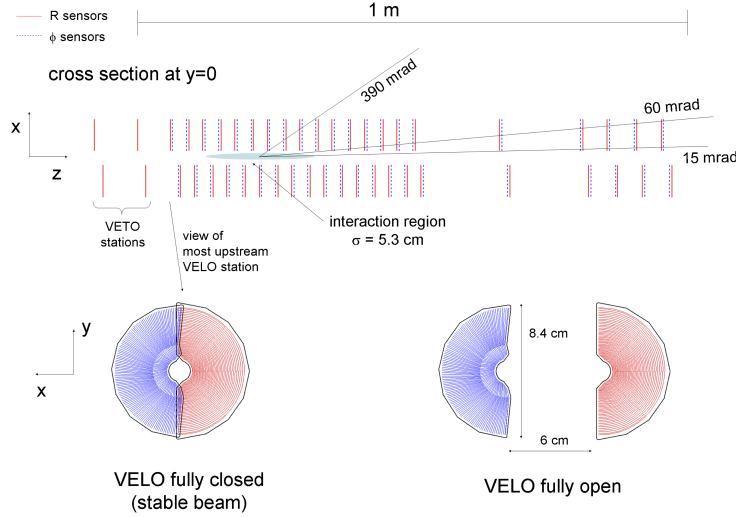
FIGURE 1.5: Illustrative scheme of the VELO sensors.

Source: [12].

1.2.3   Tracking system

The LHCb tracking stations [7, 14, 15] - Tracker Turicensis (TT) and T1-T3-
together with the VELO detector, are able to efficiently reconstruct charged-
particle tracks. The tracking stations (see Figure 1.6) are composed by two
distinct detector technologies: (i) ST uses silicon micro strips ($200\,\mu\text{m}$) de-
tectors comprising the TT and inner part of the T1-T3 stations - the IT; (ii)
the OT corresponds to the largest fraction of the detector sensitive area in
stations T1-T3 and uses straw-tube (inner diameter of $4.9\,\text{mm}$) drift cham-
bers.

The TT, located upstream the magnet, allows reconstruction of low-
momentum particles ($<3\,\text{GeV}/c$), while T1-T3 stations, situated downstream
the magnet, detects the trajectory of high momentum charged particles.

The ST consists of a total of 4 stations (one for TT and 3 for T-stations).
Each station has four detections layers following the x-u-v-x arrangement
where the first and last layers have vertical strips and the second and third
layers are rotated by $+5°$ and $-5°$, respectively. Concerning the dimen-
sions, the TT stations has $150\,\text{cm}$ wide and $130\,\text{cm}$ high and, the IT stations
are $120\,\text{cm}$ wide and $40\,\text{cm}$ high. The OT detection layers, each with dimen-
sions $5\,\text{m}$ wide and $6\,\text{m}$ high, are also arranged according to the x-u-v-x
geometry.

(a)

(b)

(c)

(d)
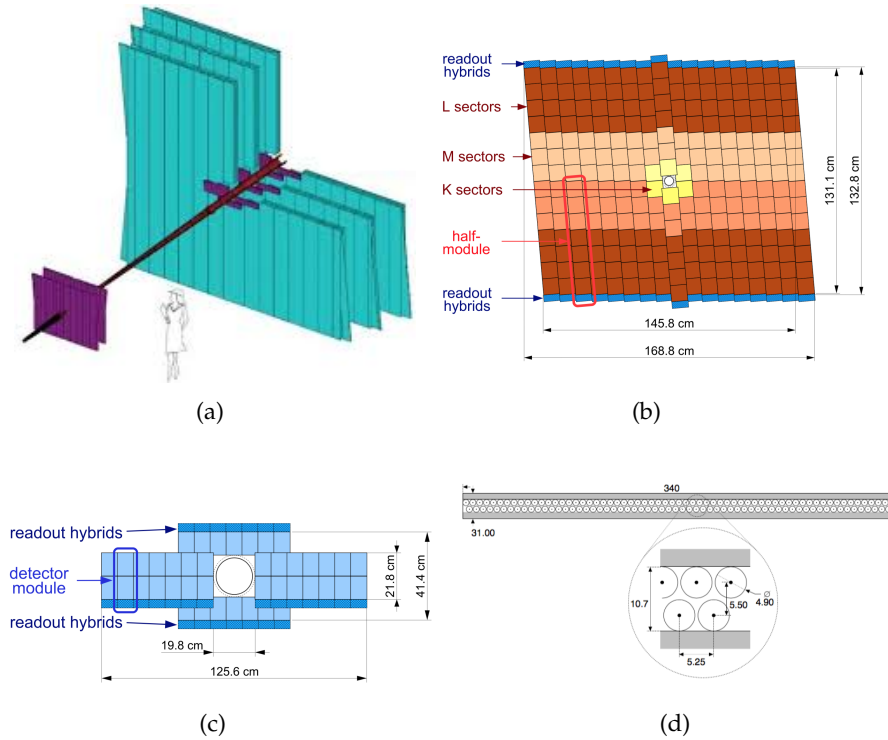
FIGURE 1.6: Illustration of the tracking stations:(a) overview of the ST (in purple) and the OT (in cyan) stations; (b) layout of the third TT detection layer; (c) one IT detection layer; (d) cross section of a straw-tubes module. The drift-tubes have an inner diameter of 4.90 mm and they are arranged in two staggered layers.

Source: [7].

With regard to the performance, the OT has a very high hit efficiency (99.2%) and a position resolution better than $200\,\mu\text{m}$ [16], the IT has a hit efficiency larger than 99% [17], leading to an average efficiency of the tracking system better than 95% in the momentum region $5\,\text{GeV}/c < p < 200\,\text{GeV}/c$ and in the pseudorapidity[3] region $2 < \eta < 5$ [18].

1.2.4 RICH detectors

The main task of RICH (Ring Imaging Cherenkov) detectors [7, 19] is to identify pions, kaons and protons in LHCb, which is essential in the analysis of hadronic decays.

The LHCb is equipped with two RICH detectors denominated as RICH1 and RICH2 (see Figure 1.7) to cover the momentum range of particles between 1 and $150\,\text{GeV}/c$. RICH1, located between the VELO and TT, covers the full LHCb acceptance from ± 25 mrad to ± 300 mrad (horizontal) and

---

[3]Pseudorapidity is defined as $\eta = -\ln(\tan(\theta/2))$, where θ is the angle between the particle momentum vector and the positive direction of the beam axis.
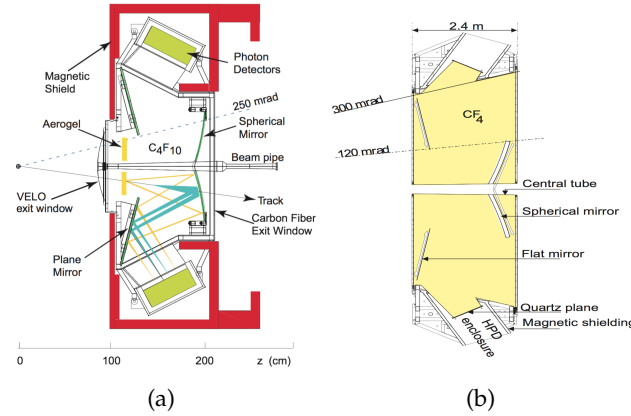
FIGURE 1.7: Schematic layout of the (a) RICH1 and (b) RICH2 detectors.

Source: [7].
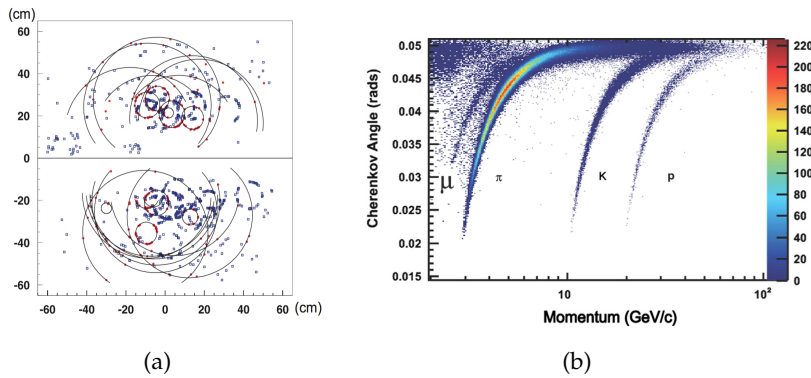
FIGURE 1.8: (a) Photon signal detected by RICH1 detector in a typical LHCb event; (b) particle identification for C_4F_{10} radiator (cherenkov angle dependence on the particle momentum).

Source: [7],[20] .

± 250 mrad (vertical). It was developed to identify the low momentum (1-60 GeV/c) charged particles tracks. The RICH2 detector, placed between the T3 and the first muon station, has a limited acceptance ± 15 mrad to ± 120 mrad (horizontal) and ± 100 mrad (vertical) which is sufficient to cover the high momentum particles (15 to 150 GeV/c). The radiators (the medium the particles traverse) are aerogel and C_4F_{10} for RICH1 and CF_4 for RICH2.

The working principle of RICH detectors lies on the emission of Cherenkov light, emitted as a forward cone with a specific angle θ_c with $\cos(\theta_c) = 1/n\beta$, where n is the medium refractive index and $\beta = v/c$ with v as the particle speed. This light is focused by a combination of flat and spherical mirrors into Hybrid Photon Detectors (HPD) and the output signal are circles such as shown in Figure 1.8(a). The analyses of these Cherenkov radiation rings together with the momentum information allows the separation of particles

(see Figure 1.8(b)).

1.2.5 Calorimeters

The calorimeters perform several functions: (i) select transverse energy (E_{T}) for hadron, electron and photon candidates; (ii) provide identification of electrons, photons and hadrons together with their energy and position measurements; (iii) reconstruct with good accuracy π^0 and prompt photons (essential for the B meson analysis).

The LHCb calorimeter system [7, 21] is composed by four sub-detectors: SPD (Scintillator Pad Detector), PS (Pre Shower), ECAL (Electronic Calorimeter) and HCAL (Hadronic Calorimeter). Except for the SPD - constituted only by scintillator plates - all of them follow the same basic principle: when a particle traverses the radiator (a material with high Z, such as lead), a particle cascade is generated due to electromagnetic or strong interaction. The excitation of the radiator molecules generates scintillation light that are transported by WLS (wavelength shifting) fibres and collected by photodetectors.

Since the density of particles can be very different according to the calorimeter region, all of the sub-detectors adopt a distinct segmentation. While PS, SPD and ECAL have three well-defined regions, HCAL has only two as can be seen in Figure 1.9.

The SPD/ ps detector consists of a $15\,\mathrm{mm}$ thick lead ($2.5X_0$) which is sandwiched between almost two identical rectangular scintillator pads. The SPD identifies charged particles and allows electrons to be separated from photons. The ps distinguishes electrons from hadrons. Both of them have a sensitive area of about $7.6\,\mathrm{m}$ wide and $6.2\,\mathrm{m}$ high.

The ECAL is a sampling scintillator/lead structure, i.e. with alternating layers of lead and scintillator, equivalent to $25\ X_0$. It provides the separation of electrons from photons. The energy resolution of the ECAL modules is $\sigma_E/E = a/E \oplus b \oplus c/E$ (E in GeV), where a, b and c are the stochastic, constant and noise terms respectively [22]. The HCAL is also a sampling calorimeter with the scintillator tiles interspaced with 1 cm iron corresponding to $5.6\ \lambda_{int}$. Its main function is to measure the energy of hadrons providing auxiliary information for their identification as well. The energy resolution for the HCAL is $\sigma_E/E = (69 \pm 5)\%/3\sqrt{E} \oplus (9 \pm 2)\%$ (E in GeV) [22].

Concerning the calorimeter identification capabilities, a typical performance study for electrons from $J/\psi \to e^+e^-$ in $B^\pm \to J/\psi K^\pm$ events gives an average identification efficiency in the complete calorimeter system a value of $(91.9 \pm 1.3)\%$ and $(4.54 \pm 0.02)\%$ for a misidentification rate. If additional information from the RICH detectors is considered, the average

identification efficiency can be improved up to 97% and the misidentification rate can be lower than 2% [22].
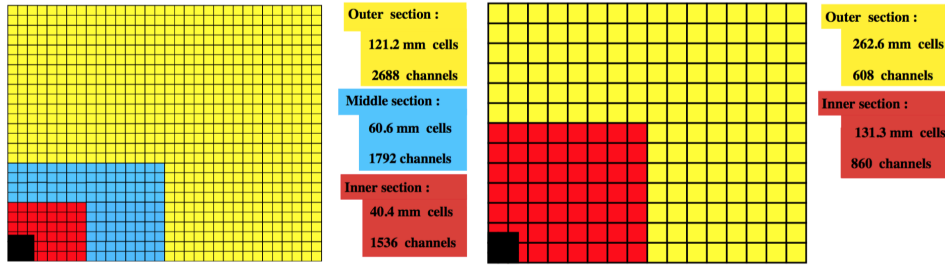
FIGURE 1.9: Illustration of one quadrant segmentation cells of the SPD/PS and ECAL (left) and of the HCAL (right).

Source: [7].

1.2.6   Muon system

The muon system [7, 23] allows to select and identify muons. Muons are present in the final states of several CP-sensitive B decays and also on rare decays such as $B_S^0 \rightarrow \mu^+ \mu m$ may reveal new physics beyond the SM.

The muon system, shown in Figure 1.10, is composed of five stations (M1-M5) and covers the acceptance of ± 300 mrad (horizontal) and ± 250 mrad (vertical). M1 station is located between RICH2 and the calorimeters while M2-M5 are downstream the calorimeters. In order to avoid particles which are not muons to reach muon chambers (mainly pions) and guaranteeing that only muons traverse the muon system, M2-M5 are interleaved with $800\,\mathrm{mm}$ thick iron absorbers. Each station is divided into four regions (see Figure 1.10) in which R1 corresponds to the most inner part (close to the beam pipe) and R4 is the most outer region. The granularity of each region was chosen according to the expected density of particles in order to maintain the occupancy constant along the detector surface.

M1-M5 stations are composed of MWPC - Multi-Wire Proportional Chamber - technology, except in the most inner part of M1 which is built from GEM (Gaseous Electron Multiplier) technology to cope with a more intense flux of particles. Both detectors are filled with a gaseous mixture of Ar, CO_2 and CF_4 with different proportions to optimize the charge collection.

The working principle of such detectors is based on the excitation of the gas molecules by the ionizing particles. The electrons are guided to a very strong electric field close to the anode wires and generate an electron avalanche, leading to a readable electric signal.

With regard to the performance of the muon system, it is possible to reach a muon detection efficiency well above the design requirement of 99% in all the 5 muon stations [24].
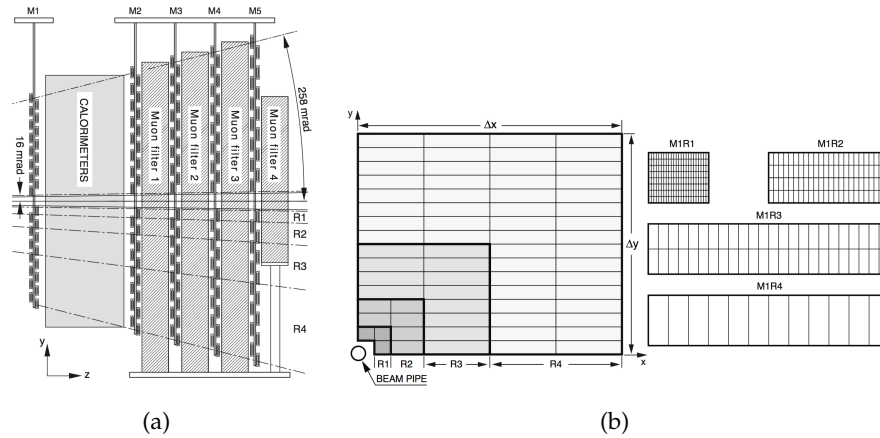
FIGURE 1.10: (a) Sideview of the muon system; (b) a quadrant of a muon station with different granularities of the four regions of M1 station.

Source: [7].

1.2.7 The trigger and stripping selections

The main task of the trigger system [7, 25, 26] is to select among all the events, as fast as possible, which events should be recorded and stored, reducing the LHC beam crossing rate of 40 MHz to the rate of few kHz.

The online event selection is divided in two levels: L0 (Level 0 Trigger) and HLT (High Level Trigger). The L0 trigger is fully implemented in hardware while the HLT is performed in a software level executing algorithms on a dedicated computer farm consisting of 29000 (52000) CPUs in Run I[4] (Run II[5]).

The purpose of the L0 trigger is to reduce the event rate from 40 MHz to below 1 MHz, which is the rate at which the whole detector can be readout. Since B mesons decays often produce particles with large p_T and E_T, the L0 trigger is based on the selection of events with either high p_T muons or large E_T clusters in the calorimeters.

The HLT has the task to reduce even more the event rate from 1 MHz to few kHz and it is subdivided in two stages: HLT1 and HLT2. The HLT1 performs a partial event reconstruction of charged particles trajectories using information from the VELO and TT stations. Events which were selected by HLT1 are then fully reconstructed in the HLT2 stage. The HLT is implemented as several exclusive selections denominated as alleys.

During the LHCb working period there were different trigger settings that are summarised in Figure 1.11. During the Run I period the HLT was operating synchronously with the LHC clock. In 2012 the trigger was improved by the introduction of the deferred trigger which stores about 25%

---

[4]Run I is the data taking period of 2010-2012.

[5]Run II concerns the data taking period between 2015-2018.
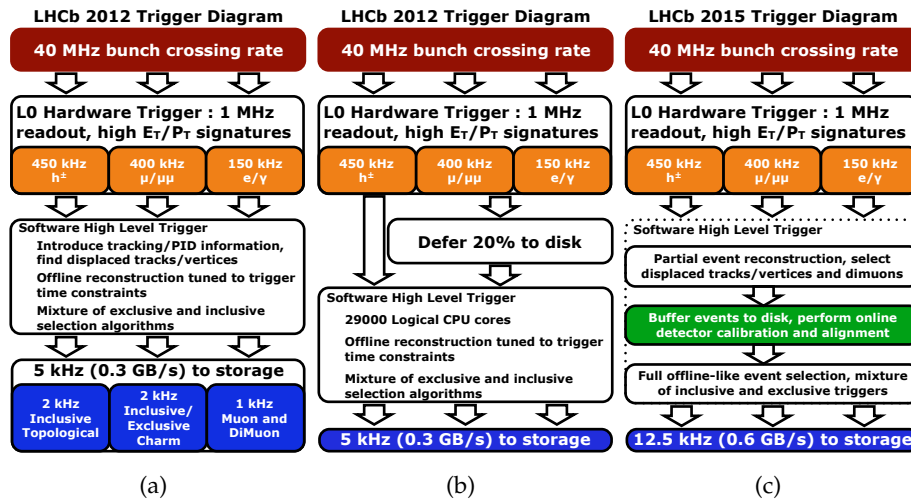
FIGURE 1.11: The trigger layout for (a) Run I (b) Run I with
deferred trigger and (c) Run II.

Source: [27].

of all the L0 accepted events to local disks. These events are later processed
by the HLT selection during the inactivity of the farm computers between
fill. In 2015, the HLT1 and HLT2 run as two independent processes and
asynchronously, allowing a high-quality alignment and calibration of the
detectors and consequently improving the full reconstruction. [28]

Once triggered by the L0 and HLT, the saved data is processed by an-
other selecting phase denominated as stripping. The stripping is also con-
stituted by several exclusive and inclusive selections denominated as strip-
ping lines in view of classifying and completely reconstruct the decays of
interest. The striping lines are sub-divided in streams, such as the B hadron
stream. Each stream has numerous lines with exclusive and inclusive selec-
tions corresponding to more specific analysis. After the stripping, the last
stage of the data processing in the LHCb, the data can be further analysed
by the collaboration.

1.2.8   Online system

The online system [7, 29] is responsible for transporting the data from the
front-end electronics to permanent storage and guaranteeing that all the
detector channels are synchronised with the LHC clock.

1.2.9   The LHCb softwares

A software structure was developed for the LHCb to process the selected
events as well as simulate all the stages of the experiment - from the colli-
sion to the detector output. Simulation helps in the comprehension of the

real detector response and also provides the selecting efficiencies.

The LHCb software is organised in projects containing a collection of packages with specific functions. Some of them are briefly explained below:

- **Gauss**: simulates not only the generation of pp collisions and the decay of the particles produced but also the particle interaction with the detector [30];

- **Boole**: simulates the detector response with the hits generated with Gauss application. It also includes the readout electronics, as well as of the Level 0 trigger selection. The output file is digitized data that mimics the data coming from the real detector [31];

- **Moore**: performs the HLT decision on both simulated and real data [32];

- **Brunel**: is devoted to the reconstruction of the events [33];

- **DaVinci**: is the physics analysis package which generates output files denominated as ntuples in ROOT format [34];

- **Panoramix**: is used to display the events in the LHCb detector [35].

1.3   LHCb upgrade

The LHC Run III is planned to start in 2021 and LHCb is going to run at luminosities of $2 \times 10^{33} \, \mathrm{cm}^{-2}\mathrm{s}^{-1}$. Due to this increase in luminosity and beam energy, all subdetectors need to cope with an increase in occupancy and data transfer rates while maintaining and/or improving their performance. This can only be achieved by performing a detector upgrade.

Concerning the physics program, the LHCb has shown an excellent performance during Run I and the current Run II phases. Results achieved cover rare decays such as the observation of $B_s^0 \to \mu^+ \, \mu^-$ [36] and studies of CP violation, such as the B_s^0-$\overline{B}_s^0$ oscillation frequency [37] and the most precise measurement of γ [38], in addition to results in the lepton sector such as the test of lepton universality[39]. An increase in sensitivity of the mentioned measurements and many others are expected with the upgraded conditions.

The next subsections detail the main modifications in the LHCb subdetectors and also on the trigger decision.

1.3.1   Trigger system

The current trigger is sub-divided in a hardware (L0) and a software (HLT) levels. The main role of the L0 decision trigger is to reduce the collision rate

to 1 MHz within a fixed latency. By increasing the luminosity by a factor of five with respect to the current conditions, the 1 MHz readout becomes a bottleneck. The limited information available to the Level 0 trigger leads to prohibitive efficiency losses in particular for purely hadronic final states. The proposed trigger upgrade [40, 41, 42] consists of a trigger-less readout system (see Figure 1.12) that allows to read out the detector at the 40 MHz bunch crossing rate. This requires a change of all the front-end electronics of all detectors.

The L0 hardware trigger will be replaced by software trigger denominated as Low Level Trigger (LLT) which is more robust and flexible. It will operate using a similar criteria as the current L0 trigger looking for high E_T in calorimeters cells and high p_T tracks in muon system.

LHCb Upgrade Trigger Diagram

30 MHz inelastic event rate (full rate event building)

Software High Level Trigger

Full event reconstruction, inclusive and exclusive kinematic/geometric selections

Buffer events to disk, perform online detector calibration and alignment

Add offline precision particle identification and track quality information to selections

Output full event information for inclusive triggers, trigger candidates and related primary vertices for exclusive triggers

2-5 GB/s to storage

FIGURE 1.12: Designed trigger during initial phase of Run III.

Source: [27].

1.3.2 VELO

In order to face the new LHC conditions, it is necessary a complete replacement of the silicon sensors and electronics. The main modifications are: (i) the new detector will be based on hybrid pixel sensors (while the old one was based on silicon strips) which can be readout at 40 MHz; (ii) when closed, the VELO detector will be placed at a distance of 5.1 mm from the
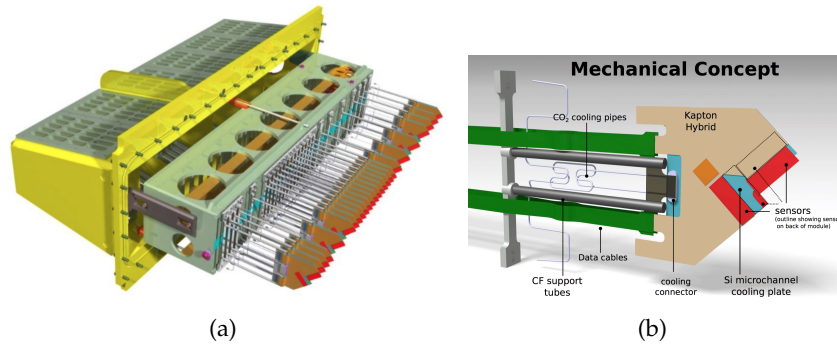
FIGURE 1.13: The VELO upgrade detector layout: (a) one of
the retractable halves composed with 26 L-shaped sensors;
(b) the mechanical concept of a VELO module.

Source: [43].

beam pipe whereas currently it is $8.1\,\mathrm{mm}$; (iii) the upgrade cooling is integrated with the module by evaporative CO_2 circulating within microchannels in the silicon substrate in contrast to the current VELO where the modules are cooled with CO_2 passing through a series of cooling blocks attached to the base of the module. [43]

Figure 1.13 illustrates the layout of the upgraded VELO detector [40, 44, 43] which consists of 52 L-shaped silicon modules and each of them contains four $200\,\mu\mathrm{m}$-thick sensors. The silicon pixel sensors ($55\,\mu\mathrm{m}$ x $55\,\mu\mathrm{m}$ pitch) are bump-bonded to a row of the readout chip called VeLoPix ASIC (at $40\,\mathrm{MHz}$). The upgraded VELO corresponds to 21% X_0 in contrast to 20% X_0 to the current VELO.

The fact that VELO is going to be placed at a closer distance results in higher data rates but also higher radiation doses and higher hit occupancy. The expected accumulated neutron dose-equivalent rates around $8 \times 10^{15}\,\mathrm{n_{eq}/\,cm^2}$ and up to an accumulated integrated luminosity of $10\,\mathrm{fb}^{-1}$ requiring the electronics to be radiation hard. The performance of the upgraded VELO is going to be improved with a more robust track reconstruction algorithm (compared with the current version) together with an overall enhanced resolution for the impact parameter as can be seen in Figure 1.14 [43].

1.3.3 Upstream Tracker

Although the Tracker Turicensis has shown an excellent performance, it is not designed (i) to survive in the radiation harsh environment, (ii) to cope with an unacceptable high occupancies and (ii) to readout at $40\,\mathrm{MHz}$- all expected in the upgrade conditions. The TT is going to be replaced by the Upstream Tracker (UT) [40, 45, 46] and will use new micro-strips silicon technology.
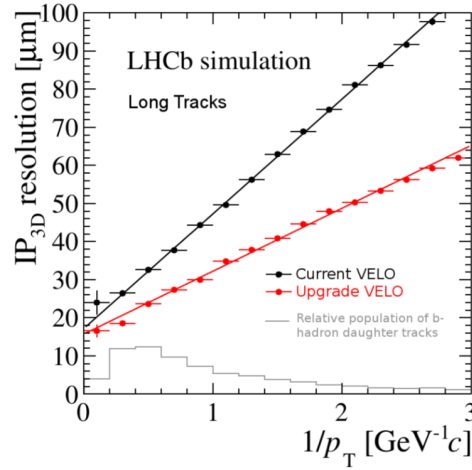
FIGURE 1.14: 3D impact parameter as a function of the particle inverse transverse momentum. There is a considerable improvement on the resolution for the upgraded detector (in red) with respect to the current one (in black).

Source: [43].

Figure 1.15(a) illustrates the layout of the UT. Similarly to the TT, the new tracker will consist of four planar detection layers in the x-u-v-x geometry. The four detection layers are arranged in pairs (separated by a distance of $27\,\mathrm{cm}$ in the z-axis) in view of helping the tracking reconstruction algorithms. Four types of silicon micro-strip sensors (A,B,C and D) with different readout strip geometries will be used in each detection layer according to the density of charged particles expected in detector surface. Each detection layer is constituted by staves (see Figure 1.15(b)); the two upstream (downstream) planes contains 16 (18) staves.

Concerning radiation damage, simulation studies showed that the maximum fluence expected for the sensors placed in the innermost region is $1.4 \times 10^{14}\ \mathrm{n_{eq}/\,cm^2}$ which corresponds to 12 MRad [47].

In summary, compared to the TT, the UT is designed to survive in the upgraded running conditions, it has a finer granularity to cope with the higher occupancy, it is placed closer to the beam pipe improving the small-angular acceptance and the readout front-end electronics is going to be transfer data at $40\,\mathrm{MHz}$.

1.3.4   SciFi Tracker

In the upgraded running conditions, the hottest regions of the OT would suffer prohibitive occupancies - larger than 25% which is the maximum for no loss in tracking efficiency. In addition, the readout of the events at $40\,\mathrm{MHz}$ also requires the replacement of the both the IT and OT readout electronics.
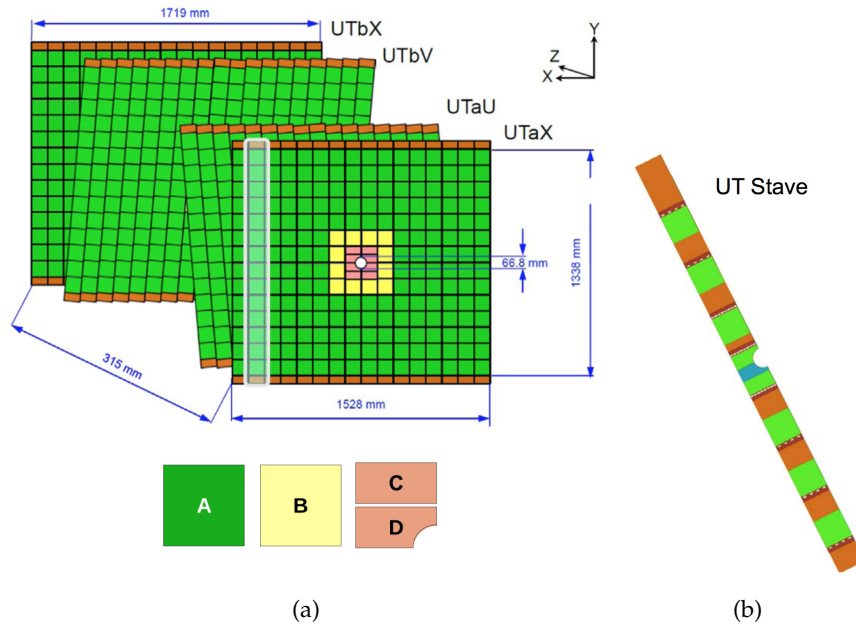
FIGURE 1.15: The Upstream Tracker detector: (a) overview of the UT where each rectangle corresponds to a silicon sensor and the different colors means different sensor geometries; (b) illustration of a UT stave.

Source: [45, 46].

The T1-T3 Trackers are going to be replaced by the LHCb SciFi Tracker [40, 45, 48]. Figure 1.16 shows the design of the SciFi Tracker. The active material of the SciFi are 250 μm-diameter scintillating fibres. The detector modules are going to be built out of 2.5 m length fibres arranged in six staggered layers (see Figure 1.16). The fibres are going to be readout by Silicon Photomultipliers (SiPMs) located in the top and bottom edges of the detector. Each detector module consists of four half-modules placed in the bottom and another four placed in the upper part with a mirror foil placed in the middle of them in order to increase light collection. The detector design consist of 12 detection planes with a total of 144 modules which corresponds to more than 10 000 km of fibres. The planes are arranged in three stations. The first and the last layer in each station have no stereo angle with respect to the y-axis, while the middle two layers are tilted by $+5°$ and $-5°$, respectively.

In order to cope with the upgraded conditions, the SciFi tracker must satisfy the following requirements: (i) hit efficiency should be as large as possible ($\approx$99%); (ii) single hit spatial resolution in x-axis should be lower than 100 μm; (iii) the detector performance should not be affected by the expected radiation damage which, according to simulations, can reach up to 35 kGy; (iv) readout electronics at 40 MHz.
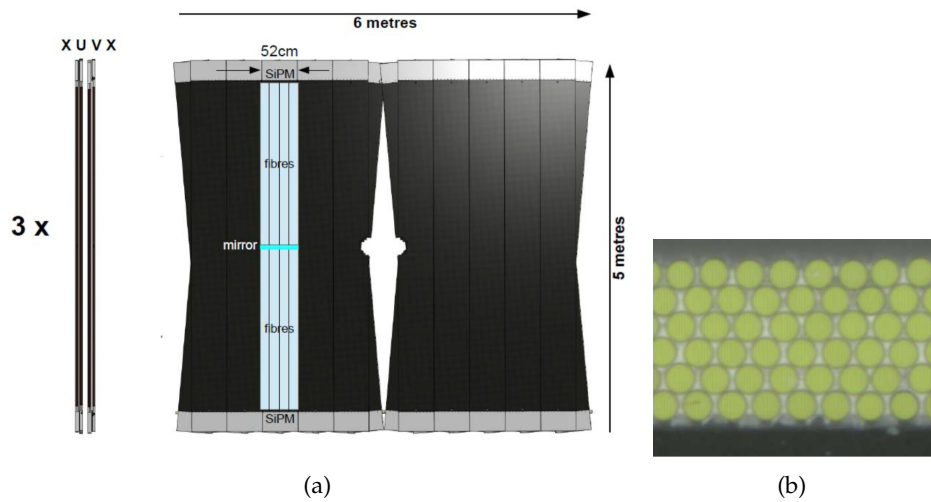
FIGURE 1.16: The SciFi Tracker: (a) overview of one SciFi detection layer and a lateral cross-section of the station with the x-u-v-x geometry; (b) photo of the fibres arranged in six-staggered layers.

Source: [48].

1.3.5   RICH

The upgraded RICH detectors [40, 49, 50] consist basically on significant changes: (i) the aerogel radiator in RICH1 is going to be removed due to its low photon yield and worse resolution even at the current operational luminosities when compared to the gas radiators. This will affect the coverage of momentum range of particles from 1-150 GeV/c to 10-150 GeV/c (in the upgraded version); (ii) the luminosity increase will lead to an increase of the number of hits in the RICH detectors. Simulations show that RICH2 suffers negligible degradation whereas occupancy in RICH1 exceeds upper limits and will affect PID performance. In order to maintain the same PID performance, a modification of the optical arrangement is planned (see Figure 1.17); (iii) the current HPDs able to a maximum readout rate is 1 MHz are going to be replaced by Multi Anode PMT (MaPMT) technology.

1.3.6   Calorimeter system

The upgrade of the calorimeter system [40, 49] remains almost unchanged with respect to the current one. The modifications concerns the front-end boards which requires a 40 MHz readout of the data and also on the PMTs gain settings.

1.3.7   Muon system

The current muon system has to suffer few modification in order to run in the upgraded conditions. In the upgraded muon system [40, 49], the M1
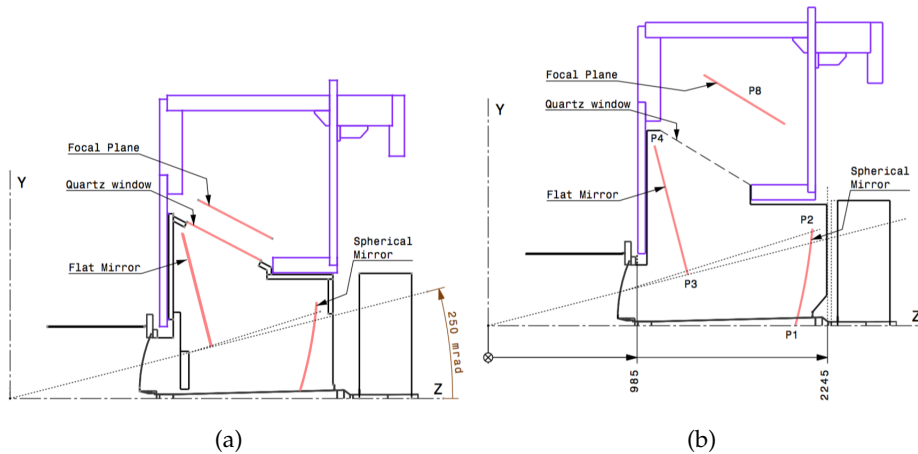
FIGURE 1.17: The optical arrangement of the 1.17(a) current
RICH1 detector and 1.17(b) its upgraded version.

Source: [49].

station is going to be removed. To reduce the occupancy in the inner most region of M2 station, an extra shielding close to the beam pipe is going to be installed behind the HCAL. In addition, although the current front end electronics is already read out at 40 MHz, the data acquisition system readout electronics provides reconstruction data at 1 MHz which must be redesigned. Concerning the performance, the muon identification algorithm efficiency is going to be about 90% (5% lower than the current value).

Part I

Three-body charmeless $B^{\pm}$ decays

Chapter 2

Theoretical background

In this chapter, we start with a brief history of the achieved steps towards the Standard Model (SM) of particle physics, focusing on the quark flavour mixing in the electroweak sector and CP violation. Subsequently, we detail the formalism to treat three-body decays in order to extract information about the dynamics involved in the transitions. Finally, we present the decays of interest of this work.

2.1   The Standard Model of particle physics

The Standard Model (SM) of particle physics describes very well all the known matter in the Universe and their microscopic interactions due to the strong, weak and electromagnetic forces. The gravitational force is not included. Among other things, the strong interaction is responsible for keeping together the protons and the neutrons in the atomic nuclei. Whereas the weak interaction is responsible for radioactive beta decay and it plays a role in the energy production in the stars. And the electromagnetic interaction binds the electrons to the nuclei in atoms or atoms in molecules.

The SM is a quantum field theory based on the $SU(3)_c \otimes SU(2)_L \otimes U(1)_Y$ algebra. The $SU(3)_c$ corresponds to the symmetry group of the strong interaction, where the c subscript is related to color (described below). The $SU(2)_L \otimes U(1)_Y$ is the gauge group of the unified weak and electromagnetic interactions, where $SU(2)_L$ is the weak isospin group acting on the left-handed fermions, and the $U(1)_Y$ is the hypercharge group and correspond to the electromagnetic sector.

The matter fields are composed of fermions (particles with spin 1/2) which follow the Fermi-Dirac statistics. The fermions, classified into quarks and leptons, are organized into three families:

$$\begin{pmatrix} \nu_l \\ l^- \end{pmatrix}_L, l_R^- \begin{pmatrix} q_u \\ q_d \end{pmatrix}_L, (q_u)_R (q_d)_R,$$

where the left-handed fermions, indicated by the L subscript, form isospin doublets, while the right-handed singlets, with the R subscript, do not participate in the processes involving weak interactions. The quarks q_u are up-type (u, c and t) with electric charge of +2/3, while quarks q_d are down-type (d, s and b) with -1/3 as electric charge. Each quark type is known as flavour. The l^- corresponds to the leptons: electron (e^-), muon (μ^-) and tau (τ^-).

A second type of elementary particles called as Gauge bosons (spin-1) intermediate the interactions among the elementary particles. Quarks interact strongly by exchanging colour and gluons are the quanta of the colour field. The theory that describes these interactions is the quantum chromodynamics (QCD). Colour can be of three types, so that each quark flavour has three replicas. The property of colour is not seen in nature due to the effect know as colour confinement, where quarks are grouped to produce colourless hadrons. Hadrons are classified into mesons and baryons. Mesons are particles made of one quark and one antiquark such as π^+ ($u\,\bar{d}$), while baryons are constituted of three quarks as the proton composed of u $u\,d$.

The spontaneous breaking of the electroweak symmetry $\mathrm{SU}(2)_L \otimes \mathrm{U}(1)_Y$, which is associated with the Englert-Brout-Higgs mechanism, generate the massive bosons $W^\pm$ and Z^0 by requiring a massless photon γ (all spin-1). This mechanism assume the existence of the Higgs field, which manifests itself through a scalar Higgs boson, detected in ATLAS and CMS collaborations in 2012 [51, 52]. Also the Higgs coupling to the fermions is proportional to their masses, which are not predicted by the theory. In the SM, all quarks and charged leptons are massive, while the neutrinos are considered to be massless. Nevertheless, in 1998, it was found that neutrinos must have a nonzero mass [53] due to flavour oscillations, similar to what happens in the quark sector.

In summary, in the SM there are 12 quarks, with three colours each, 12 leptons (considering both matter and anti-matter), and 13 bosons (including the 8 types of gluons), leading to a total of 61 particles. Figure 2.1 depicts the fundamental particles of the SM.

2.2 CP **violation**

In physics, symmetries of a system represent a transformation that leaves it invariant. Symmetries play a significant role in physics and are associated with conservation laws according to Noether's theorem.

In this section, we focus on three types of discrete symmetries: charge conjugation (C), parity (P) and time reversal (T). The first one, C, transforms particles into antiparticles and vice-versa. It is the only one that does
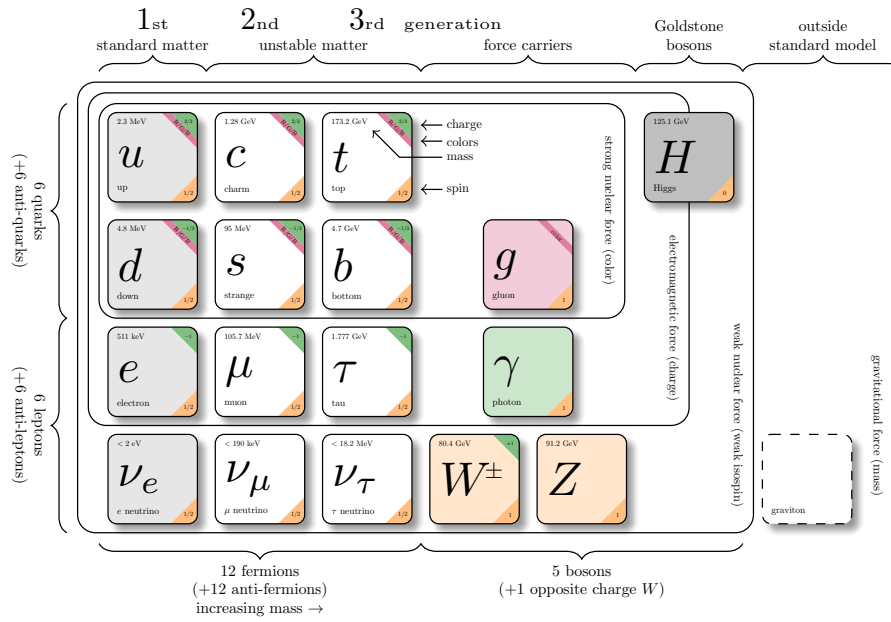
FIGURE 2.1: Diagram of elementary particles.

Source: [54].

not have a classical analogue. Parity and time reversal corresponds to the inversion of the spatial and time coordinates, respectively.

For the electromagnetic interaction CP and T separately were found to be good symmetries. In fact, until 1956, physicists took for granted that C, P and T would also be obeyed by the newly discovered weak and strong interactions. In that year, Lee and Yang proposed that parity could be violated in the weak interactions [55] as a solution for the $\tau - \theta$ puzzle: two particles $\tau^{\pm}$ and $\theta^{\pm}$ (with same mass and lifetime) decay into three and two pions, respectively, which are states with opposed parity.

In 1958, Marshak, Sudarshan, Feynman and Gell-Mann proposed the V-A (vector-axial-vector) theory in the weak lagrangean term that violated C and P separately [56]. The non-conservation of parity implied a lack of space isotropy or, in other words, that right and left components could behave differently. This symmetry was replaced by CP, a more fundamental symmetry in nature which transforms particles of left helicity[1] into right-helicity particles and vice-versa. Until 1964, CP symmetry was assumed to be conserved in weak interactions as well. This assumption was based in the solid and still valid CPT theorem which states that all quantum field

---

[1]Helicity h of a particle is defined as:

$$h = \frac{\vec{s} \cdot \vec{p}}{|\vec{s}||\vec{p}|},$$

where $\vec{s}$ is the spin and $\vec{p}$ is the momentum of the particle.

theories must be symmetric under CPT transformation. Then, the violation of CP implies the violation of the time-reversal symmetry. In that year, the first evidence of CP violation was discovered in the system of neutral kaons [57]. Recently, CP violation was observed in B meson decays, and also in Λ_b baryon decays [58] with the first experimental evidence published this year.

In 1973, CP violation mechanism was implemented in the SM by introducing a mixing matrix, in which the weak eigenstates d',s' and b' correspond to a combination of the mass eigenstates d, s and b (see Eq. (2.1)). Makoto Kobayashi and Toshihide Maskawa, who introduced the third quark family into the Cabibbo matrix[2], won the Nobel Prize in 2008 for their prediction.

$$\begin{pmatrix} d' \\ s' \\ b' \end{pmatrix} = \begin{pmatrix} V_{ud} & V_{us} & V_{ub} \\ V_{cd} & V_{cs} & V_{cb} \\ V_{td} & V_{ts} & V_{tb} \end{pmatrix} \begin{pmatrix} d \\ s \\ b \end{pmatrix} \tag{2.1}$$

The CKM matrix V is a complex and unitary matrix that describes the coupling in the weak charged currents:

$$J_W^\mu = \bar{q}_u \gamma^\mu \frac{1}{2}(1 - \gamma_5)(V_{ud}\, q_d + V_{us}\, q_s + V_{ub}\, q_b)$$

Flavour changing-neutral currents are highly suppressed by the GIM mechanism and cannot exist in the SM in tree level (or leading terms). The unitary conditions $VV^\dagger = V^\dagger V = I$ imply that the CKM matrix depends on three angles and a phase. There exist several possible parametrizations that allow expressing a unitary matrix with three rotational angles and a phase. The "standard" parametrization is:

$$V = \begin{pmatrix} c_{12}c_{13} & s_{12}c_{13} & s_{13}e^{-i\delta} \\ -s_{12}c_{23} - c_{12}s_{23}s_{13}e^{i\delta} & c_{12}c_{23} - s_{12}s_{23}s_{13}e^{i\delta} & s_{23}c_{13} \\ s_{12}s_{23} - c_{12}c_{23}s_{13}e^{i\delta} & -c_{12}s_{23} - s_{12}c_{23}s_{13}e^{i\delta} & c_{23}c_{13} \end{pmatrix}$$

where $c_{ij} = \cos\theta_{ij}$ and $s_{ij} = \sin\theta_{ij}$, θ_{ij} correspond to the Euler angles between the families i and j and δ is the phase that allows CP violation. In this parametrization, it is clear the rotational aspect among the quark families. The fit results for the magnitudes of the V_{ij} elements are [59]:

$$V = \begin{pmatrix} 0.97434^{+0.00011}_{-0.00012} & 0.22506 \pm 0.00050 & 0.00357 \pm 0.00015 \\ 0.22492 \pm 0.00050 & 0.97351 \pm 0.00013 & 0.0411 \pm 0.00013 \\ 0.00875^{+0.00032}_{-0.00033} & 0.0403 \pm 0.0013 & 0.99915 \pm 0.00005 \end{pmatrix}$$

---

[2]In 1963, Cabibbo introduced the mixing angle θ_c known as mixing angle, so that $d' = \cos\theta_c d + \sin\theta_c s$ and $s' = -\sin\theta_c d + \cos\theta_c s$, with $\theta_c \sim 13°$.

As expected, the elements of the diagonal are ~ 1 and the more distant from the diagonal the more suppressed is the probability of the transition.

Another very common parametrization was introduced by Wolfestein [60] which expresses the CKM elements as an expansion in powers of the parameter $\lambda = s_{12} = \sin\theta_{12}$ where θ_{12} is the Cabibbo angle. Up to order λ^3, it is:

$$V = \begin{pmatrix} 1 - \lambda^2 & \lambda & A\lambda^3(\rho - i\eta) \\ -\lambda & 1 - \lambda^2/2 & A\lambda^2 \\ A\lambda^3(1 - \rho - i\eta) & A\lambda^2 & 1 \end{pmatrix}$$

where the parameters λ, A and η are related to the "standard" parametrization as $\lambda = s_{12}$, $A\lambda^2(\rho - i\eta) = s_{13}e^{-i\delta}$.

The unitary conditions for the CKM matrix provide nine equations in which three are normalization relations and six are orthogonality relations. The latter relations read (where the order of magnitude in λ is expressed):

$$\underbrace{V_{ud}^*V_{us}}_{\mathcal{O}(\lambda)} + \underbrace{V_{cd}^*V_{cs}}_{\mathcal{O}(\lambda)} + \underbrace{V_{td}^*V_{ts}}_{\mathcal{O}(\lambda^5)} = 0 \tag{2.2}$$

$$\underbrace{V_{us}^*V_{ub}}_{\mathcal{O}(\lambda^4)} + \underbrace{V_{cs}^*V_{cb}}_{\mathcal{O}(\lambda^2)} + \underbrace{V_{ts}^*V_{tb}}_{\mathcal{O}(\lambda^2)} = 0 \tag{2.3}$$

$$\underbrace{V_{ub}^*V_{ud}}_{\mathcal{O}(\lambda^3)} + \underbrace{V_{cb}^*V_{cd}}_{\mathcal{O}(\lambda^3)} + \underbrace{V_{tb}^*V_{td}}_{\mathcal{O}(\lambda^3)} = 0 \tag{2.4}$$

$$\underbrace{V_{ud}V_{cd}^*}_{\mathcal{O}(\lambda)} + \underbrace{V_{us}V_{cs}^*}_{\mathcal{O}(\lambda)} + \underbrace{V_{ub}V_{cb}^*}_{\mathcal{O}(\lambda^5)} = 0 \tag{2.5}$$

$$\underbrace{V_{td}V_{cd}^*}_{\mathcal{O}(\lambda^4)} + \underbrace{V_{ts}V_{cs}^*}_{\mathcal{O}(\lambda^2)} + \underbrace{V_{tb}V_{cb}^*}_{\mathcal{O}(\lambda^2)} = 0 \tag{2.6}$$

$$\underbrace{V_{td}V_{ud}^*}_{\mathcal{O}(\lambda^3)} + \underbrace{V_{ts}V_{us}^*}_{\mathcal{O}(\lambda^3)} + \underbrace{V_{tb}V_{ub}^*}_{\mathcal{O}(\lambda^3)} = 0 \tag{2.7}$$

These equations can be represented as unitary triangles in the complex plane. Only Eqs. (2.4) and (2.7) have the sides with the same order of magnitude, $\mathcal{O}(\lambda^3)$. Figure 2.2 depicts these two triangles in the complex plane.

The sides of the triangles are associated with the decay amplitudes while the angles are related with the *CP* violation. The fit for the Wolfenstein parameters gives:

$$\lambda = 0.22506 \pm 0.00050 \quad A = 0.811 \pm 0.026$$
$$\bar{\rho} = 0.124^{+0.019}_{-0.018} \quad \bar{\eta} = 0.356 \pm 0.011$$
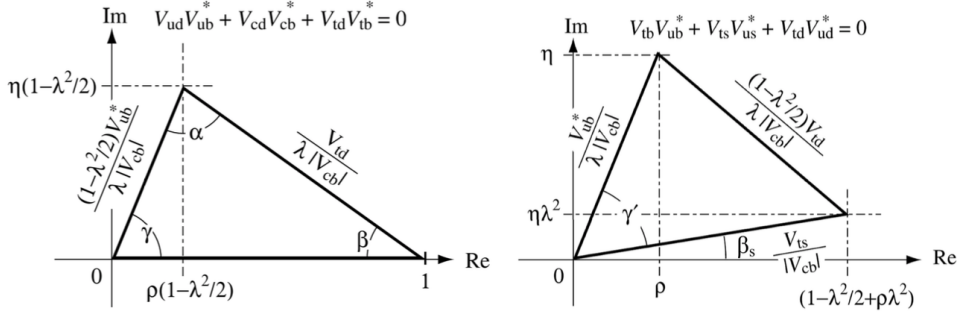
FIGURE 2.2: Triangles from equations (2.4) and (2.7) in the Wolfstein parametrisation.

Source: [61].

2.3 CP **violation and new physics**

The Standard Model of particle physics is a successful theory. Several predictions were confirmed by the experiments such as the charm and top quarks, the mass of the $W^\pm$ and Z^0 bosons and more recently the Higgs boson. However, this model is unable to answer several questions, for instance, (i) What is the origin of the enormous matter and antimatter asymmetry in the Universe? (ii) How do we unify the fundamental interactions? (iii) What about gravity? Does the graviton exist? (iv) What about the neutrinos mass?

We are going to focus on the first question. From cosmology, the baryon asymmetry of the Universe is determined as the difference between the number of baryons NB and antibaryons $N_{\bar{B}}$ divided by the number of photons N_γ which is resulted from the annihilation processes. This ratio is estimated from Cosmic Microwave Background radiation as:

$$\eta = \frac{N_{B-N_{\bar{B}}}}{N_\gamma} \sim \mathcal{O}(10^{-10}),$$

which means there was a tiny excess of baryons in the past. Thus, how could some matter survive in the primordial annihilation? In 1967, Sakharov [62] described the following three conditions that are required for any baryogenesis to occur, regardless of the exact mechanism:

1. There must exist a process that violates the barionic number;

2. The symmetries C and CP need to be violated;

3. The baryogenesis process must happen under conditions outside the thermal equilibrium, so that CPT is conserved. In thermal equilibrium T is a good symmetry.

Thus, *CP* violation is an essential ingredient for the generation of matter and antimatter imbalance in the Universe. However the *CP* violation mechanism due to the CKM matrix lead to an asymmetry at least ten orders of magnitude smaller than observed.

This discrepancy implies that the SM is an incomplete theory and the additional sources of *CP* violation must exist. Therefore, any disagreement between reliable predictions of *CP* violation in SM and experimental results may reveal new physics.

In this context, B meson charmless decays can give us a hint about non-SM physics through the different processes by which a decay can occur.

2.4 Types of *CP* violation

It is possible to distinguish three different types of *CP* violation (CPV). They are classified as:

- *CP* violation in the decays: occurs when physical decay amplitudes for *CP* conjugate processes into final states f and $\bar{f}$ are different in modulus, i.e.:

$$|A_f| \neq |\bar{A}_{\bar{f}}|.$$

  It is a direct *CP* violation once it describes processes with flavour change $\Delta F = 1$.

- *CP* violation in the mixing: occurs when a transition of a neutral meson $P^0 \to \bar{P}^0$ has a different probability with respect to the *CP*-conjugate $\bar{P}^0 \to P^0$. It is an indirect *CP* violation describing processes with flavour change $\Delta F = 2$.

- CP violation in the interference of mixing and decay: occurs not only via the decay amplitude $A(P^0 \to f)$, but also through the process in which P^0 first oscillates to $\bar{P}^0$ and, subsequently, it decays to the final state f via $A(\bar{P}^0 \to f)$. In the second case, both the mixing and the decay play a role in the *CP* violation.

Since charged particles are forbidden to mix due to charge conservation, the last two types of *CP* violation are only allowed for neutral meson decays. These have been studied in B^0-$\overline{B}^0$ [63] and D^0-$\overline{D}^0$ decays [64]. Therefore, in order to describe *CP* violation in the charged B meson decays, we are going to focus on the first type.

The decay amplitudes can have more than one dominant contribution with different phases. The phases can be classified as weak (or *CP*-odd) and strong (or *CP*-even). Weak phases are the ones where the transition amplitude for a process and the transition amplitude for the *CP* conjugate

process have opposite sign. While the strong phase has the same sign for both amplitudes.

In the Standard Model the only source of weak phases are the CKM matrix elements that are involved in the weak interaction. Since the Lagrangian is Hermitian, the complex phases in the CKM matrix change sign through the CP operation. Strong phases may arise from quark loops such as penguin diagrams. They can also manifest through hadronic final state interactions (FSI) which allow the final state particles of the weak decay to interact via non-weak interactions. Hence, the total decay amplitude should include these intermediate states.

These phases are arbitrary and non-physical, but the relative phase of two partial amplitudes in general implies in observable consequences. Thus, the direct CPV arises from the phase difference between $|A_f|^2 - |\bar{A}_{\bar{f}}|^2$, where A_f is the decay amplitude of a certain decay leading to a final state f and $\bar{A}_{\bar{f}}$ is the decay amplitude leading to $\bar{f}$:

$$A_f = \langle f|T|i \rangle,$$
$$\bar{A}_{\bar{f}} = \langle \bar{f}|T|\bar{i} \rangle,$$

where T is the transition amplitude.

To verify that CP violation naturally arises when $|A_f| \neq |\bar{A}_{\bar{f}}|$, the following amplitudes are considered:

$$A_f = \langle f|T|i \rangle = A_1 e^{i(\delta_1 + \phi_1)} + A_2 e^{i(\delta_2 + \phi_2)},$$
$$\bar{A}_{\bar{f}} = \langle \bar{f}|T|\bar{i} \rangle = A_1 e^{i(\delta_1 - \phi_1)} + A_2 e^{i(\delta_2 - \phi_2)}, \tag{2.8}$$

where A_1 and A_2 are real and positive numbers, ϕ_1 and ϕ_2 are the weak phases and δ_1 and δ_2 are the strong phases. These interfering amplitudes may represent, for example, two different Feynman diagrams resulting in the same final state. Note that:

$$|A_f|^2 - |\bar{A}_{\bar{f}}|^2 = -4A_1 A_2 \sin(\delta_1 - \delta_2) \sin(\phi_1 - \phi_2).$$

Thus, CP violation arises from processes with interfering amplitudes with different weak and strong phases. A more interesting quantity that can be observed by experiments is the asymmetry $\mathcal{A}_{CP}$, which is defined as:

$$\mathcal{A}_{CP} = \frac{|\langle f|T|i \rangle|^2 - |\langle \bar{f}|T|\bar{i} \rangle|^2}{|\langle f|T|i \rangle|^2 + |\langle \bar{f}|T|\bar{i} \rangle|^2} \tag{2.9}$$

By substituting Eq. (2.8) into Eq. (2.9), we get:

$$\mathcal{A}_{CP} = \frac{-2A_1 A_2 \sin(\delta_1 - \delta_2) \sin(\phi_1 - \phi_2)}{A_1^2 + A_2^2 + 2A_1 A_2 \cos(\delta_1 - \delta_2) \cos(\phi_1 - \phi_2)}$$

Hence, the asymmetry is going to be large in the following conditions:

1. $\delta_1 - \delta_2 \approx \pi/2$

2. $\phi_1 - \phi_2 \approx \pi/2$

3. $A_1 \approx A_2$

2.5 Three-body decays formalism

Electrons, protons, photons and neutrinos are the only known stable particles in nature. All the others decay into lighter particles. The study of the decaying phenomena, theoretically and experimentally, can shed a light into the interaction processes leading to several possible decays.

A crucial observable related to a particle is its lifetime τ. It is directly associated with the dominant type of the interaction that governs the transition to the final states. Moreover, the same particle can decay into several final states (or decay channels) so that the total decay rate (Γ_{total}) of a particle can be defined as $\Gamma_{\text{total}} = \sum_i \Gamma_i$ where Γ_i corresponds to the decay rate of each channel. The relation between the lifetime and the decay rate is given by $\tau = 1/\Gamma_{\text{total}}$.

The decay rate of a particle with mass M and quadrimomenta P leading to n-body final states with mass m_i and quadrimomenta p_i and energy E_i, derived from the Fermi's golden rule, is given by ([65]):

$$\Gamma = \frac{(2\pi)^4}{2M} \int |\mathcal{M}|^2 \delta^4(P - \sum_{i=1}^{n} p_i) \prod_{i=1}^{n} \frac{d^3 p_i}{(2\pi)^3 2E_i},$$

where $\mathcal{M}$ is the decay amplitude.

2.5.1 Dalitz plot

In 1953, Richard Dalitz developed a technique to conveniently represent three-body decays in a two-dimensional plot [66], where characteristic patterns express information about the spin and parity of the decaying particles. Dalitz plot was thought to unveil the nature of the τ-meson[3] by determining its spin and parity. His work exceeded his original purpose and Dalitz plot has become one of main tools used in high energy physics, leading to the discovery of about 100 resonances (short-lived particles)[67].

Consider a particle P that decays to the final state $P_1 P_2 P_3$. The possible combinations of two particles are: $P_1 P_2$, $P_2 P_3$ and $P_1 P_3$. The two coordinate axes of a Dalitz plot are the invariant masses squared of two of the three

---

[3]From the $\tau - \theta$ puzzle.

possible pairs:

$$s_{12} = m_{12}^2 = (p_1 + p_2)^2,$$
$$s_{23} = m_{23}^2 = (p_2 + p_3)^2,$$
$$s_{31} = m_{31}^2 = (p_3 + p_1)^2,$$

where p_i are the four-momenta of the P_i particle and s_{ij} are one of the Mandelstam variables. For a decay with identical particles, two of them have the same sign and are therefore undistinguishable. In this case, the Dalitz plot is symmetrised and its axes are chosen as the lower and the higher value of the two possible combinations. Take for instance the $B^{\pm} \to \pi^{\pm}\pi^+\pi^-$ decay, in this case the Dalitz plot axes are: $m_{\pi^+\pi^-\,\text{low}}$ and $m_{\pi^+\pi^-\,\text{high}}$.

Thus each decay $P \to P_1 P_2 P_3$ corresponds to a dot in the two-dimensional Dalitz plot. The kinematics of the decay delimits the boundaries of the phase space as illustrated in Figure 2.3.
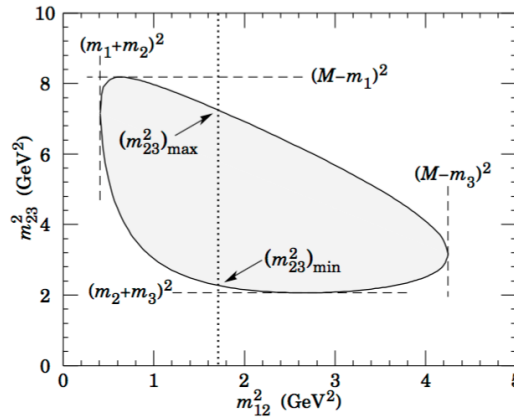
FIGURE 2.3: Example of a Dalitz plot for a three-body decay.

Source: [65].

The reader may wonder if two variables are enough to describe a decay. To completely specify a three-body decay configuration, the information of each momentum components and energy of the final states particles should be known. Hence we would need 12 degrees of freedom to describe the kinematics of the decay. However, energy and momentum conservation impose some constraints. Total energy and three-momenta $\vec{p_i}$ conservation plus the energy-momentum relation ($E_i^2 = m_i^2 + |\vec{p_i}|2$) reduces the number of degrees of freedom to 5. If all the particles involved in the decay are spinless, the resulting decay distribution must be isotropic in the rest frame of the decaying particle. Therefore, the orientation of the linear momenta are irrelevant and two variables suffice to describe a three-body decay. In

this very special case, the decay rate is given by[65]:

$$dΓ = \frac{1}{(2π)^3 32M^3} |\mathcal{M}|^2 dm_{12}^2 dm_{23}^2.$$

The $|\mathcal{M}|^2$ contains the dynamics of the decay. If $|\mathcal{M}|^2$ is constant, the events will be uniformly distributed inside the Dalitz boundaries. Any slight variation in the event distribution over the Dalitz plot is due to dynamic effects due to the interference of the quantum mechanical amplitudes of the final state particles.

2.5.2 Three-body decays

A three-body final state can be resulted from resonant and nonresonant decays. The former proceeds through resonances, particles that interact via the strong force and has a very short lifetime (10^{-23} s). While, in the latter, the decaying particle disintegrates directly into three final state particles (see Figure 2.4).

(a) (b)
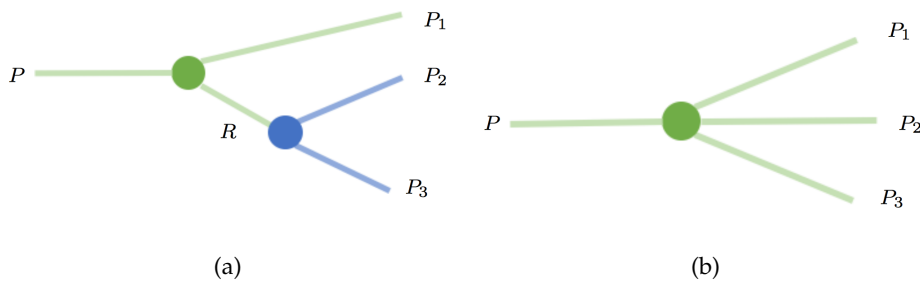
FIGURE 2.4: Illustration of a (a) resonant and (b) a nonresonant decay for a $P \rightarrow P_1 P_2 P_3$ decay.

Figure 2.5 exemplifies possible contributions in the Dalitz plot of a three-body decay. The plot on the left shows the phase space equally populated. The middle plot depicts the effect of the three-body decay intermediated by a scalar resonance: an enhanced line is seen across the phase space and the width is given by the resonance width. The left plot illustrates a resonant decay via a vector resonance. The angular dependence is manifested in the Dalitz though the presence of one node.

The most common model adopted by experimentalists to describe the decay amplitude is the isobar model. For three-body decays, the total decay amplitude is described as a coherent sum of all two-body amplitudes and a nonresonant contribution:

$$\mathcal{A}(m) = a_{NR} \, e^{i\phi_{NR}} \, \mathcal{A}_{NR}(m) + \sum_r a_r \, e^{i\phi_r} \, \mathcal{A}_r(m), \qquad (2.10)$$
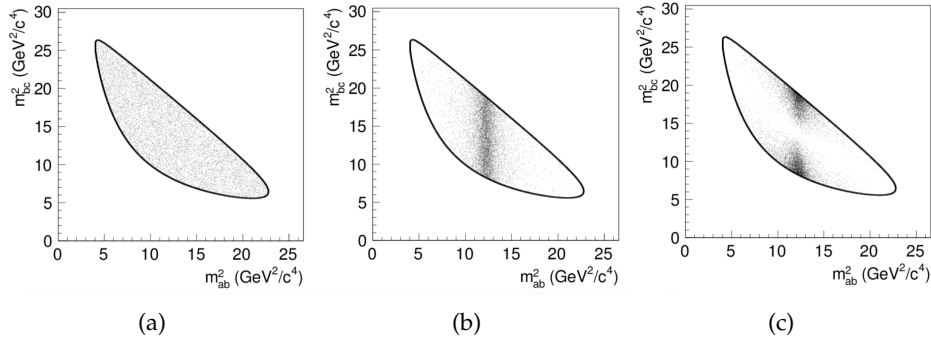
FIGURE 2.5: Example of possible contributions Dalitz plot: (a) phase space homogeneously populated; (b) a scalar resonance which decayed to ab particles; (c) a vector resonance (spin 1) which decayed to ab particles. Resonances leading to bc and ac final states are also possible and their manifestation in the Dalitz plot would be similar.

Source: [68].

where the subscripts r and NR stands for resonant and nonresonant components, respectively. $\mathcal{A}_{NR}$ and $\mathcal{A}_r$ describe the dynamical properties of the decay and the phases include both weak and strong phases.

This formalism is a phenomenological approach to describe these amplitudes. The non-resonant amplitude is often considered to be constant along the phase. While $\mathcal{A}_r$ is described by the product of the propagator of the resonance, barrier factors and angular probability distribution. The first term gives the line-shape of the resonance commonly expressed by the Breit-Wigner excitation curve. The last terms are spin dependent. If the resonant state has spin s and all the particles involved are spinless or have spin-0, which is the case of pions, kaons and $B^\pm$ meson, then the second term is given by the Legendre Polynomial.

In particular, B mesons decays with three hadrons as final state involve both short and long distance QCD effects. This means the calculation of the decaying amplitudes contains both short-distance perturbative effects and non-perturbative QCD, which makes the description of such decays a challenge [68]. For this reason, there are several phenomenological models and techniques which are based on experimental results. In those circumstances, measurements of B meson decays can elucidate the dynamics involved in both weak and strong interactions.

2.6   Charmless three-body B decays

The charmless three-body $B^\pm \to h^\pm h^+ h^-$ decays include: $B^\pm \to K^\pm \pi^+ \pi^-$, $B^\pm \to \pi^\pm \pi^+ \pi^-$, $B^\pm \to K^\pm K^+ K^-$ and $B^\pm \to \pi^\pm K^+ K^-$. They are often

dominated by intermediate two-body resonant states. The branching fractions for those decays are of the order of 10^{-5}, which means that the analysis of such decays are only possible for experiments with high luminosity, such as the LHCb experiment.

Here we introduce the particles of interest of this work. The positive (negative) charged B meson is composed of $u\,\overline{b}$ ($\overline{u}\,b$) with a rest mass of $\sim 5.28\,\mathrm{GeV}/c^2$ and a mean lifetime of $\sim 1.638\,\mathrm{ps}$ [59]. Charged kaons, composed of $u\,\overline{s}$ or $\overline{u}\,s$, have about half the mass of the proton ($\sim 494\,\mathrm{MeV}/c^2$) with a mean lifetime of about 12 ns. Pions are the lightest mesons composed by $u\,\overline{d}$ or $u\,\overline{d}$ with rest mass $\sim 140\,\mathrm{MeV}/c^2$, decaying with a mean lifetime of about 26 ns.

Figures 2.6 and 2.7 depict two Feynman diagrams for the $B^{\pm} \to \pi^{\pm}\pi^{+}\pi^{-}$ and $B^{\pm} \to \pi^{\pm}K^{+}K^{-}$ decays, respectively. In the tree diagram (Figures 2.6(a) and 2.7(a)), the b decay occurs through a virtual W^{-} boson emission resulting in a π^{-} and R^{0}. For the $B^{\pm} \to \pi^{\pm}\pi^{+}\pi^{-}$ ($B^{\pm} \to \pi^{\pm}K^{+}K^{-}$) decay, the R^{0} represents any neutral resonance that decays in $\pi^{+}\ \pi^{-}$ ($K^{+}\ K^{-}$). In the penguin diagram (Figures 2.6(b) and 2.7(b)), the b decay is due to a virtual W^{-} boson emission and absorption together with a gluon emission. The magnitudes of the amplitudes are proportional to the product of the CKM elements, made explicit in each diagram.

Figures 2.8 and 2.9 show two Feynman diagrams for the $B^{\pm} \to K^{\pm}K^{+}K^{-}$ and $B^{\pm} \to K^{\pm}\pi^{+}\pi^{-}$, respectively. In the tree diagram, the b decay happens through a virtual W^{-} boson emission resulting in a K^{-} and a neutral resonance R^{0}. For the $B^{\pm} \to K^{\pm}K^{+}K^{-}$ ($B^{\pm} \to \pi^{\pm}\pi^{+}\pi^{-}$) decay, the R^{0} decays in $K^{+}\ K^{-}$ ($\pi^{+}\ \pi^{-}$). While in the penguin diagram, the b changes flavour due to a virtual W^{-} boson emission and absorption and a gluon emission. The magnitudes of the amplitudes are shown.

Previous measurements on $B^{\pm} \to h^{\pm}h^{+}h^{-}$ decays indicate large CP asymmetry along the phase-space [69, 70, 71, 72]. As mentioned in section 2.2, CP violation manifests from processes with interfering amplitudes with
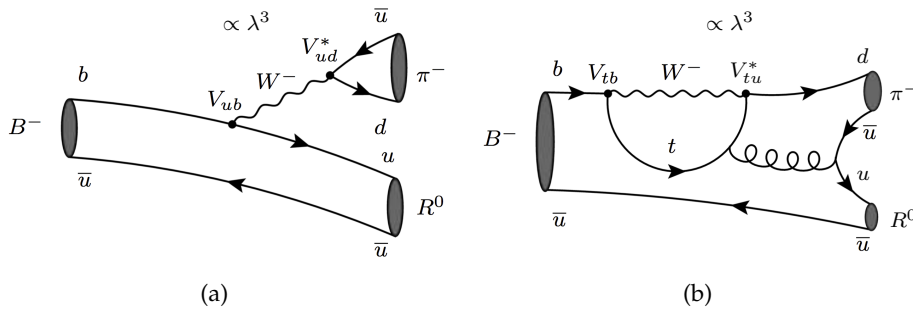
FIGURE 2.6: $B^{-} \to \pi^{-}\,\pi^{+}\,\pi^{-}$ dominant Feynman diagrams:
(a) tree (b) penguin.
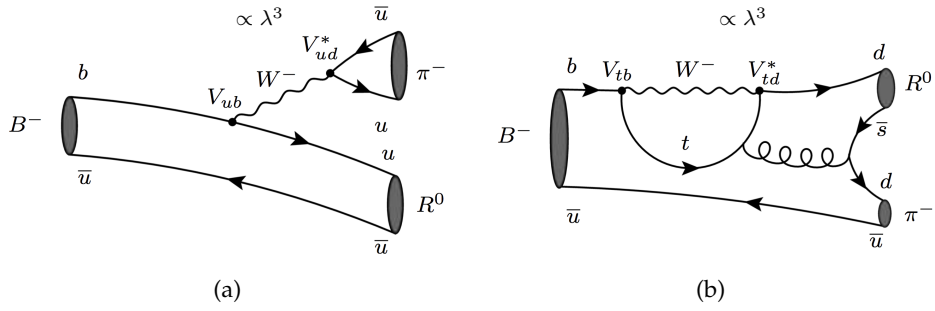
FIGURE 2.7: $B^- \to \pi^- K^+ K^-$ dominant Feynman diagrams: (a) tree (b) penguin.
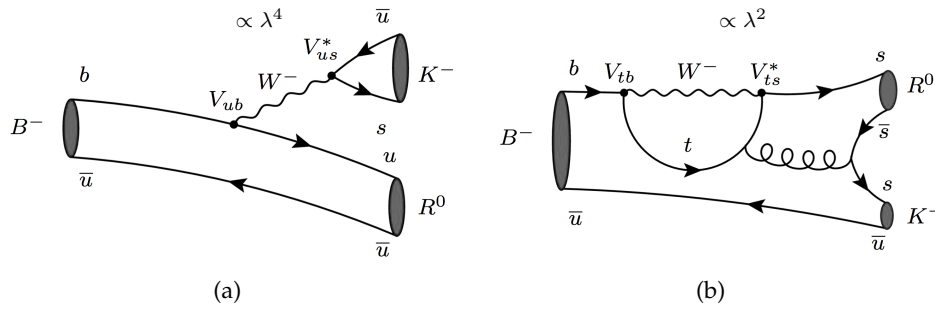
FIGURE 2.8: $B^- \to K^- K^+ K^-$ dominant Feynman diagrams: (a) tree (b) penguin.
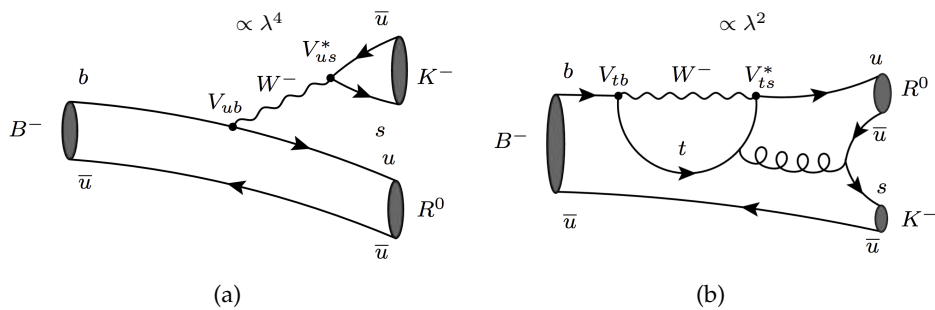
FIGURE 2.9: $B^- \to K^- \pi^+ \pi^-$ dominant Feynman diagrams: (a) tree (b) penguin.

different weak and strong phases that are only accessible through amplitude (Dalitz) analysis. While the weak phases arise from CKM matrix elements,the sources of the strong phase difference due to hadronic interaction is not fully elucidated. In the particular case of charmless three-body decays, the strong phase difference may be attributed to three different sources. The first source is related to short-distance processes, i.e, the *CP* asymmetry arises from the interference between tree and penguin quark level diagrams owning different weak and strong phases (BSS model [73]). The second source is induced by interference effects between intermediate states of the decay, which leads to local asymmetries in the phase space. Another possible source can be associated with final state interactions such as $KK \leftrightarrow \pi\pi$ rescattering effects [74]. These may occur between two or more decay channels with the same flavor quantum numbers, such as the $B^{\pm} \to K^{\pm} K^+ K^-$ and $B^{\pm} \to K^{\pm}\pi^+\pi^-$. Reference [75] denominates it as "compound *CP* violation". This effect is constrained by CPT conservation, thus the sum of the partial decay widths, for all channels with the same final-state quantum numbers, must be equal for charge-conjugated decays.

Figure 2.10 shows the Dalitz plot for the $B^{\pm} \to K^{\pm}\pi^+\pi^-$ and $B^{\pm} \to K^{\pm} K^+ K^-$ decays analysed by the BaBar collaboration. Although the signal yield in these analysis are of the order of few thousand, overpopulated regions are easily spotted indicating the interference of different amplitudes, and the presence of resonances.

(a) (b)
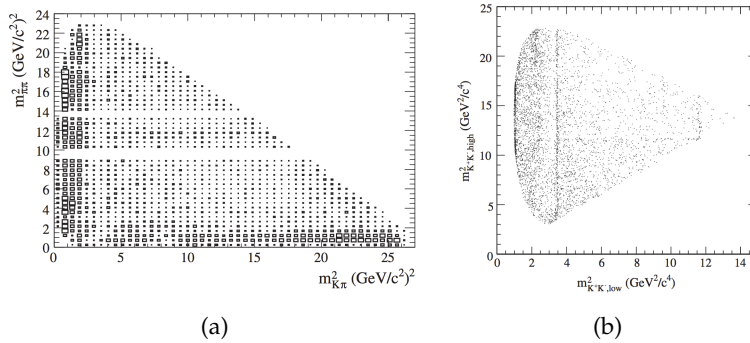
FIGURE 2.10: Dalitz plot of (a) $B^{\pm} \to K^{\pm}\pi^+\pi^-$ and (b) $B^{\pm} \to K^{\pm}K^+K^-$ decays from BaBar experiment. In (a) the area of the boxes is proportional to the number of entries.

Source: [70, 71]

Chapter 3

CP violation measurements on the $B^{\pm} \to h^{\pm}h^{+}h^{-}$ decays

The basic procedure to obtain the CP asymmetry includes counting the number of B^{+} and B^{-} candidates in the data samples. To perform this measurement we need to select events containing the charged B meson decays into three hadrons. Several aspects related to the decay topology and kinematics are taken into account in all the selection stages. Subsequently, we count the $B^{\pm}$ candidates by means of modeling the signal distribution in the invariant mass spectrum. In this chapter, we detail all those steps and present the results on the global asymmetry measurement.

3.1 Selection variables

To facilitate the comprehension of the selection stages, this section describes the main variables used in the selection of the $B^{\pm} \to h^{\pm}h^{+}h^{-}$ samples. Figure 3.1 illustrates the interaction pp region and the B^{+} particle decays at the secondary vertex into three pions. The term cut, used throughout this thesis, refers to a threshold value at which the selection applies. Take for instance the L0 selection cut $E_T > 3.5\,\text{GeV}$ which means only events with a track with a transverse energy measured by the hadron calorimeter larger than $3.5\,\text{GeV}$ are going to be triggered.

Primary and secondary vertexes (PV/SV)

The primary vertex is the proton-proton interaction point while the secondary vertex is the point where the particle of interest decays.

Flight Distance (FD)

It is the distance between the primary vertex and the decaying vertex. The distance depends on the particle lifetime. A $B^{\pm}$ candidate has a mean lifetime of about $1.64\,\text{ps}$ which corresponds to a decay vertex located $c\tau \approx$
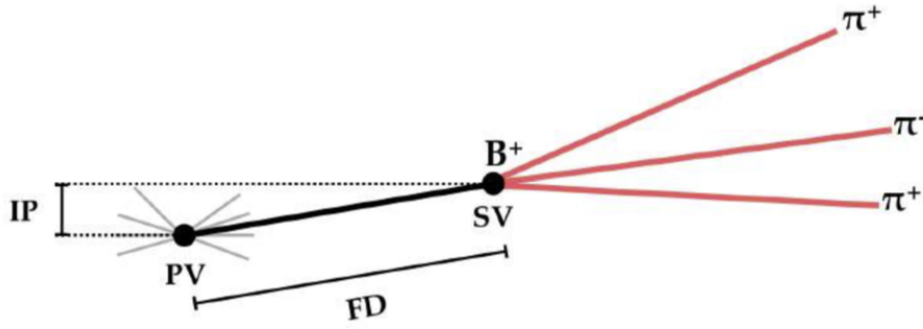
FIGURE 3.1: Topology of a particle decaying with momentum $\vec{p}$ with three particles as final states. Some of the variables used on the selection are depicted: Impact Parameter (IP), Primary Vertex (PV), Secondary Vertex (SV) and Flight Distance (FD).

$500\,\mu\mathrm{m}$ distant from the primary vertex. Hence a typical $B^\pm$ signature has a displaced vertex with respect to the primary vertex. The χ^2 FD is the FD-significance squared which might show a better separation between signal and background.

Impact parameter (IP)

In classical mechanics and nuclear physics, while studying elastic scattering, impact parameter is defined as the perpendicular distance between the initial path of the incident particle and the center of a potential field generated by the target particle. In LHCb the impact parameter is the transverse distance of the closest approach between the reconstructed track and a vertex, which is usually the primary vertex. The IP distinguishes between particles produced at the primary vertex and particles coming from long-lived particles such as B mesons. On average, the final states from a B meson have a larger impact parameter than a particle produced at the primary vertex. The χ^2 of this parameter (IP χ^2) gives the minimum χ^2 distance of a particle's trajectory with respect to the primary vertex. It corresponds to the increase in the vertex-fit χ^2 when including a particle's track.

Transverse momentum/energy ($p_\mathrm{T}/E_\mathrm{T}$)

The transverse momentum (Figure 3.3) is the component of the momentum vector projected on the plane perpendicular to the beam axis. Transverse energy seems to be a misleading term giving that energy is a scalar. It is the energy measured in the calorimeters that is converted into a transverse momentum measurement. We can assume this as true because when dealing with relativistic particles the energy is equivalent to the magnitude

of the momentum. A typical signature of a $B^{\pm}$ decay has a very high transverse momentum/energy. The advantage of using transverse energy is related with the fast measurement performed by the calorimeters which are used in the Level 0 trigger in LHCb. To measure the momentum of the particles, the reconstruction of the trajectory is essential which demands more time.
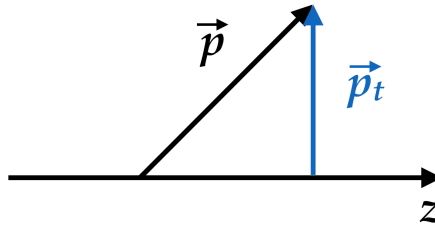
FIGURE 3.2: Illustration of the transverse momentum (p_{T}) variable.

Cosine of θ ($\cos(\theta)$)

The angle θ corresponds to the angle between the flight distance and decaying particle momentum. The cosine of this angle should be very close to 1 for a true $B^{\pm}$ candidate.
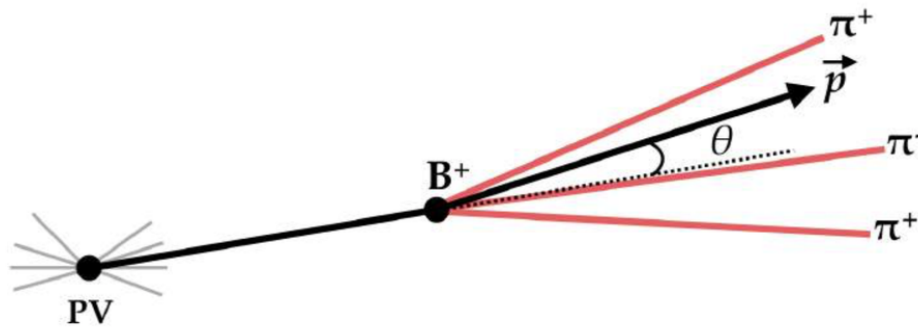
FIGURE 3.3: Illustration of the $\cos\theta$ variable. The dashed line correspond to the direction of flight of the particles and the $\vec{p}$ is te reconstructed momentum. Due to the uncertainty of measuring the mometum of teh final state particles, the reconstructed momentum has a slightly different direction from the direction of the flight of the particle. Thus, $\cos\theta$ is expected to be close to 1 for the true $B^{\pm}$ candidates.

Distance Of Closest Approach (DOCA)

It corresponds to the minimum distance between a pair of tracks from the final state particles (or daughters). It can be used to reject particles

which are not coming from the same vertex. In the case of a decay with 3 final state particles, these distances are computed from the three possible pairs of tracks. Usually the cut involves the maximum or minimum DOCA.

Reduced χ^2 of the vertex (Track χ^2/n.d.f)

The reconstruction of the secondary vertex involves a fit procedure which uses the final state tracks. A good reconstructed vertex (χ^2/n.d.f $\sim \mathcal{O}(1)$) indicates that the daughter's tracks came from the same vertex.

Particle identification variables

There are two types of particle identification variables used by the LHCb collaboration: the DLL and the `ProbNN`. The DLL is an acronym for Difference of Log-Likelihood. For each track in the event, a likelihood is assigned to each of the different mass hypotheses (electron, muon, pion, kaon and proton) based on the information of the RICH, Calorimeters and Muon System. Since the majority of the particles which traverses the detector are pions, the initial mass hypothesis choice is the mass of pions. Then, the likelihood for the other hypotheses are obtained by comparing with the likelihood under the pion hypothesis. For instance, $\text{DLL}_{K\pi} = \ln(\mathcal{L}(K))$ - $ln(\mathcal{L}(\pi))$ is the log-likelihood of the measurement under the kaon hypothesis minus the log-likelihood under the pion hypothesis.

The `ProbNN` identification method is based on multivariate techniques by combining particle identification information and tracking properties such as the tracking performance and kinematics. This algorithm results in a better performance in identifying particles and also has as output a single probability value for each particle hypothesis.

Since we perform an inclusive selection, the particle identification cuts are applied only in the final offline selection stage.

Multivariate selection

Multivariate analysis is a powerful tool to search for correlation between several variables. Recently, it has been applied to numerous analysis in high-energy physics. A multivariate selection cut consists on the combination of multiple variables into a single discriminant. As illustrated in Figure 3.4, it allows to distinguish signal from background with a linear or non-linear cut which is usually more efficient than a simple rectangular cuts.

There are several multivariate methods such as NN (Neural Networks) and BDT (Boosted Decision Tree). They are based on machine learning techniques using input samples that describe the signal and the background. The detailed description of the methods is out of the scope of this thesis and more information can be found in [76] and [77].
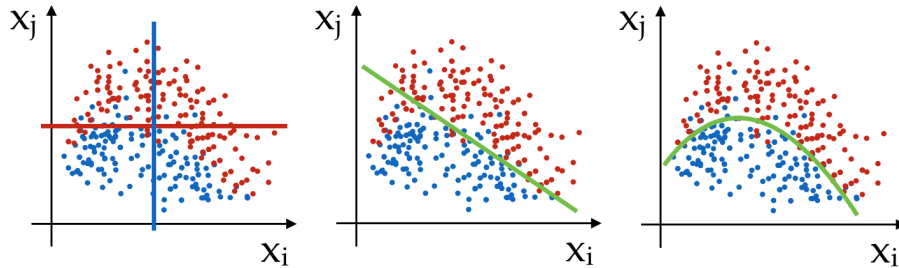
FIGURE 3.4: Illustration of the multivariate selection. The plots depicts the behavior of a sample composed of signal and background events with respect to two different variables. The plot on the left represents a simple linear cut, while the other plots corresponds to a linear (on the middle) and a non-linear (on the right) multivariate cut.

The multivariate selection is used in the HLT2 trigger line and on the offline analysis.

3.2 Dataset

In 2011 (2012) the LHC produced pp collisions with $\sqrt{s} = 7\,\text{TeV}$ ($\sqrt{s} = 8\,\text{TeV}$). Figure 3.5 shows the integrated luminosity in 2011 and 2012. The delivered luminosity refers to the luminosity seen by the LHCb experiment. In ideal conditions, both LHCb and LHC operating perfectly, all delivered luminosity would be recorded. However, issues related to LHCb sub-systems or data acquisition affect the overall efficiency related to the recorded luminosity. The data sample consists of events collected by LHCb in 2011 and 2012 with a total integrated luminosity of about 3.1 fb^{-1}.

3.3 Simulated events

The simulation of the pp interactions was generated by PYTHIA 8 [79] with a specific LHCb configuration. Decays of hadronic particles were produced by the EVTGEN [80] and the interaction of the generated particles with the detector and its response were implemented by the GEANT4 [81, 82]. Only events which are generated inside the detector acceptance were recorded for further simulation of the detector response. The simulated samples
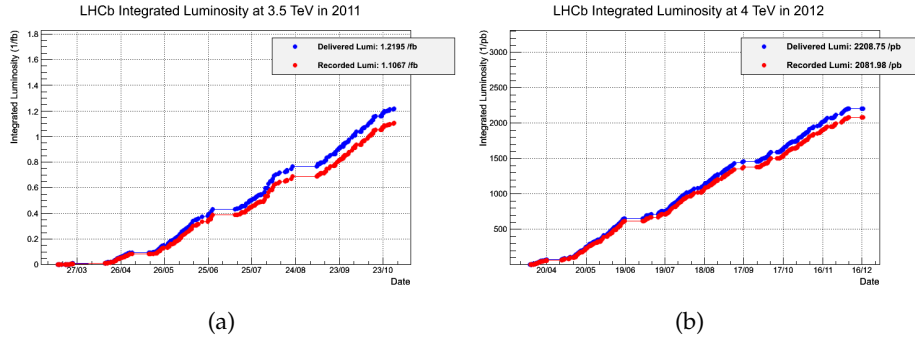
FIGURE 3.5: The integrated luminosity delivered and recorded in LHCb during (a) 2011 and (b) 2012.

Source: [78].

were generated with a flat Dalitz plot representation, i.e., with no resonant decays, and no *CP* violation.

The following Monte Carlo samples were used throughout this analysis:

- $\sim$ 1.5M events with $B^{\pm} \to K^{\pm}\pi^{+}\pi^{-}$ decay;

- $\sim$ 3.0M events with $B^{\pm} \to K^{\pm}K^{+}K^{-}$ decay;

- $\sim$ 2.5M events with $B^{\pm} \to \pi^{\pm}\pi^{+}\pi^{-}$ decay;

- $\sim$ 1.5M events with $B^{\pm} \to \pi^{\pm}K^{+}K^{-}$ decay;

- $\sim$ 5.6M events with $B^{\pm} \to J/\psi\,K^{\pm}$ decay.

3.4   Comments on the background

The main purpose of the selection cuts is to distinguish signal from background. Thus a thorough understanding of the background sources guide us to chose adequate selection cuts to improve the signal purity. We can find different types of potential background sources in the $B^{\pm} \to h^{\pm}h^{+}h^{-}$ mass spectrum. They are categorized as:

- Peaking background: fully reconstructed decays with the same final state particles as the signal or decays where one or more pions (kaons) are misidentified as kaons (pions);

- Partially reconstructed background: originally 4- or more body decays reconstructed with a missing particle;

- Combinatorial background: random combination of three tracks converging to a vertex.

3.4.1 Peaking background

- **Charmonia transitions**: the decay of $B^\pm \to J/\psi\, K^\pm$ has a very similar topology to the signal. Since π and μ have similar masses, $140\,\mathrm{MeV}/c^2$ and $106\,\mathrm{MeV}/c^2$, respectively, the reconstruction of this decay falls exactly in the signal mass window.

- **Charm intermediate states**: several B decays have a D meson as intermediate states which might produce final states equivalent to the signal. Table 3.1 lists the possible channels which can contribute to the background of the $B^\pm \to h^\pm h^+ h^-$.

- **Misidentified**: it corresponds to B decays in which one or more final state particles are mis-identified. Consider, for instance, the $B^\pm \to \pi^\pm \pi^+ \pi^-$ decay as our signal sample. In this case, the $B^\pm \to K^\pm \pi^+ \pi^-$ channel is a background source, when the kaon is misidentified as a pion, with a peaking structure located on the left of the mean B mass value in the $B^\pm \to \pi^\pm \pi^+ \pi^-$ mass spectrum. Thus each of the $B^\pm \to h^\pm h^+ h^-$ decays plays a role as background to the others if at least one of the hadrons is misidentified. This misidentification can also happen in the partially reconstructed decays. Table 3.2 lists the $B^\pm \to h^\pm h^+ h^-$ channels with their corresponding branching fractions. We also expect that double misidentification is more suppressed than single ones.

3.4.2 Partially reconstructed

The partially reconstructed background are decays reconstructed with a missing particle such as photons and π^0. In this case, the measured B invariant mass distribution is shifted to the left of the B mean mass value which may fall in the signal mass window. We are going to discuss the most relevant contributions for each of the decays. These contributions can also happen via a charm meson decay.

- Background contributions of $B^\pm \to K^\pm \pi^+ \pi^-$

  - Charmed decays: the $B^+ \to (\bar{D}^0 \to K^\pm \pi^\mp \pi^0)\pi^+$ where the D^0 meson decays to three particles and the π^0 is not reconstructed.
  - Charmless decays: the $B^\pm \to K^{*\pm}\, \pi^+\, \pi^-$ where the vector meson $K^{*\pm}$ decays into a $K^\pm \pi^0$ final state and the π^0 is not reconstructed. Also there is the $B^\pm \to \eta' K^\pm$ where the η' decays into $\rho^0(\pi^+\pi^-)\gamma$ and the photon is not reconstructed.
    Table 3.3 indicates the branching fractions of these background contributions.

- Background contributions of $B^\pm \to K^\pm K^+ K^-$

  - Charmless decays: the $B^\pm \to K^{*\pm} K^+ K^-$ where the $K^{*\pm} \to K^\pm \pi^0$ is the main contribution. There is also the $B^\pm \to \phi(K^+K^-)K^*(K^\pm\pi^0)$ and $B^\pm \to K^{*\pm}(K^\pm\pi^0)\phi(K^+K^-)$.

    Table 3.4 shows the branching fractions of these background contributions.

- Background contributions of $B^\pm \to \pi^\pm\pi^+\pi^-$

  - Charmed decays: the $B^\pm \bar{D}^0(D^0)\pi^+\pi^-$ where the D^0 decays to $\pi^+ \pi^- \pi^0$ and the π^0 is not reconstructed.

  - Charmless decays: the $B^\pm\pi^\pm\pi^+\pi^-\pi^0$ where the π^0 track is not reconstructed.

    Table 3.5 indicates the branching fractions of these background contributions.

- Background contributions of $B^\pm \to \pi^\pm K^+ K^-$

  - Charmed decays: $B_s^0 \to D_s^- (K^+ K^- \pi^-)\pi^+$ and $B^0 \to D^- (K^+ K^- \pi^-)\pi^+$ where a charged pion is not reconstructed and also $B^\pm \to D^0(K^+ K^- \pi^0)\pi^\pm$ where the π^0 is missing in the reconstruction.

  - Charmless decays: $B^\pm \to K^{*\pm} (K^\pm \pi^0)\pi^\pm K^\mp$ and $B^\pm \to K^{*\pm} (K^\pm \pi^0)\pi^\mp K^\pm$ where a charged pion and a π^0 is not reconstructed and also $B^0 \to K^+ K^- \pi^+ \pi^-$ where a charged pion is missing in the reconstruction.

    Table 3.6 indicates the branching fractions of these background contributions.

3.4.3   Combinatorial

The combinatorial background comes from random combination of three tracks converging to a vertex which satisfies the selection criteria. Opposed to the misidentified and partially reconstructed backgrounds, the combinatorial background distribution lacks of any particular structure or peaks in the mass spectrum.

3.5   Inclusive selection

The selection of charged B mesons decays into three hadrons follows an inclusive selection philosophy. An inclusive selection approach consists on applying cuts that are able to select efficiently a set of channels. As advantages, the inclusive strategy embraces more physics analysis and allows studying multiple channels with the same topology.

Description	Decay
Charmonia transitions	$B^\pm \to J/\psi\, K^\pm$
Charm intermediate states	$B^\pm \to (\bar{D}^0 \to K^+\, \pi^-)\, K^\pm$
	$B^\pm \to (\bar{D}^0 \to K^+\, K^-)\, \pi^\pm$
	$B^\pm \to (\bar{D}^0 \to K^+\, \pi^-)\, K^\pm$
	$B^\pm \to (\bar{D}^0 \to \pi^+\, \pi^-)\, \pi^\pm$

TABLE 3.1: Peaking background contributions.

Decay	BF[65]
$B^\pm \to K^\pm\pi^+\pi^-$	$5.1 \cdot 10^{-5}$
$B^\pm \to K^\pm K^+ K^-$	$3.4 \cdot 10^{-5}$
$B^\pm \to \pi^\pm\pi^+\pi^-$	$1.5 \cdot 10^{-5}$
$B^\pm \to \pi^\pm K^+ K^-$	$5.0 \cdot 10^{-6}$

TABLE 3.2: $B^\pm \to h^\pm h^+ h^-$ decays with their corresponding branching fractions.

Description	Decay	BF[65]
Charmed	$B^+ \to \bar{D}^0\pi^\pm$ with $\bar{D}^0 \to K^\pm\pi^\mp\pi^0$	$6.9 \cdot 10^{-4}$
Charmless	$B^\pm \to K^{*\pm}\, \pi^+\, \pi^-$ with $K^{*\pm} \to K^\pm\, \pi^0$	$2.5 \cdot 10^{-5}$
Resonant radiative	$B^\pm \to \eta'\, K^\pm$ with $\eta' \to \rho^0\, (\pi^+\, \pi^-)\, \gamma$	$2.1 \cdot 10^{-5}$

TABLE 3.3: Partially background contributions to $B^\pm \to K^\pm\pi^+\pi^-$ decay.

Description	Decay	BF[65]
Charmless	$B^\pm \to (K^{*\pm} \to K^\pm\, \pi^0)K^+\, K^-$	$1.2 \cdot 10^{-5}$
	$B^\pm \to \phi(K^+K^-)K^*(K^\pm\pi^0)$	$1.6 \cdot 10^{-6}$

TABLE 3.4: Partially background contributions to $B^\pm \to K^\pm K^+ K^-$ decay.

Description	Decay	BF[65]
Charmed	$B^+ \to \bar{D}^0\pi^+$ with $\bar{D}^0 \to \pi^+\, \pi^-\, \pi^0$	$7.1 \cdot 10^{-5}$
Charmless	$B^\pm \to \pi^\pm\pi^+\pi^-\pi^0$	$< 4.0 \cdot 10^{-3}$

TABLE 3.5: Partially background contributions to $B^\pm \to \pi^\pm\pi^+\pi^-$ decay.

This section describes the selection criteria (from the trigger to the offline stage) applied to the LHCb data in order to acquire $B^\pm \to h^\pm h^+ h^-$ samples.

Description	Decay		BF[65]
Charmed	$B_s^0 \to D_s^- (K^+ K^- \pi^-)\pi^+$ incl. f_s/f_d		$4.2 \cdot 10^{-5}$
	$B^{\pm} \to D^0(K^+ K^- \pi^0)\pi^{\pm}$		$1.6 \cdot 10^{-5}$
Charmless	$B^0 \to D^- (K^+K^-\pi^-)\pi^+$		$2.5 \cdot 10^{-5}$
	$B^{\pm} \to K^{*\pm} (K^{\pm} \pi^0)\pi^{\pm} K^{\mp}$		$< 3.4 \cdot 10^{-5}$
	$B^{\pm} \to K^{*\pm} (K^{\pm} \pi^0)\pi^{\mp} K^{\pm}$		$< 2.0 \cdot 10^{-6}$
	$B^0 \to K^+K^-\pi^+\pi^-$		$< 7.2 \cdot 10^{-5}$

TABLE 3.6:   Partially background contributions to $B^{\pm} \to \pi^{\pm}K^+K^-$ decay.

3.5.1   L0 trigger

At this stage, since our final state particles are hadrons, all events are required to be triggered either on signal by the `L0Hadron` trigger, or independent of signal by the `L0Global` trigger (which means that other particle independent of our signal triggers any of the other lines). Table 3.7 shows the L0 trigger lines selection cuts.

3.5.2   High level trigger

At the first level of the software stage (see Table 3.8), the inclusive trigger requires good quality track candidates with a high p_T and a significant displacement from the primary vertex. The second stage of HLT makes use of the 2-, 3- or 4-body topological triggers which use a multivariate selection algorithm. The algorithm, for a three-body decay, first combine a two-body candidate and another particle, instead of directly defining a three-body object. This procedure is advantageous since it enhances the efficiency of the HLT2 topological lines. By considering the trigger candidate only contains a subset of the final-state particles, it is not appropriate to perform a selection on the mass of B candidate. For this reason, the following variable was defined:

$$m_{cor} = \sqrt{m^2 + |p_{\mathrm{T}mis}|^2} + |p_{\mathrm{T}mis}| \tag{3.1}$$

where $p_{\mathrm{T}mis}$ is missing transverse momentum to the direction of flight of the B candidate. The direction of flight is the vector which connects the

L0 line	Cut	2011 (GeV)	2012 (GeV)	SPD (hits)
single muon	p_T	> 1.48	> 1.76	< 600
dimuon	$\sqrt{(p_T(\mu_1) \times p_T(\mu_2))}$	> 1.3	> 1.3	< 900
hadron	E_T	> 3.5	> 3.7	< 600
electron	E_T	> 2.5	> 3.0	< 600
photon	E_T	> 2.5	> 3.0	< 600

TABLE 3.7: L0 selection cuts for 2011 and 2012.

primary vertex to the secondary vertex. Essentially m_{cor} is the minimum correction to the B candidate mass if a daughter is missing. In addition, cuts are also applied to the sum of the transverse momentum of the daughter tracks, minimum momentum of the daughters, m and m_{cor} of the B candidate, distance of the closest approach (DOCA), IP significance (IPχ^2) and flight distance significance (FDχ^2).

3.5.3 Stripping

Due to the topological similarities of the $B^\pm \to h^\pm h^+ h^-$ modes, the data sample was selected using an inclusive selection approach which reconstructs all particles as kaons and applies some vertex cuts. In addition, a large three-body invariant mass window (4-7 GeV) is applied in order to include all final states of interest and, at the final analysis stage, the $B^\pm$ invariant masses are recalculated for each decay channel assigning the correct mass hypothesis.

The stripping selection imposes some loose initial restrictions on the quality of the reconstructed tracks, momenta and transverse momenta, and the maximum distance of closest approach (DOCA) between any two tracks. We also require that the three tracks form a common secondary vertex with a good significance and the SV has a large displacement with respect to the primary (PV) due to the large flight distance (FD) of the $B^\pm$ meson before decaying. The reconstructed $B^\pm$ momentum vector points to the primary vertex, resulting typically in a small impact parameter and angle θ between the momentum and the flight direction. The $B^\pm$ candidates are further required it have a corrected mass M^{COR} range, calculated when all daughters are assigned kaon masses. A summary of the stripping criteria is given in Table 3.9.

Variables	2011	2012
Track IP χ^2	> 16	> 16
Track p_{T} (GeV/c)	> 1.7	> 1.7
Track p (GeV/c)	> 10	> 3
Track χ^2/ndf	< 2	< 2
Track IP (mm)	> 0.1	> 0.1
Number of VELO hits/track	> 9	> 9
Number of missed VELO hits/track	< 3	< 3
Number of OT + IT $\times 2$ hits/track	> 16	> 16

TABLE 3.8: `Hlt1TrackAllL0` selection cuts for 2011 and 2012.

Variables	Selection cuts
Tracks P_T	$> 0.1 \, \text{GeV/c}$
Tracks P	$> 1.5 \, \text{GeV/c}$
Tracks $IP\chi^2$	> 1
Tracks $\chi^2/\text{n.d.f.}$	< 3
Probability the track is a ghost	< 0.5
Sum of P_T of tracks	$> 4.5 \, \text{GeV/c}$
Sum of P of tracks	$> 20. \, \text{GeV/c}$
Sum of $IP\chi^2$ of tracks	> 500
P_T of the highest-P_T track	$> 1.5 \, \text{GeV/c}$
Maximum DOCA	$< 0.2 \, \text{mm}$
$B^{\pm}$ candidate M_{KKK}	$5.05 - 6.30 \, \text{GeV/c}^2$
$B^{\pm}$ candidate M_{KKK}^{COR}	$4 - 7 \, \text{GeV/c}^2$
$B^{\pm}$ candidate IP χ^2	< 10
$B^{\pm}$ candidate P_T	$> 1. \, \text{GeV/c}$
Distance from SV to any PV	$> 3 \, \text{mm}$
Secondary Vertex χ^2	< 12
$B^{\pm}$ candidate $\cos(\theta)$	> 0.99998
$B^{\pm}$ Flight Distance χ^2	> 500

TABLE 3.9: Stripping inclusive line for charmless $B^{\pm}$ decays to three light hadrons (stripping 20).

3.6   Final selection

The last selection stage further refines the $B^{\pm}$ candidate. The final stage to select signal candidates with a high efficiency by using a multivariate analysis and particle identification cuts. In addition, the final selection also include D^0 and J/ψ vetoes to reject charm contributions and exclude events with more than one candidate.

Multivariate selection

In order to further refine the $B^{\pm}$ candidate selection, in the offline selection a Boosted Decision Tree (BDT) method is applied. The BDT is trained using reconstructed events of $B^{\pm} \to \pi^{\pm}\pi^+\pi^-$ decays lying in the mass window $5.40 < m(\pi^{\pm}\pi^+\pi^-) < 5.58$ GeV/c^2 as background sample and simulated events of each of the interest channels as signal samples. The number of background events is chosen to be similar to the ones in the simulated samples. To optimise the BDT response, it is required the maximisation of the figure of merit $N_S/\sqrt{N_S + N_B}$, where the numerator corresponds to the signal candidates extracted from MC samples, and the denominator is from data, both lie within an invariant mass window of around $40 \, \text{MeV}/c^2$ with respect to the signal peak. Two reasons justify the same BDT requirement for all the channels: (i) the optimisation response is similar for the

Decay	Daughter	PID selection cuts
$B^\pm \to K^\pm K^+ K^-$	all	ProbNNk > 0.2
$B^\pm \to K^\pm \pi^+ \pi^-$	pions	ProbNNpi > 0.25 & ProbNNk < 0.35
	Kaon	ProbNNk > 0.2
$B^\pm \to \pi^\pm K^+ K^-$	Kaons	ProbNNk > 0.45 & ProbNNpi < 0.5
	Pion	ProbNNpi > 0.5 & ProbNNk < 0.05
$B^\pm \to \pi^\pm \pi^+ \pi^-$	all	ProbNNpi > 0.5 & ProbNNk < 0.1

TABLE 3.10: PID selection criteria for $B^\pm$ decays.

four channels and (ii) simplification of the evaluation of the systematic uncertainties.

Particle identification cuts

The trigger and the multivariate selection play roles in removing the combinatorial background. The remaining background contributions are due to decays of beauty hadrons either fully or partially reconstructed. Particle identification cuts are essential to reject this type of background.

Particle identification at LHCb performs a multivariate analysis based on adaptive training and testing techniques on data which are optimised to determine the particle type. The particle identification cuts were chosen as a compromise between background rejection and preservation of the signal. We tested the performance of particle identification with both DLL and `ProbNN` variables. The latter performed slightly better. Table 3.10 shows the PID selection criteria for the four decay channels.

Vetoes against physical backgrounds

As mentioned in section 3.4, several B decays have a charm meson as intermediate state, usually the D^0, with the same final states as the signal (also with a missing reconstructed particle). To reject these charm contributions, we require the reconstructed invariant mass of the pairs (m_{KK}, $m_{K\pi}$ and $m_{\pi\pi}$) to lie outside the D^0 mass: we exclude the regions with a width of $30\,\mathrm{MeV}/c^2$ around the D^0 mass ($1864\,\mathrm{MeV}/c^2$).

The $B^\pm \to K^\pm \pi^+ \pi^-$ channel receives, in addition, a background contribution from the $B^\pm \to J/\psi K^\pm$ channel. To exclude the J/ψ resonance region, we require $3.05 < m_{\pi\pi} < 3.15\,\mathrm{GeV}/c^2$.

3.6.1 Control channel

The $B^\pm \to J/\psi K^\pm$ is chosen as control channel because (i) it has a negligible CP violaion, thus the raw asymmetry observed is entirely due to other effects (described later); (ii) has a similar topology to the interest channels.

The $B^{\pm} \to J/\psi K^{\pm}$ control channel is essentially selected using the same criteria as described above, however criteria used to identify charged pions are removed and the requirement $3.05 < m_{\pi\pi} < 3.15 \, \text{GeV}/c^2$ is applied in view of enhancing the selection of J/ψ mesons decaying to two muons. It is important to remark that the control channel and signals passed by exactly the same stripping, offline and trigger selection, and the same kaon particle identification selection.

3.6.2   Simulated samples

All the simulated samples were selected by the same selection criteria as for the data samples. Since it is MC simulation, the information of the true particles type is given to guarantee true B decays.

3.7   Determination of the signal yields

To determine the signal yields and raw asymmetries of the studied samples, we performed a simultaneous unbinned extended maximum likelihood fit of the B^+ and B^- invariant mass distributions in the range $5080 - 5580$ MeV/c^2. The fit functions, used to describe signal and background distributions described below, were implemented using the ROOFIT [83] package (based on C++).

3.7.1   Fit model

The reconstructed invariant mass distributions of the charged B is modelled by a sum of probability density functions (PDFs) describing the signal distribution and background contributions and each of PDF is multiplied by the corresponding number of events:

$$\mathcal{P}^{\pm} = N_{sig}^{\pm}\mathcal{P}_{sig}^{\pm} + \sum_{i=1} N_{bkg_i}^{\pm}\mathcal{P}_{bkg_i}^{\pm}, \tag{3.2}$$

The summing term represents the possible contributions of the combinatorial, peaking, misidentified or partially reconstructed background.

Signal fit model

To fit the signal events distribution, the Cruijff function [84] is adopted - with common widths, mean and tails and with common parameters for the B^+ and B^- samples. Monte Carlo studies demonstrated this particular choice not only is able to well describe the signal distribution but also provide the best fit stability for data.

   The Cruijff function $\mathcal{C}(m)$, defined in Equation (3.3), is a modified Gaussian with different widths (σ_1, σ_2) for the left and right side of the B mass

mean value and non-Gaussian tails (a_1, a_2), which accounts for the final state radiation tails on the left side of the mass peak and tails shapes on the right side, due to non-Gaussian tracking effects. While the Gaussian contribution accounts for the uncertainty on the measurement of the invariant mass distribution which is obtained from the momentum and energy parameters:

$$\mathcal{C}(m; m_0, \sigma_1, \sigma_2, a_1, a_2) = \exp\left[\frac{-(m-m_0)^2}{2\sigma_i^2 + a_i(m-m_0)^2}\right], \qquad (3.3)$$

$$\text{where} \begin{cases} i = 1 & \text{if} \quad m \le m_0 \\ i = 2 & \text{if} \quad m > m_0. \end{cases}$$

In this analysis, left and right widths parameters are considered to be equal ($\sigma_1 = \sigma_2$). Hence the final signal PDF is a modified Gaussian with different left and right tails.

Background fit models

Combinatorial background

The combinatorial background is modeled as an exponential PDF:

$$\mathcal{P}_{comb}(m) = \exp\left[b \cdot (m - 5080)\right] \qquad (3.4)$$

where b, the free parameter, is extracted from the data.

Peaking and misidentified backgrounds

The peaking and misidentified backgrounds are obtained from $B^{\pm}$ MC samples. These contributions are well modelled by Cruijff functions (see Eq. (3.3)). The parameters m_0, σ_1, σ_2, a_1 and a_2 are determined from MC studies and are fixed in the fit of the data samples.

Partially-reconstructed backgrounds

The partially reconstructed backgrounds are modelled by an Argus function [85] convolved with a Gaussian resolution. The Argus distribution is defined as:

$$\mathcal{A}(m; m_t, c, p) = \frac{2^{-p}c^{2(p+1)}}{\Gamma(p+1) - \Gamma(p+1, c^2/2)} \cdot \frac{m}{m_t^2}\left(1 - \frac{m^2}{m_t^2}\right)^p \cdot \exp\left[-\frac{1}{2}c^2(1 - \frac{m^2}{m_t^2})\right],$$

$$(3.5)$$

where $\Gamma(n)$ stands for the Gamma function, $\Gamma(n, l)$ the upper incomplete Gamma function[1], and the parameters m_t, c and p correspond to the mass threshold upper limit (cutoff), the curvature, and power which controls the falling slope, respectively.

Background fraction

The yield of a given background N_{bkg} is evaluated by the following expression:

$$N_{bkg} = f_{bkg} \cdot N_{sig} \tag{3.6}$$

where N_{sig} is the signal yield and f_{bkg} is the fraction of the background component with respect to the signal yield.

The background fraction is evaluated as:

$$f_{bkg} \equiv \frac{N_{bkg}}{N_{sig}} = \frac{f_{u(s)}}{f_u} \cdot \frac{\mathcal{B}_{bkg}}{\mathcal{B}_{sig}} \cdot \frac{\epsilon_{bkg}}{\epsilon_{sig}} , \tag{3.7}$$

where $f_{u(s)}$ is the fragmentation probability, which is the fraction of $B^{\pm}$ (B^0_s) mesons amongst all weakly-decaying botom hadrons[2], $\mathcal{B}_{sig}$ and $\mathcal{B}_{bkg}$ are the branching ratios of the signal and background channels, respectively, given by the PDG, and ϵ_{sig} and ϵ_{bkg} are the efficiencies extracted from the MC selection. The efficiency ϵ_{sig} corresponds to the ratio between the number of true signal events after all selection cuts and the number of generated events. While the ϵ_{bkg} corresponds to the ratio between the number of true events of background after the very same selection cuts (to keep the signal) and the number of generated events.

Background contributions

Channels with a background fraction less than 1% were neglected from the fit. For the channels with B^0_s partially reconstructed background contributions ($B^{\pm} \to \pi^{\pm}K^+K^-$ case), it was studied in the MC and the shape was fixed in the fit to data and fraction left to float. MC samples for the B (B^0 and $B^{\pm}$) partially reconstructed backgrounds were unavailable while performing the analysis. To overcome this issue, the shape and the relative fraction of partially reconstructed contributions of B partially reconstructed background were left to float on the data.

Table 3.11 shows the fractions of the dominant background contributions (with the shape and fraction fixed on the fit) for each of the $B^{\pm} \to h^{\pm}h^+h^-$

---

[1]The upper gamma function is defined as $\Gamma(s, x) = \int_x^{\infty} t^{s-1}e^{-t}\mathrm{d}t$.

[2]When the background studied involves a B^0_s meson decay, this ratio corresponds to $f_{u(s)}/f_u = 0.256 \pm 0.020$[86].

Signal mode	Background contribution	Fraction (%)
	$B^{\pm} \to \eta'\,(\rho^0\gamma)K^{\pm}$	6.0
$B^{\pm} \to K^{\pm}\pi^+\pi^-$	$B^{\pm} \to \pi^{\pm}\pi^+\pi^-$	7.3
	$B^{\pm} \to \pi^{\pm}K^+K^-$	1.1
$B^{\pm} \to K^{\pm}K^+K^-$	$B^{\pm} \to \pi^{\pm}K^+K^-$	1.8
$B^{\pm} \to \pi^{\pm}\pi^+\pi^-$	$B^{\pm} \to K^{\pm}\pi^+\pi^-$	4.9
$B^{\pm} \to \pi^{\pm}K^+K^-$	$B^{\pm} \to \pi^{\pm}\pi^+\pi^-$	6.8
	$B^{\pm} \to K^{\pm}\pi^+\pi^-$	9.8

TABLE 3.11: Fractions of the relevant background modes for each of the $B^{\pm} \to h^{\pm}h^+h^-$. The B_s^0 and B decays (partially reconstructed background) are fitted, but the fraction floats on the fit.

channels. Figures 3.6-3.9 are the fits of each of the dominant background contribution performed on simulated samples.

3.8 Fit procedure

The simultaneous extended maximum likelihood fits were conveniently modified to measure the raw asymmetry, defined as:

$$A_{\text{raw}} = \frac{N_{sig}^- - N_{sig}^+}{N_{sig}^- + N_{sig}^+} \tag{3.8}$$

where $N_{sig}^{\pm}$ is the signal yield for the $B^{\pm}$ decays. This asymmetry is denominated as raw asymmetry since it accounts not only for the desired CP asymmetry but also other effects which need to be corrected for and are going to be discussed later. Equation 3.8 allows to express N_{sig} as $N_{sig}^{\mp} = N(1 \pm A_{\text{raw}})/2$ where $N = N_{sig}^+ + N_{sig}^-$. Except for the combinatorial background, the asymmetry term is considered to be zero for the background components.

Figures 3.10-3.13 show the mass spectrum of the four interest channels with the full data set. These distributions were adjusted according to the fit model described above and are merely illustrative since the asymmetries were obtained from sub-samples categorised by year and trigger selection. In all these fits, the total model is in (blue) full line, the (green) filled background contribution on the left edge of the mass spectrum accounts for the partially reconstructed B decays, and the (orange) dotted line corresponds to the combinatorial contribution.

The fit of the mass spectrum of $B^{\pm} \to K^{\pm}\pi^+\pi^-$ shown in Figure 3.10 resulted in a total signal yield (combined B^+ and B^-) of about 180 k candidates with $\chi^2/NDOF$ = 1.75 for B^- and $\chi^2/NDOF$ = 1.48 for B^+ in the

(a)

(b)

(c)
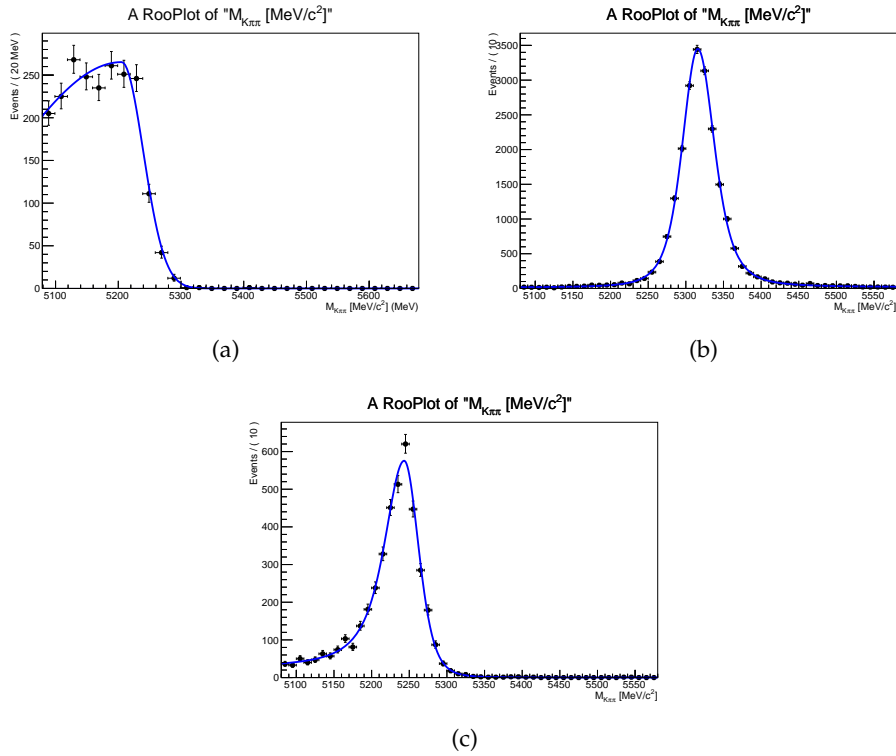
FIGURE 3.6: Misidentified and partially reconstructed background distributions for Monte Carlo in the invariant mass of $B^\pm \to K^\pm\pi^+\pi^-$: (a) $B^\pm \to \eta' (\rho^0\gamma)K^\pm$; (b) $B^\pm \to \pi^\pm\pi^+\pi^-$; (c) $B^\pm \to \pi^\pm K^+K^-$.

signal region. The (purple) filled contribution with the center a bit displaced from the center mass value of the signal peak corresponds to the misidentified background $B^\pm \to \pi^\pm\pi^+\pi^-$. The contribution from the $B^\pm \to \eta' (\rho^0\gamma)K^\pm$, hardly visible in the plots, is also considered.

Figure 3.11 shows the fit of the mass spectrum of $B^\pm \to K^\pm K^+K^-$, leading to a total signal yield of about 110 k candidates with a $\chi^2/NDOF$ = 1.68 for B^- and $\chi^2/NDOF$ = 0.77 for B^+ in the signal region. Two other contributions, localised on the right of the center value of signal peak, correspond to the misidentified background $B^\pm \to \pi^\pm K^+K^-$ and $B^\pm \to K^\pm\pi^+\pi^-$.

Figure 3.12 shows the fit of the mass spectrum of $B^\pm \to \pi^\pm\pi^+\pi^-$, leading to a total signal yield of about 25 k candidates. The $\chi^2/NDOF$ of the fits are 0.88 for B^- and 0.90 for B^+ in the signal region. Besides the combinatorial and partially reconstructed background, the contribution from the misidentified background $B^\pm \to K^\pm\pi^+\pi^-$ is shown in dotted-dashed line in the right border of the signal region.

Finally, the invariant mass fit of the $B^\pm \to \pi^\pm K^+K^-$ channel, shown in Figure 3.13, yields around 6 k candidates in total. The $\chi^2/NDOF$ of the fits are 0.60 for B^- and 0.95 for B^+ in the signal region. The partially reconstructed contribution of both the B and B_s^0 channels are visible in light green and cyan filled curves. Two other contributions, centered on the left
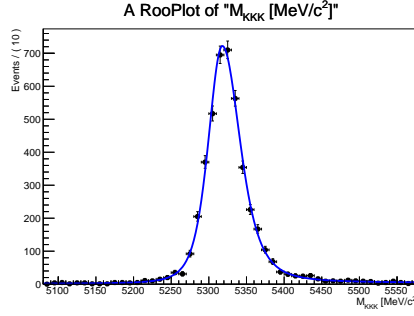
(a)

FIGURE 3.7: Misidentified background distribution for Monte Carlo in the invariant mass of $B^\pm \to K^\pm K^+ K^-$: (a) $B^\pm \to \pi^\pm K^+ K^-$.
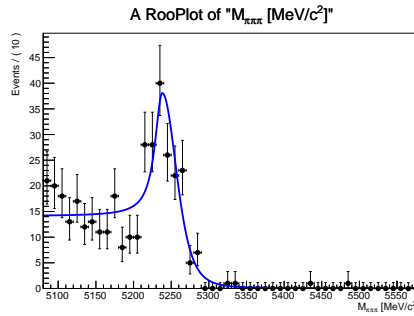
(a)

FIGURE 3.8: Misidentified background distribution for Monte Carlo in the invariant mass of $B^\pm \to \pi^\pm \pi^+ \pi^-$: (a) $B^\pm \to K^\pm \pi^+ \pi^-$.

and right of the mean value of signal peak, correspond to the misidentified backgrounds $B^\pm \to K^\pm K^+ K^-$ and $B^\pm \to K^\pm \pi^+ \pi^-$.

The total number of candidates and the raw asymmetry for each channel obtained from the merged 2011 and 2012 samples is shown in Table 3.12. Also, the asymmetry is noticeable on the height difference between the B^+ and B^- peaks. Appendix A details the fit results with plots and tables separated by year and trigger configuration.

Channel	Yield	A_{raw}
$B^\pm \to K^\pm \pi^+ \pi^-$	$181\,074 \pm 556$	$+0.010 \pm 0.002$
$B^\pm \to K^\pm K^+ K^-$	$109\,240 \pm 354$	-0.056 ± 0.003
$B^\pm \to \pi^\pm \pi^+ \pi^-$	$24\,907 \pm 222$	$+0.074 \pm 0.008$
$B^\pm \to \pi^\pm K^+ K^-$	$6\,161 \pm 172$	-0.135 ± 0.017

TABLE 3.12: Signal yield and the raw asymmetry of the four charmless three-body decays $B^\pm \to h^\pm h^+ h^-$ for the combined data set.

(a)

(b)

(c)
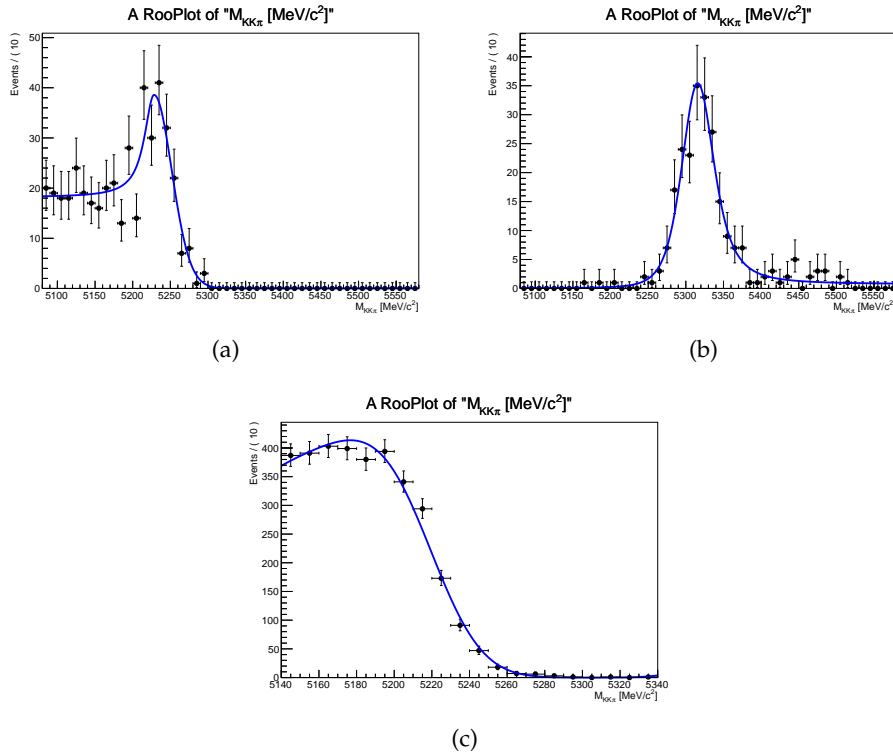
FIGURE 3.9: Misidentified background distribution for Monte Carlo in the invariant mass of $B^\pm \to \pi^\pm K^+ K^-$: (a) $B^\pm \to K^\pm K^+ K^-$; (b) $B^\pm \to K^\pm \pi^+ \pi^-$; (c) B_s^0 decays.

3.9   Inclusive CP asymmetry measurement

Once the signal yields are determined, we can evaluate CP asymmetry $(A_C P)$. In order to estimate it precisely, one needs to account for other small asymmetry terms due to production and detection effects that are described below.

Production asymmetry (A_P)

The production rate of B^+ and B^- is not expected to be the same at LHCb due to the pp nature of the collisions. Since protons are constituted of uud quarks, only u valence quarks are available, leading to different production rates for B^+ $(u\bar{b})$ and B^- $(\bar{u}b)$. We assume the production asymmetry is the same for any $B^\pm$ channels, thus we extract the production asymmetry from the $B^\pm \to J/\psi K^\pm$ channel, for which the CP asymmetry is consistent with zero $A_{CP}(J/\Psi K) = (0.1 \pm 0.7)\%$ [65].

Detection asymmetry (A_P)
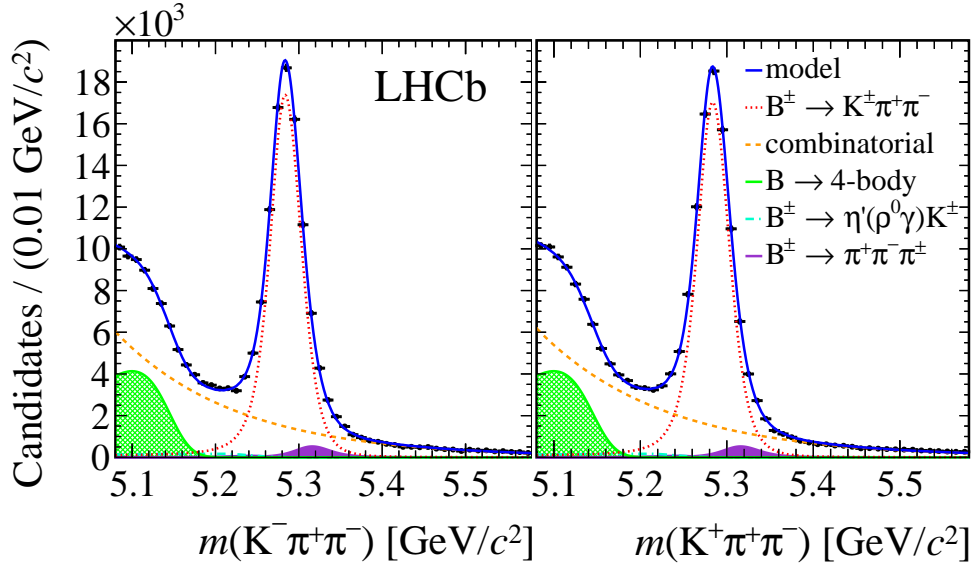
FIGURE 3.10: Fitted invariant mass distributions of $B^{\pm} \to K^{\pm}\pi^{+}\pi^{-}$, where only the prominent background distributions are shown. In each plot, the left (right) panel corresponds to the B^{-} (B^{+}) candidates.
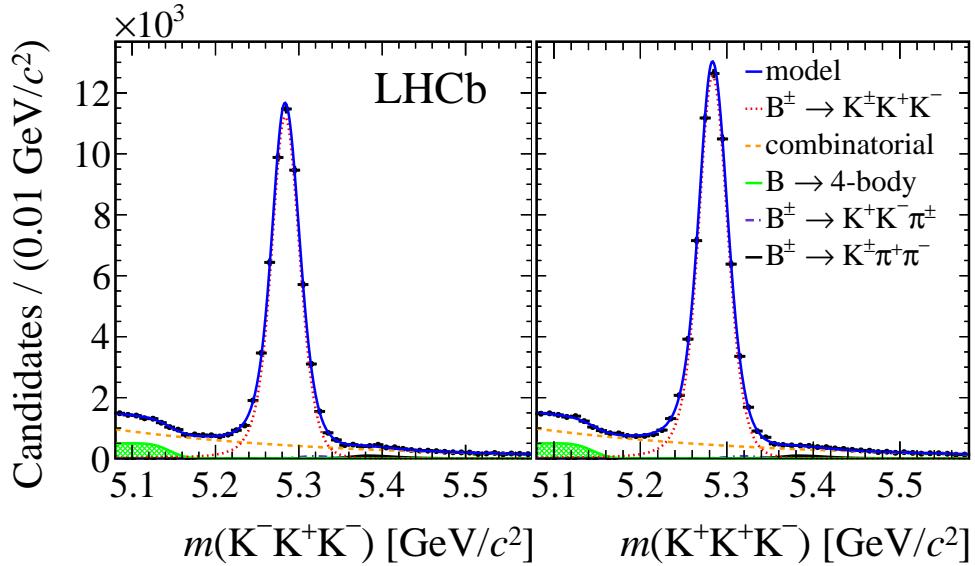
FIGURE 3.11: Fitted invariant mass distributions of $B^{\pm} \to K^{\pm}K^{+}K^{-}$, where only the prominent background distributions are shown. In each plot, the left (right) panel corresponds to the B^{-} (B^{+}) candidates.
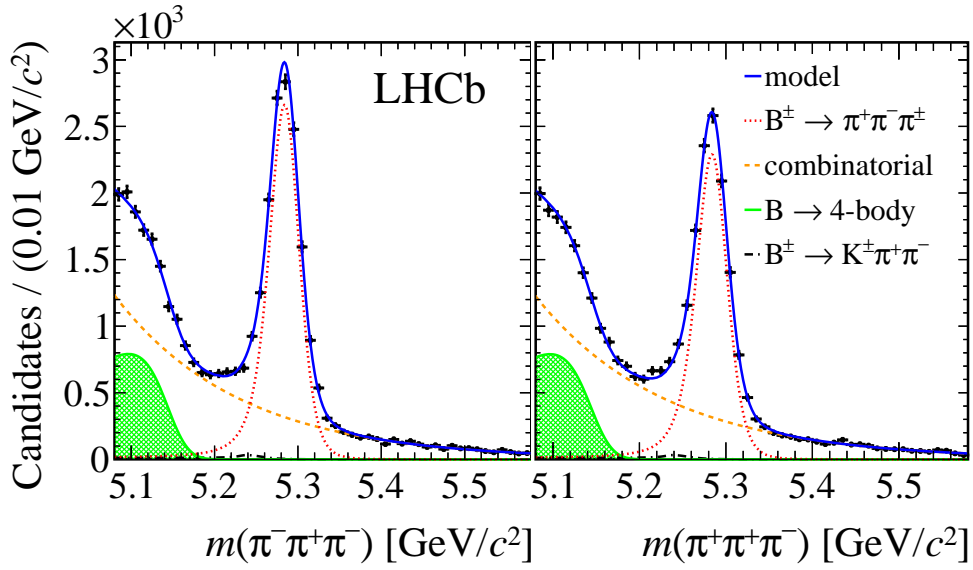
FIGURE 3.12: Fitted invariant mass distributions of $B^{\pm} \to \pi^{\pm}\pi^{+}\pi^{-}$, where only the prominent background distributions are shown. In each plot, the left (right) panel corresponds to the B^{-} (B^{+}) candidates.
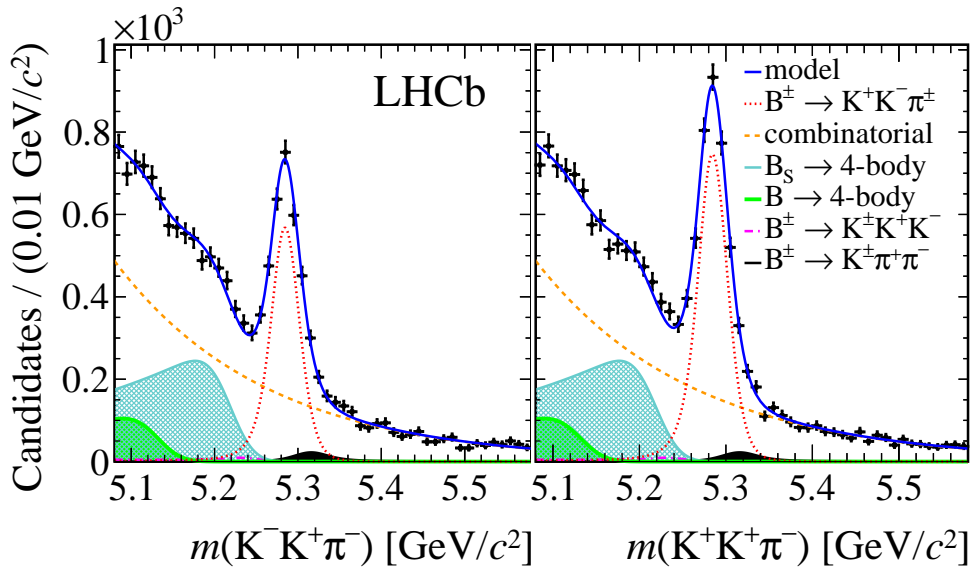
FIGURE 3.13: Fitted invariant mass distributions of $B^{\pm} \to \pi^{\pm}K^{+}K^{-}$, where only the prominent background distributions are shown. In each plot, the left (right) panel corresponds to the B^{-} (B^{+}) candidates.

The detection asymmetry accounts for any instrumental effect leading to a difference in the probability of observing a $B^+ \to h'^+h^+h^-$ with respect to a $B^- \to h'^-h^+h^-$. It includes the difference between particle and anti-particle interaction with matter, detector acceptance and reconstruction. For $B^\pm \to h'^\pm h^+h^-$ decays, we assume that the net detection asymmetry is due to the bachelor hadron h'. Thus, the term A_D expresses the difference in the interaction of the final state particles (kaons and pions) with the detector material. This distinction is expected since K^- mesons have a larger interaction cross section than K+ [65]. The former interacts via $K^-N \to Y\pi$, where N is a proton or a neutron and Y is a hyperon[3]. On the other hand, there is no such a reaction for the K^+ [87]. LHCb collaboration previously evaluated these asymmetries as $A_\mathrm{D}^K = -0.0126 \pm 0.0018$ [87], while for the pions, the detection asymmetry is found to be consistent with zero $A_\mathrm{D}^\pi = (0.00 \pm 0.25)\%$ [88].

CP **asymmetry**

The physical CP violation can be expressed as:

$$A_C P = A_\mathrm{raw} - A_P - A_D^{h'}. \tag{3.9}$$

Since the decays of interest always have a pair of h^+h^- ($h = \pi, K$), the detection asymmetry cancels for the pair. This allows us to separate the decays according to the hadron flavour of the $h'^\pm$:

- A_D^K for the $B^\pm \to K^\pm\pi^+\pi^-$ and $B^\pm \to K^\pm K^+K^-$,

- A_D^π for the $B^\pm \to \pi^\pm K^+K^-$ and $B^\pm \to \pi^\pm\pi^+\pi^-$.

Then we have the following expressions to quantify the CP asymmetry:

$$
\begin{aligned}
A_{CP}(Khh) &= A_\mathrm{raw}(hhK) - A_\mathrm{P} - A_\mathrm{D}^K & (3.10) \\
&= A_\mathrm{raw}(hhK) - A_\Delta\,, \\
A_{CP}(\pi hh) &= A_\mathrm{raw}(hh\pi) - A_\mathrm{P} - A_\mathrm{D}^\pi & (3.11) \\
&= A_\mathrm{raw}(hh\pi) - A_\Delta + A_\mathrm{D}^K - A_\mathrm{D}^\pi\,.
\end{aligned}
$$

The correction term A_Δ is measured using a $B^\pm \to J/\psi\,(\mu^+\mu^-)K^\pm$ data sample with 2.65×10^5 candidates. The correction is obtained from A_raw from the control channel $B^\pm \to J/\psi\,K^\pm$ as:

$$A_\Delta = A_\mathrm{raw}(J/\psi\,K) - A_{CP}(J/\psi\,K), \tag{3.12}$$

where we used the world average $A_{CP}(J/\psi\,K) = (0.1 \pm 0.7)\%$ [65].

---

[3]A hyperon is a baryon containing at least one strange quark, and no charm, bottom or top quarks. For example: Λ, Σ and Ξ.

The production asymmetry was estimated from $B^\pm \to J/\psi K^\pm$ sample as $A_\mathrm{P} = A_\Delta - A_\mathrm{D}^K$.

As it was mentioned, the data was separated by trigger configuration and year (2011 and 2012). Consequently, the CP asymmetry was evaluated accordingly for each sub-sample. The final result was evaluated as the weighted average of the asymmetries per trigger settings and year.

3.10   Results

Table 3.13 shows the inclusive CP asymmetries with $3.1\,\mathrm{fb}^{-1}$ dataset of the $B^\pm \to K^\pm \pi^+ \pi^-$, $B^\pm \to K^\pm K^+ K^-$, $B^\pm \to \pi^\pm \pi^+ \pi^-$ and $B^\pm \to \pi^\pm K^+ K^-$ decay modes. The first uncertainty is due to the statistics and the second is the systematics, described in the next section, due to the limited knowledge of the CP asymmetry and of the $B^\pm \to J/\psi K^\pm$ control. The significances of the inclusive charge asymmetries, calculated by dividing the central values by the sum in quadrature of the uncertainties, are 2.8 standard deviations (σ) for $B^\pm \to K^\pm \pi^+ \pi^-$ decays, 4.3σ for $B^\pm \to K^\pm K^+ K^-$ decays, 4.2σ for $B^\pm \to \pi^\pm \pi^+ \pi^-$ decays and 5.6σ for $B^\pm \to \pi^\pm K^+ K^-$ decays. The inclusive CP asymmetries are positive for $B^\pm \to K^\pm \pi^+ \pi^-$ and $B^\pm \to \pi^\pm \pi^+ \pi^-$ decays, and negative for $B^\pm \to K^\pm K^+ K^-$ and $B^\pm \to \pi^\pm K^+ K^-$ decays and in agreement with the previous measurements [69, 89].

3.11   Systematic uncertainties

Systematic uncertainties accounts for potential mis-modellings in the mass fit, phase-space acceptance corrections and trigger selection applied of the samples.

The systematics due to the fit models are intrinsically related with the yields, thus a detailed estimation is required. These are evaluated as the CP asymmetry difference resulting from variations of the model.

To estimate the choice of the signal model, the nominal model is replaced by an alternative empirical distribution [90]. The choice of the signal shape is examined by allowing means and widths of B^+ and B^- signal

Decay mode	$A_{CP} \pm \sigma_{stat} \pm \sigma_{sys} \pm \sigma_{J/\psi K^\pm}$
$B^\pm \to K^\pm \pi^+ \pi^-$	$+0.025 \pm 0.004 \pm 0.004 \pm 0.007$
$B^\pm \to K^\pm K^+ K^-$	$-0.036 \pm 0.004 \pm 0.002 \pm 0.007$
$B^\pm \to \pi^\pm \pi^+ \pi^-$	$+0.058 \pm 0.008 \pm 0.009 \pm 0.007$
$B^\pm \to \pi^\pm K^+ K^-$	$-0.123 \pm 0.017 \pm 0.012 \pm 0.007$

TABLE 3.13:   Global A_{CP} measurement for the $B^\pm \to h^\pm h^+ h^-$ channels.

peaks vary independently. The resulting values agree with the nominal ones and the difference in the value of the A_{CP} is assigned a systematic uncertainty.

The systematics related to the peaking background fractions reflects the uncertainties in the expected yields determined from simulation, and the effect on the fit results by using the separated simulated samples of 2011 and 2012 (the nominal fit uses the combined sample). For the peaking background shape, we examined the effect of increasing the width of the Gaussian function according to the observed differences between simulation and data, while for the partially reconstructed background, the effect of floating independently the Gaussian width is evaluated. The nominal fit model considers zero asymmetry for the peaking and partially reconstructed backgrounds. To evaluate a systematic uncertainty due to this simplification, these asymmetries are floated separately in B^- and B^+ fits. The signal model variations and the background asymmetry dominantly affect the systematic uncertainties of the fit procedure.

The systematic uncertainty related to the acceptance correction procedure considers the effect on the statistical uncertainty on the detection efficiency due to the finite size of the simulated samples, and the uncertainty due to the binning choice. The effect of using different trigger category samples was also investigated and found to agree with the nominal values. Therefore, no additional systematic uncertainty was assigned.

Following Equation (3.10), the uncertainties on A_{D}^K and A_{D}^π are only considered as systematics uncertainties for the $B^\pm \to h^\pm h^+ h^-$ decays with a pion as the bachelor hadron. Each of these uncertainties are summed in quadrature to result in the total systematic uncertainty.

Table 3.14 summarizes the systematics uncertainties separated per year. The total systematic uncertainty is obtained by the sum of the square of each contribution.

| Systematic | $A_{CP}(K\pi\pi)$ | | $A_{CP}(KKK)$ | | $A_{CP}(\pi\pi\pi)$ | | $A_{CP}(KK\pi)$ | |
uncertainty	2011	2012	2011	2012	2011	2012	2011	2012
Signal Model	0	0.0001	0.0002	0.0005	0.0046	0.0025	0.0028	0.0046
FracPerYear	0	0.0001	0	0	0	0.0001	0.0002	0.0001
fbkgSubSum	0	0.0001	0.0002	0.0001	0.0001	0.0001	0.001	0.0014
fbkgPart	0	0	0	0	0.0001	0	0.0001	0
bkgRes	0	0	0.0001	0	0.0001	0	0	0.0004
fbkgAsym	0.0031	0.0032	0.0015	0.0011	0.0017	0.0027	0.0011	0.0019
Acceptance corr.	0.0012	0.0018	0.0013	0.0013	0.0063	0.0051	0.0099	0.0092
A_{D}^K uncertainty	–	–	–	–	0.0018	0.0018	0.0018	0.0018
A_{D}^π uncertainty	–	–	–	–	0.0025	0.0025	0.0025	0.0025
Total	0.0034	0.0038	0.0020	0.0019	0.0090	0.0075	0.0113	0.0115

TABLE 3.14: Summary of systematics uncertainties of the CP asymmetry measurement.

3.12   Summary

In conclusion, we have measured the inclusive CP asymmetry for the charmless three-body $B^\pm$ decays based on a 3.1 fb^{-1} data sample collected by the LHCb experiment. First, we have selected the $B^\pm \to h^\pm h^+ h^-$ events via an inclusive selection criteria and specific selection cuts based on the topology and kinematics of the decays. We have determined the signal yield from fits performed on the invariant mass distributions by modelling both the signal and background contributions. We have found 181 k candidates for $B^\pm \to K^\pm \pi^+ \pi^-$ channel, 110 k candidates for the $B^\pm \to K^\pm K^+ K^-$ channel, 25 k for the $B^\pm \to \pi^\pm \pi^+ \pi^-$ channel and 6 k candidates for the $B^\pm \to \pi^\pm K^+ K^-$ decay. We have also found evidence of inclusive CP asymmetries with a significance of 5.6σ for the $B^\pm \to \pi^\pm K^+ K^-$ mode, 4.3σ for $B^\pm \to K^\pm K^+ K^-$ mode, 4.2σ for $B^\pm \to \pi^\pm \pi^+ \pi^-$ mode and 2.8σ for the $B^\pm \to K^\pm \pi^+ \pi^-$ mode. The inclusive CP asymmetries are positive for the $B^\pm \to K^\pm \pi^+ \pi^-$ and $B^\pm \to \pi^\pm \pi^+ \pi^-$ decays, and negative for $B^\pm \to K^\pm K^+ K^-$ and $B^\pm \to \pi^\pm K^+ K^-$ decays. In addition, these charge asymmetries are not uniformly distributed along the phase space, which is the subject of the next chapter.

Chapter 4

CP violation study in phase space

In the last chapter, we determined the inclusive asymmetry of each of the $B^\pm \to h^\pm h^+ h^-$ decays where we observed CP asymmetry values up to 12% - for the $B^\pm \to \pi^\pm K^+ K^-$. In this chapter, we aim to investigate the behaviour of the CP asymmetry along the phase space. The usual approach to have a complete description of a Dalitz plot is to perform an amplitude analysis. This is a complex method that determines each resonant and non-resonant contributions leading to the same final state particles. In this chapter, we perform a simple inspection of the Dalitz plot to investigate asymmetry features in the region of low invariant mass ($< 1.8\,\mathrm{GeV}/c^2$) of the phase space.

To start with, Figures 4.1 show the phase space of each of the interest channels. For this study, the signal region was defined within a mass window centered at the B mass value of $5283\,\mathrm{MeV}/c^2$ and $\sigma = 34\,\mathrm{MeV}/c^2$[1]. The white bands correspond to the J/ψ and D^0 vetoes applied in the selection. As mentioned in section 2.5.1, the phase space density of the Dalitz plot is constant; any observed structures reflects the dynamics of the decay. In particular, we can observe enhanced populations in the low two-body invariant mass regions of all channels which indicates the presence of strong resonances.

To investigate the asymmetry in the phase space, we divided the B^+ and B^- combined sample into two-dimensional bins with equal number of entries through an adaptive binning algorithm. Then, we filled this binned phase space with B^+ and B^- candidates, separately. Subsequently, we calculated the asymmetry $A_{CP}^N N^- + N^+$ in each bin (see Figure 4.2). Here, $N^\pm$ denotes the background subtracted, efficiency-corrected signal yields for $B^\pm$ decays. Background subtraction is performed via the statistical tool *sPlot*[91].[2]

---

[1]Except for the $B^\pm \to \pi^\pm K^+ K^-$ channel, where $\sigma = 17\,\mathrm{MeV}/c^2$ due to its significant background contributions.

[2]From the fit information, the *sPlot* technique computes a weight to each event as a probability to be signal or background.
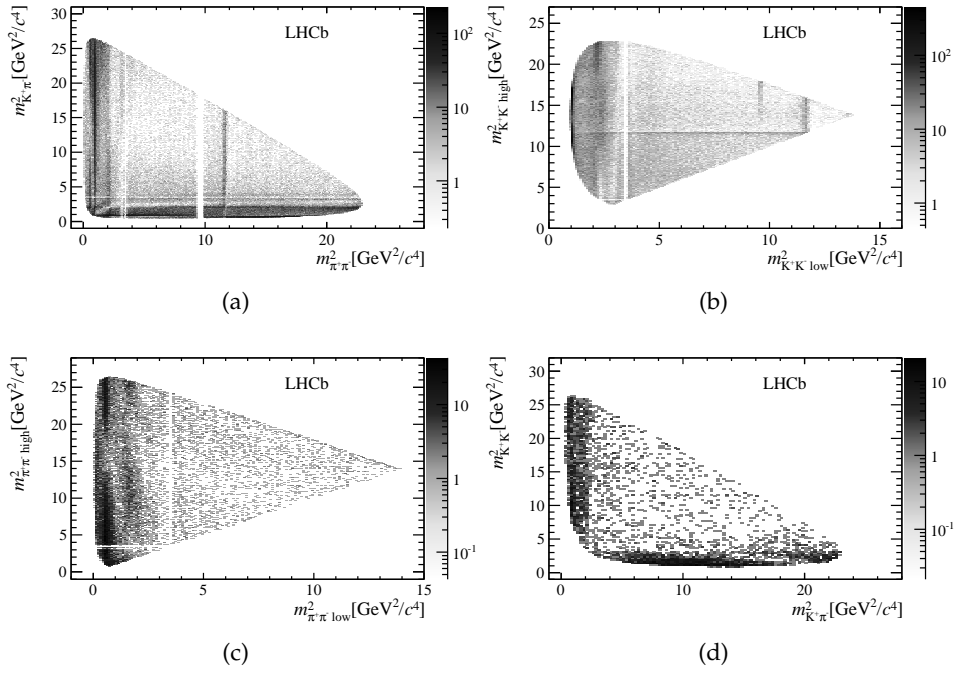
FIGURE 4.1: Dalitz plot of (a) $B^{\pm} \to K^{\pm}\pi^{+}\pi^{-}$ (b) $B^{\pm} \to K^{\pm}K^{+}K^{-}$ (c) $B^{\pm} \to \pi^{\pm}\pi^{+}\pi^{-}$ (d) $B^{\pm} \to \pi^{\pm}K^{+}K^{-}$.

A_{CP}^{N} distributions in the Dalitz plots reveal rich structures, which can also be seen in the two-body invariant mass projection plots. Figures 4.3 and 4.4 make evident large local asymmetries in the region between 1.0 and 1.5 GeV/c^2. These asymmetries are positive for channels with a π^{+} π^{-} pair (Figures 4.3(b) and 4.4(b)) and negative for those with a K^{+} K^{-} pair (Figures 4.3(a) and 4.4(a)). This indicates that the mechanism of $\pi^{+}\pi^{-} \leftrightarrow K^{+}K^{-}$ rescattering could play an essential role in CP violation in charmless three-body $B^{\pm}$ decays. Previous analysis [69, 89] showed evidence for a possible source of CP violation produced by long-distance effects via $\pi^{+}\pi^{-} \leftrightarrow K^{+}K^{-}$ rescattering. As mentioned in section 2.6, CPT theorem requires that the sum of partial widths of particles and anti-particles belonging to family of final states related to each other by strong rescattering are identical. Thus, this "compound CP violation" requires positive CP asymmetry in some channels and negative CP asymmetry in other channels of the same family, which can explain the phenomena observed in Figures 4.3 and 4.4 .

These correlations among the $B^{\pm} \to h^{\pm}h^{+}h^{-}$ channels were already observed at 2011 data [69, 89] and it was confirmed with 2011+2012 data samples [92]. In addition, the higher statistics allowed to observe new phenomena, in particular in the $B^{\pm} \to \pi^{\pm}\pi^{+}\pi^{-}$ and $B^{\pm} \to K^{\pm}\pi^{+}\pi^{-}$ low mass region, which related to the influence of the hadronic final state interaction on the strong phase of the decay amplitudes. Henceforth, we focus on the
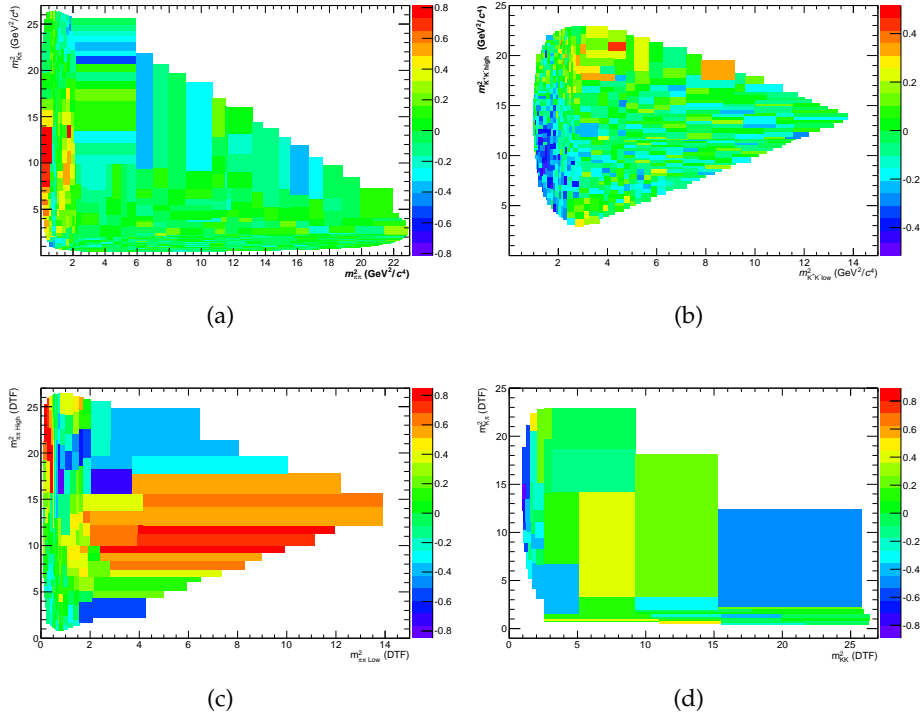
FIGURE 4.2: A_{CP}^N in Dalitz plot bins with equal number of events (sWeighted background subtracted and acceptance corrected) for (a) $B^\pm \to K^\pm \pi^+ \pi^-$, (b) $B^\pm \to K^\pm K^+ K^-$, (c) $B^\pm \to \pi^\pm \pi^+ \pi^-$ and (d) $B^\pm \to \pi^\pm K^+ K^-$.

$B^\pm \to \pi^\pm \pi^+ \pi^-$ and $B^\pm \to K^\pm \pi^+ \pi^-$ decay channels. A_{CP}^N distributions in the Dalitz plots reveal rich structures, which can be also be seen in the two-body invariant mass projection plots. These projections are split according to the sign of $\cos\theta$, where θ is helicity angle defined as the angle between the momenta of unpaired hadron and the resonance decay product with the same-sign charge. Take for instance the $B^\pm \to K^\pm \pi^+ \pi^-$ decay. In this case, for a resonance composed by $\pi^+ \pi^-$, the helicity angle lies between the momentum directions of the π^- and the bachelor particle K^- measured in the resonance rest frame.

Figure 4.5 show both the B^+ and B^- candidates distribution and the difference between B^- and B^+ as a function of the $m_{\pi\pi}$ for the $B^\pm \to K^\pm \pi^+ \pi^-$ decay. We observe that the charge asymmetry - Figures 4.5(b) and 4.5(d) - changes sign (or crosses the zero) around $0.8\,\mathrm{GeV}/c^2$ and $1\,\mathrm{GeV}/c^2$. These values correspond to the masses of the $\rho(770)$ and $f_0(980)$ resonances, respectively. While for the $B^\pm \to \pi^\pm \pi^+ \pi^-$ decay, the same distributions are shown in Figure 4.6 but as a function of the $m_{\pi^+ \pi^-\,\mathrm{low}}$. One can spot that the asymmetry changes sign around $\rho(770)$ mass value in Figures 4.6(b) and 4.6(d).

(a)

(b)
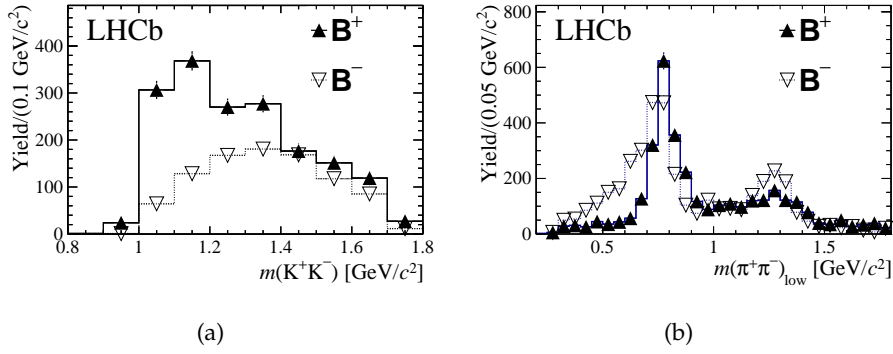
FIGURE 4.3: Projections of the number of B^- and B^+ signal events in the two-invariant mass of (a) $B^\pm \to \pi^\pm K^+ K^-$ and (b) $B^\pm \to \pi^\pm \pi^+ \pi^-$ decays.

(a)

(b)
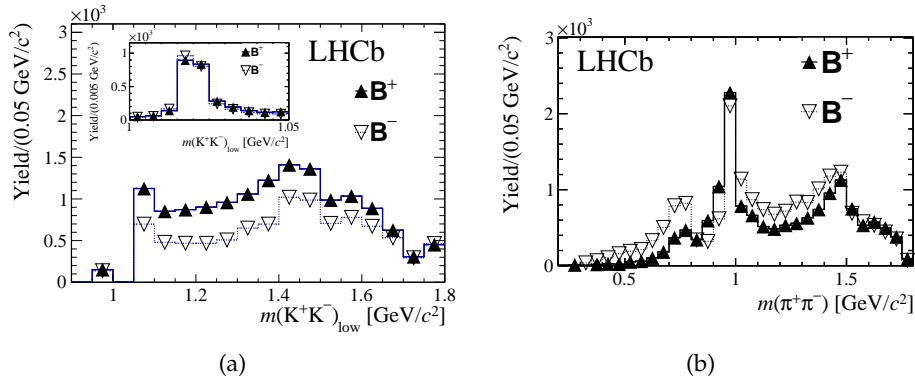
FIGURE 4.4: Projections of the number of B^- and B^+ signal events in the two-invariant mass of (a) $B^\pm \to K^\pm K^+ K^-$ and (b) $B^\pm \to K^\pm \pi^+ \pi^-$ decays.

In order to understand those features we developed a study from a simple description of the amplitude of the decay. By generating Toy MC samples with specific phases and amplitudes, it allowed us to observe *CP* violation effects in the projections of the two-invariant mass variables. Two particular cases are considered where the total decay amplitude contains contributions of (i) a vector and a non-resonant amplitude (ii) scalar and vector resonances. The first corresponds to the $B^\pm \to \pi^\pm \pi^+ \pi^-$; the latter, $B^\pm \to K^\pm \pi^+ \pi^-$.

4.1 Non-resonant and vector resonant amplitudes interference

We consider a total decay amplitude comprising a vector resonance, for example $\rho(770)$, and a scalar non-resonant amplitude. It precisely illustrates
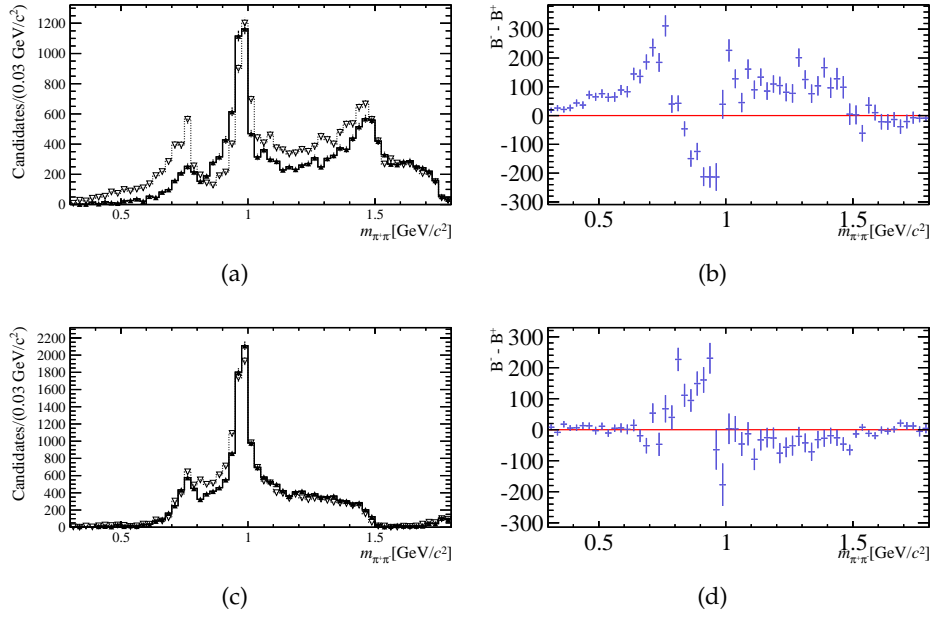
FIGURE 4.5: $B^{\pm} \to K^{\pm}\pi^+\pi^-$ zoom in the $\rho^0(770)$ and $f^0(980)$ region ($m_{\pi\pi}$ smaller than $1.8\,\mathrm{GeV}/c^2$ that is the region bellow the D^0 mass). Candidates distributions of events in the signal region with (a) $\cos\theta < 0$ and **??** $\cos\theta > 0$. Difference between B^- and B^+ candidates with (b) $\cos\theta < 0$ and (d) $\cos\theta > 0$.

the $B^{\pm} \to \pi^{\pm}\pi^+\pi^-$ decay at low invariant $\pi^+\pi^-$ mass ($<1.8\,\mathrm{GeV}/c^2$). In this region, the $\rho(770)$ is the unique resonant contribution as indicated by BaBar collaboration in the amplitude analysis of this channel in [93].

To describe a resonance R we chose relativistic Breit-Wigner excitation curves:

$$F_R^{\mathrm{BW}}(s) = \frac{1}{m_R^2 - s - i\, m_R \Gamma_R(s)} \,, \tag{4.1}$$

where m_R is the nominal mass of the resonance and $\Gamma_R(s)$ denotes the energy dependent width. Splitting Eq. (4.1) into real and imaginary terms:

$$\mathbf{Re}F_R^{\mathrm{BW}}(s) = \frac{m_R^2 - s}{(m_R^2 - s)^2 + m_R^2 \Gamma_R(s)^2} \,, \tag{4.2}$$

$$\mathbf{Im}F_R^{\mathrm{BW}}(s) = \frac{m_R \Gamma_R(s)}{(m_R^2 - s)^2 + m_R^2 \Gamma_R(s)^2} \,, \tag{4.3}$$

while the Breit-Wigner amplitude modulus $|F_R^{\mathrm{BW}}|^2$ is given by:

$$|F_R^{\mathrm{BW}}(s)|^2 = \frac{1}{(m_R^2 - s)^2 + m_R^2 \Gamma_R(s)^2} \,. \tag{4.4}$$
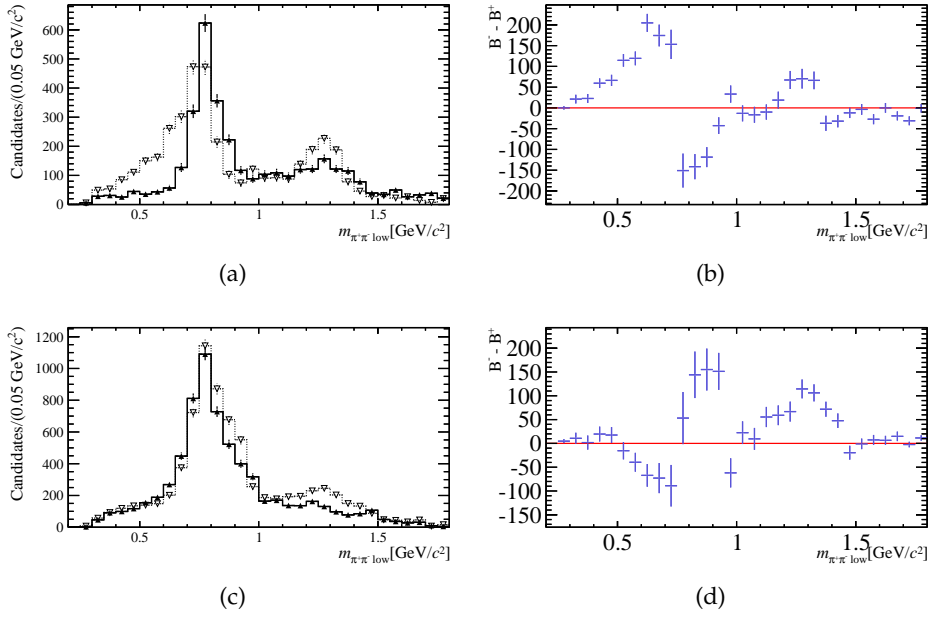
FIGURE 4.6: $B^{\pm} \to \pi^{\pm}\pi^{+}\pi^{-}$ zoom in the region of high asymmetry ($m_{\pi\pi}$ smaller than $1.8\,\text{GeV}/c^2$ that is the region bellow the D^0 mass). Candidates distributions of events in the signal region with (a) $\cos\theta < 0$ and (c) $\cos\theta > 0$. Difference between B^- and B^+ candidates with (b) $\cos\theta < 0$ and (d) $\cos\theta > 0$.

With the above equations in hands, we can already describe the amplitudes of the $B^{\pm} \to \pi^{\pm}\pi^{+}\pi^{-}$ decay at the low-mass $\pi^{+}\pi^{-}$ region where $\rho(770)$ interferes with a constant non-resonant amplitude. The amplitudes for $B^{\pm}$ decays, $\mathcal{M}_{\pm}$, can be written as:

$$\mathcal{M}_{+} = a_{+}^{\rho} e^{i\delta_{+}^{\rho}} F_{\rho}^{\text{BW}} \cos\theta + a_{+}^{nr} e^{i\delta_{+}^{nr}} F^{\text{NR}}, \qquad (4.5)$$

$$\mathcal{M}_{-} = a_{-}^{\rho} e^{i\delta_{-}^{\rho}} F_{\rho}^{\text{BW}} \cos\theta + a_{-}^{nr} e^{i\delta_{-}^{nr}} F^{\text{NR}}, \qquad (4.6)$$

where the F^{NR} is a real and scalar non-resonant amplitude, $\delta_{\pm}$ denote both the fixed weak and the strong phases, the F_{ρ}^{BW} depicts the Breit-Wigner functions representing the ρ resonance, and θ is the helicity angle. The angular term of the amplitude is expressed as $\cos\theta$ which associated with the spin 1 resonance, $\rho(770)$, and varies from +1 to -1 along the phase space. The subtraction of the squared modulus of these amplitudes gives:
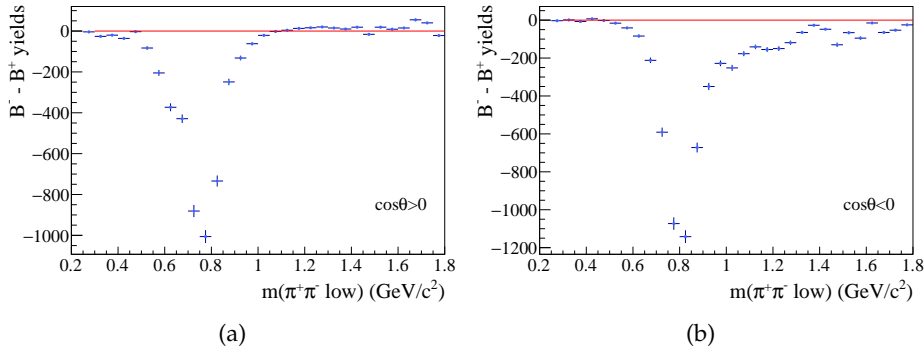
FIGURE 4.7: A simulation of the direct CP violation on the $B^{\pm} \to \pi^{\pm}\pi^{+}\pi^{-}$ channel with events split in (a) $\cos\theta > 0$ and (b) $cos\theta < 0$. Sample settings are $(a^{\rho}_{+}/a^{\rho}_{-}) = 0.8$, $(a^{nr}_{+}/a^{nr}_{-}) = 1$ and phases are zero.

$$
\begin{aligned}
\Delta|\mathcal{M}^{2}| &= |\mathcal{M}_{+}|^{2} - |\mathcal{M}_{-}|^{2} \\
&= [(a^{\rho}_{+})^{2} - (a^{\rho}_{-})^{2}]|F^{\mathrm{BW}}_{\rho}|^{2}\cos^{2}\theta + [(a^{nr}_{+})^{2} - (a^{nr}_{-})^{2}]|F^{\mathrm{NR}}|^{2} + \\
&\quad + 2\cos\theta|F^{\mathrm{BW}}_{\rho}|^{2}|F^{\mathrm{NR}}|^{2} \times \\
&\quad \{(m^{2}_{\rho} - s)\,[a^{\rho}_{+}a^{nr}_{+}\cos(\delta^{\rho}_{+} - \delta^{nr}_{+}) - a^{\rho}_{-}a^{nr}_{-}\cos(\delta^{\rho}_{-} - \delta^{nr}_{-})] \\
&\quad - m_{\rho}\Gamma_{\rho}\,[a^{\rho}_{+}a^{nr}_{+}\sin(\delta^{\rho}_{+} - \delta^{nr}_{+}) - a^{\rho}_{-}a^{nr}_{-}\sin(\delta^{\rho}_{-} - \delta^{nr}_{-})]\}. \ (4.7)
\end{aligned}
$$

Equation (4.7) consists of the addition of four terms and each of them has a characteristic signature in the $\pi^{+}\pi^{-}$ invariant mass. The first two terms are related to the direct CP violation while the last ones are associated with the Dalitz interference between neighbors resonances.

4.1.1 Direct term

The term $[(a^{\rho}_{+})^{2} - (a^{\rho}_{-})^{2}]|F^{\mathrm{BW}}_{\rho}|^{2}\cos^{2}\theta$ is equivalent to the direct CP violation induced by the short distance interference between the tree and penguin amplitudes in a same intermediary state. Using Laura++ [94], we generated a fast MC sample with 100k $B^{\pm} \to \pi^{\pm}\pi^{+}\pi^{-}$ events with the following settings: $(a^{\rho}_{+}/a^{\rho}_{-}) = 0.8$, $(a^{nr}_{+}/a^{nr}_{-}) = 1$ and phases are zero. Thus, it provides squared amplitude difference that is proportional to $\cos^{2}\theta$ in the region close to the ρ mass. Figure 4.7 depicts the expected Breit-Wigner distribution (squared) for both cosine signals.

A possible CP violation behavior of the non-resonant term $[(a^{nr}_{+})^{2} - (a^{nr}_{-})^{2}]|F^{\mathrm{NR}}|^{2}$ depends directly on the $|F^{\mathrm{NR}}|^{2}$ line shape.
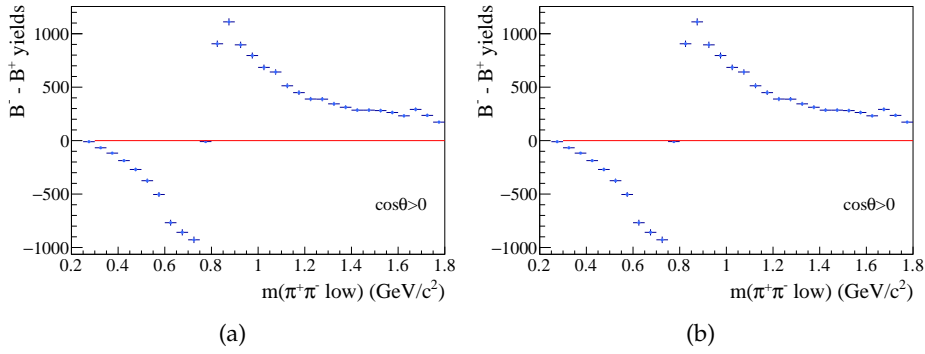
FIGURE 4.8: Simulation of CP violation of the $B^{\pm} \to \pi^{\pm}\pi^{+}\pi^{-}$ decay with the real part of interference as only contribution. The events are split in (a) $\cos\theta > 0$ and (b) $cos\theta < 0$. Sample settings are $(a_+^{\rho}/a_-^{\rho}) = 1$, $(a_+^{nr}/a_-^{nr}) = 1$, non-resonant phases are zero and $\delta_+^{\rho} = 180°$ and $\delta_-^{\rho} = 0°$.

4.1.2 DCPV real term

The real part of the interference term $2\cos\theta|F_{\rho}^{\mathrm{BW}}|^2|F^{\mathrm{NR}}|^2(m_{\rho}^2 - s)$, directly associated with the real part of the Breit-Wigner explicited on Eq. (4.2), induces the CP violation in the Dalitz. The difference between positive and negative squared amplitude produces a clear signature in the mass spectrum, followed by a zero and a sign change of the CP violation at the central value of the resonance rest mass.

To observe such a contribution, another sample of $B^{\pm} \to \pi^{\pm}\pi^{+}\pi^{-}$ with same values for positive and negative magnitudes for both ρ and non-resonant amplitudes, non-resonant phase is set to zero and, for the ρ phase, $\delta_+^{\rho} = 180°$ and $\delta_-^{\rho} = 0°$. Figure 4.8 shows the features described above: the zero and the sign change occurring at $s = m_{\rho}^2$ and it reproduces the behavior seen on the $B^{\pm} \to \pi^{\pm}\pi^{+}\pi^{-}$ data (see Figure 4.5).

4.1.3 DCPV imaginary term

The last term of Eq. (4.7) which is proportional to $2\cos\theta|F_{\rho}^{\mathrm{BW}}|^2|F^{\mathrm{NR}}|^2 m_{\rho}\Gamma_{\rho}$ is directly associated with the imaginary part of the Breit-Wigner of the resonance (see Eq.(4.3)).

To observe this Dalitz CP violation contribution, a fast MC of $B^{\pm} \to \pi^{\pm}\pi^{+}\pi^{-}$ decay was generated with the following input parameters: $(a_+^{\rho}/a_-^{\rho}) = 1$, $(a_+^{nr}/a_-^{nr}) = 1$, zero as non-resonant phases and $\delta_{\pm}^{\rho} = \pm 60°$. Figure 4.9 illustrates the expected shape which is similar to the real term contribution, with a zero when $s = m_{\rho}^2$. However there is a sign change due to the proportionality with $\cos\theta$. The imaginary term is different from zero and the real part is zero when the $\delta_+^{\rho} = -\delta_-^{\rho}$ for δ_-^{ρ} different from zero and 180°.
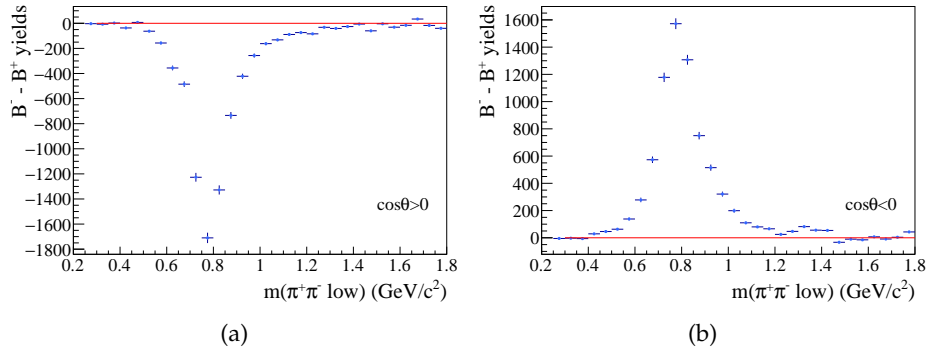
FIGURE 4.9: Simulation of CP violation of the $B^{\pm} \to \pi^{\pm}\pi^{+}\pi^{-}$ decay with the imaginary component of the interference as the only contribution. The events are split in (a) $\cos\theta > 0$ and (b) $\cos\theta < 0$. Sample settings are $(a_{+}/a_{-}) = 1$ for both resonant and non-resonant contributions, non-resonant phases are zero and $\delta^{\rho}_{\pm} = \pm 60°$.

4.2 Scalar and vector resonances interference

We have performed a similar study now considering the $B^{\pm}$ amplitudes as a sum of a scalar and a vector resonances contributions, such as $f_0(980)$ and $\rho(770)$, respectively. These particular contributions dominate at low $\pi^{+}\pi^{-}$ mass for the $B^{\pm} \to K^{\pm}\pi^{+}\pi^{-}$. Previous results on amplitude analysis of this channel can be seen in references [72, 71].

In this case, the amplitude components for $B^{\pm}$, $\mathcal{M}_{\pm}$, can be written as:

$$\mathcal{M}_{+} = a^{\rho}_{+}e^{i\delta^{\rho}_{+}}F^{\mathrm{BW}}_{\rho}\cos\theta + a^{f}_{+}e^{i\delta^{f}_{+}}F^{\mathrm{BW}}_{f}, \tag{4.8}$$

$$\mathcal{M}_{-} = a^{\rho}_{-}e^{i\delta^{\rho}_{-}}F^{\mathrm{BW}}_{\rho}\cos\theta + a^{f}_{-}e^{i\delta^{f}_{-}}F^{\mathrm{BW}}_{f}. \tag{4.9}$$

where F^{BW}_{ρ} (F^{BW}_{f}) are the Breit-Wigner functions representing the ρ (f_0) resonance, $\delta_{\pm}$ contain both the weak and the strong phases, θ is the helicity angle. Expressing the squared modulus of these amplitudes indicates that CP asymmetry will arise for non-zero weak phases. The subtraction of the squared modulus of these amplitudes gives:

$$
\begin{aligned}
|\Delta\mathcal{M}|^2 &= |\mathcal{M}_{+}|^2 - |\mathcal{M}_{-}|^2 \\
&= [(a^{\rho}_{+})^2 - (a^{\rho}_{-})^2]|F^{\mathrm{BW}}_{\rho}|^2\cos^2\theta + [(a^{f}_{+})^2 - (a^{f}_{-})^2]|F^{\mathrm{BW}}_{f}|^2 + \\
&\quad + 2\cos\theta|F^{\mathrm{BW}}_{\rho}|^2|F^{\mathrm{BW}}_{f}|^2 \times \\
&\quad \{[(m^2_{\rho} - s)(m^2_{f} - s) - m_{\rho}\Gamma_{\rho}m_{f}\Gamma_{f}] \times \\
&\quad\quad \times [a^{\rho}_{+}a^{f}_{+}\cos(\delta^{\rho}_{+} - \delta^{f}_{+}) - a^{\rho}_{-}a^{f}_{-}\cos(\delta^{\rho}_{-} - \delta^{f}_{-})] \\
&\quad - [m_{\rho}\Gamma_{\rho}(m^2_{f} - s) - m_{f}\Gamma_{f}(m^2_{\rho} - s)) \times \\
&\quad\quad \times [a^{\rho}_{+}a^{f}_{+}\sin(\delta^{\rho}_{+} - \delta^{f}_{+}) - a^{\rho}_{-}a^{f}_{-}\sin(\delta^{\rho}_{-} - \delta^{f}_{-})]\}
\end{aligned} \tag{4.10}
$$
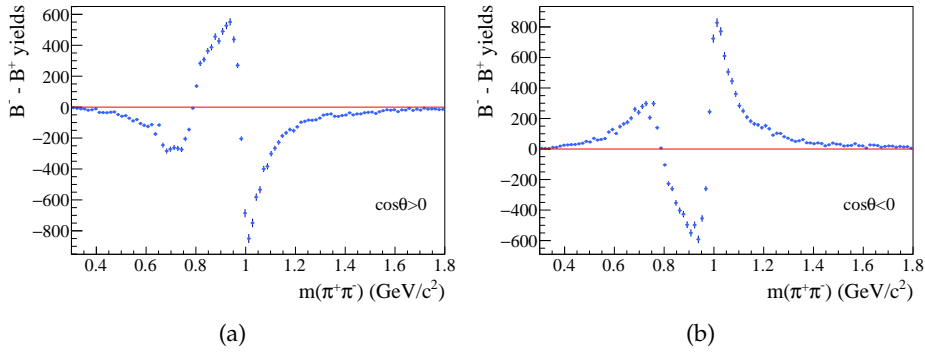
FIGURE 4.10: Simulation of *CP* violation of the $B^{\pm} \to K^{\pm}\pi^{+}\pi^{-}$ decay with only contribution of the real component of Dalitz interference *CP* violation. The events are split in (a) $\cos\theta > 0$ and (b) $cos\theta < 0$. Sample settings are $(a_{+}^{\rho}/a_{-}^{\rho}) = 1$, $(a_{+}^{f}/a_{-}^{f}) = 1$, scalar resonance phases are zero and $\delta_{+}^{\rho} = 180°$ and $\delta_{-}^{\rho} = 0°$.

Equation (4.10) is the sum of four terms, where the two first are associated with the direct *CP* violation, and thus are equivalent to the previous study. The last terms describe the interference between the ρ and f_0 resonances and are detailed below.

4.2.1 DCPV real term

We denominate the term $2\cos\theta|F_{\rho}^{\mathrm{BW}}|^2|F_{f}^{\mathrm{BW}}|^2 \times [(m_{\rho}^2 - s)(m_f^2 - s) - m_{\rho}\Gamma_{\rho}m_f\Gamma_f]$ as DCPV real since it is proportional to the square of the Breit-Wigner real component. It has a clear signature in the mass projections $m_{\pi\pi low}$, with a zero close to the mass of the vector meson ρ and another one close to the mass of scalar meson $f_0(980)$. In addition, a sign change of *CP* violation occurs due to the proportionality with $\cos\theta$.

We used Laura++ to generate 100k events of $B^{\pm} \to K^{\pm}\pi^{+}\pi^{+}$ decay with the following settings: $(a_{+}/a_{-}) = 1$ for both resonance amplitudes, zero phases for the scalar resonance and $\delta_{+}^{\rho} = 180°$ and $\delta_{-}^{\rho} = 0°$. Figure 4.10 depicts the expected characteristics aforementioned: a sign change of the *CP* violation and two zeros at the resonance masses.

4.2.2 DCPV imaginary term

We denominate the term $2\cos\theta|F_{\rho}^{\mathrm{BW}}|^2|F_{f}^{\mathrm{BW}}|^2 \times [m_{\rho}\Gamma_{\rho}(m_f^2 - s) - m_f\Gamma_f(m_{\rho}^2 - s)]$ as DCPV imaginary since it is proportional to the square of the Breit-Wigner imaginary component. The shape of this term peaks at the two interfering resonance masses. Due to the direct proportionality with $\cos\theta$, occurs a sign change of the *CP* violation when $\cos\theta$ pass through zero.

We produced a Toy MC sample of 100k events of $B^{\pm} \to K^{\pm}\pi^{+}\pi^{+}$ decay with the following settings: $(a_{+}/a_{-}) = 1$ for both resonance amplitudes,
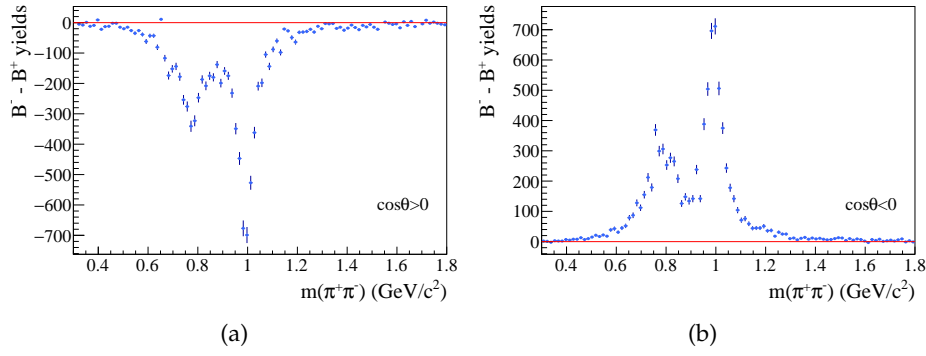
FIGURE 4.11: Simulation of CP violation of the $B^\pm \to K^\pm \pi^+ \pi^-$ decay with the imaginary component of the interference as the only contribution. The events are split in (a) $\cos\theta > 0$ and (b) $\cos\theta < 0$. Sample settings are $(a^\rho_+/a^\rho_-) = 1$, $(a^f_+/a^f_-) = 1$, scalar resonance phases are zero and $\delta^\rho_+ = \pm 60°$.

the phases related to the $f_0(980)$ resonance are zero, while $\delta^\rho_+ = 60°$ and $\delta^\rho_- = -60°$. Figure 4.11 features the expected zeros and CP sign change.

4.3 Final comments

We can interpret Figures 4.5 and 4.6 as the signature from a simple two-amplitude model, due to the direct CP violation produced by a resonance and the Dalitz CP violation real and imaginary components. The former shows a zero at the $\rho^0(770)$ mass in both plots, $\cos\theta > 0$ and $\cos\theta < 0$ for $B^\pm \to \pi^\pm \pi^+ \pi^-$ with the expected change of sign around $\cos\theta = 0$. Figure 4.5 shows two zeros for $\cos\theta < 0$: one close to the $\rho^0(770)$ mass and another at the $f_0(980)$ mass. On the other hand, the $\cos\theta > 0$ plot does not present clear a CP violation signature around the $\rho^0(770)$ mass, but a clear zero at the $f_0(980)$ mass. These experimental results suggest that CP violation at low $\pi^+ \pi^-$ mass comes from the real part of the interference between two amplitudes involving the ρ resonance. Consequently the imaginary part of the penguin contribution for the ρ resonance must be equal to zero for both $B^\pm \to K^\pm \pi^+ \pi^-$ and $B^\pm \to \pi^\pm \pi^+ \pi^-$ decays. This allows direct CP violation close to zero as experimental results indicate. Thus, Figures 4.8 and 4.10 approximately reproduced the asymmetry behaviour observed in data for $B^\pm \to \pi^\pm \pi^+ \pi^-$ and $B^\pm \to K^\pm \pi^+ \pi^-$ decays, respectively.

This qualitatitive study indicates that both two-amplitude models used are not good enough to completely describe the asymmetry found in data shown in Figures 4.5 and 4.6. Reference [95] provides a phenomenological approach with a general description of the CP violation including not only resonant contributions but also hadronic final state interactions (rescattering $\pi\pi \leftrightarrow KK$). This formulation allowed us to fit the data as can be seen in

(a)   (b)

(c)
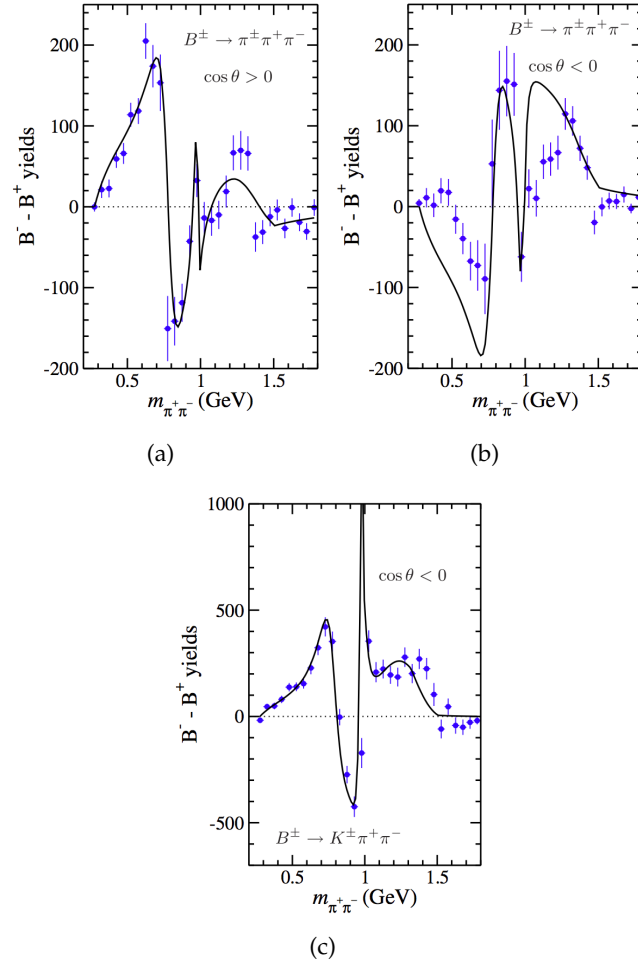
FIGURE 4.12: *CP* asymmetry of the $B^\pm \to \pi^\pm\pi^+\pi^-$ decay
(a) $\cos\theta > 0$ and (b) $\cos\theta < 0$ fitted to the experimental values (blue points); (c) *CP* asymmetry of the $B^\pm \to K^\pm\pi^+\pi^-$
decay for $\cos\theta < 0$.

Figure 4.12 confirming that this effect play an important role in *CP* violation of the $B^\pm \to h^\pm h^+ h^-$ decays.

In conclusion, the data accumulated in 2011 and 2012, corresponding to a integrated luminosity of $3.1\,\mathrm{fb}^{-1}$, allowed to observe into detail the phase space of the $B^\pm \to h^\pm h^+ h^-$ decays. Specifically, in the low mass region of the $B^\pm \to \pi^\pm\pi^+\pi^-$ and $B^\pm \to K^\pm\pi^+\pi^-$ modes, we observed that hadronic final state interaction play an important role on the strong phase of the decay amplitudes while the strong phase due to the short-distance effects is found to be negligible.

Rio group together with Bristol and Warwick are collaborating in order to obtain the first results on the amplitude analysis for each of the $B^\pm \to h^\pm h^+ h^-$ channels. It should include (i) coupling terms among the channels to describe the "compound *CP* violation" and (ii) a rescattering term to model hadronic final state interactions influence on the strong phase.

Part II

Contribution to LHCb SciFi Tracker

Chapter 5

Scintillating fibres

The LHCb SciFi Tracker [45, 48], already discussed in section 1.3.4, is going to be based on 250 µm-diameter plastic scintillating fibres produced by the Japanese company Kuraray Co. Ltd. As shown in Figure 5.1, a fibre consists of a scintillating core made of doped polystyrene (refractive index $n = 1.59$) and a double cladding structure corresponding to 6% of total diameter in thickness. The inner and outer cladding layers are composed by polymethylmethacrylate (PMMA) with a refractive index $n = 1.49$ and a fluorinated polymer $n = 1.42$, respectively.
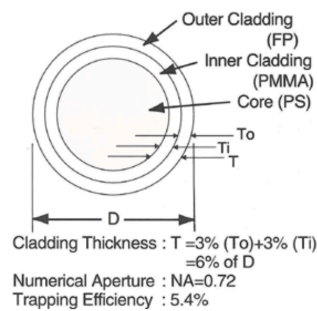
FIGURE 5.1: Illustration of a Kuraray double-clad scintillating fibre.

Source: [96].

In the following sections, I present the fundamentals of scintillating fibres by detailing the scintillation process, the trapping efficiency and the figures of merit such as attenuation length, light yield, diameter and cladding integrity, which allowed us to determine the fibre described above as the best option for the SciFi Tracker.

5.1 Scintillation process

When an ionizing particle traverses a typical plastic scintillator, the energy dissipated as excitation (based on the π-electrons of the aromatic polymer) is transformed into a luminescence emission through a multi-step process (Figure 5.2). The material base, usually polystyrene for plastic fibres, is not a good intrinsic light emitter and has a slow relaxation time. The decay

time of pure polystyrene is 16 ns [97], which is too slow for practical applications. Besides, its emission spectra (in UV-range) does not match the sensitivity of photodetectors such as photomultiplier tubes (PMT) and silicon photomultipliers (SiPMs). Hence, it is common to admix an organic fluorescent dye at 1% by weight with matched energy levels structure to improve the efficiency of the scintillation mechanism. Energy is rapidly transfered (<1 ns) from the base to this 'activator' dye molecules via a non-radiative dipole-dipole interaction denominated as Föster transfer. Subsequently, the primary dye relaxes to the ground state by the emission of a photon usually in the UV range.

Since there is some overlap between emission and absorption spectra of this primary dye (PMP for example), a fraction of the photons produced can be re-absorbed by the dye, causing a reduction of the attenuation length. A second (wavelength shifting) dye (∼0.01% by weight), which absorbs the primary photons and re-emits them at longer wavelengths, is also added in order to increase the separation of emission and absorption spectra (Stoke's shift).

5.2   Trapping fraction

Light is produced isotropically within the core of the fibre and, due to total internal reflection, only a small fraction is trapped and transported till the readout end.

5.2.1   Single cladding

Figure 5.3(a) illustrates a single-clad fibre with a circular cross section that is made of a polystyrene core and PMMA cladding material. In this case, total internal reflection gives:

$$\theta_{\mathrm{crit}} = \arcsin\left(\frac{n_{\mathrm{PMMA}}}{n_{\mathrm{core}}}\right) = \arcsin\left(\frac{1.49}{1.59}\right) \approx 69.6°. \qquad (5.1)$$

Considering that light is created in the axial axis of the fibre, the trapping efficiency $\epsilon_{\mathrm{single-clad}}$ over the total solid angle for a single-clad fibre is given by:

$$\epsilon_{\mathrm{single-clad}} = \frac{1}{4\pi}\int_0^{\pi/2-\theta_{\mathrm{crit}}} \sin\theta \, d\theta \approx 3.1\%, \qquad (5.2)$$

where n_{core} (n_{PMMA}) corresponds to the refractive index of the core (cladding) material and θ_{crit} is the angle above which the total internal reflection occurs.

Hence, for a fibre with a single cladding, only 6.2% of the light remains in the core. This trapping efficiency is underestimated though, since there
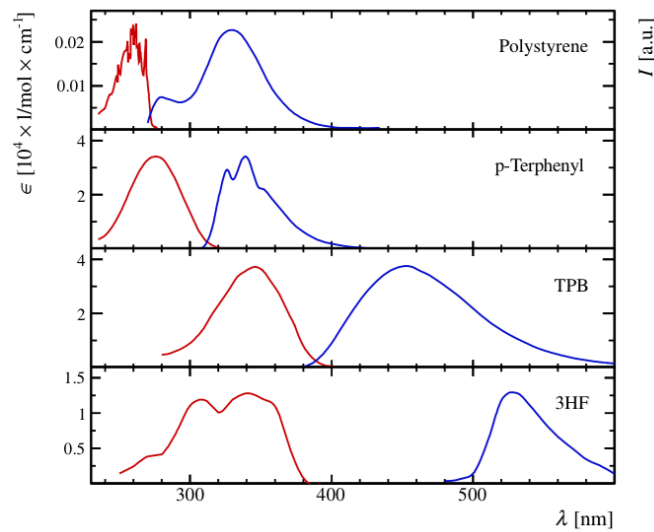
FIGURE 5.2: Absorption and emission spectra (in red and blue, respectively) of typical elements of a plastic scintillating material: a polystyrene solvent, p-Therphenyl as activator, TPB or 3HF as wavelength shifters. The scintillating process in organic materials occurs in the following steps: an ionizing particle provide part of its energy to the base material (polystyrene). Through a non-radiative dipole-dipole interaction, the absorbed energy is transfered to the activator (p-Therphenyl) which then relaxes to the ground state by the emission of a photon. The wavelength shifter absorbs the emitted primary photon and fluoresces at longer wavelengths of the light by the primary dye. TPB material presents an overlap between absorption and emission spectra indicating re-absorption of primary photons. On the other hand, 3HF exhibits a large Stoke's shift. Consequently, fibres which presents 3HF as wavelength shifter have a better performance in terms of attenuation length. However, they also have longer decay time (≈ 7 ns) when compared to SCSF-78 fibres (≈ 2.8 ns) [96].

Source: [98].

are propagation modes that transport light through the cladding. Also light propagating in helical paths, although satisfying total internal reflection condition, is highly attenuated due to the number of reflections.

5.2.2 Double cladding

Figure 5.3(b) depicts a circular double-clad fibre which is made of a polystyrene core, PMMA and a fluorinated polymer (FP) as the inner and outer cladding material, respectively. Total internal reflection condition gives:

$$\theta_{\text{crit}} = \arcsin\left(\frac{n_{\text{FP}}}{n_{\text{core}}}\right) = \arcsin\left(\frac{1.42}{1.59}\right) \approx 63.3°, \tag{5.3}$$

where n_{core} (n_{FP}) is the refractive index of the core (outer cladding) material.

The trapping efficiency $\epsilon_{\mathrm{double-clad}}$ over the total solid angle for a double-clad fibre is given by:

$$\epsilon_{\mathrm{double-clad}} = \frac{1}{4\pi} \int_0^{\pi/2-\theta_{\mathrm{crit}}} \sin\theta \, d\theta \approx 5.4\%. \tag{5.4}$$

For a double-clad fibre, more than 10% of the initial light produced remains in the core.
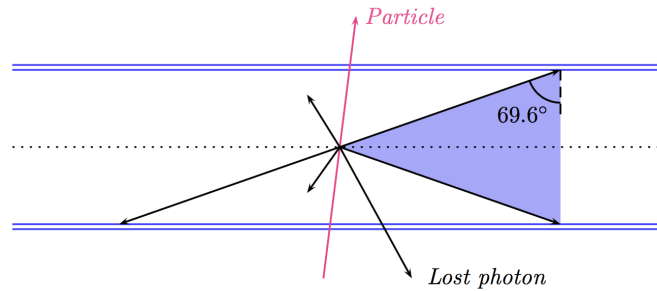
(a) Single-clad fibre with a polystyrene core and a PMMA cladding.
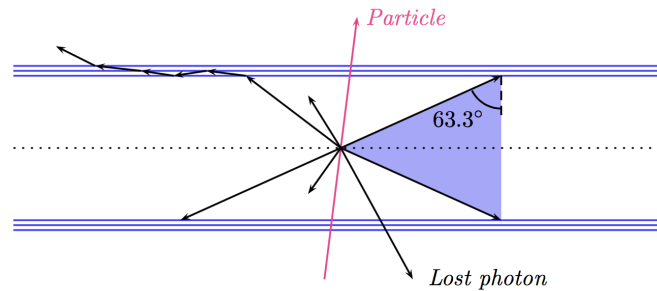
(b) Double-clad fibre with a polystyrene core, a PMMA inner cladding and a FP outer cladding.

FIGURE 5.3: Critical angle of a (a) single-clad and (b) double-clad fibre.

5.3 Figures of merit

Since CERN is in charge of the quality assurance of the LHCb SciFi Tracker scintillating fibres, one of my main tasks was to check their performance. The characterization of scintillating fibres consists on the measurements of attenuation length, light yield, radiation hardness, diameter constancy and decay time.

5.3.1 Attenuation length

Although 10.8 % of the initial light is trapped inside the core of a double-clad fibre, still it can be lost when it propagates due to, for instance: Rayleigh scattering (light scatters because of non-uniform density region), presence of air bubbles or other impurities, cladding defects. The producer [96] suggests the intensity of the light to be modeled by an single exponential decreasing with the distance from the excitation point:

$$I = I_0 \, e^{-x/\Lambda}, \tag{5.5}$$

where Λ is the attenuation length. Depending on the fibre's length a single exponential is not enough to describe the attenuation of the light over the total extent. For long fibres (>1-2 m), the intensity of light is well modeled by a double exponential:

$$I = I_0 \, \left(e^{-x/\Lambda_S} + e^{-x/\Lambda_L} \right), \tag{5.6}$$

where Λ_S and Λ_L are the short and long components of the attenuation length, respectively. The short component Λ_S accounts for the highly attenuated modes such as light travelling through the cladding and in helical paths, and is of the order of few tenths of cm. The long component Λ_L describes the light propagating through the core. In addition, the attenuation length is dependent on the wavelength λ.

As mentioned in Section 1.3.4, SciFi Tracker is going to be built of 2.5 m-length scintillating fibres. The light trapped inside those fibres need to travel distances of up to 2.5 m or even 5 m if one accounts for mirror-reflected light. The fibres that possesses an attenuation length Λ_L larger than 3.0 m are appropriated for the SciFi detector.

De facto, we observe an effective attenuation length. The reasons are the following: the measured attenuation length (i) depends on the characteristics of the used photodetector and (ii) is smaller than the bulk attenuation length because the photons trapped inside the fibre are reflected many times and travel through a zigzag path.

5.3.2 Light yield

The intrinsic scintillation yield of a fibre is the number of photons emitted by the wavelength shifting dye due to a given energy deposition. Some producers provide the yield of 7000 – 8000 photons per MeV [99]. In the case of scintillating fibres, the light yield not only depends on the amount of deposited energy but also at which length the excitation occurred once light can suffer attenuation effects.

For the purpose of comparing different fibres and monitoring their quality during the R&D phase and series production, it is sufficient to measure an effective light yield under defined and stable experimental conditions. Excitation of the fibre by an ionising particle or an x-ray photon is however mandatory. The ionising radiation cannot be replaced by UV light as this would just excite the wavelength shifting dye without promoting the scintillation process itself.

The light yield is the most important figure of merit which will determine if the fibre is adequate or not to follow to the next production steps of the LHCb SciFi Tracker.

5.3.3   Radiation hardness

Figure 5.4 indicates the expected radiation dose for LHCb detector in the upgraded conditions[1] estimated by FLUKA [100, 101] simulation.

The ionization dose was found to be up to 35 kGy in the innermost region close to the beam pipe. Exposition of the fibres to such ionization doses causes a reduction to the scintillation yield due to degradation of the transmission properties and/or scintillating and wavelength shifting dyes. A series of irradiation campaigns with different ionising particles and energies were organised in order to investigate these issues [48]. One of particular importance, which has my contribution while at CERN, was concerning the irradiation a 6-layer SciFi half-module at PS [102].

The ionising dose expected at the extremities is of few tens of Gy which poses no issues to the SiPMs. However, the fluence of neutrons and high energy hadrons causes displacements of the lattice of crystalline structures such as silicon, damaging the SiPM detectors. The displacement damage induced by neutrons can be normalized to displacement damages induced by $1\,\mathrm{MeV}$ neutrons and are usually expressed as $1\,\mathrm{MeV}$ equivalent. The neutron fluence is expected to be of up to 6×10^{11} (1 MeV equivalent)$/\,\mathrm{cm}^2$ at the outer edges of the SciFi detector.

Although these experiments try to reproduce some of the radiation parameters such as dose and dose distribution, it is impossible to attain the exact radiation effect of the real world environment [48]. Take for instance the dose rate. We do not have 10 years to test the response of the detector under the expected radiation harsh environment. Hence irradiation tests took place at significantly higher dose rate than the one expected in LHCb.

---

[1]Upgraded conditions correspond to a collision energy in the center of mass $\sqrt{s} = 14\,\mathrm{TeV}$ and an integrated luminosity of $50\,\mathrm{fb}^{-1}$.
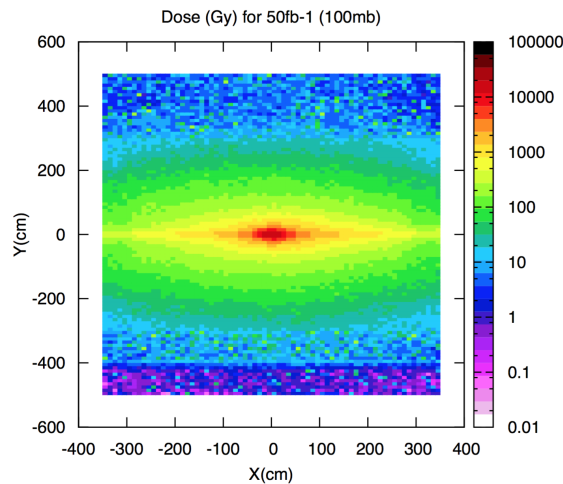
FIGURE 5.4: Expected accumulated dose in the first tracking station after an integrated luminosity of $50\,\text{fb}^{-1}$ and for a *pp* cross-section of 100 mb. The point (0,0) corresponds to the beam pipe position.

Source: [45].

5.3.4 Diameter constancy

The production of the scintillating fibres depends on the temperature of the preform (which has the same diameter proportions of core and cladding as the final fibre) and the drawing tension [103]. Diameter (ϕ) variations are denominated as bumps ($\phi > 275\,\mu\text{m}$) or necks ($\phi < 225\,\mu\text{m}$). Bumps can be produced by the presence of impurities such as glass particles or micro pieces of cotton/hair. Necks are often generated by problems in the drawing speed/temperature and are rarely found.

Figure 5.5 shows a bump distorting the winding pattern, which could affect the overall performance of the fibre mat especially the hit efficiency and spatial resolution. While the producer made all possible measures to improve the fibre quality production, the presence of bumps is unavoidable.

5.3.5 Decay time

For critical time applications, such as the LHCb SciFi Tracker, the decay time constant of the scintillating fibres should be as low as possible. Indeed, one of the key properties that is desired in scintillators in general is a short decay time (τ).

The photons generated from the scintillation mechanism are not emitted simultaneously because of their statistical nature. The necessary time to populate the levels which generate fluorescence is less than 1 ns and the decay time from these levels is only three or four times greater for the very fast
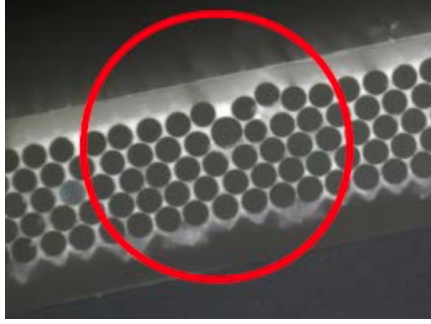
FIGURE 5.5: Photograph of a bump affecting the winding
pattern of a fibre mat.

Source: [104].

scintillators [105]. A complete description of the expected pulse shape must
take into account the finite rise time, the decay time and also the slower
component due to the delayed fluorescence.

A typical profile of the decay time light pulse has rise edge, which is
very fast (<1 ns), followed by an exponential decay. In literature, there are
few models that are used to describe the behavior of the decay time pulse
shape. One approach [106, 107, 108] describes the emission with a finite
rise time τ_r (corresponding to the time constant that describes the energy
transfer to the optical levels) and a decay time τ:

$$I = I_0 \left(e^{-t/\tau} - e^{-t/\tau_r} \right). \tag{5.7}$$

Other reference [109] suggests the pulse shape can described by the con-
volution of a Gaussian probability distribution and an exponential:

$$f(t; \tau, \mu, \sigma) = G(t; \tau, \mu, \sigma) * e^{-t/\tau}$$

$$= \frac{1}{2\tau} e^{\frac{1}{2\tau}\left(2\mu + \frac{\sigma^2}{\tau} + 2t\right)} \operatorname{erfc}\left(\frac{\mu + \frac{\sigma^2}{\tau} - t}{\sqrt{2}\sigma} \right), \tag{5.8}$$

where μ and σ are the mean and width of the Gaussian function and erfc is
the complementary error function.

A more detailed approach [110] describes the decay time measurement
for three different types of 1 mm diameter round scintillating fibres.The de-
cay times were found to be in the range of 2.08-2.36 ns, respectively. As for
comparison, SCSF-78 scintillating fibres decay time is 2.8 ns.

5.4 Fibre specification for LHCb SciFi Tracker

The LHCb SciFi tracker requires a total quantity of 11 000 km of fibres.
When concluding a purchasing contract with the company Kuraray, the

technical requirements listed in Table 5.1 were agreed. The fibres have arrived at CERN in batches containing few spools in the R&D phase up to 20 in the production phase. A spool (see Figure 5.6) has 12.5 km of fibres.
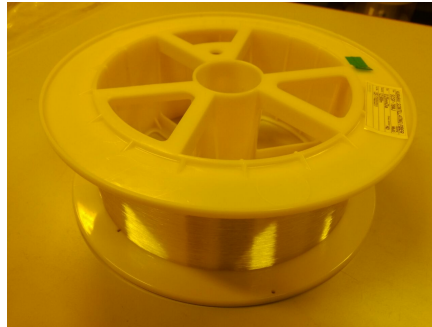
FIGURE 5.6: A fibre spool containing 12.5 km of scintillating fibres.

	Parameter	Specification
Intrinsic properties	Peak emission	≈ 450 nm
	Decay time	< 3 ns
	Light trapping fraction	$> 5\%$ per hemisphere
Geometrical requirements	Nominal diameter	250 μm
	Diameter tolerance	$\pm 2\%$ of nominal diameter
	Statistical diameter variation	≤ 3 μm
Number of defects per spool	Bumps ≥ 350 μm	≤ 8
	Necks ≤ 200 μm	≤ 8
Performance requirements	Light yield @ d=0	> 10 photoelectrons
	Attenuation length	> 300 cm when measured by Kuraray (PMT)

TABLE 5.1: Summary of the fibre specifications for the SciFi Tracker.

Chapter 6

Quality assurance and experimental setups

6.1 Attenuation length

The attenuation length of a scintillating fibre is one of the key parameters for the LHCb SciFi project. Measurement of both integral and spectral attenuation length are performed at CERN [111]. While the former uses a PIN-diode which integrates all the light (full spectrum) in a photocurrent signal, the latter uses a spectrometer to separate light into individual wavelengths, so that, for each position a spectrum distribution is measured.

6.1.1 Integral attenuation length

An experimental setup, illustrated in Figure 6.1, was developed at CERN to provide fast, consistent and reproducible measurements in view of the production phase. The setup consists of:

- a 3.5 m long optical aluminum rail;

- a custom-made Polyoxymethylen (POM) cavity, which allows the placement of 4 UV-LEDs, is equipped two holes in the middle for the passage of a fibre. The outside body is a black POM, but the inside is made from diffusely reflecting POM;

- a NewPort 818-UV Si-PIN photodiode;

- a mechanical fixation.

The fibre sample under test, with a typical length of about 3 m, is held and tensioned due to magnetic soft rubber fixation pins. A guillotine-like cutter is used for performing a precise cut on the readout end of the fibre, to guarantee an undamaged light exit surface. The readout end is positioned so that it touches the photodiode wall to maximize the light output[1] and the other end is fixed mechanically.

---

[1] The photocurrent is about 1 μA when the fibre is excited at the closest position, at 15 cm distant from the PIN-diode, for SCSF-78 Kuraray fibres.

Two particular sections of about $2\,\mathrm{cm}$ length of the fibre are black painted with Aquadag[2]. The first one is located a few centimeters close to the photo detector to suppress light that travels though the cladding. The second one, the fibre end, located $3\,\mathrm{m}$ away from the PIN-diode, to absorb light that could be reflected from the end cut (Fresnel reflection).

The 818-UV is read with a Keithley Picoammeter which is connected to a PC. The background due to room light and other sources is below 1 nA and typical photocurrents range from 100 to 1000 nA. A handled push button trigger allows the transfer of a data point to a Labview program that performs a quick and fast analysis as soon as all the data points are collected. An offline analysis is also performed later using a ROOT program.

The sensitivity characteristic curve of the photodiode is shown in Figure 6.2. The spectral sensitivity of the detector matches the spectrum of photons leaving the fibre whch ranges from about $420\,\mathrm{nm}$ up to $620\,\mathrm{nm}$.
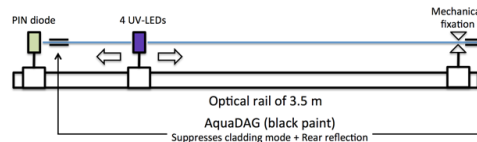
FIGURE 6.1: Illustration of the attenuation length setup. It is composed by an aluminum rail, an UV-LED cavity mounted on a carriage which can be moved along the rail, a PIN-diode detector and a mechanical fixation which is used to fix the fibre. The fibre is placed so that it touches the PIN-diode wall to maximize the light input.
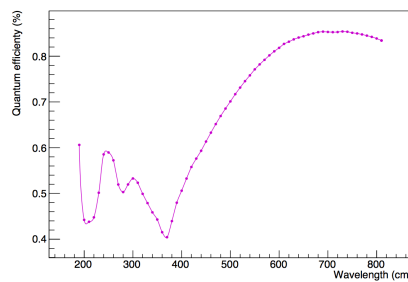
FIGURE 6.2: Quantum efficiency of the Si-PIN photodiode Newport 818-UV. The peak emission for SCSF-78 fibres is at about $450\,\mathrm{nm}$.

Offline analysis

As already mentioned, the attenuation length is described by two exponential components: 1) a short one which characterizes modes that are transported though the cladding or helical paths, and is of the order of tenths

---

[2]Water Based Graphite Coating/Additive is an aqueous-based colloidal dispersion of ultra-fine graphite. Henkel Cooperation.

of centimeters; 2) long component which describes the light propagating though the core of the fibre.

The offline analysis consists of a single exponential fit performed in the range of 100 - 300 cm, enabling a direct comparison with the attenuation length measured by the producer. In the fit range chosen, the modes characterized by the short component is sufficiently suppressed and considered negligible. An example of such a fit can be seen in Figure 6.3.
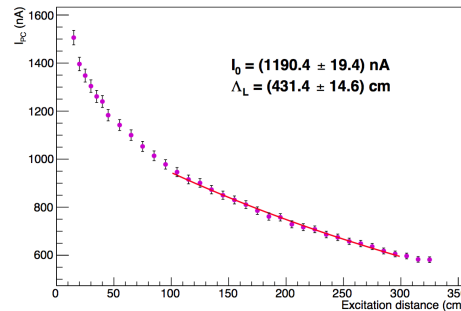
FIGURE 6.3: Example of an attenuation length fit. This sample, from a 2010 test batch, has one of the highest attenuation length ($\Lambda_L = 431$ cm) ever measured.

6.1.2 Spectral attenuation length

Measurements of the spectral attenuation length are performed once per batch. It allows to verify, for example, the presence of impurities, or whether the drawing parameters variation caused any effect on the quality of the fibre.

The setup to perform such a measurement is basically the same used for the integral attenuation length, but instead of the PIN-diode, an Ocean Optics spectrometer (type USB2000+UV-VIS-ES), covering the range from 200 to 850 nm, is used to detect the light output from the tested fibre. A tungsten halogen light source (type HL-2000-CAL) has been used to calibrate the spectrometer, ensuring that each channel of the 2048-element linear silicon CCD has the same sensitivity.

Figure 6.4(a) shows the typical emission spectra of a SCSF-78 fibre. As expected, the light intensity is attenuated with regard to the excitation distance, but more important is the fact that the spectra shifts toward longer wavelength. Figure 6.4(b) shows spectral attenuation length $\Lambda(\lambda)$ of a SCSF-78 fibre sample. Although the spectrum is highly blue peaked, the blue wavelengths have a lower attenuation length (few hundred of centimeters) when compared to the green and red part of the spectrum, reaching values larger than 10 m. The enhanced absorption at λ 535 and 605 nm is a well-known feature, attributed to the excitation of molecular vibration levels of polystyrene.
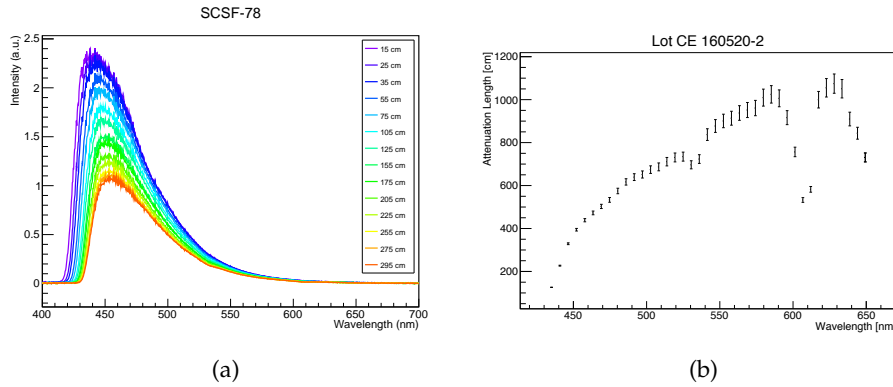
FIGURE 6.4: Attenuation length dependence on the wavelength: (a) Emission spectra distribution of a SCSF-78 Kuraray fibre excited with UV-LED light at distances ranging from 15 cm till 295 cm to the spectrometer; (b) spectral attenuation length of a SCSF-78 fibre.

6.2   Light yield

In the following we describe a light yield set-up [112] which is based on electrons from a Sr-90 source. The absolute charge calibration in photoelectrons (pe) is obtained through the photon counting capability of the SiPM photodetectors.

To determine the attenuation length of a fibre, it is enough to use UV light (which excites the wavelength shifting dye), because in that case what matters is the light losses due to transportation. However, to measure the intrinsic scintillation yield of a fibre, it is necessary to use ionising particles to induce the whole scintillation and wavelength shifting chain.

Scintillating yield is defined as the number of photons emitted by the wavelength shifting dye due to scintillation process which is then detected by a photodetector. According to [113], 7000-8000 scintillation photons are produced per MeV. Although it seems a lot of photons, considering that only 5% of them remain in the fibre, plus attenuation effects and the photodetector efficiency (PDE 30%), this number drops to only few photons.

6.2.1   Experimental set-up

The set-up that allows measuring the light yield of scintillating fibres consists of:

- A Sr-90 electron source (370 MBq) mounted inside a magnetic monochromator;

- 2 photomultiplier tubes (PMT) of type Hamamatsu H7826 for the readout of the trigger fibres;

- 1 SiPM type Hamamatsu S13360-1350CS for the readout of the signal fibres;

- a disc with 30 cm circumference in which the signal fibres are rolled in;

- Digital oscilloscope Lecroy LT344;

- NIM modules (amplifier, discriminator, coincidence).

Figure 6.5 shows the part of the set-up which is located inside a dark room. Next to it there is an illuminated room where the NIM crate, the oscilloscope and power supplies are placed.

Figure 6.6 illustrates how the fibres are positioned and aligned on the top of the monochromator exit. The choice of using three fibres under test was done for two reasons: 1) the scintillation light yield of a single fibre with 250 μm is very small, which turns it difficult to discriminate between signal and noise; 2) sufficiently high signal amplitudes were obtained with a stack three fibres. The 250 μm-diameter fibres are very fragile and mounting them in the groove is a delicate task. Measurements with four fibres were also performed, however an extra fibre is not only harder to mount, but also it is more likely to damage the sample. The signal fibres are vertically mounted in a 270 μm width groove between two plastic walls in which the trigger fibres (also $\phi = 250\,\mu m$) are precisely placed on top and below. The excitation distance, which is the fibre length between the monochromator exit hole and the SiPM, can be changed in steps of 30 cm by rolling the fibres in the disc.

The Sr-90 source together with the monochromator provides electrons with $(1.0 \pm 0.1)\,\text{MeV}$ energy [112], which can be considered as minimum ionising particles (MIP). A trigger signal is generated from a coincidence of the amplified and discriminated signals from the trigger PMTs. The voltage signal from the SiPM is sampled by the oscilloscope in a certain time window. Each signal pulse is integrated in time, generating a charge signal. After enough statistics is accumulated (about 20k events), a charge distribution is obtained which allows the determination of the calibration in photoelectrons. A typical calibration value is 1 pe = 200 pVs.

Sample preparation and arrangement into the setup

In order to prepare the fibre samples, the first step consists on cutting three pieces of fibre (from the same spool) with a length larger than 2.5 m. The ends of the sample are placed into a custom-made cylindrical end-piece with an exit hole of 0.7 mm diameter and then glued with an epoxy glue (Araldite® Rapid); the curing time is around 3 hours. After the glue is completely dry and hard, the end-piece is machined with an optical fibre
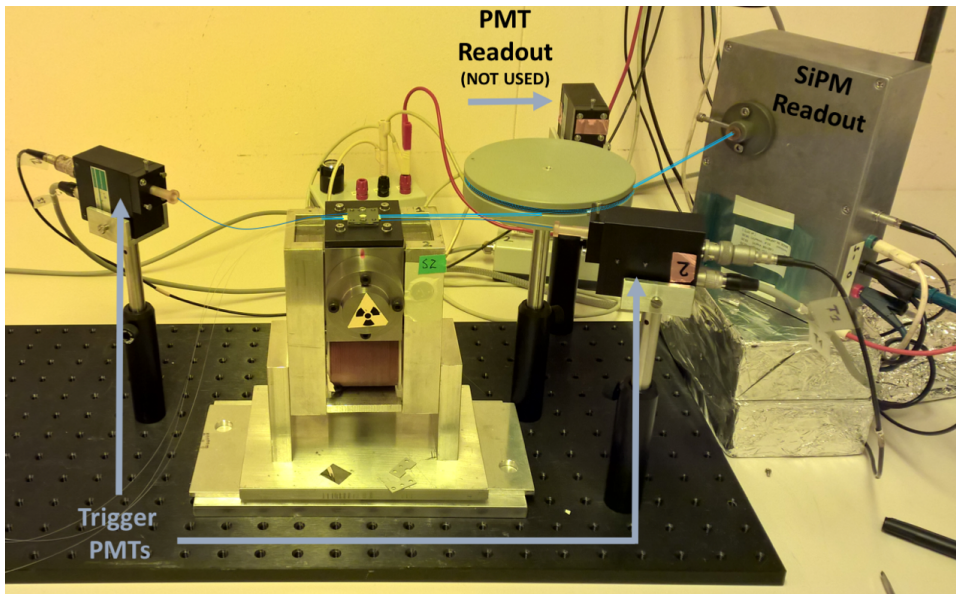
FIGURE 6.5: Light yield experimental set-up. The signal of a stack of three fibres is read out by a SiPM and it is taken into account only if there is a coincidence signal coming from the trigger PMTs.
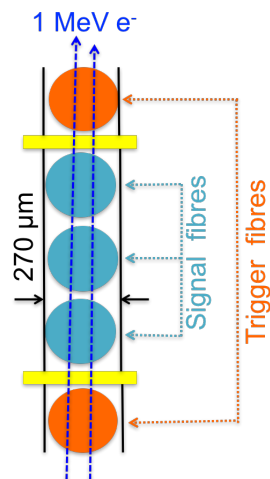
FIGURE 6.6: Fibre arrangement on the top of the electron gun exit. The alignment of the stack of three fibres is allowed by positioning them in a 270 μm width groove.

(a)   (b)
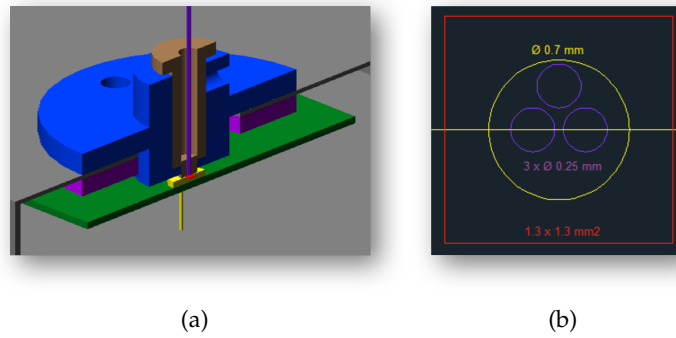
FIGURE 6.7: Details of the end-piece: (a) is a cross section
of the end-piece installed in the SiPM readout box; (a) il-
lustrates a cross section of three fibres (in purple) randomly
placed inside the end-piece (yellow circle) together with the
SiPM active surface (red square).

diamond finishing tool[3] which assures a flat and perpendicular cut of opti-
cal quality. The sample then is ready to be tested.

The end-piece is delicately placed into the SiPM box, so that it touches
the SiPM coating resin (Figure 6.7). No optical grease is added. The proce-
dure for measuring the light yield consists on positioning the sample with
excitation distances varying from 90 to 240 cm, which is achieved by rolling
the fibre along the disk circumference (1 turn $\equiv$ 30 cm). The error in the
position is estimated to be better than 2 cm.

6.2.2 SiPM details and calibration

The SiPM Hamamatsu S13360-1350CS [115] has an active area of $1.3{\times}1.3\,\mathrm{mm}^2$,
which is sufficiently large for detecting the light of the signal fibres installed
in the end-piece. Since the number of generated photoelectrons is about 15,
the large number of pixels (667 with 50 μm pitch) assures linearity of the
SiPM response, i.e., proportionality between the number of fired pixels and
the number of generated photoelectrons. It is operated at a overvoltage of
3 V, which features a high gain ($\mathcal{O}(10^6)$) with 1% cross-talk. The SiPM is
biased and read out by a Hamamatsu driver circuit C12332-01 [116] with
a temperature compensation of the overvoltage which allows stable mea-
surements. The SiPM and the driver circuit are placed inside a grounded
metal box which shields against high frequency noise and external light.

Figure 6.8 shows a peaked charge distribution with 28000 accumulated
events from a set of three fibres excited by a pulsed UV-LED light source
(PicoQuant PLS370). The data acquisition is triggered in sync with the UV-
LED light pulse. The spectrum is very well described by Eq. (6.1) which
is a convolution of a Poisson distribution and a set of Gaussians. While

---

[3]FibreFin [114].
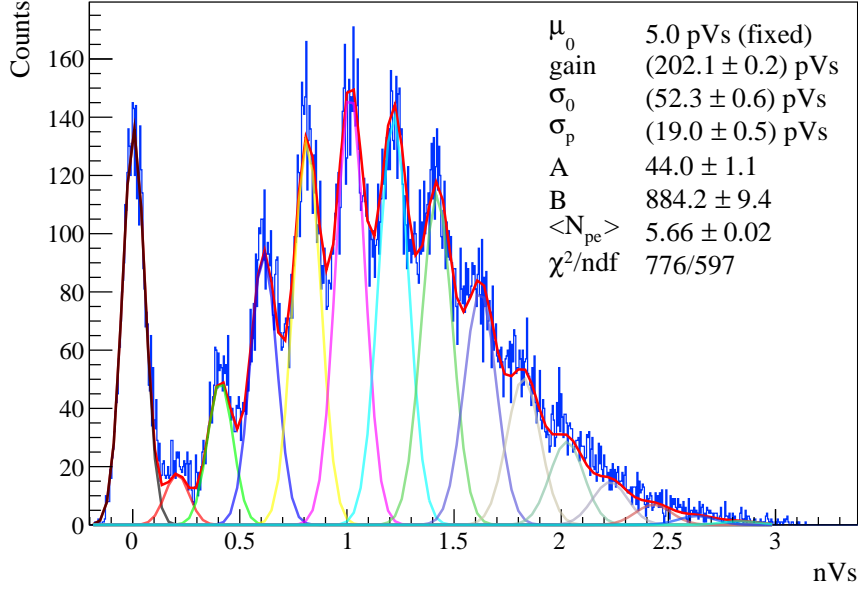
FIGURE 6.8: Example of a charge distribution with 28k events when a fibre is excited with a pulsed UV-LED. The fitted function is a convolution of a Poisson distribution and a set of Gaussians with increasing widths.

the Poisson distributions describe the photon emission (considered to be a random process), the Gaussians with increasing widths account for the fact that as the number of photoelectrons augments, the resolution gets worse. The charge gain is the distance between adjacent peaks and provides the output charge of one detected photon (=photoelectron). In this case, 1 photoelectron corresponds to 202 pVs.

$$F(\mu_0, \text{gain}, \sigma_0, \sigma_p, A, B, < N_{pe} >) = B\left[A \cdot P(0, \overline{N}_{pe}) \cdot G(x, \mu_0, \sigma_0) \quad + \right.$$

$$\left. + \quad \sum_{i=1}^{N} \cdot P(i, < N_{pe} >) \cdot G\left(x, \mu_0 + i \cdot \text{gain}, \sqrt{\sigma_0^2 + \sigma_p^2} \quad \right) \right]$$

(6.1)

6.2.3 Determination of the N_{pe}

The photoelectron spectra measured with the Sr-90 source do not show the perfect Poissonian shape of Eq. (6.1). The spectrum is modified by two main factors: (1) the energy loss of charged particles described by the asymmetric Landau curve; (2) the variations of the effective pathlength of the electrons through the fibre stack. We therefore determine the average number of photons based on the gain calibration described above.

The centre of gravity is a simple and robust method used for the determination of the average number of photoelectrons. In order to evaluate the

(a)

(b)

(c)
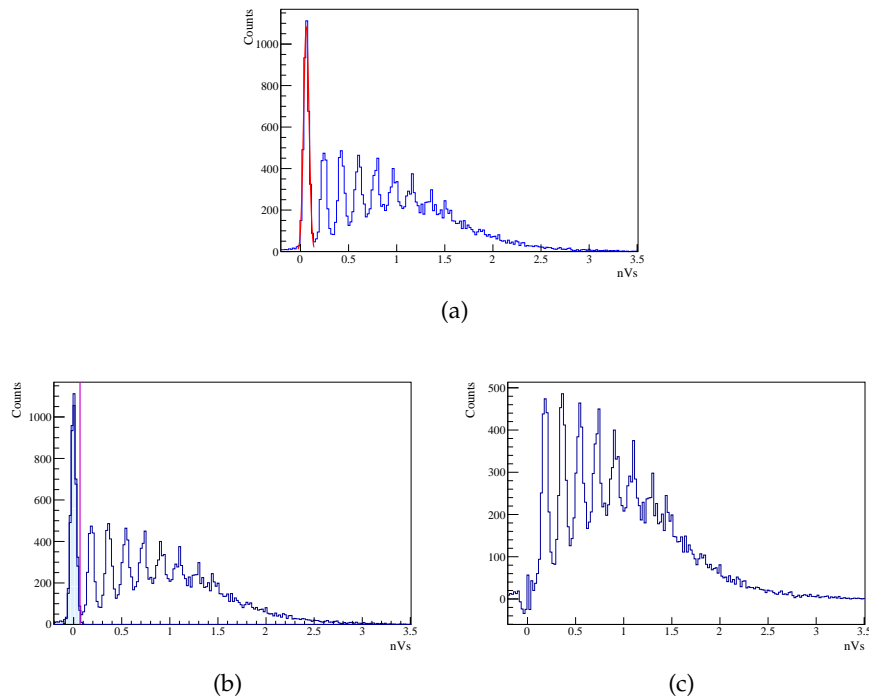
FIGURE 6.9: Measured data treated before applying the center of gravity method: (a) Gaussian fit which describes the pedestal distribution; (b) generated histogram from the Gaussian fit function with fixed parameters; (c) measured data after pedestal subtraction. The next step is to shift the distribution by the mean of the Gaussian.

N_{pe}, the pedestal peak (zero photon counts) is discarded, then the centre of gravity of the remaining distribution is calculated and divided by the charge gain obtained from the calibration fit. The pedestal peak is removed by first fitting a Gaussian to it, subsequently a histogram generated with the fitted parameters is subtracted from the measured distribution. Each of these steps is illustrated in Figure 6.9. Since the pedestal distribution mean value changes due to different measurement conditions, the (mean) (mean) (mean) (mean) (mean) (mean) (mean) (mean) (mean) signal distribution is shifted in the x-axis by the pedestal mean value. Eq. (6.2) summarizes the centre of gravity method applied to the signal (pedestal subtracted and shifted) distribution:

$$N_{pe} = \frac{\sum Q \cdot \text{Counts(Q)}}{\sum Counts(Q)} \cdot \frac{1}{\text{gain}} = \frac{M}{\text{gain}}, \qquad (6.2)$$

where M corresponds to the mean of the histogram (provided by ROOT).

A typical measurement is shown in Figure 6.10, which considers all the measured positions (90, 120, 150, 180, 210 and 240 cm) for a sample constituted of a stack of three fibres (SCSF-78). The light yield is determined by extrapolating a single exponential fit to distance 0 cm; at the given example,
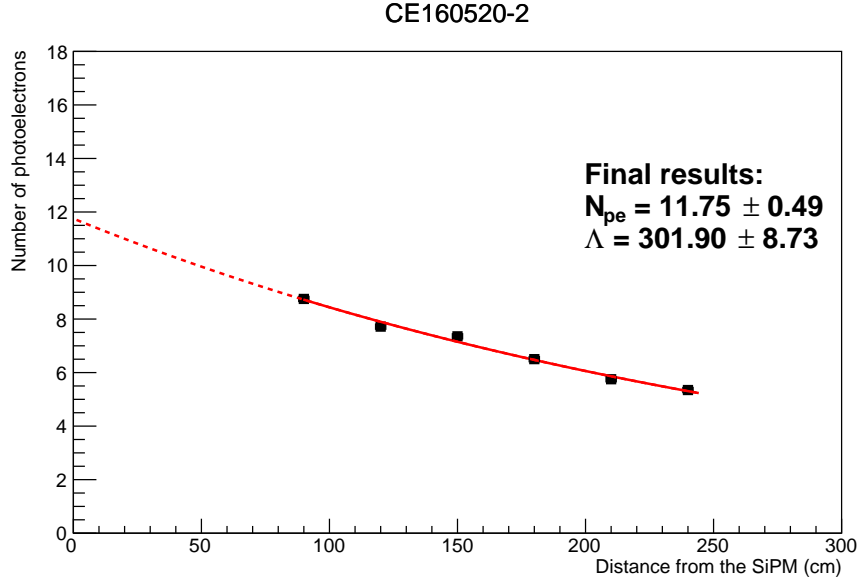
FIGURE 6.10: Light yield measurement of a set of three fibres (SCSF-78). The errors are considered but not visible.

11.75 pe are detected.

A typical measurement at a certain distance has about 20 000 events. The statistical uncertainty of the signal distribution is provided by ROOT and it is of the order of 1%. The systematic uncertainties were estimated by performing a series of repetitive measurements considering 1) the removal and re-positioning of the set of three fibres in the groove (procedure performed for every position measurement) and 2) removal followed by a rotation and re-introduction of the end-piece into the SiPM box (procedure performed once per sample; end-piece is fixed for the whole measurement). The former error is added in quadrature to the statistical error obtained directly from ROOT and was estimated to be 1%. The latter error is added linearly to the light yield error of the exponential fit and was found to be 2.5% (RMS). The uncertainties are summed up according to Eq. (6.3).

$$\sigma_{stat} = \sqrt{\left(\frac{\sigma_M}{\text{gain}}\right)^2 + \left(\frac{M \cdot \sigma_{\text{gain}}}{\text{gain}^2}\right)^2 + (0.01 \cdot N_{pe})^2} \; ;$$

$$\sigma_{sys} = 0.025 \cdot N_{pe} \; ;$$

$$\sigma_{N_{pe}} = \sigma_{stat} + \sigma_{sys} \; . \tag{6.3}$$

6.3 Diameter scan

6.3.1 Introduction

Local variations on the fibre diameter, denominated as bumps and necks, have an impact on the regularity of the winding pattern and hence the spatial resolution of the SciFi Tracker. Bumps and necks are diameter variations on small length scales (few millimeters or centimeters). Such diameter variations are observed very rarely (more than 99.9% of the fibre on a spool are free of defects). Also defects in the fibre cladding lead to light losses and inter-fibre cross talk. To inspect the diameter defects, a fibre diameter scanning machine was jointly built by Aachen and CERN [103]. It allows scanning at high throughput of the fibre diameter and the integrity of the cladding to cope with series production rate (150 km per week). We describe in this section the requirements, design principles, hardware and software implementations, in particular the bump shrinking method to remove large bumps, and the performance of CERN fibre scanner.

6.3.2 Requirements

More than 10 000 km of scintillating plastic fibres of 250 μm diameter are going to be used to construct the fibre mats. The production phase started on September 2016 and is foreseen to last about 18 months.

For the purpose of checking diameter defects at production rate, the main requirements of the fibre scanner are:

- Measurement of fibre diameter with micrometer resolution in steps of less than 0.1 mm;

- Verification of the integrity of the fibre cladding;

- Scan 150 km of fibre per week during series production;

- Tension and bending applied to the fibre must be well below the limits which can cause damage;

- Data must be recorded for later reference.

6.3.3 Design principles

The principle of operation of CERN fibre scanner is schematically illustrated in Fig. 6.11.

The fibre scanner consists of a source spool and target spool which are motor driven. The motor speed of target spool can be set to a constant value between 0 and 100 cm/s. The speed of source spool is regulated by a tensioner control in order to ensure a constant tension of about 50 cN during the rewinding process. Starting from the source spool the fibre passes
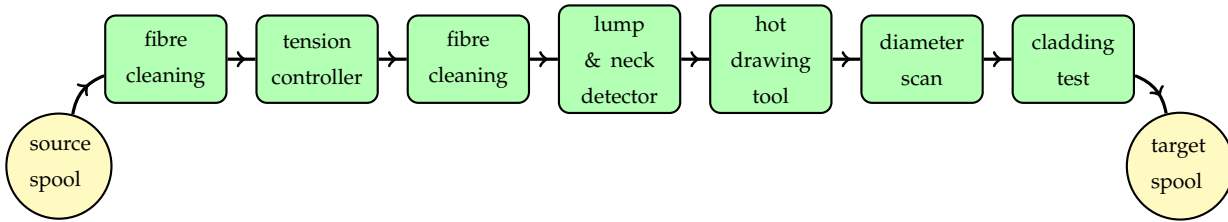
FIGURE 6.11: Flow diagram of CERN fibre scanner.

through a first cleaning set followed by the tension control unit and another cleaning device. The cleaning sections ensure that the fibre is free of dust and dirt when it enters the diameter measurement portion composed by the LN3015[4] detector, the hot drawing tool and the 2D-laser micrometer[5]. Then the fibre runs through a cladding quality test in order to check whether there is any excess of light leak. Directly before reaching the target spool, a small guiding pulley is synchronised with the rotation sped of the target spool to ensure the fibre is wound in flat layers. The distance the fibre travels in the machine is provided by a tachometer photo sensor installed with a metal plate with 60 holes on the target wheel, which gives 60 pulses per turn. The whole process of scanning a 12.5 km spool takes about 3h30 if there is no interruption during rewinding.

Cleaning devices

The first cleaning device (Figure 6.12(a)) is constituted by two fans with very thin carbon brushes as paddles. The fans turn in opposite directions so that the dust leaves the fibre in the downwards direction. In addition, the conductive and grounded carbon brushes shall avoid electrostatic charging up of fibre which would attract dust from environment. The other cleaning set (Figure 6.12(b)) is constituted by cleaning tissues class 1000 which are slightly wet by a solution of 1/3 of water and 2/3 of isopropyl alcohol. Initially the tissues were placed symmetrically, but the accumulation of dust in between was leading to occasional fibre breaking. The relative displacement of the tissue and the addition of the fans has solved this issue. During the rewinding process, the presence of dust in the most external layers of the spool was visible. In order to guarantee even more the cleanliness of the fibres, the machine operator uses an air blower in the first layers of the spool.

Lump & neck detector

The Lump and Neck Detector 3015 (LN3015) is a fast laser micrometer with programmable thresholds relative to the diameter average. The threshold

---

[4]Lump and Neck detector.
[5]Beta LaserMike AccuScan 5012.
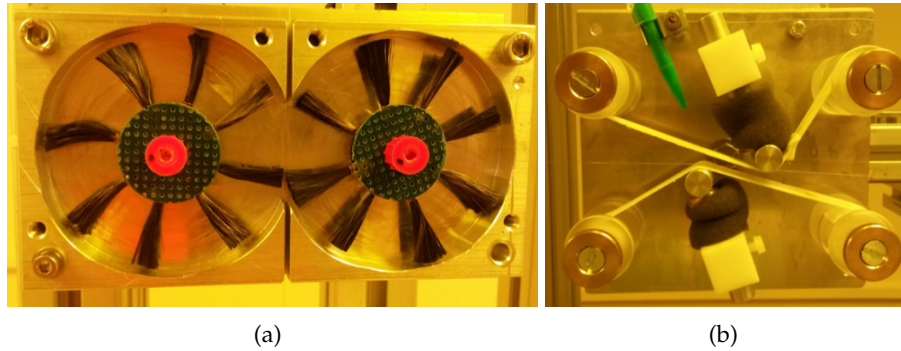
FIGURE 6.12: Fibre scanner cleaning sections: (a) shows two fans which turn in opposite directions so that the dust is thrown in the downwards direction. The paddles are made of very thin and delicate carbon brushes. (b) shows the cleaning tissues. The solution (water + alcohol) drops from the green plastic tube.

is set to $\pm$ 25 µm. It has an output signal which can be used to control the target motor speed when a defect is detected. This feature allows the machine to work in two different modes: 1) fast speed; 2) slow speed. At the fast speed mode, the target motor speed is set to $\approx 100\,\mathrm{cm/s}$. However, when a defect is detected by the LN detector, the target motor speed is automatically reduced to $\approx 15\,\mathrm{cm/s}$ for a period of 15 seconds, allowing the defect to be precisely measured by the *AccuScan* laser micrometer.

Diameter scan (AccuScan 5012)

The Beta Laser Mike AccuScan 5012 is 2D-laser scanner that measures the fibre diameter with a fast analog readout of 2400 Hz per axis with an accuracy of 0.5 µm. The analog signal signal in the range of ± 10 V is digitized by the National Instrument device NI-USB 6009.

Cladding box

The fibre passes through a dark box (see Figure 6.13) which is equipped with a UV-LED (390 nm) close to the entrance and a SiPM S13081-050CS(X) just before the exit. Both are mounted inside a integrating sphere in order to maximize fibre excitation and detection efficiency. The distance the fibre must travel from the excitation point and reach the SiPM is about 60 cm, so that light with short component attenuation length is negligible. The SiPM signal is sampled and read at a rate of 2400 Hz, together with the diameter measurements.

A hypothetical perfect fibre with a perfect outer surface, would not emit any light at a distance of 60 cm from the excitation point. Non trapped light emerging from the fibre is primarily due to an imperfect cladding-air
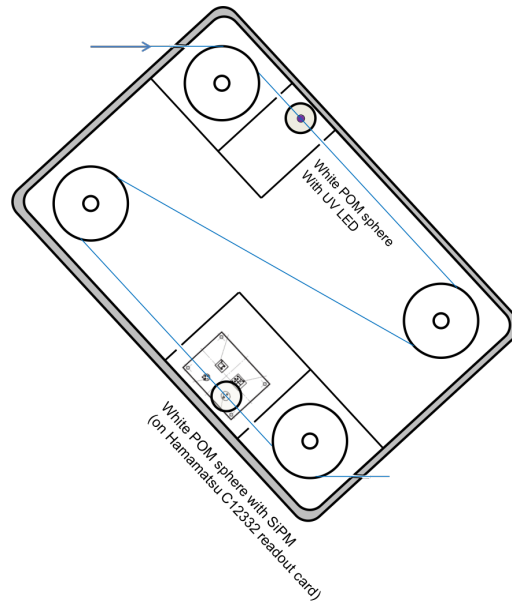
FIGURE 6.13: The cladding box. In order to guide the fibre, there are four sheaves ($\phi = 50\,\text{mm}$?) and two integrating spheres ($\phi = 40\,\text{mm}$). The UV-LED is placed just after the entrance of the box and the SiPM is $60\,\text{cm}$ distance apart close to the fibre exit.

interface. Surface roughness and defects such as scratches or little holes allow light which travels in the cladding to leave the fibre. A small amount of light escapes due to Rayleigh scattering in the fibre core. Long range variations of the fibre diameter are recognisable as a baseline modulation of the detected signal. The baseline can also be slightly affected by the ambient light level in the lab, as the fibre is exposed to it before and after entering into the cladding test box.

6.3.4 Diameter scan softwares

Online software: windingmanager

The online monitoring software is responsible for the readout of the sensors, the online plotting of measured parameters and the data storage for further analysis.It is composed by multiple threads in which each of them is responsible for a certain task, such as reading the sensor, handling the events, visualising the diameter measurements and writing the data. The software is based on the Qt framework for the user interface and build system; ROOT for the data analysis. Picture 6.14 shows the diameter measuremerent, SiPM signal from the cladding box and the counter information together with the correspondent length.

The CERN software is a modification of the original program used in Aachen. Due to the different hardware implementations at CERN, the data acquisition of the AccuScan AS 5012, the SiPM - for checking light leaks -

and also a counter - for the number of turns - is performed by a fast USB Input Output Card (NI-USB6009). A new single thread `NIUSB6009Thread.cpp` was developed in order to readout this device.

Another software change takes into account the fact that more than 99.99% of the fibre in a spool is defect free. The data is written at two different rates according to the machine speed: 1) if speed $\leq 20\,\mathrm{cm/s}$, data is stored at a rate of 2400 Hz; 2) if speed exceeds $20\,\mathrm{cm/s}$, the rate is reduced to 240 Hz (only 1/10 of the data is saved). In other words, on the first case, when the LN points out a fibre defect, the information about the fibre is saved at the maximum rate. On the other hand, when the fibre has no defects, the data is partially saved.

A last important modification is related to the output file type. Originally, the data was saved in text file format and one spool would deliver a Gb file size output. The data is stored in ROOT files as a TTree object, where each branch corresponds to a parameter, such as the x and y-axis diameters and SiPM output signal. Currently, a typical file size is a few hundred Mb.

More information about the online software can be found in [103].

Offline software: bump finder

The main purpose of the offline software is to automatically identify all the bumps and necks of a given fibre spool and, then, provide to the winding centers a list containing the defects' position and (maximum or minimum) diameter. Any consistent diameter variation which is above $300\,\mathrm{\mu m}$ or below $200\,\mathrm{\mu m}$ is considered as a defect. Fluctuations of the diameter can occur, for instance, due to spurious measurements, vibrations of the fibre and presence of dust or cleaning solution, and must be not be mis-identified as a bump or neck.

As a first step, the algorithm searches for diameter variations which are larger than $295\,\mathrm{\mu m}$ (or less than $225\,\mathrm{\mu m}$). The AccuScan laser micrometer provides the diameter in 2-orthogonal axis denominated as x and y-axis. The found entry is added to a list if it is above $295\,\mathrm{\mu m}$ (or below $225\,\mathrm{\mu m}$) in either axis. To eliminate entries which correspond to a same defect, we select only entries which have at least time difference of 2 seconds (or $30\,\mathrm{cm}$ case the machine is running with slow speed). Then the algorithm checks for each bump (neck) defect if the maximum average of any 20 (120) points in sequence, also denominated as boxcar averaging, is larger than $260\,\mathrm{\mu m}$ (less than $230\,\mathrm{\mu m}$), to distinguish real defects from fluctuations. A defect is identified as a bump or a neck after a combination of boxcar averaging. The difference in the number of points considered for the boxcar averaging between bump and neck was obtained by observing that necks have a longer length than bumps. As output, a set of files are generated:
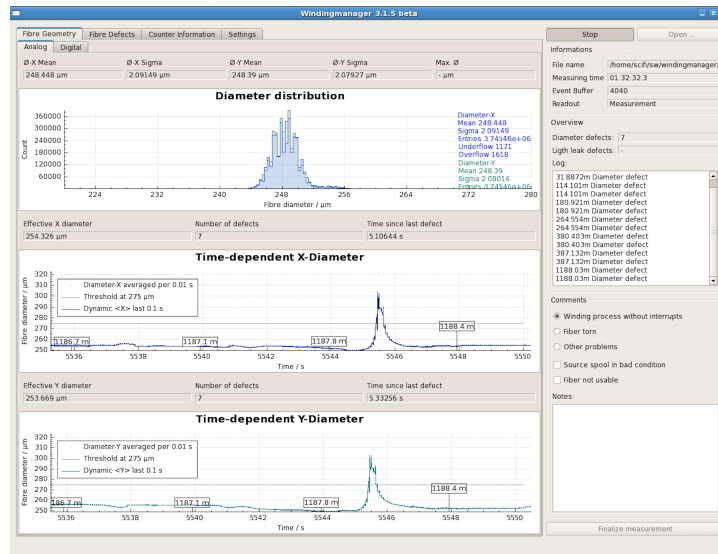
(a)
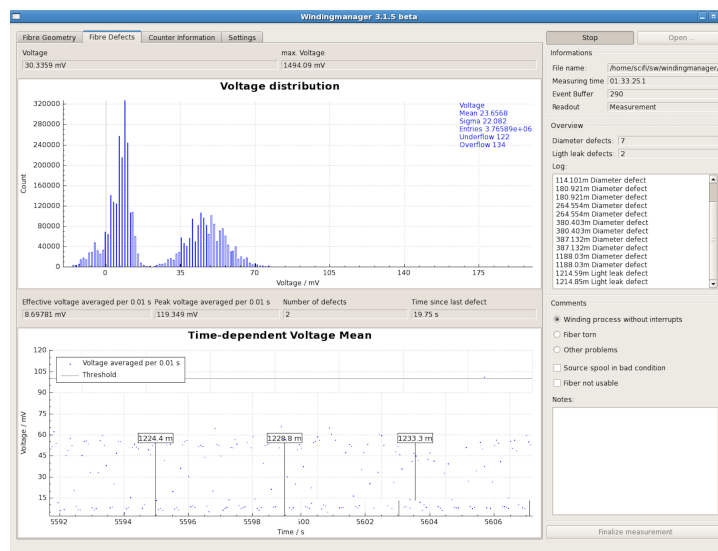
(b)

FIGURE 6.14: Printscreens of the online software. (a) shows a histogram containing all diameter measurments (but separated by axis) and plots of the diameter of both axis as a funtion of time just after a bump was scanned. (b) indicates the response of the SiPM in the cladding box when the fibre is excited by the UV-LED. Since the LED is blinking, in the histogram, the low (high) intensity peak corresponds to the background noise (signal). Also, there is the plot of the SiPM voltage as function of time which the blinking pattern can be easily spotted. Also, on the right column, there is the position information of possible diameter and cladding defects on the fibre, which is useful to compare with the procucers bump list during the scanning process.

(a)

(b)

(c)

(d)
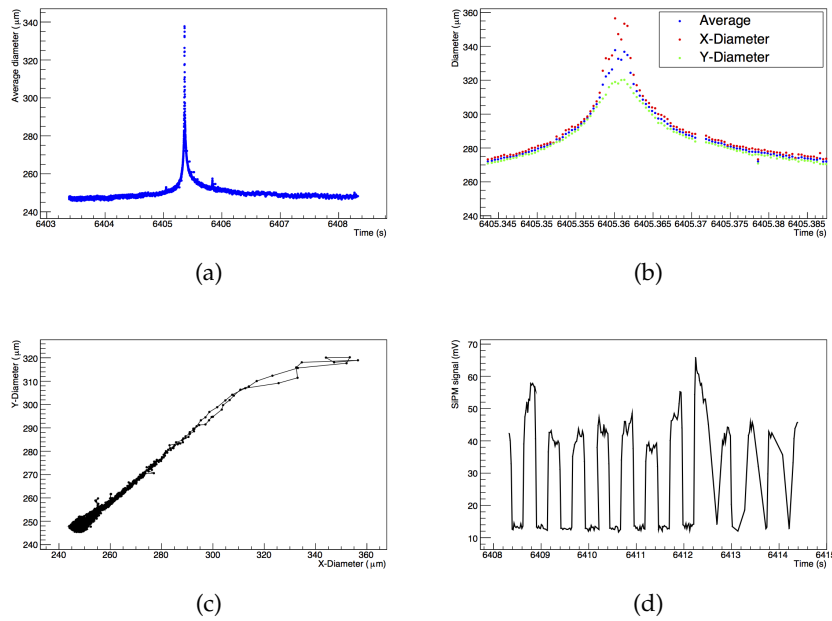
FIGURE 6.15: Plots generated for defect number 14 of spool CE160817-8: (a) the average diameter as a function of time; (b) the diameter of both axis together with the average diameter as a function of time (zoom); (c) the correlation between the diameter measured in both axis; (d) the light leak as a function of time.

- a root file containing, for each defect, diameter and light leak plots as a function of time;

- a plot of the diameter as function of the distance, including the defects measured by Kuraray;

- a plot of the diameter as function of the time;

- plots with the light leak behavior as a function of distance and time;

- a txt file with the position information and maximum or minimum diameter of each defect;

Most of the bumps are correctly identified by the bumpfinder software, but a last verification is still necessary before sending the file to the winding centers. Figures 6.15 and 6.16 are examples of identified bumps by the offline softawre, while Figure 6.17 indicates the peak dimater measurement of all idenfied defects along the length of a spool.

6.3.5 Bump shrinking method

Experience has shown that fibre defects with a diameter larger than 350 μm can cause a disarrangement over extended regions in the winding pattern of fibre mats which may affect hit efficiency and spatial resolution. Initially,

(a)

(b)

(c)

(d)
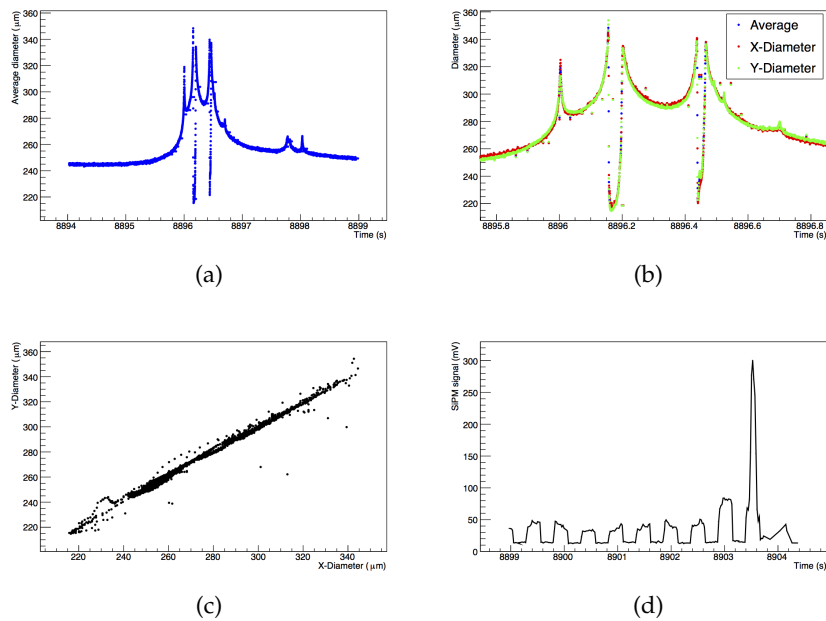
FIGURE 6.16: Plots generated for defect number 17 of spool CE160817-8, which is a shrunk bump: (a) the average diameter as a function of time; (b) the diameter of both axis together with the average diameter as a function of time (zoom); (c) the correlation between the diameter measured in both axis; (d) the light leak as a function of time.
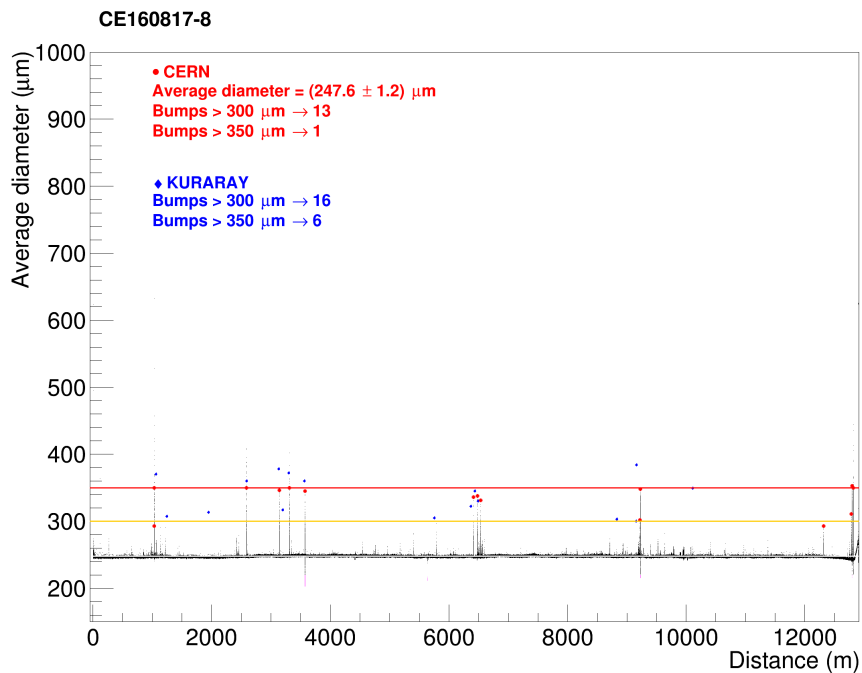
FIGURE 6.17: Diameter measurement as a function of the spool length (from both CERN and Kuraray).

the winding centers were responsible for removing the fibre defects with a diameter exceeding 350 μm. A tolerance limit of 8 bumps per spool was negotiated with the fibre producer to avoid compromising fibre mat production and the need of additional manpower resources.[6] However, such intervention is labour-intensive and would take 10-15 min to be performed.

In addition the producer has difficulties to deliver spools free of bumps larger than 350 μm. Under those circumstances, we developed a method to reduce the diameter of large bumps to a diameter of 350 μm by pulling the fibre through a hot conical tool. The method has been proven to work reliably for bumps up to 500 μm diameter. For bumps which this method does not work, a cut and glue procedure is necessary. The motivation to integrate those processes in the fibre diameter scanner at CERN is to minimise bump related issues at the winding centres of the SciFi project.

Bumps can be produced due to 1) presence of a extraneous particle (a piece of glass, cotton) in the core and/or cladding and 2) non-uniformities in the base materials of the fibre. The first source of bumps has been reduced by the fibre producer by taking effective measures at the various process steps. The second source has been addressed by attempts to obtain ingredients of higher purity, but could not be fully eliminated.

The drawing tool

First, the method was demonstrated to work with the use of a metal plate containing a set of conical holes with different graded diameters. Such plates are used in the manufacturing of jewelry to adjust e.g. the diameter of gold wires. The tests were performed with fibre sections, each containing a 350-450 μm diameter bump, which allowed us to investigate the appropriate temperature and tension to shrink them without causing any rupture.

The next step consisted of purchasing a precise drawing tool which could be integrated in the fibre scanner. The geometrical shape of such a drawing tool can be seen in Figure 6.18. The inner part is made of tungsten carbide in which the bearing length L3 is of the order of 1 mm and the smallest inner diameter of the conical hole d1 is 350 μm.

As shown in Figure 6.19, the bump shrinking set-up [117, 118], consisting of the hot drawing tool followed by a set of three sheaves with 10 cm-diameter, is placed between the LN detector and the AccuScan Laser Micrometer. When the LN detects a defect with a diameter variation of more than ±25 μm, the fibre speed is reduced from the nominal speed of 100 cm/ s

---

[6]To wind a standard 6-layer fibre mat takes 6 hours, considering no interruption for any fibre repairing, plus 20-36 hours for curing the glue. In this process, 20 min is necessary to fill up each layer and another 20 min to apply glue in-between layers. Extra time is also needed for general preparation of the winding procedure.
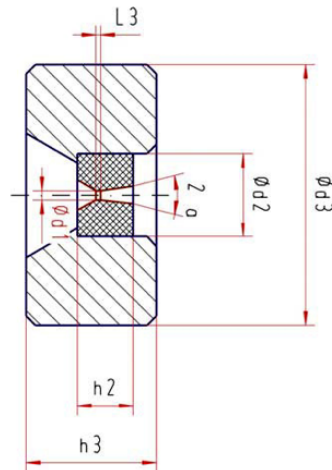
FIGURE 6.18: The drawing tool. The entrance of the tool is
located on the right and the exit on the left. The length L3 is
of the order of $1\,\mathrm{mm}$ and d1 $=350\,\mu\mathrm{m}$.

to $15\,\mathrm{cm/s}$. If a bump with diameter larger than $350\,\mu\mathrm{m}$ gets stuck in the
tool, the pivoting arm lifts and opens an electrical contact which triggers
the machine "bump shrinking mode". Both the target motor and the guid-
ing pulley (to ensure the correct winding pattern of the spool) are abruptly
stopped. The lifted arm tensions the fibre with 100 cN force and the un-
winding motor acts accordingly to maintain a tension of 50 cN upstream of
the drawing tool. The bump is locally heated and if it has sufficiently soft-
ened, the fibre can creep through the tool. Consequently, as soon as the arm
lowers down, the circuit is closed and the motors restart to run at $15\,\mathrm{cm/s}$.
The "bump shrinking mode" prevails, so that the winding process is inter-
rupted until the bump is shrunk over its full length. A successful bump
shrinking process duration can last from fractions of a second up till few
tenths of seconds depending on the shape, length and roundness of the
bump.

Based on previous tests, setting the drawing tool temperature to $100\,^\circ\mathrm{C}$
lead to successful bump shrinking results. Lower temperatures were not
sufficient to soften the fibre in one hand, while on the other hand higher
temperatures caused excessive damage to the fibre geometry. The drawing
tool temperature is regulated by a PI controller, which allows to set a set-
point and a ramp function slope. To avoid overshoot when the temperature
of the drawing tool is raised from ambient to $100\,^\circ\mathrm{C}$, the slope is set to 25 K
per minute.
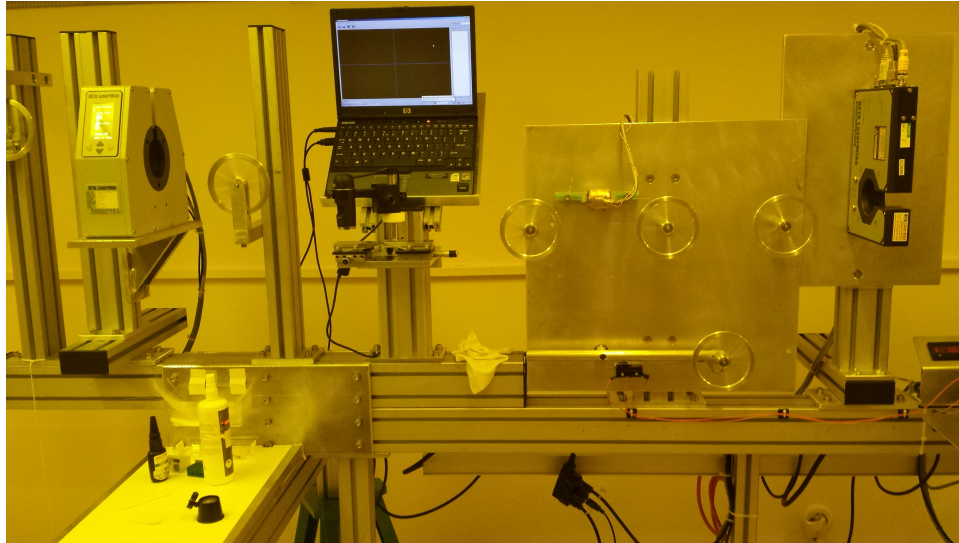
FIGURE 6.19: Bump shrinking set-up integrated to the fibre scanner machine.
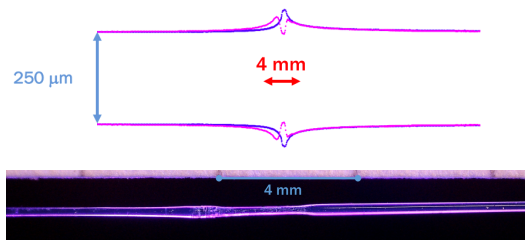
FIGURE 6.20: Above: fibre segment with a bump, measured by the AccuScan, before (in blue) and after (in magenta) passing through the bump shrinker. Below: a microscope picture of the same fibre section after the bump was shrunk. Note that the plot and the picture have different length scales. The bump extends over a length of the order of few milimeters.

Results I: bump shrinking effect

Figures 6.20 and 6.21 illustrate the effectiveness of the bump shrinking method. The bump profile is deformed in such a way that a neck is created at the position where the fibre had previously the bump peak. The fibre also seems to elongate by few milimeters so that its total volume remains unchanged. In the plot, the diameter measurements were obtained with the laser micrometer before and after the bump shrinker and it is assumed that the fibre is fully symmetric. Besides, microscopic pictures of the shrunk bump were taken, in which the fibre segment was excited by a UV-light (390 nm).
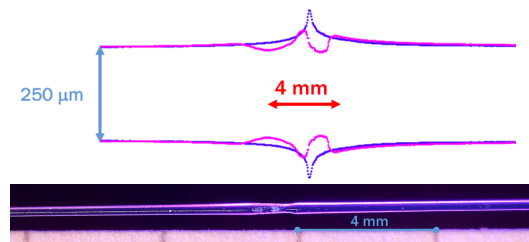
FIGURE 6.21: Another fibre segment which was measured before and after bump shrinking method.

(a)   (b)
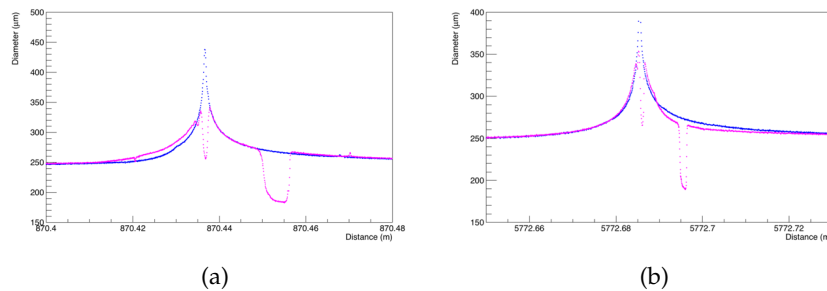
FIGURE 6.22: Fibre diameter profile measured with the laser micrometer before (in blue) and after (in magenta) bump shrinking with two tools in sequence. In both (a) and (b) measured sections, a neck with a diameter less than 200 μm was produced.

Results II: single tool vs. double tool

To cope with bumps with a diameter larger than 450 μm, which represent 10-20% of the defects in a 12.5 km spool, the original idea consisted on installing two drawing tools in sequence mounted in a common heating element. The fibre would first pass through a drawing tool with an inner diameter, d1, 450 μm; the second tool would have d1 = 350 μm. The drawback of this proposal is that it may cause more damage to the fibre. When a bump gets stuck in one of the tools, the fibre section, which is inside the other tool, may be excessively heated producing a neck in a originally defect-free segment, as shown in Figure 6.22.

Results III: light transmission across a shrunk bump

The transmission loss of a bump, which was treated by the bump shrinking method, was measured through attenuation length measurements. We selected 3 fibre samples with a shrunk bump which had a peak diameter (before shrinking) above 350 μm. Figure 6.23 shows the measured photocurrent as a function of the excitation distance for the three samples. To evaluate the transmission loss, two exponential fits were performed: 1) from 100 cm to shrunk bump position (green points); 2) from shrunk bump position till the fibre end (red points). The blue points are not considered in

(a)

(b)

(c)
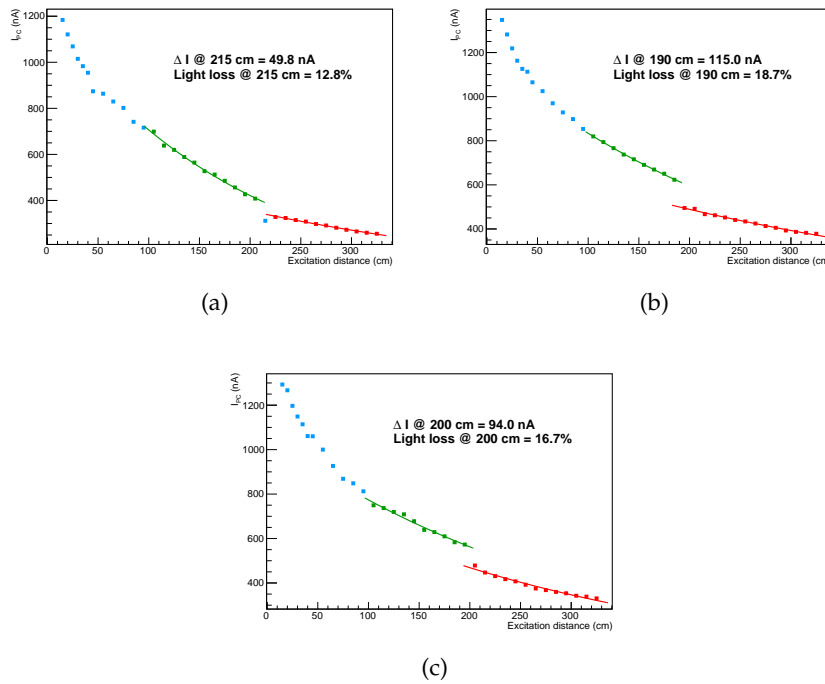
FIGURE 6.23: Light loss across a shrunk bump. Each plot shows the photocurrent as a function of the excitation distance of a fibre sample which contained a shrunk bump.

the fit. The intensity drop ΔI, indicated in the plots, is the difference of the photocurrent values at the shrunk bump position obtained from the two fitted curves. The light leaks across a shrunk bump were observed to be consistently below 20%, which corresponds to a light transmission above 80%. In other words, light transportation mechanism of the fibre is largely unaffected by the bump shrinking method.

Results IV: effect of hot drawing tool on the fibre

A crucial test for the applicability of the hot drawing method consisted in verifying that it would not deteriorate the defect-free zones of a fibre, which constitute its vast majority. It is known that the transparency of a fibre degrades at temperatures higher than $60\,°C$ due to oxidation of the polystyrene. Because of that, the original plan of the bump shrinking method consisted of, once the bump was stuck in the tool, to increase the temperature to $100\,°C$ and to reduce it to ambient temperature after the bump was removed. However, temperature rise and decrease would take about 10 minutes per intervention, leading to some delay in the scanning process. Therefore, standard quality tests were performed using good standard fibres after passing through the hot drawing tool.

For inspecting the attenuation length, the following $3\,m$ long samples from spool lot number CE160229-1 were prepared:
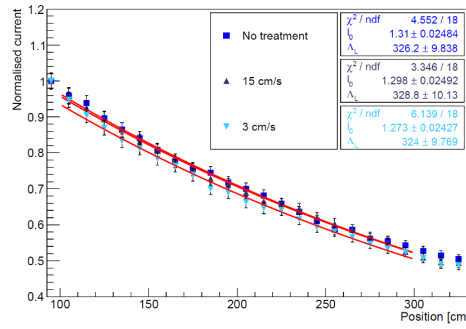
FIGURE 6.24: Averaged light attenuation of the three considered sets: untreated fibres and with drawing speeds of 3 and 15 cm/s. As usual, the attenuation length Λ_L is determined by a single exponential fit to the data from 100 to 300 cm distance from the PIN-diode. All three sets show identical values around 325 cm.

- Three samples were cut off and measured directly after being taken from the spool;

- Three samples were obtained from a fibre piece which was pulled through the drawing tool kept at $100\,^{\circ}$C with a peed of 15 cm/s;

- Three samples were taken from a fibre section which was treated by the hot drawing tool at $100\,^{\circ}$C with a speed of 3 cm/s.

The plots of the attenuation length are shown in Figure 6.24. The attenuation lengths for all the considered samples are comparable considering the typical uncertainty of 10%. The slower drawing speed of 3 cm/s was chosen in order to check if the fibre could suffer any damage caused by the temperature excess; no effect on the attenuation length was observed.

6.3.6 Cut and glue procedure

Experience has shown that bump shrinking technique successfully works 80-90% of the cases (considering bumps with a maximum diameter of 450-500 μm). Nevertheless, there are three bump categories in which this procedure is not going to work:

- Bumps larger than 450-500 μm: the bump can be stuck in the tool for several seconds.

- Long bumps: a fibre section with a bump that extends over a length of more than few millimeters with a peak diameter above 350 μm requires a large quantity of material to be deformed, preventing the progress of the shrinking method.

- Filled bumps: bumps composed of solid particles, such as a small piece of glass, cannot be shrunk.

(a)   (b)   (c)
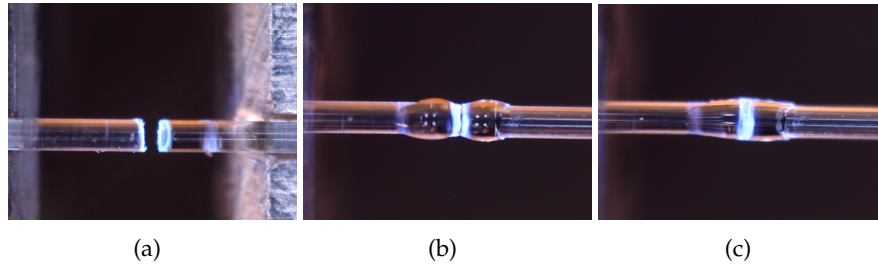
FIGURE 6.25: Microscopic images of the gluing procedure:
(a) fibre alignment, (b) small a amount of glue applied in
both fibre ends and (c) fibre ends are put into contact. The
slight glue excess leads to a formation of a sleeve around
the fibre, which reinforces the joint but, its diameter should
not exceed the 350 μm limit.
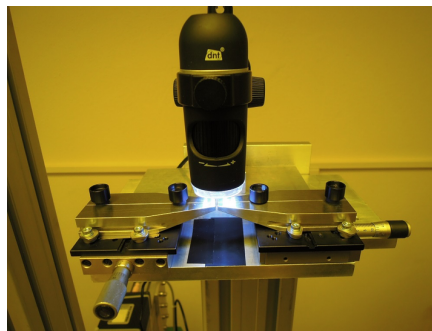
FIGURE 6.26: The precise positioning table and the USB-
microscope used to perform the cut&glue procedure.

In either case, the fibre remains stuck in the tool for several tens of sec-
onds, which may lead to an eventual rupture and manual intervention is
necessary. Under those circumstances, a cut&glue procedure based on a
fast UV curing glue was developed. The bumpy section is manually re-
moved (with scissors) after the machine is put on hold. The temperature is
set to $60\,°C$ to avoid damaging the fibre. The fibre ends are positioned in a 2
stage xy table which allows the fibre ends to be precisely aligned (see Figure
6.26). A USB microscope is used to check for the quality of the fibre cut and
the amount of glue applied. Then, we use a 300 mW UV light source for
a period of 10-15 s within about $1\,cm$ distance. Considering a well trained
operator, the cut&glue procedure can takes about 10 - 15 min.

6.4 Decay time

The decay time of scintillating fibres is due to the decay of the excited states
in the scintillators' bulk material and wavelength shifting dye, which dom-
inates the distribution. In particular, for the SciFi Tracker, simulation shows
that the minimum propagation time for a photon, which is travelling within
a standard fibre core parallel to its axis, is about 5 ns per 1 m fibre length [98].
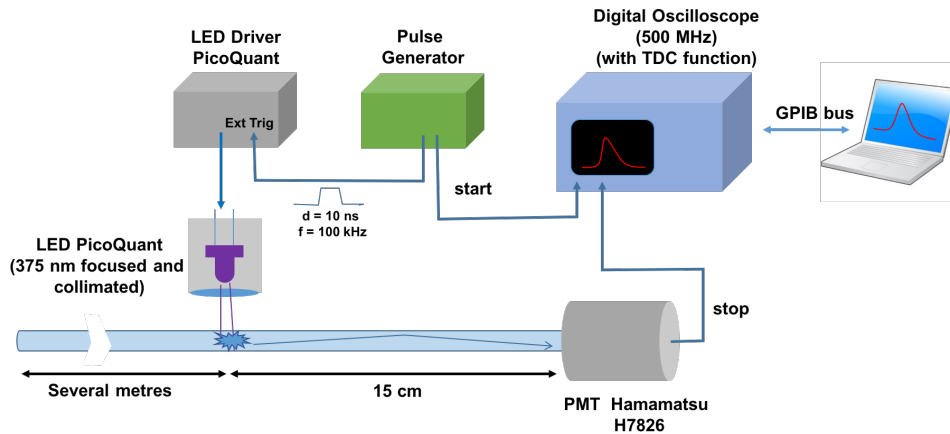
FIGURE 6.27: Set-up for measuring decay time of scintillating fibres.

If this signal propagates in the mirror direction, it travels 4 m and takes 20 ns to reach the SiPMs. Considering that the electronics affect the time shape and broadens its width, we are in the limit to detect particles at the bunch crossing rate of LHC. To measure the decay time constant of the scintillating fibres is interesting because (i) guarantees they are fast enough for the desired application (ii) can indicate the presence of pollution and material anomalies, in particular of the wavelength shifting dye.

6.4.1 Experimental set-up

An experimental set-up was conceived at CERN to precisely measure the decay time constant (tau) of scintillating fibres. The decay time of SCSF-78 fibres has been measured for the first time.

To measure the decay time of a scintillating fibre, a very fast pulsed light generated by an UV-LED[7] was used for exciting one fibre at a distance of 10-15 cm from the readout photomultiplier. Pulse waves produced by a pulse generator trigger the UV-light emission and also start each single measurement, while the signal of the PMT stops the measurement. To ensure a precise time interval measurement, the light pulses from the LED were attenuated to the single-photon level. These signals are read by a digital oscilloscope which is directly connected to the PC. Figure 6.27 illustrates the set-up.

The overall time jitter of the detecting system, which accounts for the PMT, cabling and electronic devices transit time, was evaluated by pointing the UV-LED directly to the PMT. The measured time distribution was fitted with a Gaussian with a width of about 500 ps (see Figure 6.28). There is however a non-Gaussian tail of unknown origin (estimated to be 10%) and also a second peak (1%), 6 ns delayed, caused by PMT afterpulsing.

---

[7] PicoQuant PLS370: $\lambda = 375$ nm, FWMH=518 ps, $\sigma = 220$ ns.
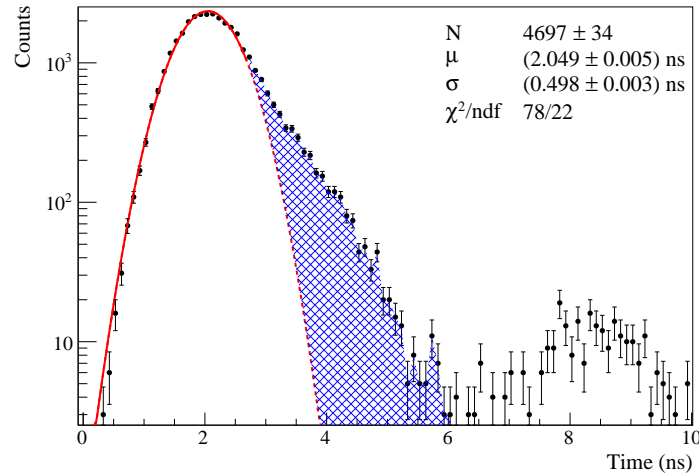
FIGURE 6.28: The transit time jitter of the overall detecting system. The black points are the measured data, the (red) solid line is the fitted Gaussian, the (red) dashed line is the extrapolation of the fitted curve and the filled blue region shows the non-Gaussian tail. Besides PMT afterpulses can be found on a second peak (with about 1% of the intensity of the main peak) which has a 6 ns delay.

6.4.2 Decay time constant measurement

The data is well described by an exponential function, which represents the decay time of the scintillation light, convoluted with a Gaussian, accounting for all the jitters and time fluctuations in the set-up:

$$f(t; \tau, \mu, \sigma) = \frac{1}{2\tau} e^{\frac{1}{2\tau}(2\mu + \frac{\sigma^2}{\tau} + 2t)} \operatorname{erfc}\left(\frac{\mu + \frac{\sigma^2}{\tau} - t}{\sqrt{2}\sigma}\right), \qquad (6.4)$$

where the erfc is the complementary error function.

Figure 6.29 shows the measured and fitted decay time distribution for a SCSF-78 fibre. The result is found to be $\tau = (2.4)$ ns with a Gaussian width of (498 ± 3) ps. In [119], the producer specifies for SCSF-78 scintillating fibres a decay time of 2.8 ns, which is 13% higher than the measured value. This difference is explained by two reasons: 1) their measurement represents the decay time of the second fluorescent dye; 2) it is not based on a fibre (information obtained via direct communication with Kuraray Co. Ltd.).
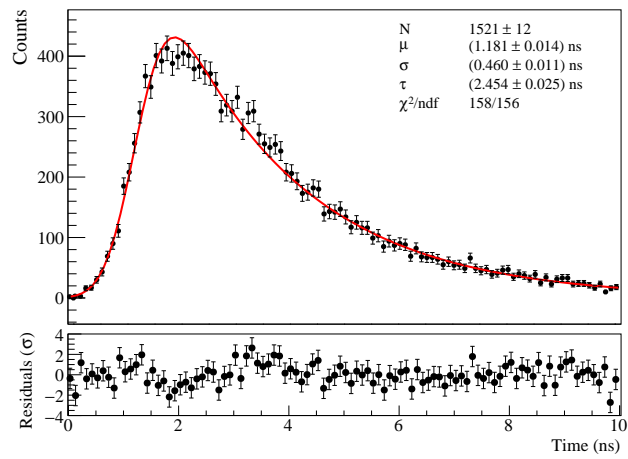
FIGURE 6.29: Decay time from a SCSF-78 standard scintillating fibre.

Chapter 7

New class of scintillating fibres

Since late 1980s, plastic scintillating fibres have been used either as active elements of particle detectors or active targets of an experiment. In 1990, the advent of the double-cladding method [120] enhanced the light trapping efficiency of the fibres. Subsequently, the development of radiation hard dyes, such as 3HF [121], has allowed detectors to be operated in radiation harsh environments.

Recent developments in the synthesis of new organic scintillators denominated as nanostructured organosilicon luminophores (NOLs) [122, 123] are proposed by a Russian group from Enikolopov Institute of Synthetic Polymeric Materials of the Russian Academy of Sciences. NOLs seem to be a promising approach leading to very short decay times and high light yield in several applications.

This chapter starts with a short introduction to this new class of scintillators, followed by a discussion of the performance of NOL based fibres (developed and produced along 2014-2016) on attenuation length, light yield and decay time.

7.1 NOL material

As mentioned in section 5.1, conventional plastic matrices for scintillators are admixed with an activator molecules (1% in weight) and wavelength shifting dyes (typically 0.1% in weight) which are independently and randomly distributed. When an ionizing particle traverses the scintillating material, the deposited energy is first converted to UV-light, which lies in the opaque region of the fibre base material (polystyrene). The wavelength shifting dye shifts the final light emission to the more transparent polystyrene region (> 400 nm) leading to higher attenuation length. However, the efficiency of these multi-step process is not very high.

Alternatively, Nanostructured Organosilicon Luminophores (NOLs) present a dendritic structure in which activator and wavelength shifters are coupled via silicon atoms (see Figure 7.1), providing a close proximity (of the

order of 1-2 nm) between the dyes. As a result, it is expected an improvement of the overall efficiency of the energy conversion process by profiting from non-radiative Förster resonance energy transfer[1]. They combine the best properties of organic luminophores and inorganic quantum dots[2]: high absorption cross-section, excellent photoluminescence quantum yield, fast luminescence decay time, good processability and low toxicity [122]. A convenient choice of pairs of donor and acceptor organic luminophores allows to design and synthesize different types of NOLs, absorbing from UV to visible region and emitting at the desired wavelengths from 390 to 650 nm which is determined by the specif applications. In addition, NOLs are compatible with a range of optical polymers such as polystyrene and PMMA, which promote the development of high-performance plastic scintillators, spectral shifting sheets. NOLs have already been employed in several applications such as in noble gas filled detectors [126], pure CsI crystal scintillator [127], organic light emitting diodes [128] and in thin film photovoltaics [129].

Reference [122] claims that plastic scintillators based on NOLs are 50% more efficient and 40% faster than conventional ones. This outcome was obtained by measuring light yield and decay time of a round plates made of different NOL samples and also of standard scintillators (UPS89 from Amcrys-H, Ukraine) with 25 mm diameter and 0.2 mm height while being excited by α-particle source from ^{239}Pu.

7.1.1   Production of NOL based fibres

CERN, LumInnoTech LLC[3] [131] and Kuraray Co. Ltd. started to collaborate on the development of NOL fibres by the of end 2014. Since then (until end 2016) a total of six campaigns were promoted leading to the production

---

[1]The non-radiative Förster Resonant Energy Transfer (FRET) refers to an energy transfer mechanism between a donor (D) molecule, residing in an excited state, and an acceptor (A) molecule in its ground state. In FRET, the energy transfer does not occur via the emission or re-absorption of a photon; it is due to a dipole-dipole interaction. Förster correctly (giving a full quantum description) derived the efficiency of energy transfer between D and A as proportional to R-6, where R is the modulus of the distance between donor and acceptor. When the rate of the energy transfer is equal to the rate of fluorescence emission, typical R values are of the order of few nanometers. Note that van der Walls interactions have a very similar approach (quantum mechanical second order perturbation theory) as FRET, but the first both donor and acceptor are in ground state. FRET offers a description of the high efficiency energy transfer in photosynthesis [124].

[2]Quantum dots are semiconductor particles with a diameter size ranging from one nanometer to a few dozen nanometers. Depending of the quantum dot characteristics, such as size, shape and material, it will emit light at an specific frequency when excited by electricity or light. However they are found to be toxic.[125]

[3]LumInnoTech LLC [131] is a small start-up company with the purpose of research and development of materials for applications in high energy physics. It was founded by a subset of the authors in 2012 and it is responsible for the commercialisation of NOL prototype dyes.
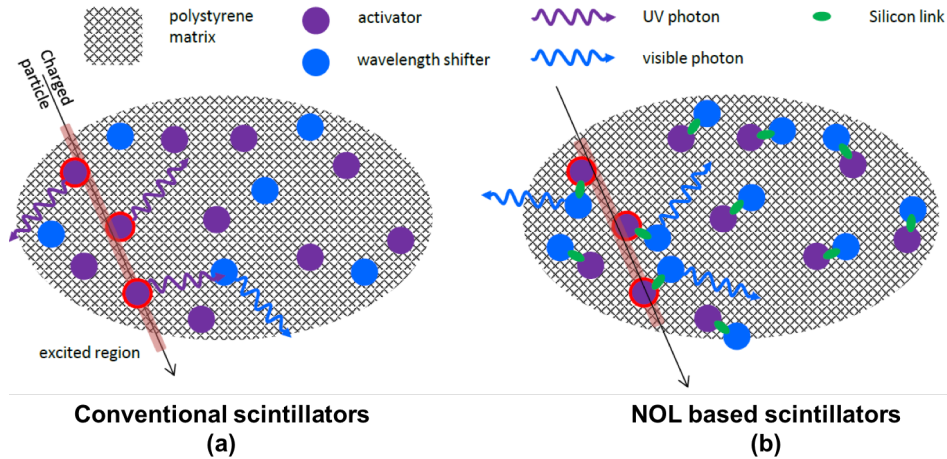
FIGURE 7.1: Standard plastic scintillators versus NOL based scintillators. (a) shows a standard scintillators where activator and wavelength shifting dyes are independently and randomly distributed in the polystyrene matrix. (b) illustrates the NOL molecules structures, where the activator and the wavelength shifter are connected via silicon atoms.

Source: [130].

of 19 NOL fibre samples with 250 μm diameter and double cladding produced by Kuraray Co. Ltd. These samples were produced in consonance with the availability of the supplier, due to the tight schedule reserved for the SciFi in the fabrication of more than 10 000 km of standard SCSF-78 fibres.

Table 7.1 summarises the information on the NOL based fibre samples produced throughout these iterations along 2015 and 2016. The total luminophore concentration and relative NOL content[4] are provided by direct communication with LumInnoTech LLC. The activator types (A or B) are undisclosed by LumInnoTech LLC. Figures 7.5 and 7.6 show the absorption and emission spectra of blue and green NOLs, respectively, chosen as luminophores for the fibre samples. In addition to the SCSF-78 standard fibres, Kuraray also fabricated 250 μm-diameter 3HF fibres with an emission peak at 530 nm [119], which serve as reference for the all performance measurements (see Table 7.2).

---

[4]The relative NOL content is considered with respect to the acceptor (or second dye) concentration in the NOL sample L121, which corresponds to 250-750 ppm of NOL. In other words, one unit of relative NOL content is equivalent to the NOL concentration applied in L121.

(a)

(b)

(c)

(d)
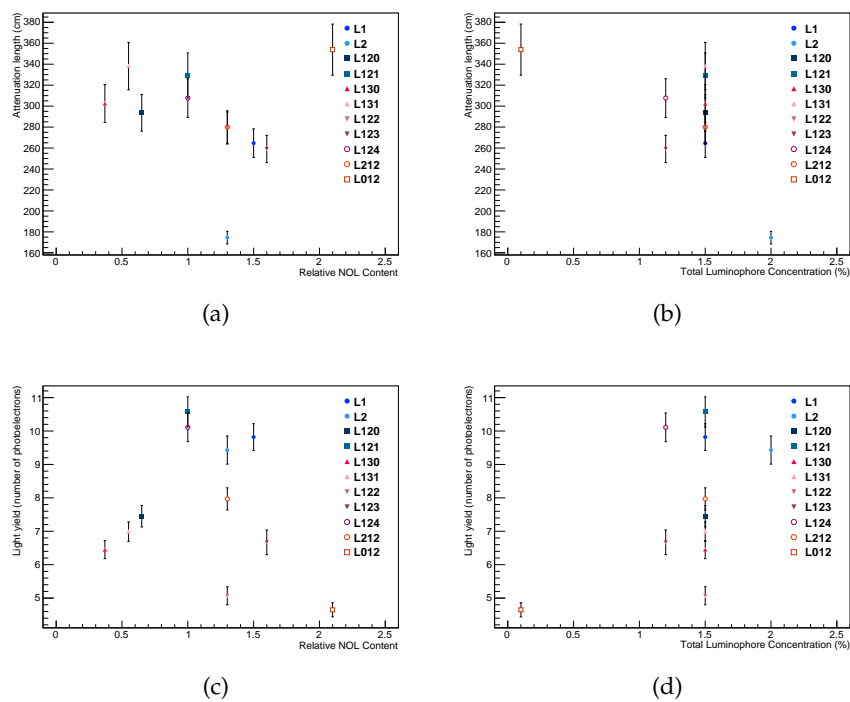
FIGURE 7.2: Influence of NOL dye on the performance of the blue fibres: (a) attenuation length versus relative NOL content; (b) attenuation length versus total luminophore concentration; (c) light yield versus relative NOL content; (d) light yield versus total luminophore concentration.
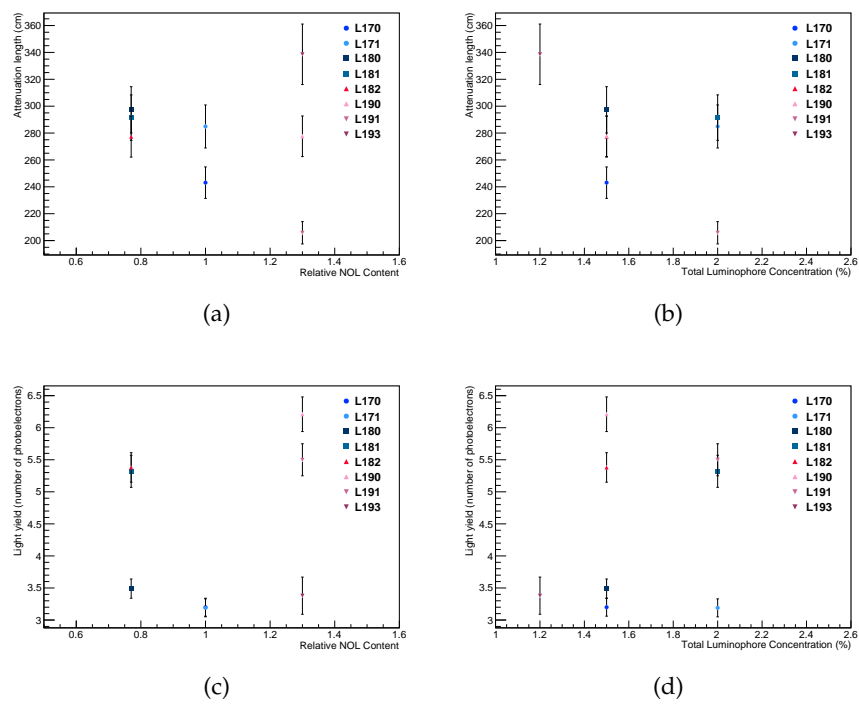
FIGURE 7.3: Influence of NOL dye on the performance of the green fibres: (a) attenuation length versus relative NOL content; (b) attenuation length versus total luminophore concentration; (c) light yield versus relative NOL content; (d) light yield versus total luminophore concentration.

Interaction (arrival at CERN)	Sample name	NOL type	Activator type	Total Luminophore Concentration (%)	Relative NOL Content
1st (JAN 2015)	L1	NOL1	A	1.5	1.5
	L2	NOL2	B	2.0	1.3
2nd (MAY 2015)	L120	NOL2	A	1.5	0.65
	L121	NOL2	A	1.5	1.0
	L130	NOL3	A	1.5	0.37
	L131	NOL3	A	1.5	0.55
3rd (SEP 2015)	L122	NOL2	A	1.5	1.3
	L123	NOL2	A	1.2	1.6
4th (NOV 2015)	L170	NOL17		1.5	1.0
	L171	NOL17		2.0	1.0
	L180	NOL18		1.5	0.77
	L181	NOL18		2.0	0.77
5th (MAR 2016)	L182	NOL18		1.5	0.77
	L190	NOL19		1.5	1.3
	L191	NOL19		2.0	1.3
6th (AGO 2016)	L193	NOL19		1.2	1.3
	L124	NOL2		1.2	1.0
	L212	NOL2		1.5	1.3
	L012	NOL2		0.1	2.1

TABLE 7.1: Summary table of NOL based samples received at CERN on 2015-2016 with the information of the total luminophore concentration and relative NOL content (in a.u.). The blue (green) color in the name of the fibre sample means its emission spectrum is blue (green) peaked.

7.2 Performance of NOL based fibres

7.2.1 1$^{\text{st}}$ iteration

In reference [122], NOL1 and NOL2 are presented as the most promising NOLs which have similar features as Kuraray standard fibres. As can be seen in Figure 7.5, both luminophores have an absorption spectrum which peaks in the UV-range as well as an emission maxima in the blue wavelength region. Then the first NOL fibres fabricated, denominated as L1 and L2, contained as base material NOL1 and NOL2 respectively. These NOL dye concentrations were determined as a convenient guess, which would be fine-tuned for the next iterations in order to improve results, in particular light yield.

The attenuation length and light yield measurements were performed as described in sections 6.1 and 6.2 and Table 7.1 presents the results. The current attenuation length of 265 cm and 175 cm, for L1 and L2 respectively, would not satisfy the requirements for the SciFi project. The scintillation light yield of the L1 and L2 samples, when extrapolated to d=0 cm (no attenuation) are comparable to the one of SCSF-78 standard material. L1 appears to have slightly better yield than L2, but this is at the limit of significance.

7.2.2 2$^{\text{nd}}$ iteration

For the second iteration, four samples L120, L121, L130 and L131 were developed with the blue-emitting luminophores NOL2 and NOL3; their concentrations were optimized to result in the production of fibres with longer attenuation lengths. Indeed, when considering only fibre samples based on luminophore NOL2 and comparing them to L2 sample, the attenuation length had an increase of 66% for L120 and 89% for L121. The attenuation length requirement for LHCb SciFi Tracker is met by all samples except L131. With regard to light yield measurements, only L121 sample satisfies the requirements with almost the same scintillation yield as the reference fibre. Hence, in general, while their attenuation length has improved with respect to the January samples, their scintillation yield is worse.

7.2.3 3$^{\text{rd}}$ iteration

In order to further increase the light yield of the NOL2 based samples, the third batch was fine-tuned by increasing the relative NOL content. This iteration generated 2 samples: L122 and L123. However, the attenuation length of L122 and L123 was found to be around 260-280 cm giving worse results than the samples of the second batch (L120,L121,L130,L131). They are significantly worse than the SCSF-78 reference samples which achieve values larger than 350 cm. In terms of scintillation yield, L122 and L123 had

5.1 and 6.7 photoelectrons, respectively. This is significantly worse than the best L121 sample from the 2nd batch, which achieved 10 photoelectrons.

7.2.4 4th **iteration**

Since the blue emitting NOL samples did not give satisfactory results, the next trial batch was based on new luminophores with green emission peaks (NOL17 and NOL18) resulting in the production of four samples: L170, L171, L180 and L181. As reported in section 6.1.2 which describes the dependence of the attenuation length on the wavelength, the more red-shifted light has longer attenuation length. Therefore, it was expected that these samples would have longer attenuation length than blue NOL fibres.

Nevertheless, the results were quite disappointing: the attenuation length was found to be around 243-297 cm and the best scintillating yield (given by L181 sample) was about 50% lower when compared to L121. In order to investigate these outcomes even further, measurements of the emission and absorption spectra of sample L170 were performed. Figure 7.4(a) shows the emission spectrum at different excitation distances superposed with the absorption spectrum (in black). While emission spectra of NOL17 shows luminescence maxima at 438 and 468 nm (see Figure 7.6), the measured emission spectrum at 2 cm (closest distance possible) shows only one peak around 468 nm. This means there is a part of the emission spectrum in the range of 400-450 nm that is not observable due to self-absorption. Figure 7.4(b) shows the spectral attenuation length of samples L170 and L180. Both distributions present a large dip centred around 470 nm, which affects the attenuation length from 450 to 520 nm. After reporting this issue with LumInnoTech, they analysed the luminophores used to produce theses samples and found the presence of an impurity (about 0.01%) that absorbs light with wavelengths from 423 to 500 nm.

7.2.5 5th **iteration**

The fifth trial consisted of preparing three fibre samples (L182, L190 and L191) composed of NOL18 and NOL19, which is a direct analogue of NOL17, with less impurities: it was reduced by a factor 10 (0.001%). While L190 and L191 have 30% more relative NOL content than their NOL17 analogues. L182 sample is kept with the same features as L180.

With regard to attenuation length, results are less than 300 cm, which are comparable (L182 and L190) or worse (L191) than previous samples. Scintillation yield have not been improved as expected as well. Take for instance L182 sample which is L180 with less impurity: although the light yield has increased more than 50% (from 3.5 to 5.4 pe.), it is far of the minimum requirement to be accepted in the SciFi Project (10 photoelectrons). For the

(a)   (b)
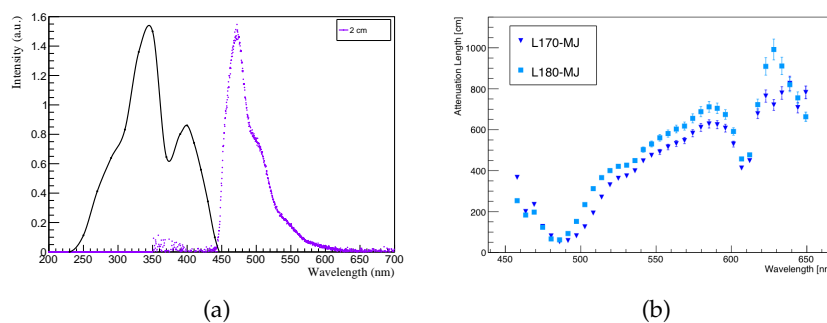
FIGURE 7.4: Results from the 4th iteration: (a) emission and absorption spectra of L170 sample. The emission spectra (purple curve) was obtained by exciting the fibre with an UV-LED at 2 cm distance from the photodiode; (b) spectral attenuation length of the L170 and L180 samples. The deep in the region of 450-500 nm indicates that light is self-absorbed.

NOL19 sample, the light yield also improved by about 70-90%, however the same conclusion is applied.

7.2.6 6th **iteration**

For the sixth iteration, four samples (L193, L124, L212, L012) were developed based on the samples with the best performance with regard to light yield. The L193 is a green NOL fibre, analogue to L190, but with a reduced relative NOL content. L124 and L212 are blue NOL fibres based on L121 and L2 samples, respectively, with a reduced relative NOL content. In order to better understand the behavior of a pure NOL fibre, L012 is a blue NOL fibre with a one-order lower concentration of NOL without the addition of any other dopant (activator). In fact, since NOL dyes are very expensive in this early R& D phase, the fibres so far (except L012) were produced by a mixture of NOL and an activator dye, which means that NOL was working as a wavelength shifter dye with an extended absorption spectrum. In addition, Kuraray sent two 3HF fibre samples, with different wavelength shifter concentrations, which allowed comparison with NOL green fibres.

The results for attenuation length and light yield of the new NOL fibres are comparable to their analogues. The attenuation length of the L012, the pure NOL sample, was found to be 354 cm, which is impressive. However, the light yield was very low (4.6 photoelectrons).

7.2.7 **Summary of NOL trials**

Table 7.1 summarises the measured values of attenuation length and light yield of all the NOL fibre samples. Appendix B contains the plots and fits

Interaction (arrival at CERN)	Samples	WLS concentration (ppm)
1st	SCSF-78	1000
6th	3HF	1500
(AGO 2016)	3HF	3000

TABLE 7.2: Summary table of Kuraray 3HF fibre samples produced for comparison with green NOL based fibres. The 3HF fibres have an emission spectra which peaks at 530 nm [119].

that resulted in the values presented in Table 7.1. To investigate even further and try to understand the relative NOL content and total luminophore concentration influence in the performance of the fibres so far, plots in Figures 7.2 and 7.3 were produced for blue and green emitting fibres, respectively. However, no correlation among these features and attenuation length or scintillation yield have been observed.

7.2.8 Decay time

The decay time measurement (as described in Section 6.4) was performed for 4 different samples: SCSF-78, L121, 3HF(1500) and L170. The measurement of SCSF-78 and 3HF serves as reference values for the NOL samples L121 and L170, respectively. The time distribution is well described by an exponential function, which represents the decay time of the scintillation light, convoluted with a Gaussian, accounting for all the jitters and time fluctuations in the set-up. Figures 7.7-7.10 show the measured time distribution together with the (red) fitted curve. Table 7.4 summarizes the information of the scintillation decay time along with the statistical error for the measured samples. Both NOL fibres were found to have a faster decay time: while the blue NOL fibre, L121, is 2 times faster than the SCSF-78 reference fibre, the green NOL L170 has a decay time which is 4.9 times faster than the 3HF scintillator. These are probably the fastest fibres ever produced.

7.3 Discussion

Since end of 2014, CERN, Kuraray and LumInnoTech collaboration resulted in the development of a series of NOL based fibres. Their performance in terms of attenuation length, light yield and decay time were measured at CERN. Concerning scintillation yield and attenuation length, the most promising results lead to samples which are as good as a Kuraray standard fibre SCSF-78. However, since then Kuraray has been improving the quality of the fibre production leading to samples with higher light yield (reaching
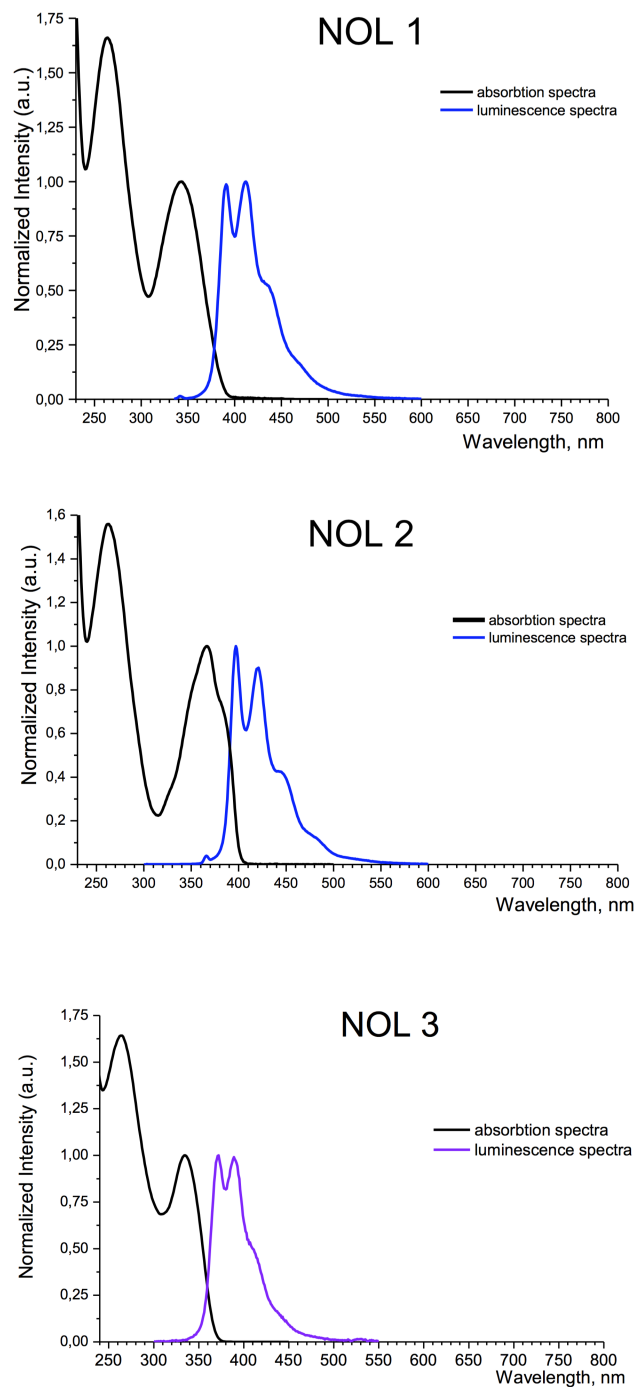
FIGURE 7.5: Absorption and emission spectra of the different NOL dyes selected for the fabrication of blue fibre samples as provided by LumInnoTech.
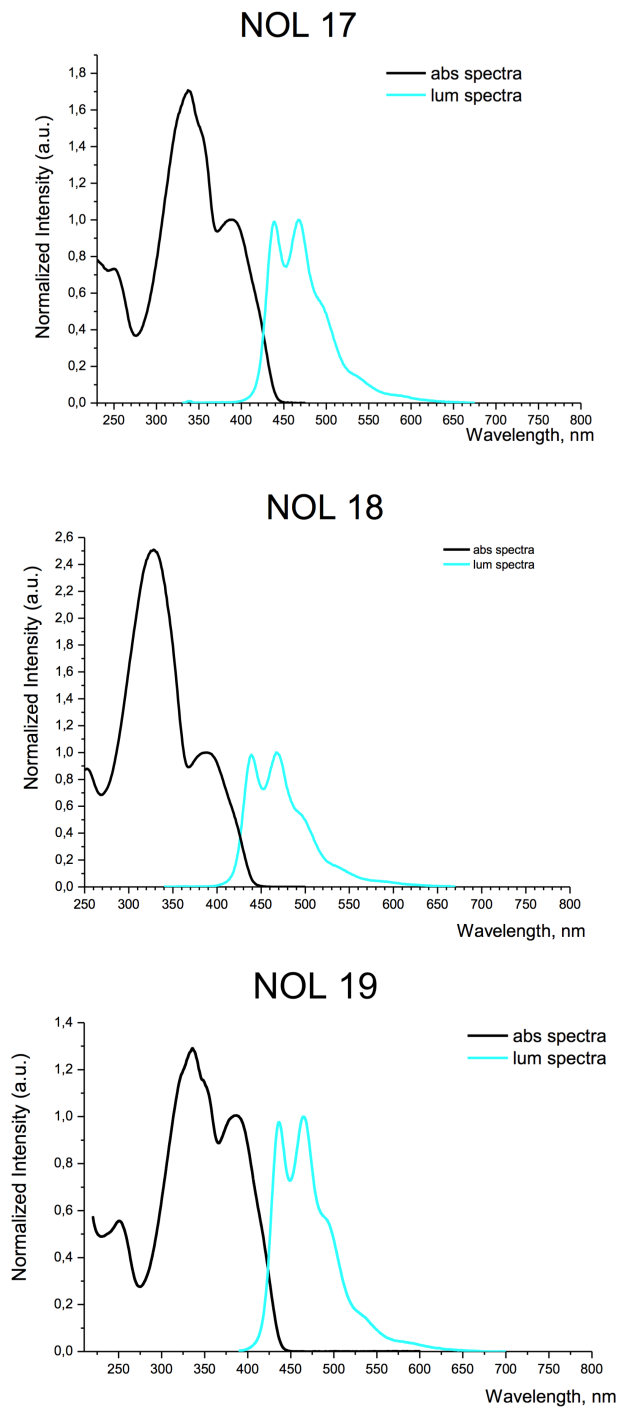
FIGURE 7.6: Absorption and emission spectra of the different NOL dyes selected for the fabrication of green fibre samples as provided by LumInnoTech..

Interaction (arrival at CERN)	Sample name	Attenuation length (cm)	Ionisaation yield PMT ($N_{pe}@d=0$ cm)	Ionisation yield SiPM ($N_{pe}@d=0$ cm)
1st (JAN 2015)	L1	264.7 ± 13.6	5.79 ± 0.25	9.82 ± 0.40
	L2	174.5 ± 6.0	5.56 ± 0.26	9.43 ± 0.42
2nd (MAY 2015)	L120	293.6 ± 17.5	4.39 ± 0.20	7.45 ± 0.32
	L121	329.2 ± 21.5	6.23 ± 0.28	10.57 ± 0.45
	L130	302.5 ± 18.1	3.80 ± 0.17	6.45 ± 0.27
	L131	338.2 ± 22.6	4.12 ± 0.18	6.99 ± 0.29
3rd (SEP 2015)	L122	279.1 ± 15.3	2.99 ± 0.17	5.07 ± 0.27
	L123	259.1 ± 13.0	3.93 ± 0.23	6.67 ± 0.37
4th (NOV 2015)	L170	243.1 ± 11.7	-	3.20 ± 0.14
	L171	284.9 ± 16.0	-	3.19 ± 0.14
	L180	297.3 ± 17.2	-	3.49 ± 0.15
	L181	291.5 ± 16.9	-	5.32 ± 0.25
5th (MAR 2016)	L182	277.3 ± 15.2	-	5.38 ± 0.23
	L190	277.6 ± 15.1	-	6.21 ± 0.27
	L191	205.8 ± 8.3	-	5.50 ± 0.25
6th (AGO 2016)	L193	338.6 ± 22.5	-	6.85 ± 0.29
	L124	307.7 ± 18.4	-	10.11 ± 0.43
	L212	280.0 ± 15.5	-	7.97 ± 0.33
	L012	353.9 ± 24.4	-	4.65 ± 0.21
	3HF(1500)	349.9 ± 24.0	-	10.54 ± 0.45
	3HF(3000)	298.2 ± 17.5	-	9.32 ± 0.39

TABLE 7.3: Summary table containing the results of attenuation length and light yield measurements of NOL based fibres a nd 3HF fibres received at CERN on 2015-2016. The blue (green) color in the name of the fibre sample means its emission spectrum is blue (green) peaked.
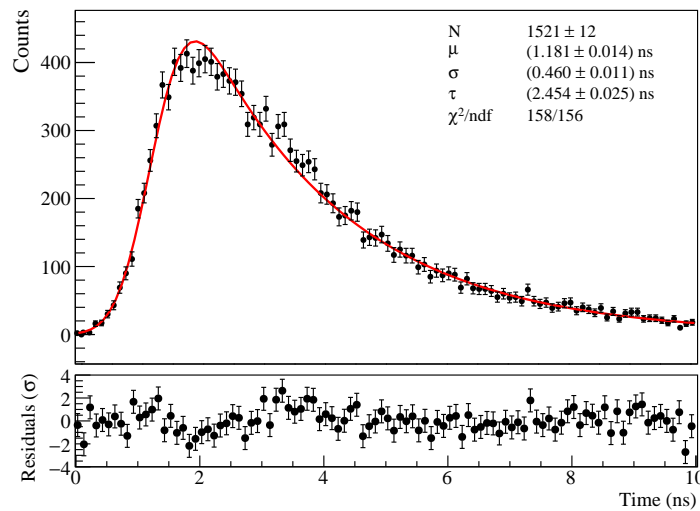
FIGURE 7.7: Time distribution of the decay time measurement of a SCSF-78 fibre sample.

N	1529 ± 13
μ	(1.174 ± 0.012) ns
σ	(0.513 ± 0.008) ns
τ	(1.221 ± 0.016) ns
χ^2/ndf	100/159
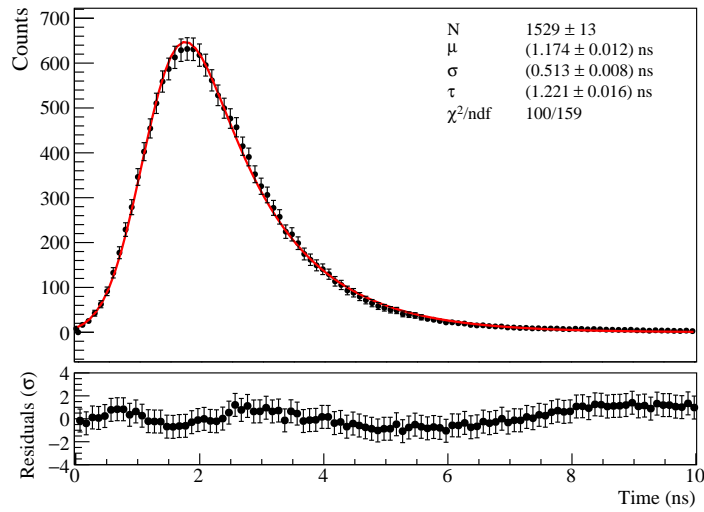
FIGURE 7.8: Time distribution of the decay time measurement of a L121 fibre sample.

N	1539 ± 12
μ	(1.176 ± 0.012) ns
σ	(0.515 ± 0.009) ns
τ	(1.200 ± 0.015) ns
χ^2/ndf	144/154
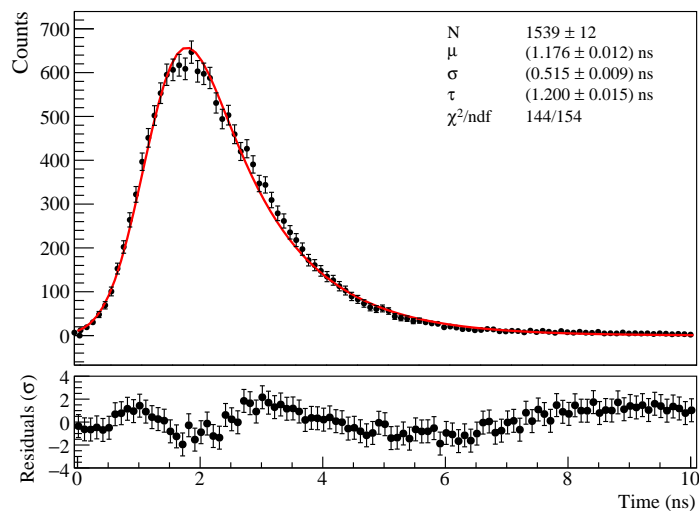
FIGURE 7.9: Time distribution of the decay time measurement of a L170 fibre sample.

Sample name	Decay time (ns)
SCSF-78	2.45
L121	1.22
L170	1.20
3HF(1500)	5.89

TABLE 7.4: Summary table of the measured scintillation decay time of SCSF-78, L121, L170 and 3HF(1500) fibre samples.
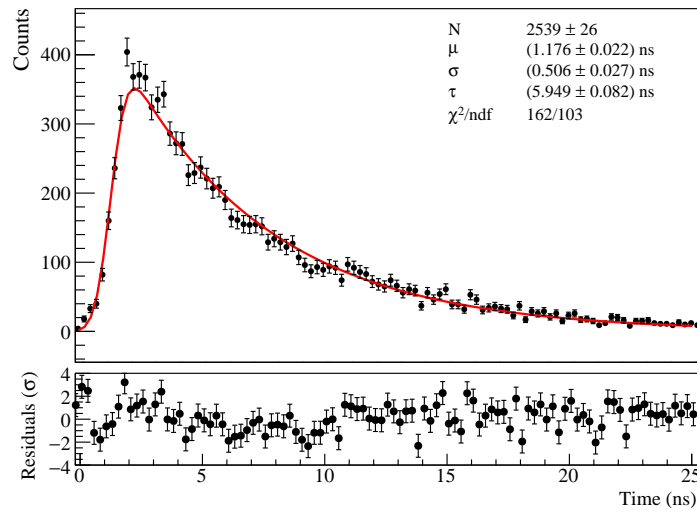
FIGURE 7.10: Time distribution of the decay time measurement of a 3HF(1500) fibre sample.

15 photoelectrons) which makes it very hard for NOL based fibres to compete with. Since the light needs to be transported over a distance of up to 2.5 m (or even 5 m if it goes to the mirror end), it is essential for the SciFi detector to be built up of fibres with largest attenuation as possible together with a high light yield. For the moment, unfortunately, NOL fibres does not seem to be a viable solution for SciFi. In case such a fibre with a 50% more light yield than the reference was developed, the center modules of the SciFi, which are going to suffer more radiation damage (irradiation tests should be made to prove that NOL material is radiation hardness), would be build up of NOL fibres. Another factor that does not contribute to NOL is time: SciFi has a tight schedule and if such a fibre (with high light yield, attenuation length as long as possible and radiation hardness) was developed, it should soon be commercially available for production.

On the other hand, in terms of decay time, NOL fibres have a superior performance which are 2 (4.9) faster for blue (green) fibres. Although, NOL fibres does not meet LHCb SciFi requirements, this fast response can be an advantage for experiments in which a high light yield or a long attenuation is not necessary such as Mu3 SciFi tracker [132].

Conclusions and final considerations

Despite the success of the Standard Model to describe the elementary particles and their interactions, some challenging questions remain unsolved. In particular, the amount of CP violation predicted by the SM is orders of magnitude insufficient to account for the matter-antimatter asymmetry in the Universe.

In the first part of this thesis, we presented new results and studies on the asymmetry of B mesons decays which are a good laboratory to investigate CP violation mechanisms. The analysis was focused on the charmless three-body $B^\pm$ decays: $B^\pm \to K^\pm\pi^+\pi^-$, $B^\pm \to \pi^\pm\pi^+\pi^-$, $B^\pm \to K^\pm K^+K^-$ and $B^\pm \to \pi^\pm K^+K^-$. The LHCb dataset corresponds to an integrated luminosity of $3.1\,\mathrm{fb}^{-1}$ acquired during 2011 and 2012 at centre-of-mass energy of $7\,\mathrm{TeV}$ and $8\,\mathrm{TeV}$, respectively. In Chapter 3 we discussed the procedure to measure inclusive CP asymmetries. Firstly, we described the selection process which allowed us to prepare the $B^\pm \to h^\pm h^+h^-$ sample for analysis. Next, we determined the signal yields by performing fits to the invariant-mass distributions, followed by the CP asymmetry measurement. The inclusive CP asymmetries were found to be positive for $B^\pm \to K^\pm\pi^+\pi^-$ and $B^\pm \to \pi^\pm\pi^+\pi^-$ decays, and negative for $B^\pm \to K^\pm K^+K^-$ and $B^\pm \to \pi^\pm K^+K^-$ decays and their magnitudes vary from 2.5% up to 12.3% for the $B^\pm \to K^\pm\pi^+\pi^-$ and $B^\pm \to \pi^\pm K^+K^-$ decay [92], respectively. In addition to the global asymmetry measurement, we investigated in Chapter 4 behavior of the charge asymmetries across the phase space. The statistics accumulated in 2011 and 2012 allowed us to observe new phenomena related to CP asymmetry concentrations at low two-body masses on the $B^\pm \to K^\pm\pi^+\pi^-$ and $B^\pm \to \pi^\pm\pi^+\pi^-$ decays.

In addition, we performed toy MC studies focused on those channels, and interpreted those results using a simple two-amplitude model to describe the behavior of charge asymmetries projections on the two-body invariant mass. We presented the result [95] that suggests the $KK \leftrightarrow \pi\pi$ rescattering affects the strong phase difference, which, together with the observation of the "compound CP violation", lead to the conclusion that hadronic final state interactions play an important role on the strong phase of the decay amplitudes.

The second part of this thesis was dedicated to my contributions to the SciFi Tracker foreseen for the LHCb upgrade. The viability of the SciFi Tracker relies on a number of crucial fibre parameters as high light yield, long attenuation length, geometrical precision and radiation tolerance. In Chapter 6, we have described the experimental setups that allowed us to characterise and improve the scintillating fibres to attend the minimum requirements stipulated in the upgraded conditions. My main contributions were related to the geometrical stability tests on the fibres: i) identification of fibre defects on diameter and cladding; ii) removal of bumps by the shrinking method. In particular, we demonstrated that bump shrinking method not only work for most of the bumps - with a diameter not larger than $\approx 550\,\mu\text{m}$- but it also keeps the faultless fibre (large majority) undamaged.

Moreover, we examined in Chapter 7 scintillating fibres composed of Nanostructured Organosilicon Luminophores, which has shown to be advantageous in terms of scintillation yield and decay time in several applications [126, 127, 128, 129]. We have characterised 20 fibre samples based on NOL emitting on the blue or green region and compared then to the fastest conventional fibres. The result is impressive for the decay time constant: two (six) times shorter than the blue (green) conventional fibres [133], implying that NOL fibres can be very attractive to fast-timing applications. The research on NOL fibres is still on-going. However, since SciFi has a tight schedule and if such a fibre was developed with fibre parameters fulfilling and exceeding the requirements, it should be soon available for production.

Appendix A

Complementary mass fits

This appendix is a complement to the results presented on section 3.8. We present the fit of the invariant mass of each of the $B^{\pm} \to h^{\pm}h^{+}h^{-}$ decays with the plots in the logaritmic scale and include the residuals and pull plots. In addition, the samples are separated by year and trigger selection. Also, Tables A.1-A.8 present the parameters obtained from the fit for each of the studied cases.
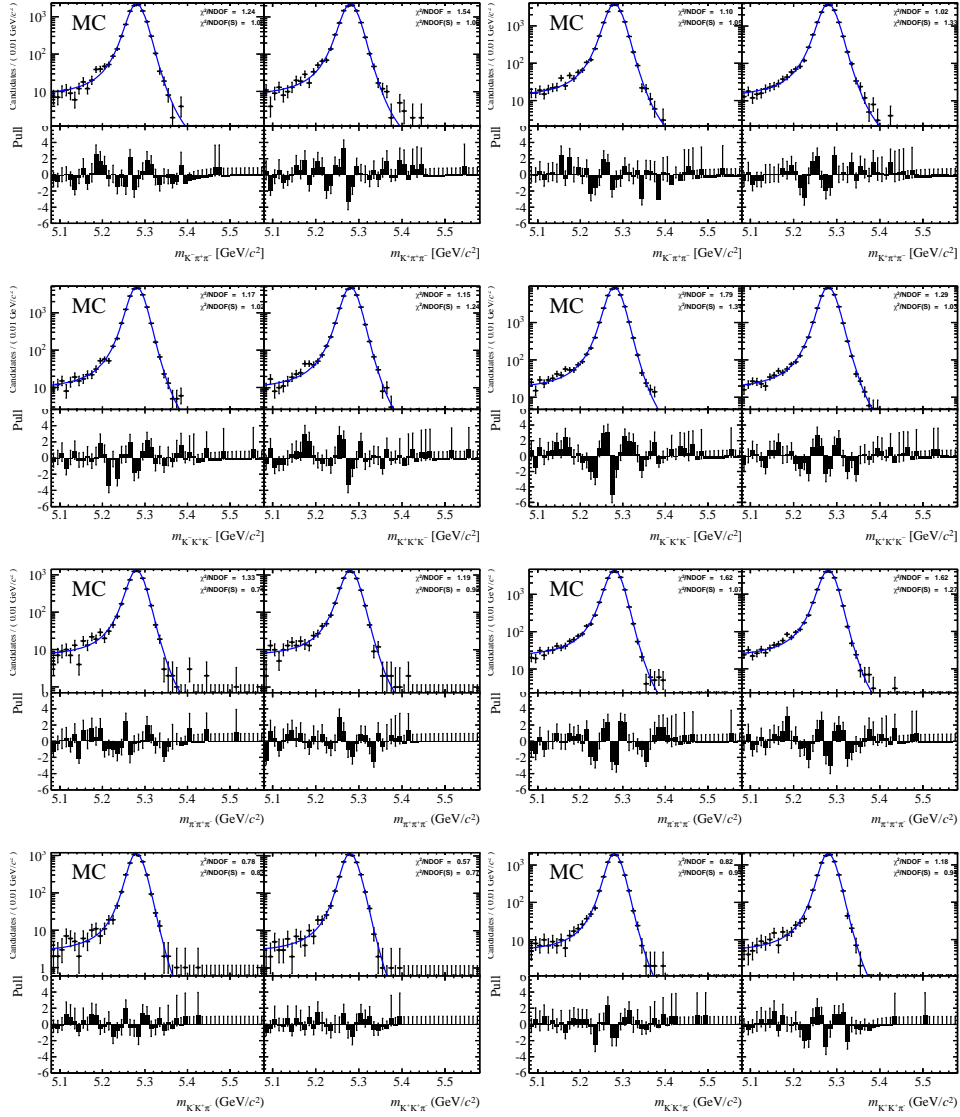
FIGURE A.1: $B^{\pm} \rightarrow K^{\pm}\pi^{+}\pi^{-}$ (first row), $B^{\pm} \rightarrow K^{\pm}K^{+}K^{-}$ (second row), $B^{\pm} \rightarrow \pi^{\pm}\pi^{+}\pi^{-}$ (third row) and $B^{\pm} \rightarrow \pi^{\pm}K^{+}K^{-}$ (last row) mass fits distributions of 2011 (left column) and 2012 (right column) MC samples. In each pair of distributions, the plot on the left is B^{-} and on the right is B^{+}.

FIGURE A.2: $B^{\pm} \to K^{\pm}\pi^{+}\pi^{-}$ mass fits distributions of 2011 (left column) and 2012 (right column) data samples accepted by L0 trigger lines "Global TIS or Hadron TOS" (first row), "Hadron TOS only" (second row) and "Global TIS only" (third row) and "Global TIS not Hadron TOS" (last row). In each pair of distributions, the plot on the left is B^{-} and on the right is B^{+}.

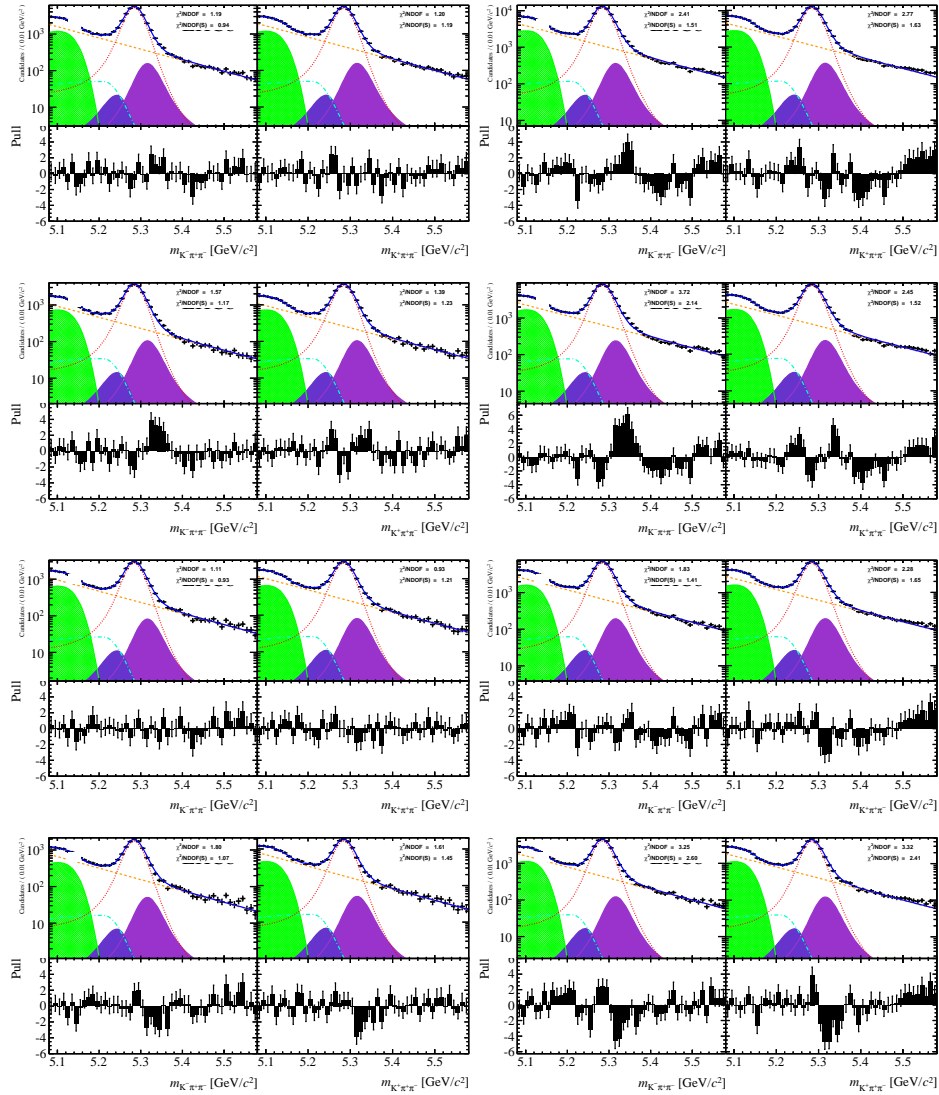|	$B^{\pm} \to K^{\pm}\pi^{+}\pi^{-}$ (2011 data)		
	L0 Global TIS or L0 Hadron TOS	L0Hadron TOS	L0 Global TIS
Signal component			
$m_0[\,\mathrm{MeV}/c^2\,]$	5283.5 ± 0.20464	5283.5 (C)	5283.5 (C)
$\sigma_1[\,\mathrm{MeV}/c^2\,]$	16.928 ± 0.17431	16.928 (C)	16.928 (C)
$\sigma_2[\,\mathrm{MeV}/c^2\,]$	18.690 ± 0.16031	18.690 (C)	18.690 (C)
a_1	0.17326 (C)	0.17326 (C)	0.17326 (C)
a_2	0.097079 (C)	0.097079 (C)	0.097079 (C)
A_{raw}	0.011487 ± 0.0047708	$0.0056253 \pm {\scriptstyle(-0.0060871, +0.0059846)}$	$0.020146 \pm {\scriptstyle(-0.0069464, +0.0069519)}$
N_S	$53544 \pm {\scriptstyle(-281.87, +302.10)}$	$36106 \pm {\scriptstyle(-217.92, +219.06)}$	$28125 \pm {\scriptstyle(-195.97, +197.10)}$
Combinatorial component			
b	$-0.00706945 \pm 0.000058957$	$-0.00697774 \pm 0.000085450$	$-0.00708162 \pm 0.000083493$
A_{comb}	-0.0214402 ± 0.0055944	-0.0159862 ± 0.0077670	-0.0277869 ± 0.0073711
N_{comb}	51042 ± 487.68	29888 ± 397.99	31032 ± 394.24
$B \to$ 4-body (partially rec. component)			
$\sigma\,[\,\mathrm{MeV}/c^2\,]$	18.010 (C)	18.010 (C)	18.010 (C)
$m_t\,[\,\mathrm{MeV}/c^2\,]$	5157.1 ± 2.4936	5157.1 (C)	5157.1 (C)
c	-49.9931 ± 44.335	-49.9931 (C)	-49.9931 (C)
p	0.97428 ± 0.94161	0.97428 (C)	0.97428 (C)
$Fraction[\%]$	0.57235 ± 0.013123	0.52338 ± 0.016486	0.59927 ± 0.021157
A_{bkg}	0.0000 (C)	0.0000 (C)	0.0000 (C)
$B^{\pm} \to \eta'(\rho^0\gamma)K^{\pm}$ component			
$m_0\,[\,\mathrm{MeV}/c^2\,]$	5211.0 (C)	5211.0 (C)	5211.0 (C)
$\sigma_1\,[\,\mathrm{MeV}/c^2\,]$	196.10 (C)	196.10 (C)	196.10 (C)
$\sigma_2\,[\,\mathrm{MeV}/c^2\,]$	27.500 (C)	27.500 (C)	27.500 (C)
a_1	0.0000 (C)	0.0000 (C)	0.0000 (C)
a_2	0.086300 (C)	0.086300 (C)	0.086300 (C)
$Fraction[\%]$	0.059600 (C)	0.059600 (C)	0.059600 (C)
A_{bkg}	0.0000 (C)	0.0000 (C)	0.0000 (C)
$B^{\pm} \to \pi^{\pm}\pi^{+}\pi^{-}$ component			
$m_0\,[\,\mathrm{MeV}/c^2\,]$	5315.9 (C)	5315.9 (C)	5315.9 (C)
$\sigma_1\,[\,\mathrm{MeV}/c^2\,]$	19.470 (C)	19.470 (C)	19.470 (C)
$\sigma_2\,[\,\mathrm{MeV}/c^2\,]$	20.830 (C)	20.830 (C)	20.830 (C)
a_1	0.17700 (C)	0.17700 (C)	0.17700 (C)
a_2	0.19100 (C)	0.19100 (C)	0.19100 (C)
$Fraction[\%]$	0.073400 (C)	0.073400 (C)	0.073400 (C)
A_{bkg}	0.0000 (C)	0.0000 (C)	0.0000 (C)
$B^{\pm} \to \pi^{\pm}K^{+}K^{-}$ component			
$m_0\,[\,\mathrm{MeV}/c^2\,]$	5243.3 (C)	5243.3 (C)	5243.3 (C)
$\sigma_1\,[\,\mathrm{MeV}/c^2\,]$	24.640 (C)	24.640 (C)	24.640 (C)
$\sigma_2\,[\,\mathrm{MeV}/c^2\,]$	18.380 (C)	18.380 (C)	18.380 (C)
a_1	0.32000 (C)	0.32000 (C)	0.32000 (C)
a_2	0.11700 (C)	0.11700 (C)	0.11700 (C)
$Fraction[\%]$	0.011200 (C)	0.011200 (C)	0.011200 (C)
A_{bkg}	0.0000 (C)	0.0000 (C)	0.0000 (C)

TABLE A.1: List of the $B^{\pm} \to K^{\pm}\pi^{+}\pi^{-}$ mass fit model parameters extracted from the 2011 sample fit. The numbers followed by a "(C)" were fixed in the corresponding fit.

	$B^{\pm} \to K^{\pm}\pi^{+}\pi^{-}$ (2012 data)		
	L0 Global TIS or L0 Hadron TOS	L0Hadron TOS	L0 Global TIS
Signal component			
m_0[MeV/c^2]	5283.1 ± 0.12866	5283.1 (C)	5283.1 (C)
σ_1[MeV/c^2]	16.669 ± 0.11189	16.669 (C)	16.669 (C)
σ_2[MeV/c^2]	19.387 ± 0.10454	19.387 (C)	19.387 (C)
a_1	0.17124 (C)	0.17124 (C)	0.17124 (C)
a_2	0.098587 (C)	0.098587 (C)	0.098587 (C)
A_{raw}	0.0093456 ± 0.0031232	$0.011830 \pm \genfrac{}{}{0}{}{(-0.0040571,}{+0.0040375)}$	$0.010851 \pm \genfrac{}{}{0}{}{(-0.0045565,}{+0.0045673)}$
N_S	123917 ± 404.93	$81683 \pm \genfrac{}{}{0}{}{(-330.53,}{+332.47)}$	$66169 \pm \genfrac{}{}{0}{}{(-303.05,}{+303.70)}$
Combinatorial component			
b	$-0.00685960 \pm 0.000038416$	$-0.00678051 \pm 0.000052679$	$-0.00684417 \pm 0.000051429$
A_{comb}	$-0.00923672 \pm 0.0034906$	-0.0111203 ± 0.0048521	$-0.00978025 \pm 0.0046655$
N_{comb}	126475 ± 796.52	74612 ± 608.62	77050 ± 602.82
$B \to 4$-body (partially rec. component)			
σ [MeV/c^2]	18.010 (C)	18.010 (C)	18.010 (C)
m_t [MeV/c^2]	5155.3 ± 1.1948	5155.3 (C)	5155.3 (C)
c	-49.9823 ± 49.983	-49.9823 (C)	-49.9823 (C)
p	0.90974 ± 0.22378	0.90974 (C)	0.90974 (C)
$Fraction[\%]$	0.58572 ± 0.0094295	0.52834 ± 0.011029	0.62538 ± 0.013606
A_{bkg}	0.0000 (C)	0.0000 (C)	0.0000 (C)
$B^{\pm} \to \eta'(\rho^0\gamma)K^{\pm}$ component			
m_0 [MeV/c^2]	5211.0 (C)	5211.0 (C)	5211.0 (C)
σ_1 [MeV/c^2]	196.10 (C)	196.10 (C)	196.10 (C)
σ_2 [MeV/c^2]	27.500 (C)	27.500 (C)	27.500 (C)
a_1	0.0000 (C)	0.0000 (C)	0.0000 (C)
a_2	0.086300 (C)	0.086300 (C)	0.086300 (C)
$Fraction[\%]$	0.059600 (C)	0.059600 (C)	0.059600 (C)
A_{bkg}	0.0000 (C)	0.0000 (C)	0.0000 (C)
$B^{\pm} \to \pi^{\pm}\pi^{+}\pi^{-}$ component			
m_0 [MeV/c^2]	5315.9 (C)	5315.9 (C)	5315.9 (C)
σ_1 [MeV/c^2]	19.470 (C)	19.470 (C)	19.470 (C)
σ_2 [MeV/c^2]	20.830 (C)	20.830 (C)	20.830 (C)
a_1	0.17700 (C)	0.17700 (C)	0.17700 (C)
a_2	0.19100 (C)	0.19100 (C)	0.19100 (C)
$Fraction[\%]$	0.073400 (C)	0.073400 (C)	0.073400 (C)
A_{bkg}	0.0000 (C)	0.0000 (C)	0.0000 (C)
$B^{\pm} \to \pi^{\pm}K^{+}K^{-}$ component			
m_0 [MeV/c^2]	5243.3 (C)	5243.3 (C)	5243.3 (C)
σ_1 [MeV/c^2]	24.640 (C)	24.640 (C)	24.640 (C)
σ_2 [MeV/c^2]	18.380 (C)	18.380 (C)	18.380 (C)
a_1	0.32000 (C)	0.32000 (C)	0.32000 (C)
a_2	0.11700 (C)	0.11700 (C)	0.11700 (C)
$Fraction[\%]$	0.011200 (C)	0.011200 (C)	0.011200 (C)
A_{bkg}	0.0000 (C)	0.0000 (C)	0.0000 (C)

TABLE A.2: List of the $B^{\pm} \to K^{\pm}\pi^{+}\pi^{-}$ mass fit model parameters extracted from the 2012 sample fit. The numbers followed by a "(C)" were fixed in the corresponding fit.
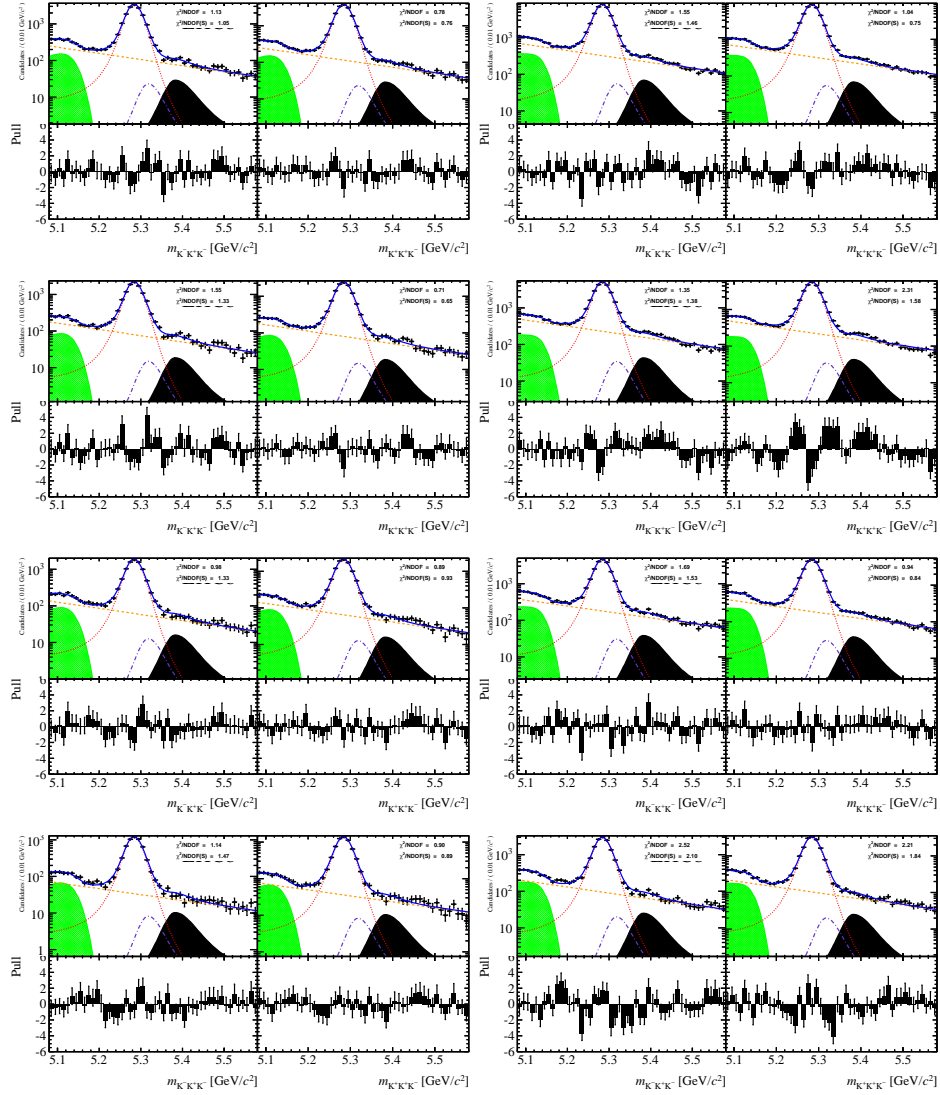
FIGURE A.3: $B^{\pm} \rightarrow K^{\pm}K^{+}K^{-}$ mass fits distributions of 2011 (left column) and 2012 (right column) data samples accepted by L0 trigger lines "Global TIS or Hadron TOS" (first row), "Hadron TOS only" (second row) and "Global TIS only" (third row) and "Global TIS not Hadron TOS" (last row). In each pair of distributions, the plot on the left is B^{-} and on the right is B^{+}.

	$B^{\pm} \to K^{\pm}K^+K^-$ (2011 data)		
	L0 Global TIS or L0 Hadron TOS	L0Hadron TOS	L0 Global TIS
Signal component			
m_0[MeV/c^2]	5283.2 ± 0.29187	5283.2 (C)	5283.2 (C)
σ_1[MeV/c^2]	15.073 ± 0.21460	15.073 (C)	15.073 (C)
σ_2[MeV/c^2]	16.902 ± 0.19979	16.902 (C)	16.902 (C)
a_1	0.15624 (C)	0.15624 (C)	0.15624 (C)
a_2	0.092333 (C)	0.092333 (C)	0.092333 (C)
A_{raw}	$-0.0608613 \pm {}^{(-0.0059641,}_{+0.0059424)}$	$-0.0600013 \pm {}^{(-0.0074603,}_{+0.0074726)}$	$-0.0670499 \pm {}^{(-0.0080057,}_{+0.0080033)}$
N_S	$32396 \pm {}^{(-204.92,}_{+207.20)}$	$20774 \pm {}^{(-157.21,}_{+157.54)}$	$17873 \pm {}^{(-144.75,}_{+145.28)}$
Combinatorial component			
b	$-0.00389930 \pm 0.00013288$	$-0.00396114 \pm 0.00013334$	$-0.00389979 \pm 0.00015040$
A_{comb}	-0.0115357 ± 0.012468	-0.00346902 ± 0.014723	-0.0242313 ± 0.016769
N_{comb}	11132 ± 265.63	7753.5 ± 167.42	6171.3 ± 150.34
$B \to$ 4-body (partially rec. component)			
σ [MeV/c^2]	15.960 (C)	15.960 (C)	15.960 (C)
m_t [MeV/c^2]	5154.7 ± 10.864	5154.7 (C)	5154.7 (C)
c	-59.0768 ± 35.381	-59.0768 (C)	-59.0768 (C)
p	0.93555 ± 0.88928	0.93555 (C)	0.93555 (C)
$Fraction[\%]$	0.12014 ± 0.010444	0.10480 ± 0.0099211	0.12913 ± 0.010556
A_{bkg}	0.0000 (C)	0.0000 (C)	0.0000 (C)
$B^{\pm} \to \pi^{\pm}K^+K^-$ component			
m_0 [MeV/c^2]	5317.9 (C)	5317.9 (C)	5317.9 (C)
σ_1 [MeV/c^2]	17.560 (C)	17.560 (C)	17.560 (C)
σ_2 [MeV/c^2]	22.300 (C)	22.300 (C)	22.300 (C)
a_1	0.16000 (C)	0.16000 (C)	0.16000 (C)
a_2	0.19200 (C)	0.19200 (C)	0.19200 (C)
$Fraction[\%]$	0.017600 (C)	0.017600 (C)	0.017600 (C)
A_{bkg}	0.0000 (C)	0.0000 (C)	0.0000 (C)

TABLE A.3: List of the $B^{\pm} \to K^{\pm}K^+K^-$ mass fit model parameters extracted from the 2011 sample fit. The numbers followed by a "(C)" were fixed in the corresponding fit.

	$B^{\pm} \to K^{\pm}K^+K^-$ (2012 data)		
	L0 Global TIS or L0 Hadron TOS	L0Hadron TOS	L0 Global TIS
Signal component			
m_0[MeV/c^2]	5283.5 ± 0.18877	5283.5 (C)	5283.5 (C)
σ_1[MeV/c^2]	15.384 ± 0.14172	15.384 (C)	15.384 (C)
σ_2[MeV/c^2]	16.959 ± 0.13232	16.959 (C)	16.959 (C)
a_1	0.15642 (C)	0.15642 (C)	0.15642 (C)
a_2	0.091074 (C)	0.091074 (C)	0.091074 (C)
A_{raw}	-0.0546451 ± 0.0039010	$-0.0531568 \pm {}^{(-0.0049337,}_{+0.0049475)}$	$-0.0521354 \pm {}^{(-0.0052024,}_{+0.0052067)}$
N_S	$76858 \pm {}^{(-320.31,}_{+319.48)}$	$48553 \pm {}^{(-243.41,}_{+244.12)}$	$43104 \pm {}^{(-227.34,}_{+227.76)}$
Combinatorial component			
b	$-0.00381838 \pm 0.000075146$	$-0.00382377 \pm 0.000076844$	$-0.00373201 \pm 0.000086492$
A_{comb}	-0.0119836 ± 0.0072175	0.00058939 ± 0.0084716	-0.0246152 ± 0.0096971
N_{comb}	31926 ± 424.02	22332 ± 275.51	17864 ± 247.77
$B \to$ 4-body (partially rec. component)			
σ [MeV/c^2]	15.960 (C)	15.960 (C)	15.960 (C)
m_t [MeV/c^2]	5146.4 ± 3.3065	5146.4 (C)	5146.4 (C)
c	-0.589162 ± 5.3778	-0.589162 (C)	-0.589162 (C)
p	0.048284 ± 0.079883	0.048284 (C)	0.048284 (C)
$Fraction$[%]	0.12208 ± 0.0068872	0.097153 ± 0.0068463	0.14001 ± 0.0070925
A_{bkg}	0.0000 (C)	0.0000 (C)	0.0000 (C)
$B^{\pm} \to \pi^{\pm}K^+K^-$ component			
m_0 [MeV/c^2]	5317.9 (C)	5317.9 (C)	5317.9 (C)
σ_1 [MeV/c^2]	17.560 (C)	17.560 (C)	17.560 (C)
σ_2 [MeV/c^2]	22.300 (C)	22.300 (C)	22.300 (C)
a_1	0.16000 (C)	0.16000 (C)	0.16000 (C)
a_2	0.19200 (C)	0.19200 (C)	0.19200 (C)
$Fraction$[%]	0.017600 (C)	0.017600 (C)	0.017600 (C)
A_{bkg}	0.0000 (C)	0.0000 (C)	0.0000 (C)

TABLE A.4: List of the $B^{\pm} \to K^{\pm}K^+K^-$ mass fit model parameters extracted from the 2012 sample fit. The numbers followed by a "(C)" were fixed in the corresponding fit.
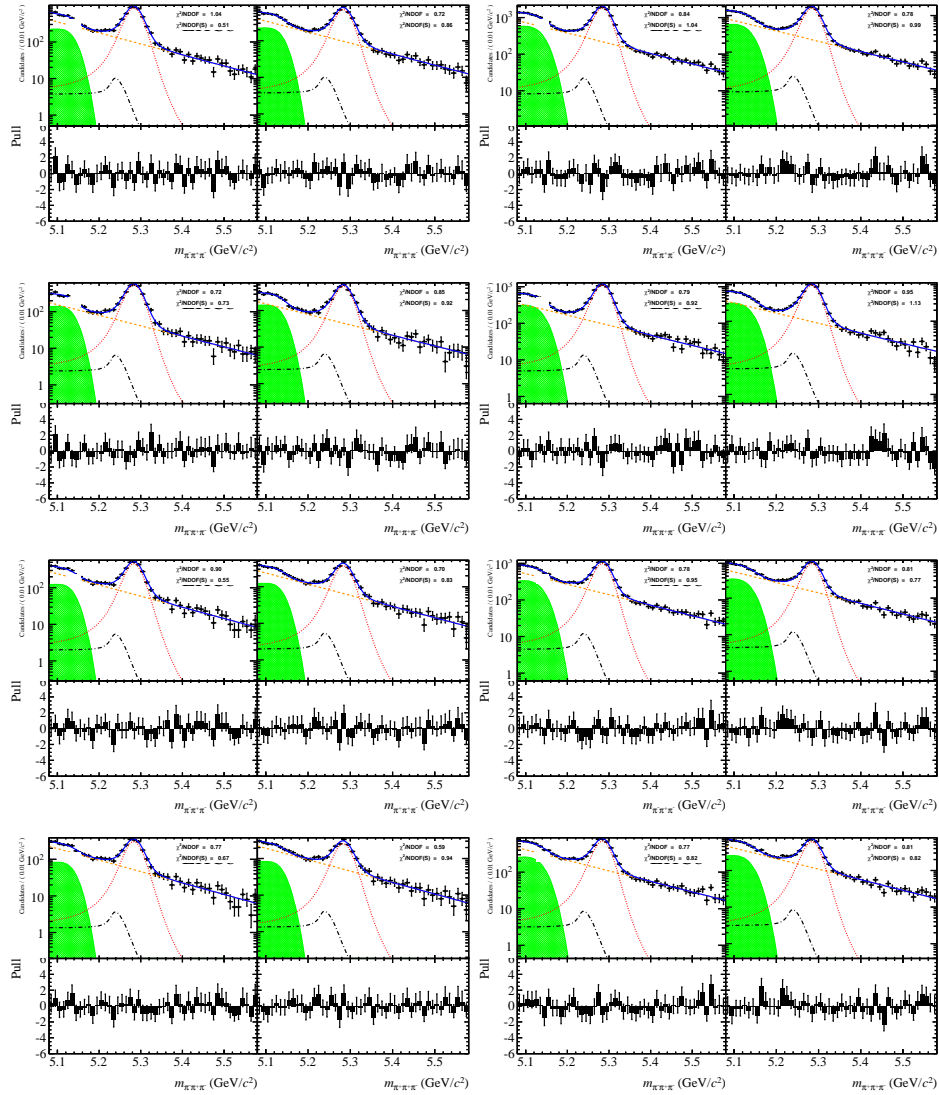
FIGURE A.4: $B^{\pm} \to \pi^{\pm}\pi^{+}\pi^{-}$ mass fits distributions of 2011 (left column) and 2012 (right column) data samples accepted by L0 trigger lines "Global TIS or Hadron TOS" (first row), "Hadron TOS only" (second row) and "Global TIS only" (third row) and "Global TIS not Hadron TOS" (last row). In each pair of distributions, the plot on the left is B^{-} and on the right is B^{+}.

	$B^\pm \to \pi^\pm \pi^+ \pi^-$ (2011 data)		
	L0 Global TIS or L0 Hadron TOS	L0Hadron TOS	L0 Global TIS
Signal component			
$m_0 [\,\mathrm{MeV}/c^2\,]$	5283.1 ± 0.69139	5283.1 (C)	5283.1 (C)
$\sigma_1 [\,\mathrm{MeV}/c^2\,]$	16.885 ± 0.61264	16.885 (C)	16.885 (C)
$\sigma_2 [\,\mathrm{MeV}/c^2\,]$	17.357 ± 0.49707	17.357 (C)	17.357 (C)
a_1	0.18626 (C)	0.18626 (C)	0.18626 (C)
a_2	0.091750 (C)	0.091750 (C)	0.091750 (C)
A_raw	$0.081704 \pm {\scriptstyle(-0.013434,\ +0.013433)}$	$0.075840 \pm {\scriptstyle(-0.016342,\ +0.016363)}$	$0.098441 \pm {\scriptstyle(-0.018777,\ +0.018860)}$
N_S	$7845.4 \pm {\scriptstyle(-121.35,\ +121.93)}$	$5021.8 \pm {\scriptstyle(-83.438,\ +84.265)}$	$4182.3 \pm {\scriptstyle(-80.391,\ +81.232)}$
Combinatorial component			
b	$-0.00693428 \pm 0.00015141$	$-0.00663514 \pm 0.00019193$	$-0.00704257 \pm 0.00015839$
A_{comb}	0.010796 ± 0.011996	0.012567 ± 0.018562	0.0074801 ± 0.014145
N_{comb}	11160 ± 286.96	5086.4 ± 148.08	7618.2 ± 174.64
$B \to$ 4-body (partially rec. component)			
$\sigma [\,\mathrm{MeV}/c^2\,]$	17.833 (C)	17.833 (C)	17.833 (C)
$m_t [\,\mathrm{MeV}/c^2\,]$	5141.6 ± 3.6854	5141.6 (C)	5141.6 (C)
c	-2.42050 ± 30.597	-2.42050 (C)	-2.42050 (C)
p	0.0000016953 ± 0.67766	0.0000016953 (C)	0.0000016953 (C)
$Fraction[\%]$	0.71187 ± 0.051563	0.69384 ± 0.043801	0.74194 ± 0.061992
A_{bkg}	0.0000 (C)	0.0000 (C)	0.0000 (C)
$B^\pm \to K^\pm \pi^+ \pi^-$ component			
$m_0 [\,\mathrm{MeV}/c^2\,]$	5238.1 (C)	5238.1 (C)	5238.1 (C)
$\sigma_1 [\,\mathrm{MeV}/c^2\,]$	10.520 (C)	10.520 (C)	10.520 (C)
$\sigma_2 [\,\mathrm{MeV}/c^2\,]$	17.910 (C)	17.910 (C)	17.910 (C)
a_1	1.0100 (C)	1.0100 (C)	1.0100 (C)
a_2	0.15000 (C)	0.15000 (C)	0.15000 (C)
$Fraction[\%]$	0.049300 (C)	0.049300 (C)	0.049300 (C)
A_{bkg}	0.0000 (C)	0.0000 (C)	0.0000 (C)

TABLE A.5: List of the $B^\pm \to \pi^\pm \pi^+ \pi^-$ mass fit model parameters extracted from the 2011 sample fit. The numbers followed by a "(C)" were fixed in the corresponding fit.

	$B^{\pm} \to \pi^{\pm}\pi^{+}\pi^{-}$ (2012 data)		
	L0 Global TIS or L0 Hadron TOS	L0Hadron TOS	L0 Global TIS
Signal component			
m_0[MeV/c^2]	5284.6 ± 0.34207	5284.6 (C)	5284.6 (C)
σ_1[MeV/c^2]	17.732 ± 0.32531	17.732 (C)	17.732 (C)
σ_2[MeV/c^2]	16.529 ± 0.25538	16.529 (C)	16.529 (C)
a_1	0.18492 (C)	0.18492 (C)	0.18492 (C)
a_2	0.091147 (C)	0.091147 (C)	0.091147 (C)
A_{raw}	0.070896 ± $^{(-0.0091579,}_{+0.0091543)}$	0.072871 ± $^{(-0.011345,}_{+0.011393)}$	0.059239 ± $^{(-0.012665,}_{+0.012752)}$
N_S	17081 ± $^{(-186.08,}_{+185.18)}$	10458 ± $^{(-121.62,}_{+122.18)}$	9355.4 ± $^{(-121.79,}_{+122.98)}$
Combinatorial component			
b	-0.00650942 ± 0.000083110	-0.00635100 ± 0.00013421	-0.00663448 ± 0.00010557
A_{comb}	-0.00218220 ± 0.0077383	0.0016905 ± 0.012879	-0.00338991 ± 0.0095393
N_{comb}	24350 ± 329.15	10753 ± 226.42	17356 ± 275.80
$B \to$ 4-body (partially rec. component)			
σ [MeV/c^2]	17.833 (C)	17.833 (C)	17.833 (C)
m_t [MeV/c^2]	5158.2 ± 8.1964	5158.2 (C)	5158.2 (C)
c	-45.6399 ± 30.762	-45.6399 (C)	-45.6399 (C)
p	0.99985 ± 0.60407	0.99985 (C)	0.99985 (C)
$Fraction[\%]$	0.86116 ± 0.027778	0.76629 ± 0.032314	0.91686 ± 0.043993
A_{bkg}	0.0000 (C)	0.0000 (C)	0.0000 (C)
$B^{\pm} \to K^{\pm}\pi^{+}\pi^{-}$ component			
m_0 [MeV/c^2]	5238.1 (C)	5238.1 (C)	5238.1 (C)
σ_1 [MeV/c^2]	10.520 (C)	10.520 (C)	10.520 (C)
σ_2 [MeV/c^2]	17.910 (C)	17.910 (C)	17.910 (C)
a_1	1.0100 (C)	1.0100 (C)	1.0100 (C)
a_2	0.15000 (C)	0.15000 (C)	0.15000 (C)
$Fraction[\%]$	0.049300 (C)	0.049300 (C)	0.049300 (C)
A_{bkg}	0.0000 (C)	0.0000 (C)	0.0000 (C)

TABLE A.6: List of the $B^{\pm} \to \pi^{\pm}\pi^{+}\pi^{-}$ mass fit model parameters extracted from the 2012 sample fit. The numbers followed by a "(C)" were fixed in the corresponding fit.
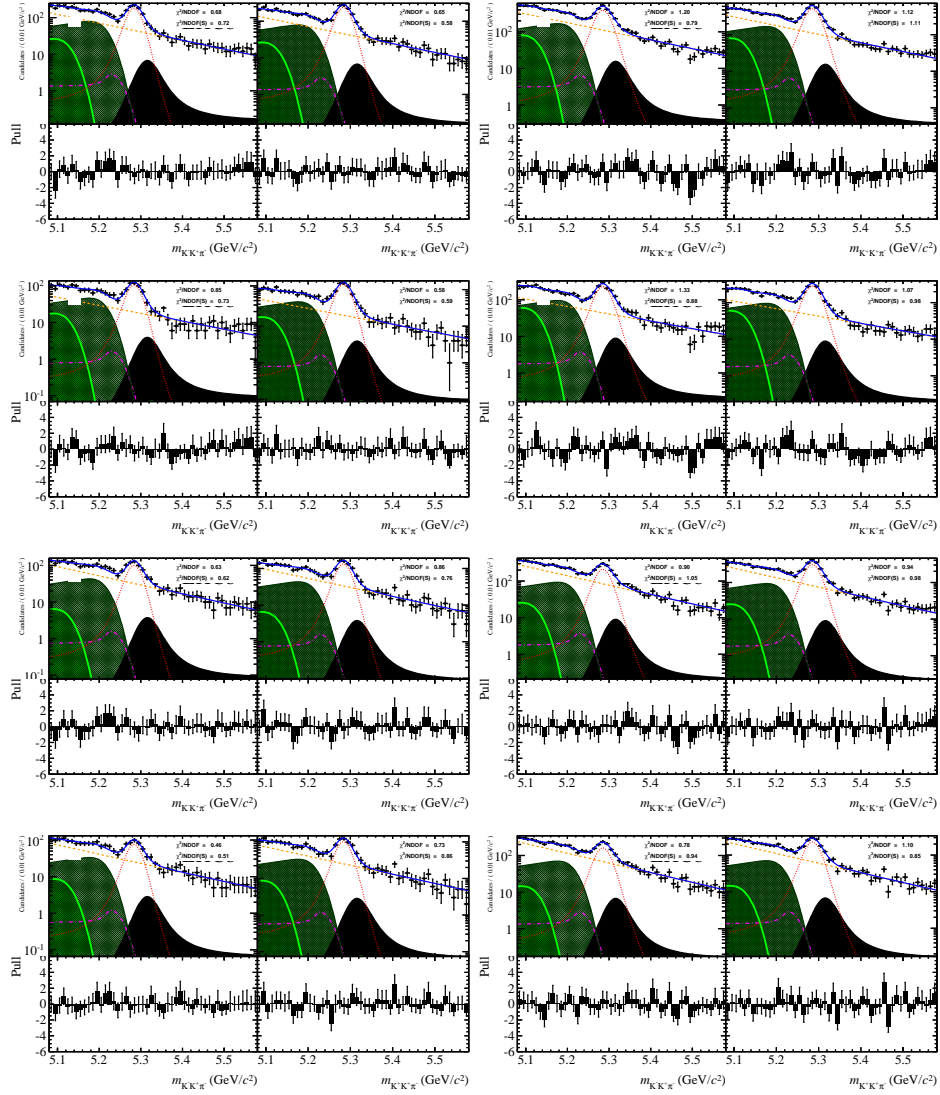
FIGURE A.5: $B^{\pm} \rightarrow \pi^{\pm} K^+ K^-$ mass fits distributions of 2011 (left column) and 2012 (right column) data samples accepted by L0 trigger lines "Global TIS or Hadron TOS" (first row), "Hadron TOS only" (second row) and "Global TIS only" (third row) and "Global TIS not Hadron TOS" (last row). In each pair of distributions, the plot on the left is B^- and on the right is B^+.

	$B^{\pm} \to \pi^{\pm}K^{+}K^{-}$ (2011 data)		
	L0 Global TIS or L0 Hadron TOS	L0Hadron TOS	L0 Global TIS
Signal component			
$m_0 [\,\mathrm{MeV}/c^2\,]$	5283.5 ± 1.5182	5283.5 (C)	5283.5 (C)
$\sigma_1 [\,\mathrm{MeV}/c^2\,]$	15.419 ± 1.4373	15.419 (C)	15.419 (C)
$\sigma_2 [\,\mathrm{MeV}/c^2\,]$	16.017 ± 1.1293	16.017 (C)	16.017 (C)
a_1	0.16222 (C)	0.16222 (C)	0.16222 (C)
a_2	0.074152 (C)	0.074152 (C)	0.074152 (C)
A_{raw}	$-0.133648 \pm \,^{(-0.029603,}_{+0.029372)}$	$-0.128641 \pm \,^{(-0.037174,}_{+0.037291)}$	$-0.132041 \pm \,^{(-0.040916,}_{+0.041079)}$
N_S	$1865.6 \pm \,^{(-85.566,}_{+87.155)}$	$1083.2 \pm \,^{(-47.405,}_{+48.093)}$	$1038.4 \pm \,^{(-51.003,}_{+51.311)}$
Combinatorial component			
b	$-0.00547404 \pm 0.00043539$	$-0.00506869 \pm 0.00056432$	$-0.00573310 \pm 0.00041446$
A_{comb}	-0.00592102 ± 0.019667	-0.0164490 ± 0.031731	-0.0128276 ± 0.021694
N_{comb}	4688.2 ± 443.98	1998.9 ± 230.74	3462.0 ± 293.87
$B_s^0 \to$ 4-body (partially rec. component)			
$\sigma [\,\mathrm{MeV}/c^2\,]$	22.147 (C)	22.147 (C)	22.147 (C)
$m_t [\,\mathrm{MeV}/c^2\,]$	5217.7 (C)	5217.7 (C)	5217.7 (C)
c	-9.79980 (C)	-9.79980 (C)	-9.79980 (C)
p	0.0000 (C)	0.0000 (C)	0.0000 (C)
$Fraction[\%]$	2.1845 ± 0.21661	2.1991 ± 0.23621	2.1385 ± 0.30005
A_{bkg}	0.0000 (C)	0.0000 (C)	0.0000 (C)
$B \to$ 4-body (partially rec. component)			
$m_t [\,\mathrm{MeV}/c^2\,]$	5130.6 (C)	5130.6 (C)	5130.6 (C)
$Fraction[\%]$	0.31081 ± 0.14622	0.35928 ± 0.13624	0.13669 ± 0.19031
A_{bkg}	0.0000 (C)	0.0000 (C)	0.0000 (C)
$B^{\pm} \to K^{\pm}K^{+}K^{-}$ component			
$m_0 [\,\mathrm{MeV}/c^2\,]$	5228.3 (C)	5228.3 (C)	5228.3 (C)
$\sigma_1 [\,\mathrm{MeV}/c^2\,]$	15.050 (C)	15.050 (C)	15.050 (C)
$\sigma_2 [\,\mathrm{MeV}/c^2\,]$	23.550 (C)	23.550 (C)	23.550 (C)
a_1	1.3300 (C)	1.3300 (C)	1.3300 (C)
a_2	0.023000 (C)	0.023000 (C)	0.023000 (C)
$Fraction[\%]$	0.068100 (C)	0.068100 (C)	0.068100 (C)
A_{bkg}	0.0000 (C)	0.0000 (C)	0.0000 (C)
$B^{\pm} \to K^{\pm}\pi^{+}\pi^{-}$ component			
$m_0 [\,\mathrm{MeV}/c^2\,]$	5315.9 (C)	5315.9 (C)	5315.9 (C)
$\sigma_1 [\,\mathrm{MeV}/c^2\,]$	20.110 (C)	20.110 (C)	20.110 (C)
$\sigma_2 [\,\mathrm{MeV}/c^2\,]$	20.380 (C)	20.380 (C)	20.380 (C)
a_1	0.14000 (C)	0.14000 (C)	0.14000 (C)
a_2	0.26000 (C)	0.26000 (C)	0.26000 (C)
$Fraction[\%]$	0.098400 (C)	0.098400 (C)	0.098400 (C)
A_{bkg}	0.0000 (C)	0.0000 (C)	0.0000 (C)

TABLE A.7: List of the $B^{\pm} \to \pi^{\pm}K^{+}K^{-}$ mass fit model parameters extracted from the 2011 sample fit. The numbers followed by a "(C)" were fixed in the corresponding fit.

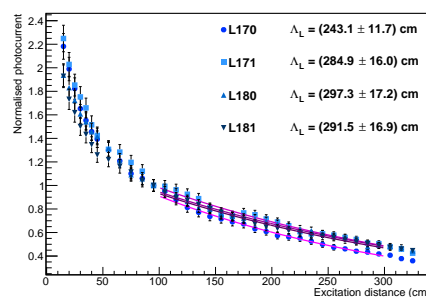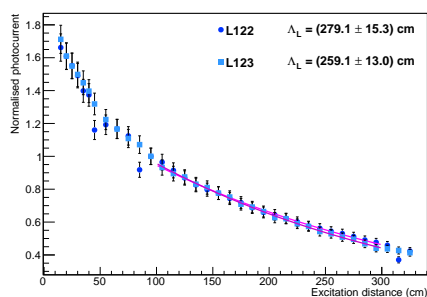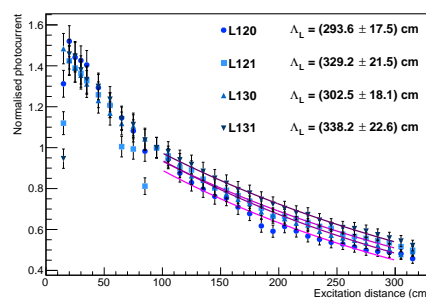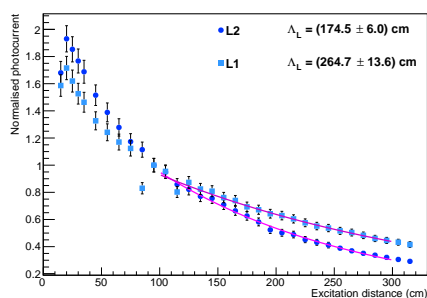|	$B^{\pm} \to \pi^{\pm} K^+ K^-$ (2012 data)		
	L0 Global TIS or L0 Hadron TOS	L0Hadron TOS	L0 Global TIS
Signal component			
m_0[MeV/c^2]	5284.8 ± 0.99991	5284.8 (C)	5284.8 (C)
σ_1[MeV/c^2]	16.192 ± 1.0258	16.192 (C)	16.192 (C)
σ_2[MeV/c^2]	17.434 ± 0.84996	17.434 (C)	17.434 (C)
a_1	0.16290 (C)	0.16290 (C)	0.16290 (C)
a_2	0.084922 (C)	0.084922 (C)	0.084922 (C)
A_{raw}	$-0.135091 \pm {}^{(-0.019992,}_{+0.019919)}$	$-0.107331 \pm {}^{(-0.025228,}_{+0.025257)}$	$-0.191580 \pm {}^{(-0.026973,}_{+0.027312)}$
N_S	$4316.0 \pm {}^{(-150.39,}_{+153.35)}$	$2453.8 \pm {}^{(-73.832,}_{+74.157)}$	$2489.2 \pm {}^{(-81.629,}_{+84.172)}$
Combinatorial component			
b	$-0.00549747 \pm 0.00029570$	$-0.00471687 \pm 0.00036730$	$-0.00593480 \pm 0.00026861$
A_{comb}	0.0016610 ± 0.012337	-0.0207763 ± 0.021267	0.018437 ± 0.013400
N_{comb}	11751 ± 779.22	4519.7 ± 338.50	8937.6 ± 499.00
$B_s^0 \to$ 4-body (partially rec. component)			
σ [MeV/c^2]	22.147 (C)	22.147 (C)	22.147 (C)
m_t [MeV/c^2]	5217.7 (C)	5217.7 (C)	5217.7 (C)
c	-9.79980 (C)	-9.79980 (C)	-9.79980 (C)
p	0.0000 (C)	0.0000 (C)	0.0000 (C)
$Fraction$[%]	2.0057 ± 0.15641	2.0042 ± 0.15252	1.9309 ± 0.20904
A_{bkg}	0.0000 (C)	0.0000 (C)	0.0000 (C)
$B \to$ 4-body (partially rec. component)			
m_t [MeV/c^2]	5130.6 (C)	5130.6 (C)	5130.6 (C)
$Fraction$[%]	0.41073 ± 0.10475	0.53884 ± 0.084035	0.22498 ± 0.13545
A_{bkg}	0.0000 (C)	0.0000 (C)	0.0000 (C)
$B^{\pm} \to K^{\pm} K^+ K^-$ component			
m_0 [MeV/c^2]	5228.3 (C)	5228.3 (C)	5228.3 (C)
σ_1 [MeV/c^2]	15.050 (C)	15.050 (C)	15.050 (C)
σ_2 [MeV/c^2]	23.550 (C)	23.550 (C)	23.550 (C)
a_1	1.3300 (C)	1.3300 (C)	1.3300 (C)
a_2	0.023000 (C)	0.023000 (C)	0.023000 (C)
$Fraction$[%]	0.068100 (C)	0.068100 (C)	0.068100 (C)
A_{bkg}	0.0000 (C)	0.0000 (C)	0.0000 (C)
$B^{\pm} \to K^{\pm} \pi^+ \pi^-$ component			
m_0 [MeV/c^2]	5315.9 (C)	5315.9 (C)	5315.9 (C)
σ_1 [MeV/c^2]	20.110 (C)	20.110 (C)	20.110 (C)
σ_2 [MeV/c^2]	20.380 (C)	20.380 (C)	20.380 (C)
a_1	0.14000 (C)	0.14000 (C)	0.14000 (C)
a_2	0.26000 (C)	0.26000 (C)	0.26000 (C)
$Fraction$[%]	0.098400 (C)	0.098400 (C)	0.098400 (C)
A_{bkg}	0.0000 (C)	0.0000 (C)	0.0000 (C)

TABLE A.8: List of the $B^{\pm} \to \pi^{\pm} K^+ K^-$ mass fit model parameters extracted from the 2012 sample fit. The numbers followed by a "(C)" were fixed in the corresponding fit.
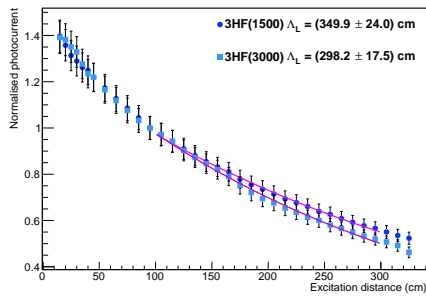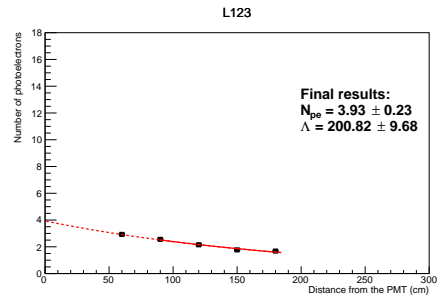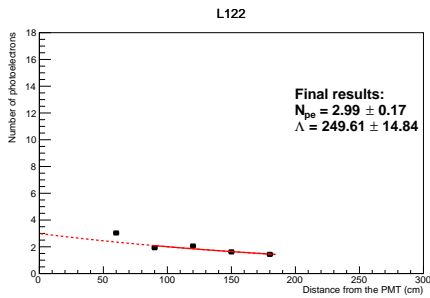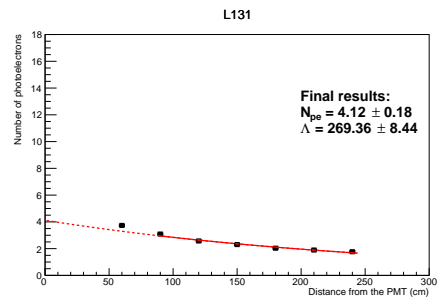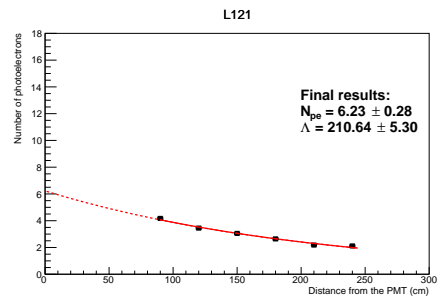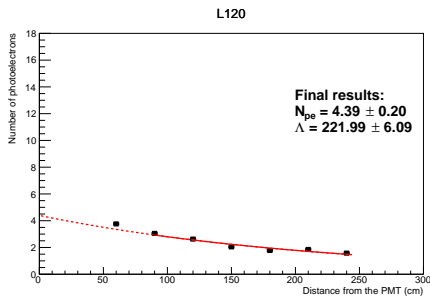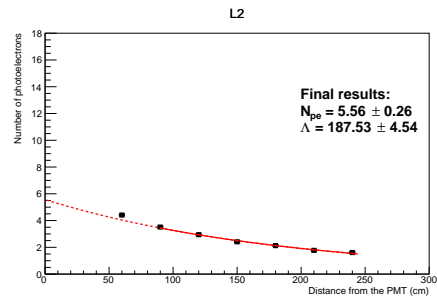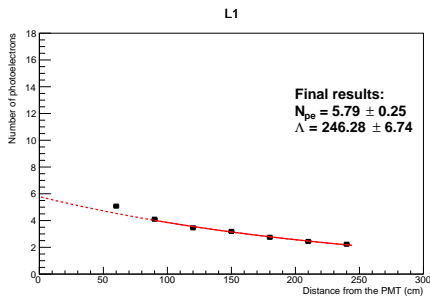
Appendix B

NOL extra plots

This appendix chapter contains all the attenuation length and light yield plots plots which resulted in the information summarised on the Table 7.3.
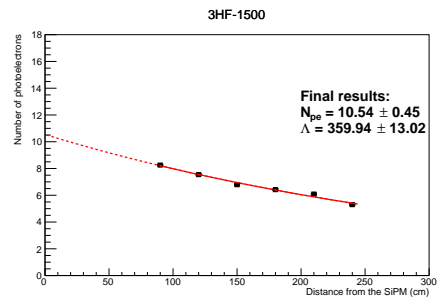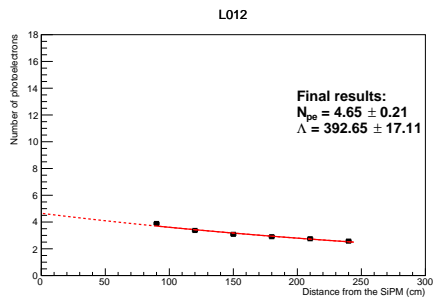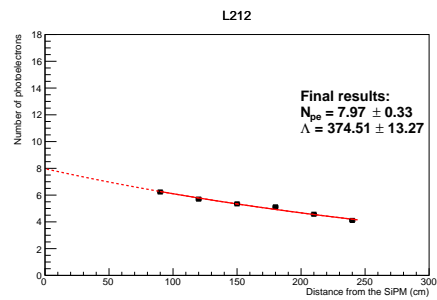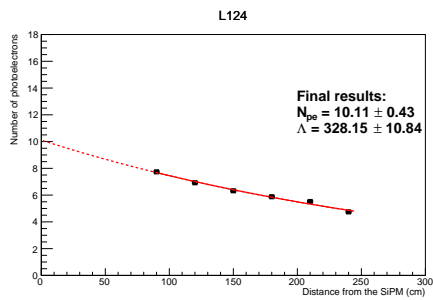
B.1 Attenuation length plots

B.2 Light yield plots

L170

Final results:
N$_{pe}$ = 3.20 ± 0.14
Λ = 319.93 ± 11.94

L171

Final results:
N$_{pe}$ = 3.19 ± 0.14
Λ = 318.25 ± 11.01

L180

Final results:
N$_{pe}$ = 3.49 ± 0.15
Λ = 296.83 ± 10.04

L181

Final results:
N$_{pe}$ = 5.32 ± 0.25
Λ = 187.17 ± 4.54

L182

Final results:
N$_{pe}$ = 5.38 ± 0.23
Λ = 276.74 ± 8.16

L190

Final results:
N$_{pe}$ = 6.21 ± 0.27
Λ = 275.37 ± 8.18

L191

Final results:
N$_{pe}$ = 5.50 ± 0.25
Λ = 229.07 ± 6.08

L193

Final results:
N$_{pe}$ = 6.85 ± 0.29
Λ = 347.56 ± 12.13

L124

Final results:
N$_{pe}$ = 10.11 ± 0.43
Λ = 328.15 ± 10.84

L212

Final results:
N$_{pe}$ = 7.97 ± 0.33
Λ = 374.51 ± 13.27

L012

Final results:
N$_{pe}$ = 4.65 ± 0.21
Λ = 392.65 ± 17.11

3HF-1500

Final results:
N$_{pe}$ = 10.54 ± 0.45
Λ = 359.94 ± 13.02

3HF-3000

Final results:
N_{pe} = 9.32 $\pm$ 0.39
Λ = 431.77 $\pm$ 18.10

Appendix C

List of publications during Ph.D. thesis work

C.1   LHCb puclic notes

- **Ana Bárbara Rodrigues Cavalcante**, Laura Gavardi, Christian Joram and Robert Kristic
  A setup to perform X-ray irradiation tests on scintillating fibres for the SciFi project
  CERN-LHCb-PUB-2017-008 (2017)

- **Ana Bárbara Rodrigues Cavalcante**, François Garnier, Laura Gavardi, Christian Joram, Robert Kristic, Gerhard Pierschel and Thomas Schneider
  Shrinking of bumps by drawing scintillating fibres through a hot conical tool
  CERN-LHCb-PUB-2016-010 (2016)

- **Ana Bárbara Rodrigues Cavalcante**, Laura Gavardi and Christian Joram
  Quality of scintillating fibres after hot bump shrinking
  CERN-LHCb-PUB-2016-009 (2016)

- **Ana Bárbara Rodrigues Cavalcante**, Laura Gavardi, Maurice Glaser, Christian Joram, Matthias Karacson, Robert Kristic, Federico Ravotti and Nicolas Riggaz
  Irradiation of a $2.5\,\mathrm{m}$ long SciFi module with $24\,\mathrm{GeV}/c$ protons to the dose profile expected in LHCb
  CERN-LHCb-PUB-2016-001 (2016)

- **Ana Bárbara Rodrigues Cavalcante**, Robert Ekelhof, Francois Garnier, Pierre-Ange Giudici, Roman Greim, Philip Hebler, Christian Joram, Thomas Kirn, Gerhard Pierschel, Tobias Schateikis, Holger Stevens, Andreas Bach- lechner, Mirco Deckenhoff, Waclaw Karpinski, Florian Kruse, Arndt Schultz Von Dratzig, Georg Schwering, Krzysztof Piotr Swientek and Michael Wlochal

LHCb Scintillating Fibre Tracker: Test Beam Report 2015
CERN-LHCb-PUB-2015-025 (2015)

- **Ana Bárbara Rodrigues Cavalcante**, Cesare Alfieri, Christian Joram and Matthew Kenzie
  An experimental set-up to measure Light Yield of Scintillating Fibres
  CERN-LHCb-PUB-2015-012 (2015)
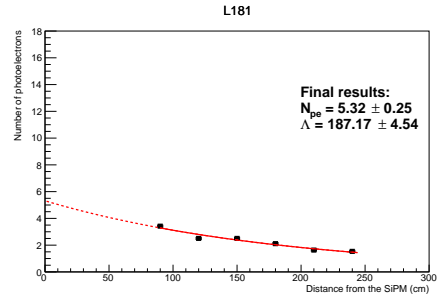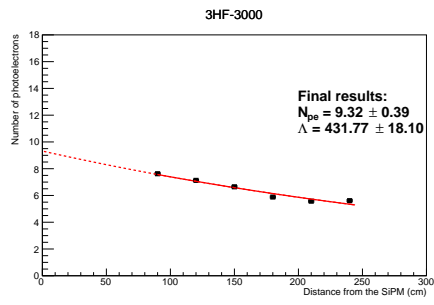
- **Ana Barbara Rodrigues Cavalcante**, Cesare Alfieri and Christian Joram
  A set-up to measure the optical attenuation length of scintillating fibres
  CERN-LHCb-PUB-2015-011 (2015)

- **Ana Bárbara Rodrigues Cavalcante**, Robert Ekelhof, François Garnier, Pierre-Ange Giudici, Roman Greim, Philip Hebler, Christian Joram, Thomas Kirn, Gerhard Pierschel, Tobias Schateikis, Holger Stevens, Andreas Bachlechner, Mirco Deckenhoff, Waclaw Karpinski, Florian Kruse, Arndt Schultz Von Dratzig, Geog Schwering, Krzysztof Piotr Swientek and Michael Wlochal
  Scanners for the quality control of scintillating plastic fibres
  CERN-LHCb-PUB-2015-009 (2015)

C.2   Peer-reviewed publications

- O. Borshchev, O.; Cavalcante, A.B.R.; Gavardi, L.; Gruber, L; Joram, C; Ponomarenko, S.; Shinji, O.; Surin, N.
  Development of a New Class of Scintillating Fibres with Very Short Decay Time and High Light Yield
  Journal of Instrumentation 12 5013 (2017), DOI: 10.1088/1748-0221/12/05/P05013

- Alvarenga Nogueira, J.H. ; Bediaga, I. ; Cavalcante, A.B.R. ; Frederico, T.; Lourenço, O.
  CP violation: Dalitz interference, CPT and FSI
  Phys. Rev. D92 (2015), DOI: 10.1103/PhysRevD.92.054010

- LHCb collaboration
  Measurements of CP violation in the three-body phase space of charmless $B^{\pm}$ decays
  Phys. Rev. D90 (2014), 112004, DOI: 10.1103/PhysRevD.90.112004

Bibliography

[1] O. S. Bruning, P. Collier, P. Lebrun, S. Myers, R. Ostojic, J. Poole, and P. Proudlock. "LHC Design Report Vol.1: The LHC Main Ring". In: (2004). URL.

[2] H Baer, V. Barger, P. Huang, D. Mickelson, A. Mustafayev, and X. Tata. "Post-LHC7 fine-tuning in the minimal supergravity/CMSSM model with a 125 GeV Higgs boson". In: *Phys. Rev.* D87.3 (2013), p. 035017. DOI: 10.1103/PhysRevD.87.035017.

[3] *CERN website: LHC report (2016).* URL.

[4] ATLAS Collaboration, G. Aad et al. "The ATLAS Experiment at the CERN Large Hadron Collider". In: *JINST* 3 (2008), S08003. DOI: 10.1088/1748-0221/3/08/S08003.

[5] CMS Collaboration, S. Chatrchyan et al. "The CMS Experiment at the CERN LHC". In: *JINST* 3 (2008), S08004. DOI: 10.1088/1748-0221/3/08/S08004.

[6] ALICE Collaboration, K. Aamodt et al. "The ALICE experiment at the CERN LHC". In: *JINST* 3 (2008), S08002. DOI: 10.1088/1748-0221/3/08/S08002.

[7] LHCb Collaboration, A. Augusto Alves Jr. et al. "The LHCb Detector at the LHC". In: *JINST* 3 (2008), S08005. DOI: 10.1088/1748-0221/3/08/S08005.

[8] *CERN website: LHC.* URL.

[9] *CERN website: $b\bar{b}$ production angles.* URL.

[10] "LHCb magnet: Technical Design Report". In: (2000). URL.

[11] *CERN website: lhcb magnet.* URL.

[12] "LHCb VELO TDR: Vertex Locator. Technical Design Report". In: (2001). URL.

[13] D. Dossett. "Performance of the LHCb VELO". In: *Nucl. Instrum. Meth.* A718 (2013), pp. 310–311. DOI: 10.1016/j.nima.2012.10.113.

[14] "LHCb: Inner tracker Technical Design Report". In: (2002). URL.

[15] "LHCb: Outer tracker Technical Design Report". In: (2001). URL.

[16] LHCb Outer Tracker Group, R Arink et al. "Performance of the LHCb Outer Tracker". In: *JINST* 9.01 (2014), P01002. DOI: 10.1088/1748–0221/9/01/P01002.

[17] LHCb Collaboration, G. A. Cowan. "Performance of the LHCb silicon tracker". In: *Nucl. Instrum. Meth.* A699 (2013), pp. 156–159. DOI: 10.1016/j.nima.2012.05.074.

[18] LHCb Collaboration, R. Aaij et al. "Measurement of the track reconstruction efficiency at LHCb". In: *JINST* 10.02 (2015), P02007. DOI: 10.1088/1748–0221/10/02/P02007.

[19] "LHCb: RICH Technical Design Report". In: (2000). URL.

[20] LHCb RICH, C. Matteuzzi. "The LHCb RICH system: Detector performance". In: *Nucl. Instrum. Meth.* A766 (2014), pp. 245–249. DOI: 10.1016/j.nima.2014.04.076.

[21] "LHCb calorimeters: Technical Design Report". In: (2000). URL.

[22] LHCb Collaboration, P. Perret and X. Vilasís-Cardona. "Performance of the LHCb calorimeters during the period 2010-2012". In: *J. Phys. Conf. Ser.* 587.1 (2015), p. 012012. DOI: 10.1088/1742–6596/587/1/012012.

[23] "LHCb muon system: Technical Design Report". In: (2001). URL.

[24] A. A. Alves Jr. et al. "Performance of the LHCb muon system". In: *JINST* 8 (2013), P02022. DOI: 10.1088/1748–0221/8/02/P02022.

[25] "LHCb trigger system: Technical Design Report". In: (2003). URL.

[26] T. Head. "The LHCb trigger system". In: *JINST* 9 (2014), p. C09015. DOI: 10.1088/1748–0221/9/09/C09015.

[27] *CERN website: trigger scheme*. URL.

[28] LHCb Collaboration, B. Sciascia. "LHCb Run 2 trigger performance". In: *PoS* BEAUTY2016 (2016), p. 029.

[29] "LHCb online system: Technical Design Report: Data acquisition and experiment control". In: (2001). URL.

[30] *CERN website: Gauss project*. URL.

[31] *CERN website: Boole project*. URL.

[32] *CERN website: Moore project*. URL.

[33] *CERN website: Brunel project*. URL.

[34] *CERN website: DaVinci project*. URL.

[35] *CERN website: Panoramix project*. URL.

[36] LHCb and CMS Collaborations, V. Khachatryan et al. "Observation of the rare $B_s^0 \to \mu^+\mu^-$ decay from the combined analysis of CMS and LHCb data". In: *Nature* 522 (2015), pp. 68–72. DOI: 10.1038/nature14474.

[37] LHCb Collaboration, R. Aaij et al. "Precision measurement of the B_s^0-$\bar{B}_s^0$ oscillation frequency with the decay $B_s^0 \to D_s^-\pi^+$". In: *New J. Phys.* 15 (2013), p. 053021. DOI: 10.1088/1367-2630/15/5/053021.

[38] LHCb Collaboration, R. Aaij et al. "Measurement of the CKM angle γ from a combination of LHCb results". In: *JHEP* 12 (2016), p. 087. DOI: 10.1007/JHEP12(2016)087.

[39] LHCb Collaboration, R. Aaij et al. "Test of lepton universality with $B^0 \to K^{*0}\ell^+\ell^-$ decays". In: *JHEP* 08 (2017), p. 055. DOI: 10.1007/JHEP08(2017)055.

[40] LHCb Collaboration, I. Bediaga et al. "Framework TDR for the LHCb Upgrade". In: (2012). URL.

[41] "LHCb Trigger and Online Upgrade: Technical Design Report". In: (2014). URL.

[42] J. Albrecht, C. Fitzpatrick, V. Gligorov, and G. Raven. "The upgrade of the LHCb trigger system". In: *JINST* 9.10 (2014), p. C10026. DOI: 10.1088/1748-0221/9/10/C10026.

[43] K. Hennessy. "LHCb VELO Upgrade". In: *Nucl. Instrum. Meth.* A845 (2017), pp. 97–100. DOI: 10.1016/j.nima.2016.04.077.

[44] "LHCb VELO Upgrade: Technical Design Report". In: (2013). URL.

[45] "LHCb Tracker Upgrade: Technical Design Report". In: (2014). URL.

[46] LHCb Upstream Tracker Group, O. Steinkamp. "The upstream tracker for the LHCb upgrade". In: *Nucl. Instrum. Meth.* A831 (2016), pp. 367–369. DOI: 10.1016/j.nima.2016.03.022.

[47] A. Abba, M. Artuso, S. R. Blusk, A. Bursche, A. Davis, A. M. Dendek, B. Dey, S. E. Ely, D. C. Forshaw, J. Fu, M. J. Kelsey, F. Lionetto, P. M. Manning Jr, R. Mountain, N. Neri, A. L. Papula, M. Petruzzo, M. M. Pikies, M. S. Rudolph, M. D. Sokoloff, S. Stone, T. Szumlak, and J. Wang. *Study of prototype sensors for the Upstream Tracker Upgrade*. Tech. rep. LHCb-PUB-2016-007. CERN-LHCb-PUB-2016-007. URL. 2016.

[48] C. Joram, U. Uwer, B. D. Leverington, T. Kirn, S. Bachmann, R. J. Ekelhof, and J. Müller. *LHCb Scintillating Fibre Tracker Engineering Design Review Report: Fibres, Mats and Modules*. Tech. rep. LHCb-PUB-2015-008. CERN-LHCb-PUB-2015-008. URL. 2015.

[49]   "LHCb PID Upgrade: Technical Design Report". In: (2013). URL.

[50]   LHCb RICH, S. Easo. "Upgrade of LHCb-RICH detectors". In: *Nucl. Instrum. Meth.* A766 (2014), pp. 110–113. DOI: 10.1016/j.nima.2014.04.084.

[51]   ATLAS Collaboration, G. Aad et al. "Observation of a new particle in the search for the Standard Model Higgs boson with the ATLAS detector at the LHC". In: *Phys. Lett.* B716 (2012), pp. 1–29. DOI: 10.1016/j.physletb.2012.08.020.

[52]   CMS Collaboration, S. Chatrchyan et al. "Observation of a new boson at a mass of 125 GeV with the CMS experiment at the LHC". In: *Phys. Lett.* B716 (2012), pp. 30–61. DOI: 10.1016/j.physletb.2012.08.021.

[53]   Super-Kamiokande, Y. Fukuda et al. "Evidence for oscillation of atmospheric neutrinos". In: *Phys. Rev. Lett.* 81 (1998), pp. 1562–1567. DOI: 10.1103/PhysRevLett.81.1562.

[54]   *Diagram of the Standard Model of particle phsics*. URL. (Visited on).

[55]   T. D. Lee and C. Yang. "Question of Parity Conservation in Weak Interactions". In: *Phys. Rev.* 104 (1956), pp. 254–258. DOI: 10.1103/PhysRev.104.254.

[56]   R. P. Feynman and M. Gell-Mann. "Theory of Fermi interaction". In: *Phys. Rev.* 109 (1958), pp. 193–198. DOI: 10.1103/PhysRev.109.193.

[57]   J. H. Christenson, J. W. Cronin, V. L. Fitch, and R. Turlay. "Evidence for the 2π Decay of the K_2^0 Meson". In: *Phys. Rev. Lett.* 13 (1964), pp. 138–140. DOI: 10.1103/PhysRevLett.13.138.

[58]   Gauthier Durieux and Yuval Grossman. "CP violation: Another piece of the puzzle". In: *Nature Phys.* 13.4 (2017), pp. 322–322. DOI: 10.1038/nphys4068.

[59]   Particle Data Group, C. Patrignani et al. "Review of Particle Physics". In: *Chin. Phys.* C40.10 (2016), p. 100001. DOI: 10.1088/1674-1137/40/10/100001.

[60]   L. Wolfenstein. "Parametrization of the Kobayashi-Maskawa Matrix". In: *Phys. Rev. Lett.* 51 (1983), p. 1945. DOI: 10.1103/PhysRevLett.51.1945.

[61]   P. Koppenburg. "CP violation and CKM studies". In: *PoS* EPS-HEP2015 (2015), p. 028.

[62]   A. D. Sakharov. "Violation of CP Invariance, c Asymmetry, and Baryon Asymmetry of the Universe". In: *Pisma Zh. Eksp. Teor. Fiz.* 5 (1967), pp. 32–35. DOI: 10.1070/PU1991v034n05ABEH002497.

[63] CDF, A. Abulencia et al. "Observation of $B_s^0 - \bar{B}_s^0$ Oscillations". In: *Phys. Rev. Lett.* 97 (2006), p. 242003. DOI: `10.1103/PhysRevLett.97.242003`.

[64] LHCb, R Aaij et al. "Observation of $D^0 - \overline{D}^0$ oscillations". In: *Phys. Rev. Lett.* 110.10 (2013), p. 101802. DOI: `10.1103/PhysRevLett.110.101802`.

[65] Particle Data Group, J. Beringer et al. "Review of Particle Physics (RPP)". In: *Phys. Rev.* D86 (2012), p. 010001. DOI: `10.1103/PhysRevD.86.010001`.

[66] R. H. Dalitz. "On the analysis of τ-meson data and the nature of the τ-meson". In: *Phil. Mag. Ser.7* 44 (1953), pp. 1068–1080. DOI: `10.1080/14786441008520365`.

[67] F. Close. "Richard Dalitz". In: *The Guadian* (Jan. 11, 2004).

[68] Belle and BaBar Collaborations, A. J. Bevan et al. "The Physics of the B Factories". In: *Eur. Phys. J.* C74 (2014), p. 3026. DOI: `10.1140/epjc/s10052-014-3026-9`.

[69] LHCb Collaboration, R Aaij et al. "Measurement of CP violation in the phase space of $B^\pm \to K^\pm \pi^+ \pi^-$ and $B^\pm \to K^\pm K^+ K^-$ decays". In: *Phys. Rev. Lett.* 111 (2013), p. 101801. DOI: `10.1103/PhysRevLett.111.101801`.

[70] BaBar Collaboration, J. P. Lees et al. "Study of *CP* violation in Dalitz-plot analyses of $B^0 \to K^+ K^- K_S^0$, $B^+ \to K^+ K^- K^+$, and $B^+ \to K_S^0 K_S^0 K^+$". In: *Phys. Rev.* D85 (2012), p. 112010. DOI: `10.1103/PhysRevD.85.112010`.

[71] BaBar Collaboration, B. Aubert et al. "Evidence for Direct CP Violation from Dalitz-plot analysis of $B^\pm \to K^\pm \pi^\mp \pi^\pm$". In: *Phys. Rev.* D78 (2008), p. 012004. DOI: `10.1103/PhysRevD.78.012004`.

[72] Belle Collaboration, A. Garmash et al. "Evidence for large direct CP violation in $B^\pm \to \rho(770)^0 K^\pm$ from analysis of the three-body charmless $B^\pm \to K^\pm \pi^\pm \pi^\mp$ decay". In: *Phys. Rev. Lett.* 96 (2006), p. 251803. DOI: `10.1103/PhysRevLett.96.251803`.

[73] M. Bander, D. Silverman, and A. Soni. "CP Noninvariance in the Decays of Heavy Charged Quark Systems". In: *Phys. Rev. Lett.* 43 (1979), p. 242. DOI: `10.1103/PhysRevLett.43.242`.

[74] I. Bediaga, T. Frederico, and O. Lourenço. "CP violation and CPT invariance in $B^\pm$ decays with final state interactions". In: *Phys. Rev.* D89.9 (2014), p. 094013. DOI: `10.1103/PhysRevD.89.094013`.

[75] H. Cheng, C. Chua, and A. Soni. "Final state interactions in hadronic B decays". In: *Phys. Rev.* D71 (2005), p. 014030. DOI: `10.1103/PhysRevD.71.014030`.

[76] J. Therhaag. "TMVA Toolkit for multivariate data analysis in ROOT". In: *PoS* ICHEP2010 (2010), p. 510.

[77] L. Breiman, J. Friedman, R. A. Olshen, and C. J. Stone. *Classification and regression trees*. Chapman and Hall/CRC, 1984.

[78] *CERN website: Luminosity*. URL.

[79] T. Sjostrand, S. Mrenna, and P. Z. Skands. "A Brief Introduction to PYTHIA 8.1". In: *Comput. Phys. Commun.* 178 (2008), pp. 852–867. DOI: `10.1016/j.cpc.2008.01.036`.

[80] D. J. Lange. "The EvtGen particle decay simulation package". In: *Nucl. Instrum. Meth.* A462 (2001), pp. 152–155. DOI: `10.1016/S0168-9002(01)00089-4`.

[81] GEANT4, S. Agostinelli et al. "GEANT4: A Simulation toolkit". In: *Nucl. Instrum. Meth.* A506 (2003), pp. 250–303. DOI: `10.1016/S0168-9002(03)01368-8`.

[82] GEANT4 Collaboration, J. Allison, K. Amako, J. Apostolakis, H. Araujo, P.A. Dubois, et al. "Geant4 developments and applications". In: *IEEE Trans.Nucl.Sci.* 53 (2006), p. 270. DOI: `10.1109/TNS.2006.869826`.

[83] W. Verkerke and D. P. Kirkby. "The RooFit toolkit for data modeling". In: *eConf* C0303241 (2003), MOLT007. arXiv: `physics/0306116 [physics]`.

[84] BaBar Collaboration, P. del Amo Sanchez et al. "Study of $B \to X\gamma$ Decays and Determination of $|V_{td}/V_{ts}|$". In: *Phys. Rev.* D82 (2010), p. 051101. DOI: `10.1103/PhysRevD.82.051101`.

[85] ARGUS, H. Albrecht et al. "Exclusive Hadronic Decays of B Mesons". In: *Z. Phys.* C48 (1990), pp. 543–552. DOI: `10.1007/BF01614687`.

[86] LHCb Collaboration, R Aaij et al. "Measurement of the fragmentation fraction ratio f_s/f_d and its dependence on B meson kinematics". In: *JHEP* 04 (2013), p. 001. DOI: `10.1007/JHEP04(2013)001`.

[87] M. Vesterinen and D. Mueller. *Measurement of the Kaon Detection Asymmetry using Double-tagged Partially Reconstructed D^0 Decays*. Tech. rep. LHCb-INT-2013-054. CERN-LHCb-INT-2013-054. URL. 2013.

[88] LHCb Collaboration, R. Aaij et al. "Measurement of the $D_s^+ - D_s^-$ production asymmetry in 7 TeV pp collisions". In: *Phys. Lett.* B713 (2012), pp. 186–195. DOI: `10.1016/j.physletb.2012.06.001`.

[89] LHCb Collaboration, R. Aaij et al. "Measurement of CP violation in the phase space of $B^\pm \to K^+K^-\pi^\pm$ and $B^\pm \to \pi^+\pi^-\pi^\pm$ decays". In: *Phys. Rev. Lett.* 112.1 (2014), p. 011801. DOI: 10.1103/PhysRevLett.112.011801.

[90] D. Martínez Santos and F. Dupertuis. "Mass distributions marginalized over per-event errors". In: *Nucl. Instrum. Meth.* A764 (2014), pp. 150–155. DOI: 10.1016/j.nima.2014.06.081.

[91] M. Pivk and F. R. Le Diberder. "SPlot: A Statistical tool to unfold data distributions". In: *Nucl. Instrum. Meth.* A555 (2005), pp. 356–369. DOI: 10.1016/j.nima.2005.08.106.

[92] LHCb Collaboration, R. Aaij et al. "Measurements of CP violation in the three-body phase space of charmless $B^\pm$ decays". In: *Phys. Rev.* D90.11 (2014), p. 112004. DOI: 10.1103/PhysRevD.90.112004.

[93] BaBar Collaboration, B. Aubert et al. "Dalitz Plot Analysis of $B^\pm \to \pi^\pm \pi^\pm \pi^\mp$ Decays". In: *Phys. Rev.* D79 (2009), p. 072006. DOI: 10.1103/PhysRevD.79.072006.

[94] LAURA++. http://laura.hepforge.org/.

[95] J. H. Alvarenga Nogueira, I. Bediaga, A. B. R. Cavalcante, T. Frederico, and O. Lourenço. "CP violation: Dalitz interference, CPT, and final state interactions". In: *Phys. Rev.* D92.5 (2015), p. 054010. DOI: 10.1103/PhysRevD.92.054010.

[96] *Kuraray website: Scintillating Fibres*. URL. (Visited on 10/27/2016).

[97] Particle Data Group, K. A. Olive et al. "Review of Particle Physics". In: *Chin. Phys.* C38 (2014), p. 090001. DOI: 10.1088/1674-1137/38/9/090001.

[98] M. Deckenhoff. "Scintillating Fibre and Silicon Photomultiplier Studies for the LHCb upgrade". URL. PhD thesis. TU Dortmund, 2015.

[99] *Saint Gobain Scintillating Fibres*. URL. (Visited on 10/27/2016).

[100] T. T. Böhlen, F. Cerutti, M. P. W. Chin, A. Fassò, A. Ferrari, P. G. Ortega, A. Mairani, P. R. Sala, G. Smirnov, and V. Vlachoudis. "The FLUKA Code: Developments and Challenges for High Energy and Medical Applications". In: *Nucl. Data Sheets* 120 (2014). URL, 211–214. 4 p.

[101] A. Ferrari, P. R. Sala, A. Fassò, and J. Ranft. *FLUKA: A multi-particle transport code (program version 2005)*. URL. 2005.

[102]   A. B. Rodrigues Cavalcante, L. Gavardi, M. Glaser, C. Joram, M.
        Karacson, R. Kristic, F. Ravotti, and N. Riggaz. *Irradiation of a 2.5
        m long SciFi module with 24 GeV/c protons to the dose profile expected in
        LHCb*. Tech. rep. LHCb-PUB-2016-001. CERN-LHCb-PUB-2016-001.
        URL. 2015.

[103]   A. B. Rodigues Cavalcante, R. Ekelhof, F. Garnier, P. Giudici, R. Greim,
        P. Hebler, C. Joram, T. Kirn, G. Pierschel, T. Schateikis, H. Stevens, A.
        Bachlechner, M. Deckenhoff, W. Karpinski, F. Kruse, A. Schultz Von
        Dratzig, G. Schwering, K. P. Swientek, and M. Wlochal. *Scanners for
        the quality contol of scintillating plastic fibres*. Tech. rep. LHCb-PUB-
        2015-009. CERN-LHCb-PUB-2015-009. URL. 2015.

[104]   C. Joram. *LHCb SciFi, the new Fibre Tracker for the LHCb*. URL.

[105]   G. Knoll. *Radiation Detection and Measurement (4th ed.)* URL. Hobo-
        ken, NJ: John Wiley, 2010. ISBN: 9780470131480.

[106]   Y. Koechlin and A. Raviart. "Analyse par échantillonnage sur pho-
        tons individuels des liquides fluorescents dans le domaine de la sub-
        nanoseconde". In: *Nuclear Instruments and Methods* 29 (1964). URL,
        pp. 45–53. DOI: 10.1016/0029-554X(64)90008-4.

[107]   F. J. Lynch. "New liquid scintillators with higher speed and effi-
        ciency". In: *IEEE Transactions on Nuclear Science* 15.3 (1968), pp. 102–
        106.

[108]   J. M. Flournoy. "Measurement of decay times of fast scintillating
        fibers". In: *Radiation Physics and Chemistry* 41.1–2 (1993). URL, pp. 389–
        394. DOI: 10.1016/0969-806X(93)90076-7.

[109]   B. Bengtson and M. Moszyński. "Energy-transfer and light-collection
        characteristics for different types of plastic scintillators". In: *Nuclear
        Instruments and Methods* 117.1 (1974). URL, pp. 227–232. DOI: 10.
        1016/0029-554X(74)90401-7.

[110]   C.M. Hawkes, M. Kuhlen, B. Milliken, R. Stroynowski, E. Wicklund,
        T. Shimizu, and O. Shinji. "Decay time and light yield measurements
        for plastic scintillating fibers". In: *Nuclear Instruments and Methods
        in Physics Research Section A: Accelerators, Spectrometers, Detectors and
        Associated Equipment* 292.2 (1990). URL, pp. 329–336. DOI: 10.1016/
        0168-9002(90)90388-M.

[111]   C. Alfieri, A. B. Rodrigues Cavalcante, and C. Joram. *A set-up to mea-
        sure the optical attenuation length of scintillating fibres*. Tech. rep. LHCb-
        PUB-2015-011. CERN-LHCb-PUB-2015-011. URL. 2015.

[112] C. Alfieri, A. B. Rodrigues Cavalcante, C. Joram, and M. W. Kenzie. *An experimental set-up to measure Light Yield of Scintillating Fibres*. Tech. rep. LHCb-PUB-2015-012. CERN-LHCb-PUB-2015-012. URL. 2015.

[113] *Saint Gobain website: Scintillating Fiber*. URL.

[114] *FiberFin website: POF Diamond Finishing*. URL.

[115] *Hamamatsu website: MPPC (Multi-Pixel Photon Counter) S13360 Series*. URL.

[116] *Hamamatsu website: Driver circuit for MPPC*. URL.

[117] A. B. Rodrigues Cavalcante, L. Gavardi, and C. Joram. *Quality of scintillating fibres after hot bump shrinking*. Tech. rep. LHCb-PUB-2016-009. CERN-LHCb-PUB-2016-009. URL. 2016.

[118] A. B. Rodrigues Cavalcante, F. Garnier, L. Gavardi, C. Joram, R. Kristic, G. Pierschel, and T. Schneider. *Shrinking of bumps by drawing scintillating fibres through a hot conical tool*. Tech. rep. LHCb-PUB-2016-010. CERN-LHCb-PUB-2016-010. URL. 2016.

[119] *Kuraray website: Plastic Scintillating Fibres (Materials and Structures)*. URL. (Visited on 10/27/2016).

[120] C. D'Ambrosio, T. Gys, H. Leutz, and D. Puertolas. "Particle tracking with scintillating fibers". In: *IEEE Trans. Nucl. Sci.* 43 (1996), pp. 2115–2127. DOI: 10.1109/23.502305.

[121] K. Hara, K. Hata, S. Kim, M. Sano, Y. Seiya, K. Takikawa, M. Tanaka, K. Yasuoka, and M. Mishina. "Radiation hardness and mechanical durability of Kuraray optical fibers". In: *Nucl. Instrum. Meth.* A411 (1998), pp. 31–40. DOI: 10.1016/S0168-9002(98)00281-2.

[122] S. A. Ponomarenko, N. M. Surin, O. V. Borshchev, Y. N. Luponosov, D. Y. Akimov, I. S. Alexandrov, A. A. Burenkov, A. G. Kovalenko, V. N. Stekhanov, E. A. Kleymyuk, O. T. Gritsenko, G. V. Cherkaev, A. S. Kechek'yan, O. A. Serenko, and A. M. Muzafarov. "Nanostructured organosilicon luminophores and their application in highly efficient plastic scintillators". In: *Scientific Reports* 4 (2014), 6549 EP -. DOI: 10.1038/srep06549.

[123] T. Yu. Starikova, N. M. Surin, O. V. Borshchev, S. A. Pisarev, E. A. Svidchenko, Yu. V. Fedorov, and S. A. Ponomarenko. "A novel highly efficient nanostructured organosilicon luminophore with unusually fast photoluminescence". In: *J. Mater. Chem. C* 4 (21 2016). URL, pp. 4699–4708. DOI: 10.1039/C6TC00979D.

[124] R. M. Clegg. "The History of Fret". In: *Reviews in Fluorescence*. Ed. by C. D. Geddes and J. R. Lakowicz. Boston, MA: Springer US, 2006, pp. 1–45. DOI: `10.1007/0-387-33016-X_1`.

[125] S. Ornes. "Quantum dots". In: *PNAS* 113.11 (2016), pp. 2796–2797. DOI: `10.1073/PNAS.1601852113`.

[126] D. Yu. Akimov et al. "Development of VUV wavelength shifter for the use with a visible light photodetector in noble gas filled detectors". In: *Nucl. Instrum. Meth.* A695 (2012), pp. 403–406. DOI: `10.1016/j.nima.2011.12.036`.

[127] Y. Jin, H. Aihara, O. V. Borshchev, D. A. Epifanov, S. A. Ponomarenko, and N. M. Surin. "Study of a pure CsI crystal readout by APD for Belle II end cap ECL upgrade". In: *Nucl. Instrum. Meth.* A824 (2016), pp. 691–692. DOI: `10.1016/j.nima.2015.07.034`.

[128] Y. N. Luponosov, N. M. Surin, Susarova D. K., Buzin. M. I, D. V. Anokhin, D. A. Ivanov, P. A. Troshin, and S. A. Ponomarenko. "Nanostructured Organosilicon Luminophores for Effective Light Conversion in Organic Light Emitting Diodes". In: *Organic Photonics and Photovoltaics* 3.1 (2015), pp. 148–155. DOI: `10.1515/oph-2015-0010`.

[129] T. Uekert, A. Solodovnyk, S. Ponomarenko, Osvet A., I. Levchuk, J. Gast, M. Batentschuk, K. Forberich, E. Stern, H. Egelhaaf, and C. J. Brabec. "Nanostructured organosilicon luminophores in highly efficient luminescent down-shifting layers for thin film photovoltaics". In: *Solar Energy Materials and Solar Cells* 155.Supplement C (2016), pp. 1–8. ISSN: 0927-0248. DOI: `https://doi.org/10.1016/j.solmat.2016.04.019`.

[130] C. Joram, G. Haefeli, and B. Leverington. "Scintillating Fibre Tracking at High Luminosity Colliders". In: *JINST* 10.08 (2015), p. C08005. DOI: `10.1088/1748-0221/10/08/C08005`.

[131] *LumInnoTech LLC website*. URL. (Visited on 12/30/2016).

[132] Mu3e, A. Bravar. "The Mu3e Experiment at PSI". In: *Nucl. Part. Phys. Proc.* 260 (2015), pp. 155–159. DOI: `10.1016/j.nuclphysbps.2015.02.033`.

[133] O. Borshchev, A. B. R. Cavalcante, L. Gavardi, L. Gruber, C. Joram, S. Ponomarenko, O. Shinji, and N. Surin. "Development of a New Class of Scintillating Fibres with Very Short Decay Time and High Light Yield". In: *JINST* 12.05 (2017), P05013. DOI: `10.1088/1748-0221/12/05/P05013`.